LEABHARLANN CHOLÁISTE NA TRÍONÓIDE, BAILE ÁTHA CLIATH | TRINITY COLLEGE LIBRARY DUBLIN
Ollscoil Átha Cliath | The University of Dublin

Terms and Conditions of Use of Digitised Theses from Trinity College Library Dublin

Copyright statement

All material supplied by Trinity College Library is protected by copyright (under the Copyright and Related Rights Act, 2000 as amended) and other relevant Intellectual Property Rights. By accessing and using a Digitised Thesis from Trinity College Library you acknowledge that all Intellectual Property Rights in any Works supplied are the sole and exclusive property of the copyright and/or other IPR holder. Specific copyright holders may not be explicitly identified. Use of materials from other sources within a thesis should not be construed as a claim over them.

A non-exclusive, non-transferable licence is hereby granted to those using or reproducing, in whole or in part, the material for valid purposes, providing the copyright owners are acknowledged using the normal conventions. Where specific permission to use material is required, this is identified and such permission must be sought from the copyright holder or agency cited.

Liability statement

By using a Digitised Thesis, I accept that Trinity College Dublin bears no legal responsibility for the accuracy, legality or comprehensiveness of materials contained within the thesis, and that Trinity College Dublin accepts no liability for indirect, consequential, or incidental, damages or losses arising from use of the thesis for whatever reason. Information located in a thesis may be subject to specific use constraints, details of which may not be explicitly described. It is the responsibility of potential and actual users to be aware of such constraints and to abide by them. By making use of material from a digitised thesis, you accept these copyright and disclaimer provisions. Where it is brought to the attention of Trinity College Library that there may be a breach of copyright or other restraint, it is the policy to withdraw or take down access to a thesis while the issue is being resolved.

Access Agreement

By using a Digitised Thesis from Trinity College Library you are bound by the following Terms & Conditions. Please read them carefully.

I have read and I understand the following statement: All material supplied via a Digitised Thesis from Trinity College Library is protected by copyright and other intellectual property rights, and duplication or sale of all or part of any of a thesis is not permitted, except that material may be duplicated by you for your research use or for educational purposes in electronic or print form providing the copyright owners are acknowledged using the normal conventions. You must obtain permission for any other use. Electronic or print copies may not be offered, whether for sale or otherwise to anyone. This copy has been supplied on the understanding that it is copyright material and that no quotation from the thesis may be published without proper acknowledgement.

Investigation of nanosecond and femtosecond pulsed laser deposition and application of some metal nanoparticle films

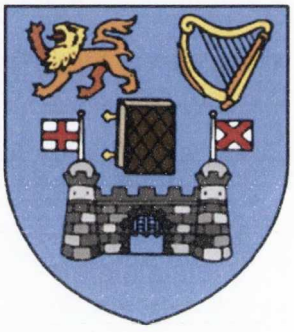

By
Inam Mirza

A thesis submitted for the degree of
Doctor of Philosophy
in the University of Dublin

School of Physics,
Trinity College Dublin,
2012

Declaration

I hereby declare that this thesis has not been submitted as an exercise for a degree in any other university.

This thesis is entirely my own work, except for the advice and assistance mentioned in the acknowledgements.

I agree to allow the library of Trinity College Dublin copy or lend a section or this entire thesis on request.

TRINITY COLLEGE
2 4 MAY 2013
LIBRARY DUBLIN

Thesis 9924

Dedicated to my family,
especially to my late mother

Acknowledgments

All praise to almighty Allah for his blessing in creating us, for giving us the power to find the answers we do not know, to advance in knowledge. Blessing and peace be upon the Holy prophet Muhammad (P.B.U.H) who showed us the right way to become good, happy and successful in life.

I would like to express my deepest gratitude to my supervisor Prof. James Gerard Lunney, Head of School of Physics, Trinity College Dublin, for
his fruitful suggestions, timely guidance, invaluable comments and friendly behaviour. As a supervisor he provided an ideal environment of study and research.

I would like to thank my senior group members Dr. Tony Donnelly, Dr. Enrique Sterling and Dr. Clalia Pagano for their keen interest and skilful guidance in the initial phase of my PhD.

I feel fortune to have lab fellows like Gearoid O' Connell, Isaac Tobin, Dr. Mubarak Mujawar and our new member James Creel for their great cooperation, keen interest and encouragements during my research work. Special thanks to Isaac Tobin for helping me throughout my writing procedure.

I would like to thank Prof. Eithne McCabe, Ciarán Smyth and Dr. Soon Jung from CRANN (Centre of Research in Adaptive Nanoscience and Nanotechnology) with whom I performed my collaborative research work.

I would also wish to thank Dr. Jing Jing Wang from CRANN for his technical support during my work in the photonics lab. Special thanks to Dr Karsten Rode, Dr Karsten Fliesher, Dr Markus Bose, Cathal MacAuley and David O' Mahony and all team members in the CRANN, Advanced Microscopy Research Lab (AML) and the mechanical workshop for the training and support.

I feel grateful to have friends like Ciarán, Niall, Rob, Dave, Vasilis, Shishir, Umar, Kaan Farukh, Irfan, Atif, Arshad and Husayin, the memories and time we spent together will always be cherished by me.

Last but not the least, I wish to express my deepest, heartfelt gratitude to my father, late mother, all my brothers and sisters and especially my wife Semanur for their unceasing support and loving prayers.

Abstract

Pulsed laser deposition (PLD) is a convenient and flexible technique which can be applied to all elemental and compound solids. In conventional PLD a nanosecond (ns) laser is used to ablate the surface of a solid target and a small amount of material expands rapidly from the target as an ionised vapour plume. Condensation of the plume on a non-wetting substrate, together with surface diffusion, leads to the formation of a nanoparticle film; the thickness is controlled by the number of laser pulses. On the other hand with femtosecond (fs) laser irradiation, very rapid heating leads to nanoscale fragmentation of a small amount of target material. Nanoparticles are expelled from the target and can be captured on a substrate. In the present work we have studied the ns- and fs-PLD of some noble and transition metals in vacuum for laser fluence well above the ablation threshold (~1.5 J cm^{-2}). A range of techniques such as Langmuir ion probe, the time and space resolved fast imaging and optical emission spectroscopy and electron microscopy was applied to characterize the laser ablation plumes and to study the morphology of nanoparticle films.

The work can be divided into three parts. In the first part the ns- and fs-ablation plumes were characterized using a Langmuir ion probe to obtain the ion and the atom fluence. The ion and the atom fluence comparison show that for all metals the fs-ablation plume contains a small (~ 1-2 %) fraction of ionized material as compared to the ns-ablation. The morphology of nanoparticle films prepared using both deposition methods was also studied using scanning transmission electron microscopy. The size distribution analysis of nanoparticle films show that the average nanoparticle size for both, ns- and fs-PLD films increases with the equivalent thickness.

In the second part the fs-ablation was studied using fast photography and time and space resolved optical emission spectroscopy. The results show that the plume consists of two distinct components, a fast atomic cloud leaving the target surface with velocity of a few km s^{-1} followed by a slower nanoparticle plume moving normal to the target surface with velocity almost 10 times smaller than the atomic cloud. The spectral radiance of nanoparticle plume was observed to be quite different for different materials.

The final part presents the applications of metal nanoparticle films in the fields of optics and material science. This includes investigation of third order nonlinear optical properties of Au nanoparticles films (Im and Re(χ^3)), the surface enhanced Raman spectroscopy (SERS) using Ag nanoparticle films, the catalytic growth of carbon nanotubes (CNT) using Ni catalysts prepared by PLD and Au nanowire growth which is based on a surface energy driven phenomenon.

TABLE OF CONTENTS

Chapter1 Introduction

Laser ablation is a simple but versatile experimental method that is used for patterning a wide range of materials. The technique has also become a powerful tool for thin film deposition of a diverse range of materials for research and technology purposes. The basic mechanism of laser ablation is based on a high instantaneous power laser pulse focused on to a target surface in order to vaporize a small amount (a few nanograms) of material from the target. In the case of metals, a laser fluence of ≥ 1 J cm^{-2} is required to remove a thin layer of material from the target surface. The first reports on uses of laser radiation to remove or ablate material from solid targets were followed by the development and demonstration of the first working laser in early 1960 by Theodore Miaman [1]. Initially theoretical and experimental studies were carried out in order to understand the interaction of coherent light sources with different solid, liquid and gaseous materials. In 1965 Smith and Turner performed the first experimental study of the deposition of laser ablated material onto a substrate placed normal to the target surface using a ruby laser with a power density of ~ 10^4 W cm^{-2} [2]. However the material selection was limited at that time due to the available laser fluence and wavelength, since the ablation threshold varies for different materials and the optical absorption coefficient of materials is wavelength dependent (absorption coefficient $\alpha = 4\pi k/\lambda$, where k is the imaginary part of the refractive index). As a result of technological development, a major milestone in this field came with the implementation of a reliable Q-switching method and the development of pulsed laser sources such as the pulsed Nd-YAG (neodymium - yttrium aluminium garnet doped crystal solid state) lasers. These lasers could produce ns laser pulses with a power density as high as 10^8 W cm^{-2}. High efficiency second harmonic

generation was also one of the great advancements in laser technology, producing shorter wavelength laser light. The availability of pulsed excimer lasers operating in the ultraviolet (UV) region in 1970s made it possible to have lower absorption depth (higher absorption coefficient) and smaller heated volume since most materials show a strong absorption in 200-400 nm UV-region.

During the 1980s thin films of some complex superconducting materials were prepared using PLD. In 1983, Zaitsev-Zotov and co-workers reported superconductivity for the first time in pulsed laser evaporated oxide superconducting films ($BaPb_{(1-x)}Bi_{(x)}O_3$) after heat treatment [3]. The major breakthrough for the PLD method however came when the technique was successfully used for the epitaxial growth of high temperature superconducting material $YBa_2Cu_3O_7$ at Bell Research Laboratories[4]. These films showed better quality as compared to those prepared by other methods; this also showed that the stoichiometry of the target is maintained during thin film growth.

Later on, the discovery of Ti-sapphire (Ti^{3+}: Sapphire, transition-metal-doped gain media) made it possible to produce ultra-short pulsed lasers with pulse duration of the order of a few hundred of femtoseconds. Ti-sapphire lasers quickly replaced most of the dye lasers which had previously dominated the fields of ultra-short pulse generation and widely tuneable lasers. Todays modern ultra-short pulsed lasers can produce < 70 fs pulses in the wavelength range 650-1100 nm, with a repetition rate of 60-80 MHz[5]. The pulse energy is however of the order of few hundred of micro-Joule (μJ), which is substantially lower than the modern ns pulsed lasers such as, Q-switched Nd-YAG and KrF Excimer lasers, but a tightly focused few hundred μJ pulse can be sufficient to reach the ablation threshold of most materials.

The ablation of solids using fs laser pulses has several interesting features. It has been recently shown that the ultrafast laser ablation in vacuum is a straight-forward route to nanoparticle synthesis. In the last few years Amoruso et al[6] have extensively studied ultrafast laser ablation of several solid materials and concluded that the ablation of any solid target using ultra-short laser pulses with fluences close to the ablation threshold leads to the emission of nanofragments of target material. The materials which have extensively been studied were Ni, Si, Fe and Au. The results of their studies were also in line with the theoretical calculations. The mechanism for fs-laser ablation is quite different as compared to ablation using ns pulses. For long ns pulses, the laser energy is absorbed by a thin layer on the material surface (~ 10 nm in depth) and this causes the surface temperature to rise above the melting point of the target material. As the material melts it continues to absorb energy from the laser pulse and is evaporated, the laser energy is also absorbed by this evaporated material causing it to become ionised forming a plasma plume in front of the target surface.

In fs-laser ablation the pulse-width is shorter than the electron-phonon coupling time by 2-3 orders of magnitude and all the significant processes, such as transient change in lattice structure and material removal from the target surface takes place after the laser pulse. Briefly, the laser energy is delivered to the lattice in a very short time scale (few ps) and the absorption of laser energy and heating occur at nearly solid density. The heated region can thus reach initially very high temperature resulting in very strong pressure gradients within the material. A nearly adiabatic expansion of the heated material eventually occurs with a consequent decrease in its density and temperature. It is during this adiabatic cooling that parts of the system can be driven into a metastable region of the phase diagram, resulting in the production of a large fraction of nanoparticles as described by recent numerical analysis

of fs-laser ablation of solid targets[7]. However, PLD using both ns and fs pulsed lasers has successfully been applied to the deposition of high quality thin films of metals and different complex oxides [8]. A more detailed discussion of the applications of PLD for functional material growth such as polymers, organic thin films, Nitrides and different noble and transition metals can be found in review by Eason [9].

For a lot of applications it is important to monitor the thickness of the deposited films accurately. Most commonly a quartz crystal deposition monitor (QCM) can be used to measure the equivalent thickness (area density/solid density). The QCM can be placed at the position of the substrate and be used to monitor the thickness during deposition. Other techniques for thickness monitoring involve measuring the reflectivity of a thin film, like in *in-situ* optical reflectrometry in which optical reflectivity of a growing thin film in the vacuum chamber is measured at a single wavelength. By comparing the measured reflectivity with the Fresnel calculations, the thickness of the deposited material can be obtained. The X-ray reflectivity of a thin film can also be measured using a X-ray diffractometer to obtain the equivalent solid density thickness[10]. This technique is called grazing incidence X-ray reflectivity (XRR) (since the reflectivity is measured at a shallow angle $< 6^{o}$)[11], the explanation of this method will be given in Ch 3. XRR has an advantage over methods as it measures simultaneously the thickness the average density and the rms value of surface and interface roughness of the deposited film. In this work we have used QCM and XRR methods to control and measure the thickness of the deposited material.

One of the undesirable results of PLD is that the particle emission from the laser ablation plume is highly forward peaked, which results in non-uniform film thickness. Several methods have been purposed to yield a homogeneous thickness over a large substrate area.

These include utilising a rotating target and computer controlled translation of the substrate which has been used to deposit uniform films over 5 cm diameter substrates[12].

PLD can also be used in a reactive gas environment. The background gas is mainly used for two purposes; first the formation of multi-cation thin films requires reactive species e.g. molecular oxygen for oxide growth. Interaction of ablated material with the background gas produces molecular species in the ablation plume. These species facilitate muti-cation phase formation. The background gas in the ablation chamber can also be used to reduce the kinetic energy of the ablated species. Time-of-flight measurements of ions in the ablation plume at low pressure inert gas environment have shown that the background gas can significantly reduce the plume energies, which further reduces the resputtering effect of already deposited material[13]. A 10% decrease in the sputtering yield was observed in an Ar pressure of ~ 4×10^{-2} mbar in Ag film prepared by ns-PLD[13].

1.1 Laser ablation for nanomaterial synthesis

Laser interaction with materials has the unique advantage of rapid synthesis and processing as well as *in-situ* characterization of the nanoparticles. Laser vaporization has been a tool for the synthesis of metal clusters by mass spectrometry[14]. In 1985, a successful experiment was performed in which graphite was vaporized using a high power laser to form a carbon plasma which resulted in the discovery of stable clusters such as C_{60}[15]. The aim in this experiment was to understand the mechanism by which long-chain carbon molecules are formed in interstellar space.

In the following years, laser ablation was also applied to vaporise and deposit multi-component targets (carbon and metal catalysts) at high substrate temperature and in a

background gas environment to synthesise carbon nanotubes and semiconductor nanowires[16]. These discoveries and investigations promoted the use of lasers in nanomaterial synthesis and a lot of interest in understanding the underlying mechanisms. The fabrication of nanoparticle films of different elemental and compound solids using PLD is more recent. It has been observed that ultrathin films (< 10 nm) produced by ns-PLD are nanostructured. The nanoparticle growth takes place when high energy (~100 eV) species from ns ablation plume impinge on the substrate surface and make some nucleation sites. The ions in the ablation plume are also sufficiently energetic enough to provide the activation energy for surface diffusion. The surface diffusion along with the coalescence between small nanoparticles leads to growth of nanostructures on the substrate surface, motion of adatoms up to 12 nm has been reported in ultrathin films produced by ns-PLD[17]. In general, the nucleation and growth mechanisms depend on experimental parameters such as fluence (J cm^{-2}), deposition flux, substrate temperature, and the background gas pressure. Generally the nucleation density on the substrate surface increases with the deposition flux. Depending on the experimental conditions, three growth modes are possible for PLD films[12]; (i) Three dimensional island growth mode (the Volmer-Weber growth mode) (ii) Two dimensional full monolayer growth mode (Frank-Van der Merwe) and (iii) two-dimensional growth of full monolayers followed by three dimensional islands (Stranski-Krastinov)[18]. These growth modes are usually applied to steady state deposition processes, such as conventional thermal evaporation (molecular beam epitaxy (MBE)) and sputtering.

Optical emission spectroscopy and fast photography based experiments show the ablation plume in fs-PLD is composed of two main components. A fast atomic cloud which leaves the target at expansion velocities of a few kilometre per second followed by a slow nanoparticle

plume moving normal to the target surface with velocity of a few hundred meters per second. By placing the substrate in the path of this forward directed plume, nanoparticles can be collected on the substrate surface. A more detailed theory of fs-laser ablation is given in Ch. 2, the experimental results of fs-PLD of Ni, Au and Ag nanoparticle films is given in Ch. 5.

1.2 Outline of thesis

One of the aims of this thesis work was to make a thorough comparison of PLD of nanoparticle films with ns and fs laser pulses, including their morphology, size distribution, and optical absorption spectra. We also analyze the laser ablation plumes in both cases using an electrostatic Langmuir ion probe[19]. The Langmuir ion probe analysis gives us information about several physical quantities of the laser produced plasma (LPP) including the ionization fraction, ion densities as well as the energy distribution of particles in the ablation plume. A homemade energy selective time-of-flight mass spectrometer (ES-TOFMS) was also used to analyze the fs-laser ablation plume.

The investigation of nanoparticles was further examined by optical emission spectroscopy (OES). The fs-ablation plumes of Ag, Au and Ni metals were studied using time- and spatially-resolved OES. The optical emission from the fs nanoparticle plume was used to estimate its velocity and temperature. The last part of this thesis was devoted to describe some of the applications of metal nanoparticle films in the fields of nonlinear optics, surface enhanced Raman spectroscopy, and the preparation of metal-semiconductor alloys for metal (Au) nanowire growth.

1.3 Overview of chapters

Chapter 2

The theoretical description of laser ablation and the main process involved in ns- and fs-laser ablation of metals is described. The detail of the ablation plume expansion model developed by Anisimov et al[20] is also given. The model describes the three dimensional adiabatic expansion of laser ablation plume in vacuum. Theoretical description of the optical properties of metal nanoparticles and the detail of models which can be used to simulate the optical absorption of nanoparticle films is given.

Chapter 3

The experimental methods used in this thesis are described. The detail of lasers and the vacuum system used for ns and fs-PLD is given; the pulse width of ns and fs lasers was also measured using a fast photodiode and an autocorrelation method respectively. An introduction to the use of a Langmuir ion probe for laser produced plasma (LPP) characterization is given. Furthermore, thin film characterization methods, and the detail of optical emission spectroscopy of the fs-laser ablation plume is also given.

Chapter 4

The ns- and fs-laser ablation plumes are characterized using the Langmuir ion probe by measuring the ion fluence, the atom fluence and average ion energies in the ablation plume. The ns- and fs-ablation material removal and ion production efficiency (ions and atoms ablated per mJ of laser energy) was also calculated. The spatial profile of the fs laser was also measured for spot size and fluence measurements. The morphology of Ag, Ni and Au nanoparticle films prepared using ns- and fs-PLD was studied using scanning transmission

electron microscopy. The optical absorption spectra of Ag nanoparticle films prepared using ns and fs-PLD was measured to study the surface plasmon resonance feature and the optical absorption was also compared with existing theoretical models.

Chapter 5

The fs-ablation plume of Ag, Au and Ni was studied using space and time resolved fast imaging and optical emission spectroscopy. The interesting feature in fs-laser ablation of metals is the emission of a fast (v ~ few km s^{-1}) atomic and a slow (v ~ few m s^{-1}) nanoparticle plume. The velocity of the atomic and nanoparticle plumes were calculated from the space and time resolved ICCD images. The plasma parameters (such as density and temperature) and the temperature of nanoparticles were obtained from the intensity-calibrated optical emission spectra of both plumes.

Chapter 6 and 7

These chapters describe the application of metal nanoparticle films in the field of optics and material science. In chapter 6, third order nonlinear optical properties of Au nanoparticle prepared using ns and fs-PLD were studied. The third order nonlinear refractive index and absorption coefficient were obtained using a simple technique called z-scan. Chapter 7 describes the results of experiments in which the Ag, Ni and Au nanoparticle films were used for SERS, catalytic growth of CNT and for the preparation of metal-semiconductor alloys for metal nanowire growth.

Chapter 8

The main conclusion resulting from the work in this thesis and the possibilities of future work are given in this chapter.

Part of this thesis work was published / submitted to following journals

1- Surface-enhanced Raman spectroscopy (SERS) using Ag nanoparticle films produced by pulsed laser deposition
C. A. Smyth, I. Mirza, J. G. Lunney and E. M. McCabe
(Accepted by Applied Surface Science)

2-Fabrication of metal nanoparticle films using pulsed laser deposition
Inam mirza and James G Lunney
(30th ICPIG, August 28th – September 2nd 2011, Belfast, Northern Ireland, UK)
(http://mpserver.pst.qub.ac.uk/sites/icpig2011/187_D13_Mirza.pdf)

3-Fabrication of Ag nanoparticle films using femtosecond pulsed laser deposition
Inam Mirza, Jing Jing Wang and James G. Lunney
Submitted to Nanotechnology

4- Surface-enhanced Raman spectroscopy using silver nanoparticle films produced by nanosecond and femtosecond pulsed laser deposition
I. Mirza, C. A. Smyth, J. J. Wang, J. G. Lunney and E. M. McCabe
(Submitted)

5-Surface-enhanced Raman spectroscopy of pterins
Ciarán A. Smyth, Inam Mirza, James G. Lunney, and Eithne M. McCabe
Proc. SPIE 8234, 82341G (2012);

6-Poster contribution in national Ireland Nanotechnology conference
(Nanoweek Conference 2011-2012: Nanotechnology: Research Excellence & Commercial Opportunities) Inam Mirza, Gearoid O'Connell and James G. Lunney.

1.4 References

1 T. H. Maiman, Nature **187** (4736), 493 (1960).

2 H. M. Smith and and A. F. Turner, Appl. Opt. **4** (1), 147 (1965).

3 R.A. Martynyuk S.V. Zaitsev-Zotov, and E.A. Protasov, Soviet Physics Solid State **25**, 100 (1983).

4 D. Dijkkamp, T. Venkatesan, X. D. Wu, S. A. Shaheen, N. Jisrawi, Y. H. Min-Lee, W. L. McLean, and M. Croft, Applied Physics Letters **51** (8), 619 (1987).

5 Coherent 900 family; modelocked Ti:Sapphire laser system (http://www.coherent.com/products/?921/Mira-Family).

6 S. Amoruso et al., Journal of Physics D: Applied Physics **40** (2), 331 (2007).

7 S. Eliezer, N. Eliaz, E. Grossman, D. Fisher, I. Gouzman, Z. Henis, S. Pecker, Y. Horovitz, M. Fraenkel, S. Maman, and Y. Lereah, Physical Review B **69** (14), 144119 (2004).

8 H. M. Christen and G. Eres, Journal of Physics: Condensed Matter **20** (26), 264005 (2008).

9 E. Robert, in *Pulsed laser deposition of thin films applications-led growth of functional materials* (John Wiley & Sons, Inc., 2006).

10 S. Banerjee, M. K. Sanyal, A. Datta, S. Kanakaraju, and S. Mohan, Physical Review B **54** (23), 16377 (1996).

11 T. C. Huang and W. Parrish, Adv in X-ray Anal **35A**, 137 (1992).

12 D.B. Chrisey and G.K. Hubler, *Pulsed laser deposition of thin film.* (John Wiley & Sons, Inc., New York, 1994).

13 K. Sturm, S. Fähler, and H. U. Krebs, Applied Surface Science **154–155** (0), 462 (2000).

14 T. G. Dietz, M. A. Duncan, D. E. Powers, and R. E. Smalley, The Journal of Chemical Physics **74** (11), 6511 (1981).

15 H. W. Kroto, J. R. Heath, S. C. O'Brien, R. F. Curl, and R. E. Smalley, Nature **318** (6042), 162 (1985).

16 X. Duan and C. M. Lieber, Advanced Materials **12** (4), 298 (2000).

17 A. V. Zenkevich, M. A. Pushkin, V. N. Tronin, V. I. Troyan, V. N. Nevolin, G. A. Maximov, D. O. Filatov, and E. Lægsgaard, Physical Review B **65** (7), 073406 (2002).

18 G. D. Spiller and M. Hanbucken J. A. Venables, Rep. Prog. Phys. **47**, 399.

19 B. Doggett and J.G. Lunney, Journal of Applied Physics **105** (3), 033306 (2009).

20 S. I. Anisimov, B. S. Luk'yanchuk, and A. Luches, Applied Surface Science **96-98**, 24 (1996).

Chapter 2 Theory

2.1 Laser ablation

The basic mechanism of laser ablation is based on a high instantaneous power (~ 10-100 MW) pulsed laser beam focused on a target surface in order to vaporise a small amount (few nanograms) of material from the target. In the case of metals, a laser fluence of ≥ 1 J cm^{-2} is required to remove a thin layer of material from the target. The absorption of laser light in this vaporised material leads to ionization of the evaporated atoms and hence a thin layer of dense plasma is formed on the target surface. The steep pressure gradient in this plasma layer drives it mainly in the forward direction i.e. the transverse component of velocity is much smaller than the forward component of velocity. This expanding puff of plasma is called the laser ablation plume, a theoretical expansion model of this plasma plume has been described by Anisomov[1]. By placing a substrate in the path of this plume, the material in the plasma can be deposited on the substrate which is known as pulsed laser deposition (PLD). Both ns and fs pulsed lasers can be used for the ablation and deposition process. Below the mechanisms involved for each of the pulsed laser systems are described.

2.2 Nanosecond laser ablation

The main parameters involved in laser matter interactions are the surface reflectivity at a particular laser wavelength, the optical absorption depth and the thermal diffusion depth during the laser pulse. The optical absorption depth is given by:

$$d_{opt} = \frac{\lambda}{4\pi k} \qquad 2\text{-}1$$

where k is the imaginary part of complex refractive index and λ is the laser wavelength. The optical absorption coefficient α can be written as $\alpha = (d_{opt})^{-1}$. Also the heat diffusion depth is given by:

$$d_{th} = \sqrt{4D\tau_l} \qquad 2\text{-}2$$

where D [cm^2 s^{-1}] is the thermal diffusitivity of the target material and τ_l is the laser pulse duration. Thermal diffusivity tells us how fast heat moves through the substance and is given by:

$$D = \frac{\kappa}{\rho c_p} \qquad 2\text{-}3$$

where κ is the thermal conductivity, ρ is the mass density and c_p is the specific heat capacity of the material. In the case of metals, the laser radiation is absorbed by the electrons at the target surface which cause excitation of conduction electrons at the metal surface, the electron goes to the excited state (well above Fermi level) and thermalize over a time scale τ_e (few hundreds of fs). Energy from the conduction electrons is then transferred to the lattice by electron-phonon coupling which occur on a time scale of τ_{ep}. For most metals the electron-phonon coupling time (τ_{ep}) is of the order of few picoseconds and $\tau_e << \tau_{ep}$. In the case of the nanosecond pulsed laser, the pulse length (τ_l) is longer than the electron-phonon coupling time (τ_{ep}) i.e. $\tau_e << \tau_{ep} << \tau_l$. The temperature of electron and phonon subsystems

equilibrates at a very early stage of the laser pulse duration. Melting of the target starts early in the laser pulse and further heating increases the temperature of this melt layer to boiling point. As the temperature approaches boiling point vapour is formed on the target surface. Typically this occurs long before the end of the laser pulse (provided the laser fluence is large enough). The latter part of the pulse is then absorbed in the vapour. This laser absorption leads to heating and ionisation of vapour and a plasma plume is formed on the target surface which is known as a laser produced plasma (LPP). Figure 2-1 illustrates the essential steps of nanosecond (ns) laser ablation of a solid target.

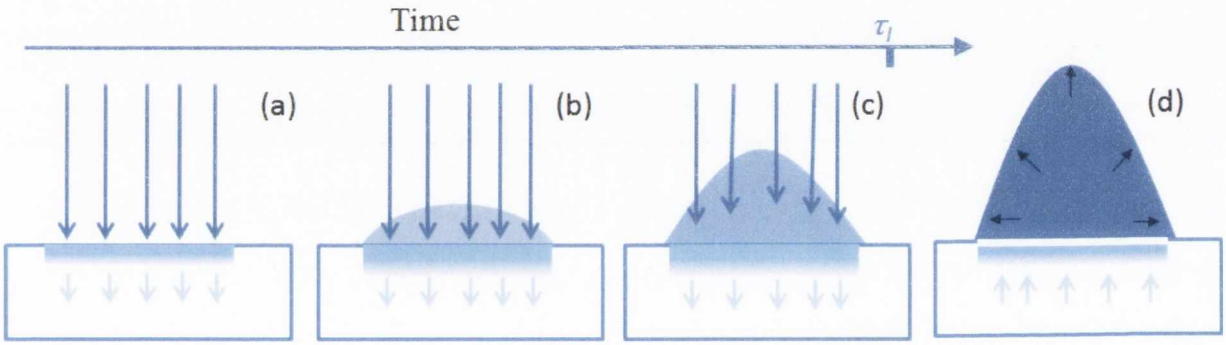

Figure 2-1 Schematic illustration of pulsed laser ablation of a solid target (a) Initial absorption of laser radiation (indicated by long arrows) at the target surface, melting and vaporization begin (shaded area indicates melted material, short arrows indicate the motion of solid–liquid interface). (b) Melt front propagates into the solid, vaporization continues and laser-plume interactions start. (c) Absorption of incident laser radiation by the plume, plasma formation. (d) Melt front recedes leading to re-solidification of the irradiated area and 3-dimension adiabatic expansion of the plasma plume.

The values of specific heat capacity, thermal conductivity and mass density of Ag are 0.235 J g^{-1} K^{-1} and 4.27 W cm^{-1} K^{-1} and 10.49 g cm^{-3} (at 300 K) which gives a value for the thermal diffusivity D = 1.71 cm^2 s^{-1}. The melting and boiling point values are ≈ 1235 K and 2435 K respectively [2] . If we take the example of a Ag target irradiated with a KrF Excimer laser

with λ = 248 and τ_l = 25 ns, the thermal diffusion depth $d_{th} \sim 2.6\,\mu m$ and the optical absorption depth at λ = 248 nm is $d_{opt} \sim 12\,nm$. Which shows that the thermal or heat diffusion depth is much larger than the optical absorption depth i.e. ($d_{opt} \ll d_{th}$) hence the radiant energy flux from the laser can be treated as a source term at the surface and the laser heating can be modeled as a surface heat source. The laser heating can then be described by the following equations:

$$\rho c_p \left(\frac{\partial T}{\partial t}\right) = -\frac{\partial}{\partial z}\big(Q(z)\big) + \mathrm{S} \qquad 2\text{-}4$$

where

$$Q(z) = -\kappa\left(\frac{\partial T}{\partial z}\right),\ \mathrm{S} = I_o(1-R)\alpha\exp(-\alpha z)$$

Here z is the direction perpendicular to the target surface, $Q(z)$ is the heat flux, S is the laser heating source term, I_o is the laser intensity, R and α are the surface reflectivity and optical absorption coefficient of the target, c_p is the specific heat capacity of the system, and κ is the thermal conductivity.

An analytic solution of this problem for temperature T as a function of time t and distance z from the target surface is given by Tokarev and Kaplan [3]:

$$T(z,t) = \frac{2(1-R)I_o}{c_p\rho}\sqrt{t/D}\ ierfc\left(\frac{z}{2\sqrt{Dt}}\right) + T_i \qquad 2\text{-}5$$

Where T_i is the initial surface temperature and *ierfc* is the first integral of the error function (*erfc).* Letting $z = 0$, the surface temperature as a function of time is given by:

$$T(0,t) = \frac{2(1-R)I_o}{c_p\rho}\sqrt{t/\pi D} + T_i \qquad 2\text{-}6$$

which can be used to predict the surface temperature during the laser pulse for ns pulsed laser ablation. After the end of laser pulse the surface temperature is described by:

$$T(0,t>\tau_l) = \frac{2(1-R)I_o}{c_p\rho}(1/\pi D)^{\frac{1}{2}}\left(t^{1/2} - (t-\tau_l)^{1/2}\right) + T_i \qquad 2\text{-}7$$

Figure 2-2 shows the temperature profile of a Ag target irradiated using a KrF excimer (248 nm, 23 ns) laser pulse at 0.5, 0.8 and 1 J cm^{-2}. The reflectivity of Ag was taken to be 0.27 for 248 nm wavelength [4] and the values of c_p and D are the same as before. The above model was developed to describe the surface heating and to obtain the melt depth during the pulse and maximum melt depth without taking the vaporisation of the target into account. It can be seen that at laser fluence of 0.5 J cm^{-2} is just enough to increase the surface temperature of the Ag target towards melting point (≈1235 K). It should be noted that for the above calculation constant values of c_p, D and κ were used, though in fact the thermal properties of high-temperature materials (materials with high melting point) depends on temperature [2] for which it would be more appropriate to use temperature dependent values of the thermo-

physical parameters. Furthermore, the optical properties of such materials like absorption, reflectivity and emissivity are also temperature dependent[5].

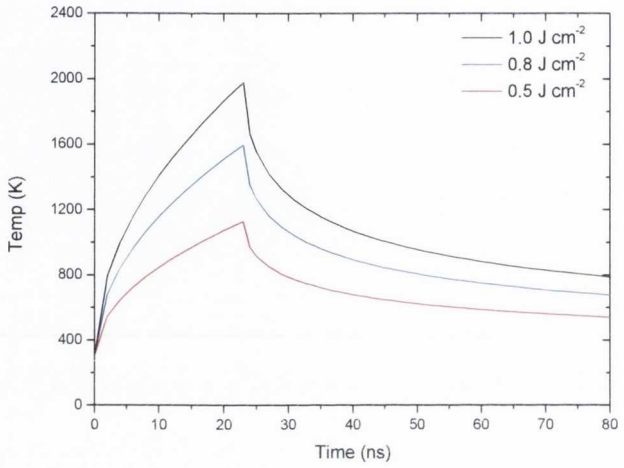

Figure 2-2 Surface temperature of Ag target irradiated using 248 nm and 23 ns laser pulses with various laser fluences. The temperature before and after the laser pulse was calculated using Eq. 2-26 and 2-27 respectively.

A more detailed theoretical description for ns-laser ablation of metals can be found in the model described by S. Amoruso [6] and by Lunney *et al.*[7]. The model developed by Lunney *et al.* gives a simple solution of the above problem and will be described in the following section.

According to this model the laser beam first interacts with the target surface, resulting in the vaporization of material from the surface layer. Following this the interaction of the vaporized material with the incident laser results in the heating and ionization of this vapor and thus in plasma formation. The model also gives an insight to the mechanisms by which the laser gets absorbed in the evapourated material. As has been described previously, in ns-

laser ablation the heat diffusion depth is larger than the optical diffusion depth, hence laser heating can be considered as a surface heating source term. The change in the target's surface temperature can be described by Duhamal's theorem:

$$T_s(t) = T_i - \frac{L_F}{c_p} + \frac{1}{\sqrt{\pi\kappa\rho c_p}} \int_0^t \frac{I_s(t-\tau)}{\sqrt{\tau}} d\tau \qquad 2\text{-}8$$

Where L_F is latent heat of fusion, T_0 is the initial target temperature, I_s is the laser irradiance reaching the target surface and the quantities $T_i\ \kappa\ \rho\ c_p$ are as in Eq 2-4

$$I_s = (1 - R_L) I_L \exp\left(-\frac{\sigma n l}{cos\theta}\right) + I_p(1 - R_p) - \left(\frac{d(Nl)}{dt}\right) L_V \qquad 2\text{-}9$$

Where I_L, I_p are laser and plasma irradiance respectively, θ represents the angle of incidence of the laser. R_L and R_p are the target reflectivity for the laser and plasma emissions respectively. N is the average particle density (atoms+ions) in the vapour, l is the thickness of vapour layer and L_V is the heat of vaporisation per atom. The product $Nl\sigma$ is the optical opacity of the plasma layer, hence the first term in the above equation accounts for the absorption of the incident laser irradiance I_L by the evaporated particles, the second term accounts for the irradiance due to the plasma self-emission and the last term accounts for the heat of vaporisation loss by the target material. The rate of change of the number of particles per unit area (Nl) in the plasma is related to the vapour pressure $P_v(T_s)$:

$$\frac{d(Nl)}{dt} = P_v(T_s)\sqrt{\frac{1}{2\pi M k_B T_s}} \qquad 2\text{-}10$$

Where M is the atomic mass, and k_B is the Boltzmann constant. The vapour pressure P_v depends strongly on the surface temperature T_s and is given by the Clausius-Clapeyron equation:

$$P_v(T_s) = P_0 exp\left[\frac{L_v}{k}\left(\frac{1}{T_0} - \frac{1}{T_s}\right)\right] \qquad 2\text{-}11$$

Where P_0 is the equilibrium vapour pressure at temperature T_0 which is usually taken as the boiling point at atmospheric pressure and k_B is the Boltzmann`s constant.

The absorption of laser in the evaporated material leads to heating and ionization of the vapor thus forming plasma. The vapour layer thus reduces the energy reaching the target surface; as a result the ablation rate is reduced. In the ionized vapour, a sufficient number of electrons will be present. For a plasma in local thermodynamic equilibrium the ionization can be calculated through the following Saha equation [8]:

$$\frac{n_{l+1} n_e}{n_l} \cong 2\left(\frac{2\pi m_e k_B T}{h^2}\right)^{3/2} e^{-E_i^{l+1}/k_B T} \qquad 2\text{-}12$$

Where n_l is the number density of lth ions (where $l = 0, 1, ...$ and $l = 0$ corresponds to number density of neutrals) and n_e is the density of electrons respectively, k_B is the

Boltamann constant and E_i^{l+1} is the ionization energy of $(l+1)th$ ionization state. It can be seen that in the plasma inverse bremsstrahlung (IB) will be one of the mechanisms of absorption. In IB absorption, an electron may absorb a photon in the presence of the electric field of an ion and thus gain kinetic energy (K.E). This will further produce ionization of atoms or ions via collisions. The IB coefficient at a photon energy $h\nu$ is given by [7,8]:

$$\alpha_{IB} = \frac{2\sqrt{2}\, z^6}{3\sqrt{3\pi}\hbar\, m\, z^{3/2} k^{1/2}} \frac{Z^2 n_i n_e}{T_P^{7/2}} \left(\frac{k_B T_p}{h\nu}\right)^3 \left(1 - exp\left(-\frac{h\nu}{KT_p}\right)\right) cm^{-1} \qquad 2\text{-}13$$

Where z represents the ionisation state, T_p is plasma electrons and ions temperature, n_i and n_e are electron and ion densities in cm^{-3} respectively. For typical experimental conditions of laser ablation of metals, such as iron using an excimer laser ($\lambda = 248nm$), the plasma layer parameters would be; $k_B T_p = 3eV$, $Z=2$, $n \approx 5\times 10^{18}\ cm^{-3}$ [7] which gives $\alpha_{IB}=0.18\ cm^{-1}$. Lunney *et al*[7]. suggested that the absorption due to IB is significantly small for ionization of vapour and plasma formation, hence there must be other absorption mechanisms which need to be taken into account. Another absorption mechanism which exists in the plasma is photoionization. In photoionization, the bound electron absorbs a photon of energy higher than its ionization potential. As a result, the electron is freed and the excess photon energy goes into the K.E. of the electron. The exact calculation of absorption and self-emission from a dense LPP is complicated. It requires detailed calculation of the population of bound-states and information of Stark broadening. Lunney *et al.* simplified the problem by assigning a single photoionization absorption cross section to both atoms and

ions. The value was taken to be the threshold value of hydrogen-like photoionization cross section [8].

$$\sigma_P = 7.9 \times 10^{-18} \left(\frac{E_1^*}{h\nu}\right) \left(\frac{I_H}{E_1^*}\right)^{1/2} cm^2 \qquad 2\text{-}14$$

where I_H is the ionization energy of the hydrogen atom, E_1^* is the typical ionization energy of the excited states which can be photoionized. Taking E_1^* equals to the photon energy of the laser, i.e. 5 eV ($\lambda = 248nm$), gives $\sigma_P = 1.3 \times 10^{-17} cm^2$. The absorption cross section for IB is given by $\sigma_{IB} = \frac{\alpha_{IB}}{Zn_e} = 1.8 \times 10^{-20} cm^2$. This shows that the photoionization absorption coefficient is about 3-orders of magnitude greater than the IB absorption coefficient at short or UV wavelengths.

Above a description was presented of a simple theoretical model for ns-laser ablation, which describes target heating and laser absorption mechanisms in the vapour. In principle LPP absorb and emit radiation with three main mechanisms known as bound-bound, bound-free and free-free transitions. In bound-bound transitions the electron can absorb photon of energy equal to the energy difference between discrete energy levels. The examples of bound-free and free-free transitions have been described above as photoionization and IB absorption. Figure 2-3 represents a general energy level diagram representing these three kinds of process.

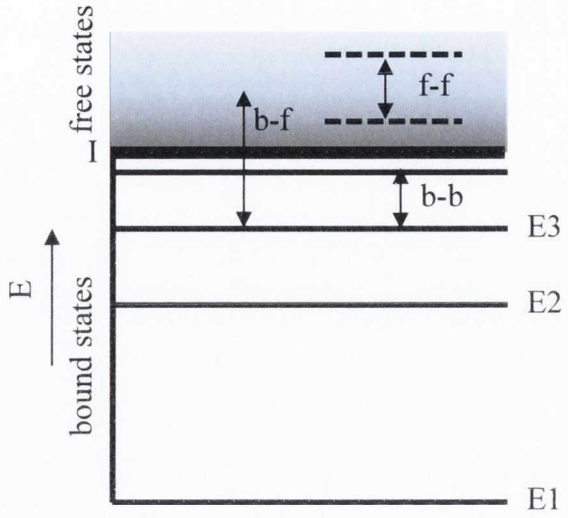

Figure 2-3 Electronic transitions in a LPP, *I* (the thick horizontal black line) represents the ionization limit.

However bound-bound transitions are more significant in the later stage of plasma expansion. It has been observed via optical emission spectroscopy that the early stage (< 10 ns) emission from the laser produced plasma is a continuum. After a short time delay, when the plasma starts to expand and cool, the atomic spectra with discrete spectral lines start to appear[9, 10]. Generally the absorption coefficient for such plasmas α_{pl} are written as $\alpha_{pl} = \alpha_{IB} + \alpha_p$ (where α_{IB} accounts for absorption coefficient for both electron-atom and electron-ion collisions) in order to calculate the attenuation of the laser intensity in ablation plume. The starting point in the theoretical modeling is usually Beer-Lambert law i.e $I_0 = I_{inc}\exp(-\alpha_{pl}x)$ where I_{inc} is the incident laser intensity. It has also been suggested that in ns-laser ablation, the ablated material may contain small clusters of the target material, which are generated by the condensation of supersaturation vapour in the ablation plume. Hence the absorption of light

by these small clusters should also be taken into account for the laser absorption in the plume [11]. The appropriate absorption coefficient for nanoclusters with a size smaller than the wavelength of light *($r<\lambda$)* is given by the Mie absorption coefficient $\alpha_{Mie}=n_{cl}\sigma_{Mie}$, where σ_{Mie} is the Mie absorption cross section and n_{cl} is the number density of the clusters [12]. The exact nature of the early stage continuum emission is however not clear at this stage. A recent review article by Deepak Marla *et al*[13]. gives more detail and a summary of significant contributions in ns-laser ablation modeling.

2.3 Femtosecond laser ablation

The physical mechanisms involved in fs-laser ablation are quite different to those described above for ns-laser ablation. Typically in the case of metals, the deposited laser energy is absorbed by the conduction band electrons near the metal surface. This deposited laser energy equilibrates quickly (~ 200 fs) among electrons and more slowly is transferred to the lattice, depending on the electron-phonon coupling time of the target material. Finally, a thermal equilibrium is established between electrons and phonons and heat flow from the surface region to the bulk of the irradiated target can be described by common thermal diffusion.

In the case when the laser pulse is less than the time needed for electron-phonon thermalisation, a state of non-equilibrium is created by laser irradiation. The absorption of laser energy and redistribution of this energy as heat in the lattice can, in this case, can be described by a so-called two temperature model (TTM) [14].

$$C_e(T_e)\frac{\partial T_e}{\partial t} = \frac{\partial}{\partial z}\left(k_e(T_e)\frac{\partial T_e}{\partial z}\right) - G(T_e)(T_e - T_l) + S(z,t) \qquad 2\text{-}15$$

$$C_l(T_l)\frac{\partial T_l}{\partial t} = \frac{\partial}{\partial z}\left(k_l(T_l)\frac{\partial T_l}{\partial z}\right) + G(T_e)(T_e - T_l) \qquad 2\text{-}16$$

Where C_e and C_l are the volumetric heat capacities at constant pressure and κ_e and κ_l are the thermal conductivities for the electrons and the lattice respectively (subscripts e and l represent electron and lattice). T_e and T_l are the electron and lattice temperatures and G is the electron-phonon coupling constant. The constant $S(z,t)$ is the laser source term which defines the local laser energy transfer per unit volume and unit time by the laser pulse during its pulse duration. To find the temporal variation of T_e and T_l, the above coupled differential equations can be solved numerically, and under certain assumptions, analytical solutions can also be found.

As an illustration of the model, a temperature profile of a 50 nm Ni thin film taken from Ref. [15] is shown in the Figure 2-4, the laser pulse duration in this case is 200 fs. From this calculation it can be seen that the electrons are subjected to an extraordinary heating rate while the lattice remains comparably cold in the early stages. After a period of time which is determined by energy transfer time between electrons and the lattice via electron-phonon scattering, the lattice temperature increases and the electron temperature reduces correspondingly. After a few ps the lattice temperature increases further, passing the melting point (T_m) (see Figure 2-4), and finally electron and lattice temperature becomes approximately equal at ~ 20 ps

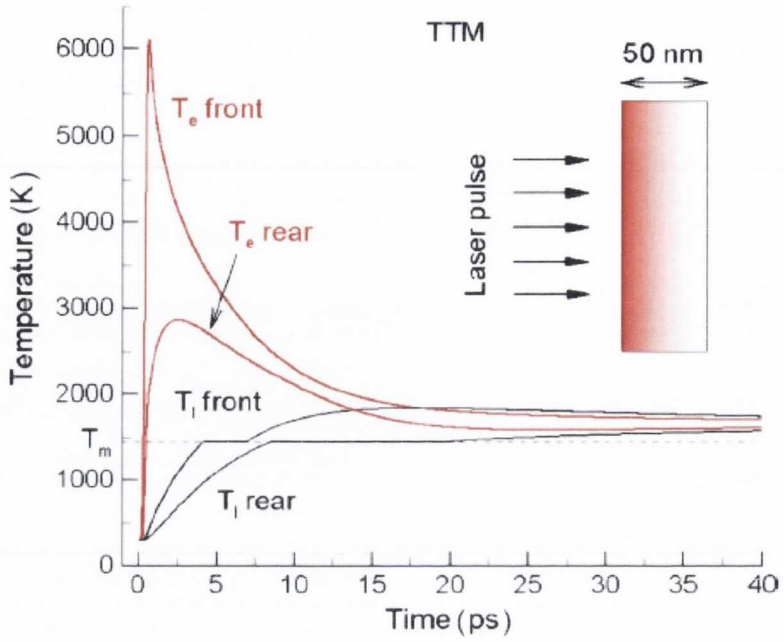

Figure 2-4 Time dependent temperature profile of electron and lattice predicted by the two temperature model (TTM). For a 50 nm Ni film irradiated with a 200 fs laser pulse at an absorbed fluence of 430 J/m2. Notations front and rear refer to front & rear surface of the film. From Ref. [15].

The electron-phonon relaxation time i.e the time at which the laser energy is transferred from electron-to-lattice via e-phonon scattering is usually taken as the time during which the temperature difference between electron and phonon decreses by a factor of 'e'[15,16]. From the plot in Figure 2-4 this time is ≈ 9 ps. The initial increase in electron temperature depend on laser fluence, a higher fluence will lead to a higher initial electron temperature (which increases in just initial few tens of fs) but this will not significantly affect the electron-phonon relaxation time.

Several other models have been proposed for the fs-laser ablation of solid targets in the form of molecular dynamic (MD) and hydrodynamic simulation[15,17,18]. MD simulation involves

numerically solving the equation of motion of interacting particles (atoms and molecules) at different interval of time, and takes into account the force between interacting particles as well as their positions and acceleration. Amoruso *et al.* have studied the fs-laser ablation of Ni both experimentally and theoretically using a MD simulation for 300 fs-laser pulses at 527 nm and ~ 0.8 J cm^{-2} [18]. Their theoretical predictions also agree well with the experimental results. They also have shown that the fs-ablation plume consists of mainly two components: (a) a cloud of fast atomic species which leaves the target with very high expansion velocity (~ 10 km/sec), (b) a secondary plume component constituted of nanoparticles expending in vacuum with a velocity almost ten times smaller than the velocity of the atomic components. The second component can be characterized by quite different dynamics. As an example, a visible self-emission ICCD image of an ablation plume at time delay of 400 ns and 1.0 μs after the laser pulse onset, and the snapshot and molecular dynamic simulation image of the ablation process for a fs-laser ablation of Ni in vacuum (from Ref. [18]) is shown in Figure 2-5.

Figure 2-5 (a) and (b) indicates that at short time delays (< 100 ns) both a fast forward-directed component (atomic species) and a slow long-lasting component are present (see intensity profile of the plume emission image). At later time, the fast plume gradually moves away from the target, while its overall emission drops rapidly with time and the slow part of plume expands in vacuum and remains close to the target surface up to a very long time delay. Figure 2-5 (c) shows a snapshot of the ablation plume molecular dynamic (MD) simulation taken at a time delay of 150 ps after the laser pulse onset, the negative *z* values correspond to position inside the original surface. In the MD-simulation image we can see

that the ablation has already reached a free expansion regime with very few collisions between atoms and the final ablation depth ~100 nm.

The origin of the decomposition of irradiated material into the two classes of species observed in the fs-ablation plumes has been described in terms of the relaxation path of the irradiated material in its temperature-density diagram. It has been suggested that after irradiation of a metal target by an ultrashort laser pulse, different layers of material located at different depths in the target undergo different degrees of extreme heating. This results in the simultaneous occurrence of various decomposition mechanisms. The upper most layer is over-heated and directly decomposes into a gas/plasma of fast atomic components. While the decomposition of material located more deeply in the target occurs through a phase explosion mechanism. Ivanov *et al*[15] suggested that the phase explosion is one of the primary mechanism in fs-laser ablation of metals. They studied the cases of fs-laser ablation of thin Ni and Au sheets using 200 fs laser pulses in the MD-simulation. According to their findings, the irradiation of a metal target with ultrashort laser pulses rapidly heats the target to above melting point at the temperature close to the critical point and derives the material into a metastable state. The homogeneous nucleation of the bubbles starts to occur at this stage with extremely high rate and bubbles are formed into the metastable liquid which leads to the explosive expansion of material into a mixture of liquid droplets, gas phase molecules and small clusters.

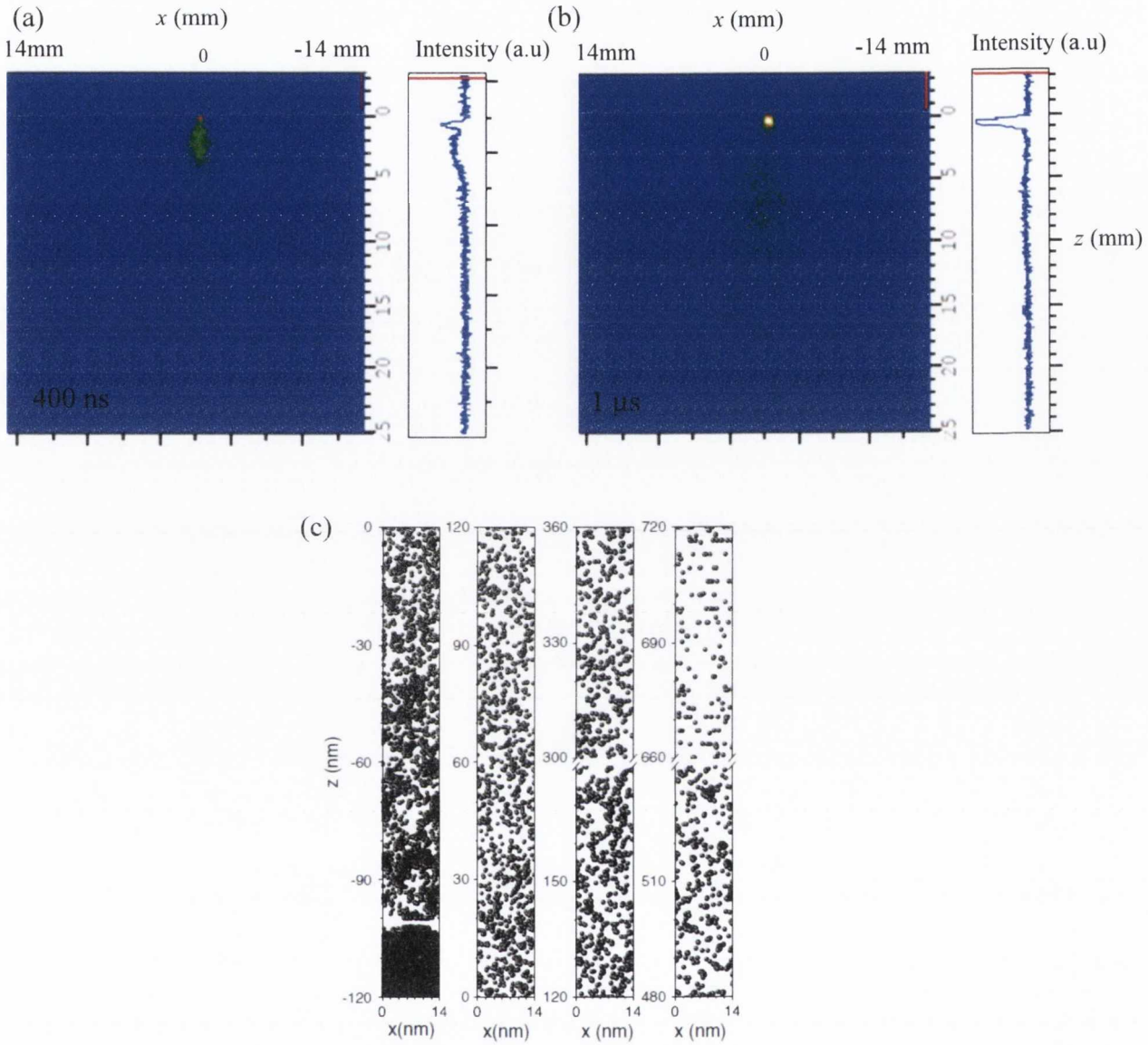

Figure 2-5 (a) and (b) ICCD Images of Ni fs-laser ablation plume (λ=800 nm, pulse duration 130 fs and peak laser fluence ~ 1.4 J/cm^2) at 400 ns and 1.0 µs time delay after the laser pulse. (c) Snapshot of MD simulation of the ablation process at 150 ps after the laser pulse onset (from Ref. [18]). Ablation parameters are; λ=527 nm, pulse duration 300 fs FWHM pulse width, laser fluence F~ 0.8 J cm^{-2}. z=0 corresponds to the surface of Ni target. Negative values of z correspond to the interior of original target material.

2.4 Ablation plume expansion

In this section the ablation plume expansion model of S. I. Anisimov[19] will be described. The model gives a gas dynamic description of the three-dimensional adiabatic expansion of a laser ablation plume. Although it was initially developed to describe the expansion of a neutral gas cloud it has been successfully used to describe the expansion of a LPP generated by ns-laser ablation in vacuum[20,21]. The model is based on certain assumptions, (i) that the plume expansion is adiabatic i.e. it expands freely in vacuum after the laser pulse ends so that no heat enters or leaves the system, (ii) the expansion is isentropic i.e. there is no heat exchange within the plasma as it propagates, (iii) the expansion is self-similar which means that the physical quantities, such as pressure and density, remains constant on semi-ellipsoid surface. Figure 2-6 is a schematic diagram of laser ablation plume expansion, the initial plume was created at time $t=0$. It is assumed that the laser spot is of elliptical shape and the radii of the initial plume in the xy plane can be taken as X_0 and Y_0 (the radii of the laser spot). The initial thickness of the plume in the z-direction can be approximated as $Z_0 \approx c_s \tau_\ell$ where c_s is the speed of sound and τ_ℓ is the laser pulse duration and the overall shape of the plume is semi-ellipsoidal.

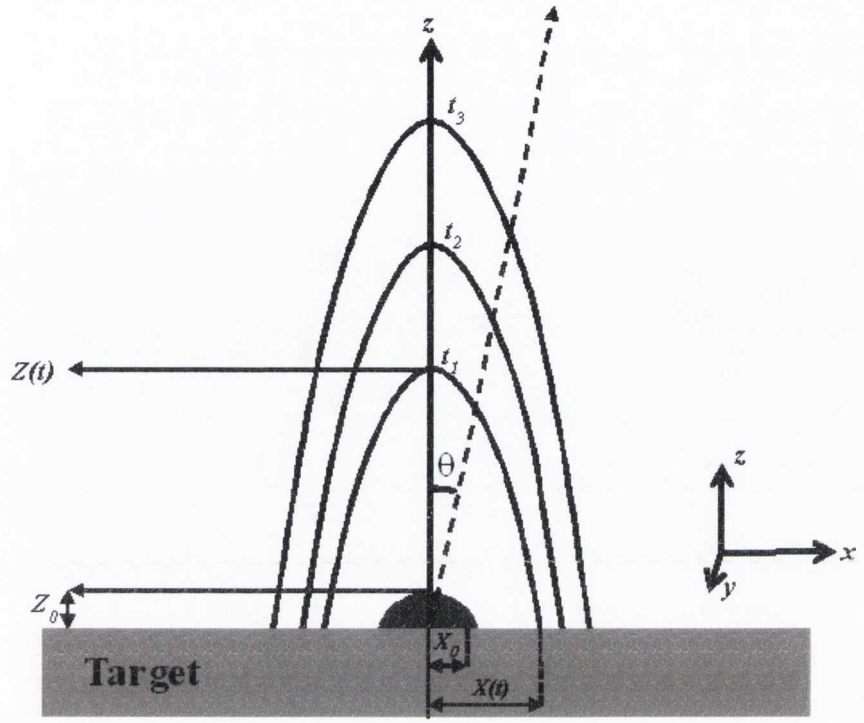

Figure 2-6 Schematic of temporal and spatial expansion of laser ablation plume.

The gas dynamic equations are:

$$\frac{\partial \rho}{\partial t} + \nabla \cdot (\rho \boldsymbol{v}) = 0$$

$$\frac{\partial \boldsymbol{v}}{\partial t} + (\boldsymbol{v} \cdot \nabla)\boldsymbol{v} + \frac{1}{\rho}\boldsymbol{\nabla} p = 0 \qquad \text{2-17}$$

$$\frac{\partial S}{\partial t} + (\boldsymbol{v} \cdot \nabla) S = 0$$

Where ρ, p, v and S are the density, pressure, velocity and entropy of the gas respectively. Furthermore the plume is considered as an ideal gas with the adiabatic constant $\gamma = \frac{C_p}{C_v}$, for a monoatomic gas at room temperature $\gamma = \frac{5}{3}$. A solution of the above gas dynamic equations was derived by Anisimov assuming that the flow parameters are constant over the ellipsoid surface. According to this solution the density and pressure profile can be written as:

$$\rho(x,y,z,t) = \frac{M_p}{I_1(\gamma)XYZ}\left[1 - \frac{x^2}{X^2} - \frac{y^2}{Y^2} - \frac{z^2}{Z^2}\right]^{\alpha} \qquad 2\text{-}18$$

$$p(x,y,z,t) = \frac{E_p}{I_2(\gamma)XYZ}\left[\frac{X_oY_oZ_o}{XYZ}\right]^{\gamma-1}\left[1 - \frac{x^2}{X^2} - \frac{y^2}{Y^2} - \frac{z^2}{Z^2}\right]^{\gamma\alpha} \qquad 2\text{-}19$$

where M_p and E_p are the mass and energy of the initial vapor cloud. The values of $I_1(\gamma)$ and $I_2(\gamma)$ are:

$$I_1(\gamma) = \frac{\pi^{3/2}\Gamma(\alpha+1)}{2\Gamma(\alpha+5/2)}, I_2(\gamma) = \frac{\pi^{3/2}\Gamma(\alpha+2)}{2(\gamma-1)\Gamma(\alpha+7/2)} \qquad 2\text{-}20$$

here $\Gamma(z)$ is the Gamma-function, and assuming the initial vapour cloud is isentropic $\alpha = 1/\gamma - 1$. The solution for the entropy is given by [1]:

$$S = \frac{1}{\gamma-1} ln\left\{\frac{E_p(\gamma-1)}{X_0Y_0Z_0I_2(\gamma)}\left(\frac{X_0Y_0Z_0I_2(\gamma)}{M}\right)^{\gamma}\left[1 - \frac{x^2}{X^2} - \frac{y^2}{Y^2} - \frac{z^2}{Z^2}\right]^{1-\alpha}\right\} \qquad 2\text{-}21$$

Using Eqs. 2-18, 2-19 and 2-20 the gas dynamic equations can be reduced to ordinary differential equations:

$$\ddot{X} = -\frac{\partial U}{\partial X}$$

$$\ddot{Y} = -\frac{\partial U}{\partial Y} \qquad 2\text{-}22$$

$$\ddot{Z} = -\frac{\partial U}{\partial Z}$$

$$U = \frac{5\gamma - 3}{\gamma - 1}\frac{E_p}{M_p}\left[\frac{X_o Y_o Z_o}{XYZ}\right]^{\gamma-1}$$

The initial conditions for above equations are set as:

$$X(0)=Y_0, Y(0)=Y_0, Z(0)=Z_0 \quad \text{and} \quad \dot{X}(0), \dot{Y}(0), \dot{Z}(0) = 0$$

In order to integrate Eq. 2-22 numerically, it can be transformed into the following dimensionless form with X_0 Y_0 and Z_0 as spatial length scales.

$$\xi\frac{\partial^2\xi}{\partial^2\tau} = \eta\frac{\partial^2\eta}{\partial^2\tau} = \zeta\frac{\partial^2\zeta}{\partial^2\tau} = \left[\frac{\eta_0\zeta_0}{\xi\eta\zeta}\right]^{\gamma-1} \qquad 2\text{-}23$$

With initial conditions as:

$$\xi(0) = 1, \eta(0) = \eta_0, \zeta(0) = \zeta_0$$

$$\dot{\xi}(0) = \dot{\eta}(0) = \dot{\zeta}(0) = 0$$

where $\eta_0 = \frac{Y_0}{X_0}$ and $\zeta_0 = \frac{Z_0}{X_0}$

In above equation ξ ,η, ζ and τ are dimensionless position and time coordinates defined as :

$$\xi = \frac{X}{X_0}, \eta = \frac{Y}{Y_0}, \zeta = \frac{Z}{Z_0}, \tau = \frac{t}{t_0}$$

2-24

$$t_0 = \frac{\sqrt{\beta}}{X_0};\ \beta = (5\gamma - 3)\frac{E_p}{M_p}$$

The numerical solution of the above set of equations gives the temporal evolution of the plume radii and hence gives the plume shape. The plume expansion behavior can be illustrated by choosing the initial parameters. The values of X_0 and Y_0 can be taken as major and minor radii of elliptical laser focal spot, for ns laser ablation the value of initial thickness can be approximated as $Z_0 \approx c_s \tau_\ell$ the velocity of sound is given by:

$$c_s = (\gamma(\gamma - 1)\varepsilon)^{1/2};\ \varepsilon = \frac{E_p}{M_p} \qquad 2\text{-}25$$

Eq. 2-23 was solved numerically using a computer program written in Mathematica. The discription of the code is given in Appendix A. Figure 2-7 shows the temporal variation of the plume radii and plume aspect ratios for some typical experimental conditions (X_0:Y_0:Z_0 =

1:0.750:0.084 mm and $\gamma = 1.25$*)*. Different plume characteristics can be observed from the above plots.

Initially the pressure gradient is greater in the z direction given that the dimension is much smaller in that direction as compared to the dimensions on the xy plane which gives the characteristic ellipsoidal shape to the plume. As the plume begins to expand, the strong pressure gradients accelerate the plume, while these pressure gradients goes to zero after some time and plume expansion becomes inertial. We can see in the Figure 2-7 (b) that the acceleration phase lasts for ~ 70-80 ns.

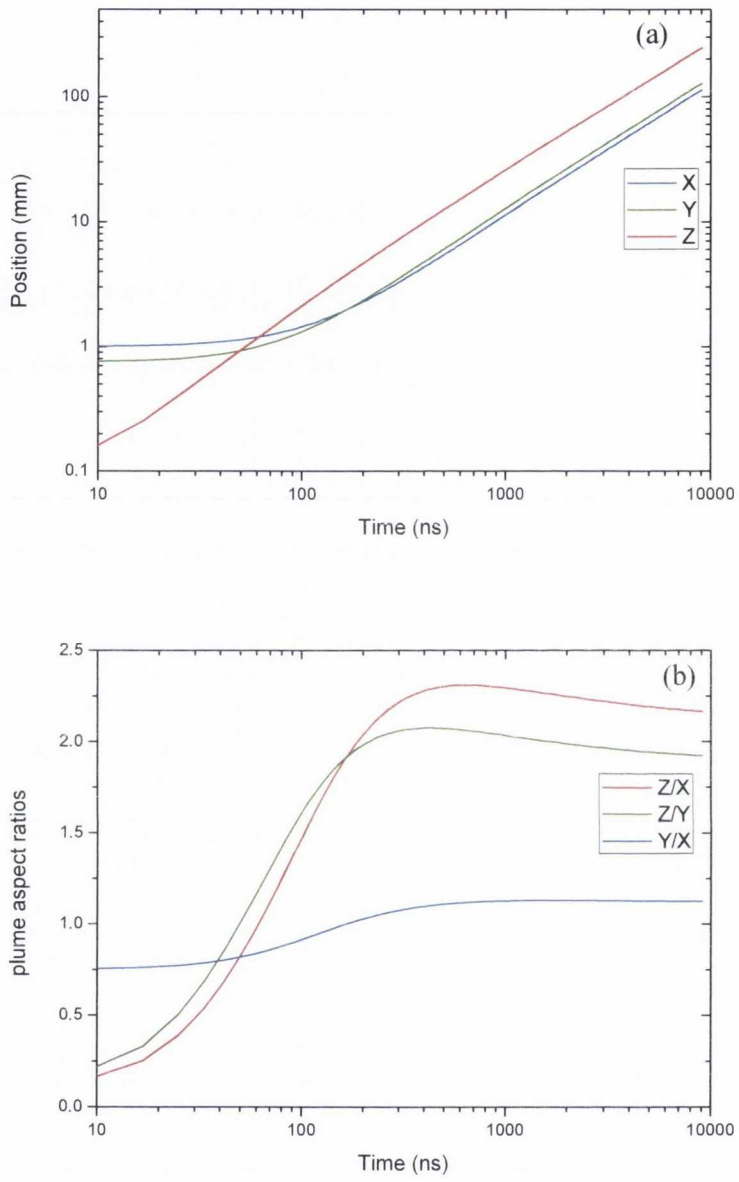

Figure 2-7 Evolution of (a) plume radii and (b) plume aspect ratio as a function time.

From the plume aspect ratios (*Z/X, Z/Y, Y/X*) it can also be seen that initially the ratio $Y/X < 1$ and becomes greater than one as the plume moves away from the target. This effect is known as flip-over effect and is a reflection of above described pressure gradients in *xz* and *yz*

planes. Furthermore the values of k_{zx} and k_{yz} determines the angular spread of the particle flux in the *yz*-plane i.e. if the plume is not cylindrically symmetric the values of k_{zx} and k_{yz} will be different. The angular distribution of the deposited material on a hemispherical substrate is given by:

$$F(\theta) = F(0)\left(\frac{1+tan^2(\theta)}{1+k_{yz}^2 tan^2(\theta)}\right)^{3/2} \qquad 2\text{-}26$$

For deposition on a plane substrate the equation is:

$$F(\theta) = F(0)\left(1+k_{yz}^2 tan^2(\theta)\right)^{-3/2} \qquad 2\text{-}27$$

where $F(0)$ is the particle flux normal to the target surface. Eqs 2-26 and 2-27 can also be used to obtain the plume aspect ratios (k_{xz}, k_{yz})) for both plasma parts and the overall plume (ions + neutrals) by fitting them to the experimental data. The distribution of ionized part can be measured using a negatively biased Langmuir ion probe[22] and for the overall plume, the material can be deposited on a transparent hemispherical substrate to get the angular distribution of deposited atoms. The explanations of Langmuir ion probe analysis and deposited thickness distribution measurement are given in Ch. 3 and the results for obtaining plume aspect ratios are given in Ch. 4. Finally the equation to measure the current density *j* in the *yz*-plane according to the Anisimov model is given by the following equation.

$$j(y,z,t) = \frac{zN}{I_1(\gamma)(XYZ)} - \left[1 - \frac{y^2}{Y^2} - \frac{y^2}{Y^2}\right]^{\frac{1}{(1-\gamma)}} \times \sqrt{(v_y^2 + v_z^2)} \qquad 2\text{-}28$$

In the above equation z is the atomic number which represents the charge state; N is the total number of particles in the plume. Figure 2-8 shows an ion signal for ns-ablation of Ag at laser fluence of ~1 J cm^{-2} fitted using the Anisimov model for two different values of adiabatic index γ.

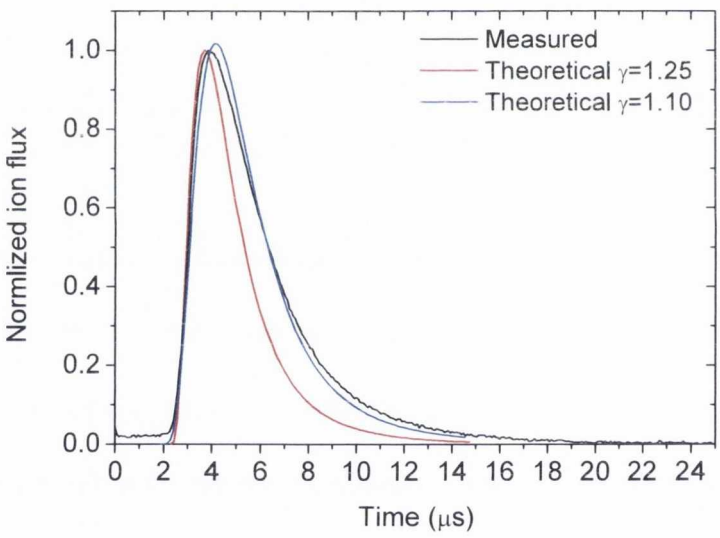

Figure 2-8 Measured TOF ion flux signal for Ag ns laser ablation fitted with Anisimov model for γ=1.25 and 1.1 respectively.

The value of adiabatic index $\gamma = c_p/c_V$ was taken from the calculation performed by Zel'dovich and Raizer [8]. According to Zel'dovich and Raizer [8] the adiabatic index of ionized gas with certain internal energy and pressure the adiabatic index can be related to gas density,

internal energy and pressure as: $\gamma = 1 + p/\rho E$ where p is the pressure, ρ is density and E is internal energy of ionized gas.

For an ideal gas at thermodynamic equilibrium, the specific heat capacities are related by $c_p = c_V + Nk$ where N is the number of particles per unit mass and k_B is the Boltzmann constant. For a monoatomic gas with translational degrees of freedom excited along *xyz* axis; $c_V = 3/2Nk$ and corresponding $c_p = 5/2Nk$. This gives us $\gamma = 1.66$. Similarly for a diatomic gas with translation as well as rotational degree of freedom excited $c_V = \frac{3}{2}Nk + Nk = 5/2Nk_B$ this gives $c_p = 5/2Nk_B$ and $\gamma = 1.4$. For laser produced plasma at temperature of several thousand kelvin and at a pressure of several hundred times greater than the atmospheric pressure, there exist sufficient degree of dissociation of molecules into atoms and ions. The dissociation process needs a large amount of energy and thus has an appreciable effect on thermodynamical properties of gas.

To see how those factors changes, let us consider a simple but practical case of a diatomic gas of molcules A_2 composed of identical atoms A. Suppose that at temperature T and gas density ρ a fraction F of atoms is dissociated into atoms or ions following the reaction $A_2 \rightarrow 2A$. If N is the initial number of molecules per unit mass, then there will be $N2F$ atoms and $N(1-F)$ molecules per unit mass of gas. The total number of particles is $N(1+F)$ so that the gas pressure is

$$P=N(1+F)\rho kT$$

For complete dissociation (i.e. for $F=1$), the pressure is twice as high as the pressure at the same temperature and density would be if the gas were undissociated. Similarly let E_{A2} be the energy of a single molecule at temperature T and E_A be the energy of a single atom. The specific internal energy of the dissociated state taken with respect to molecular state can be written as[8]

$$E=NE_{A2}(1-F)+NE_A2F+NUF$$

Where U is the energy required for dissociation of a molecule. It can be seen that the energy of the dissociated gas appreciably increases compared to the energy in the absence of dissociation $E=N_{E2}$ even for a small degree of dissociation. Correspondingly the specific heat at constant volume $C_V=(\partial E/\partial T)$ also increases appreciably and the adiabatic index decreases

Table 2-1 Calculated adiabatic index for gas of atoms for different thermodynamic parameters (from Ref . 8)

For $\rho=10^{-2}\rho_0$			
T^0(K)	**ε (eV/particle)**	***p*(atm)**	γ
8000	10.6	0.57	1.12
50000	158	11.6	1.17
250000	1080	125	1.25

as compared to the molecular state (1.4). Table 2-2 shows the values for adiabatic index for certain different values of temperature, pressure and internal energy per particle. For the ion flux in Figure 2-8 the TOF signal was calculated for γ=1.25 following the work of Doggett *et al.*[22] and γ=1.10 as well. It can be seen from the figure that the probe signal calculated using γ=1.10 fits well in terms shape of and peak TOF to the experimentally measured signal. It is hard to specify a single factor to justify the lower value of adiabatic index for this situation, however it is possible that the lower density (which is of the order of 10^{12}-10^{13} cm^{-3} and can be estimated using relation $n_i=j/ev$ where j is the ion current density) of laser produced plasma causes the lower value of adiabatic index in our case.

As we have seen the main parameters for the Anisimov model are the initial plume dimensions i.e. X_0 , Y_0 and Z_0. For fs-laser ablation it is not completely understood how to take the initial values of the plume dimensions. Donnelly *et al.* have recently studied the dynamics of fs-laser ablation plume[23]. They have used the Anisimov model to study the dynamics of a Ni fs-laser plume in the fluence range of 0.6-1.0 J cm^{-2}. According to their analysis, the focal spot size of the laser can be taken as the initial plume dimensions in xy plane i.e. X_0 Y_0 as with ns ablation. The plume thickness Z_0 can be estimated by following method. After the target irradiation with a fs-laser pulse, a rarefaction wave will move into the hot material at about sound velocity and the vapour will move away from the target surface with a maximum velocity of $2c_s/(\gamma-1)$, where γ is above mentioned adiabatic index. The formation of vapour will stop when the rarefaction wave reaches a certain depth into the hot material. This depth is usually of the order of 10-20% of the ablation depth,

which will be 10-20 nm for fluences around 1 J cm^{-2}. Hence the formation time of vapour will be around 3-6 ps.

According to the analysis of Ref. [23], the absorbed energy per atom for Ni in the fluence range of ~ 1 J cm^{-2} is 15eV, which gives C_s~3×10^3 m s^{-1}. Multiplying the maximum velocity with which the vapour moves away from the target ($2c_s/(\gamma-1)$) with the formation time of vapour one can obtain the initial thickness of the plume. For this particular case it comes out around 100-150 nm, which can be used as an initial plume thickness for the Anisimov model. As we have described in Section 2.3 two distinct plumes are emitted from the target in fs-laser ablation, a fast atomic cloud, followed by a plume containing nanoparticles of the target material. Time resolved imaging of the nanoparticle plume has revealed that this second plume also looks elliptical similar to the Anisimov model plume shape[24]. The images of Ni, Ag and Au nanoparticle plumes can also be seen in Ch 5. The initial thickness, Z_0 for this case can be taken as ablation depth per pulse. The value of adiabatic index γ is however not clear at this stage.

2.5 Optical properties of metal nanoparticle films

Before describing the optical properties of metal nanoparticle films (nanoparticles deposited on solid substrates) it will be useful to give an introduction about the optical properties of the solid materials. The response of a material to the applied electromagnetic field is described by the dielectric function. This function is derived according to the Lorentz model for dielectrics and Drude model for metals.

Lorentz Model: According to Lorentz model, when bound electrons in the lattice interact with electromagnetic radiation they oscillate around thier mean positions. Classically, we could approximate the oscillations as a driven damped harmonic oscillator i.e driven by the external electric field. The various forces which act on the damped harmonic oscillator are its driving force F_{dr}, the spring force F_s and the damping force F_d. Mathematical relations for these forces can be written as:

$$F_{dr} = -eE_x, \quad F_s = -k_s x, \quad F_d = -\beta_d \dot{x}$$

Where $E_x = E_0 e^{-i\omega t}$ is the incident electric field . Newton's second law gives:

$$m\ddot{x} = -\beta_d \dot{x} - k_s x - eE_x \qquad 2\text{-}29$$

$$\ddot{x} - \Gamma\dot{x} + \omega_0^2 x = -\frac{e}{m}\mathrm{E_x} \qquad 2\text{-}30$$

Where $\Gamma = \beta_d/m$ and $\omega_0^2 = k_s/m$, ω_0 is the natural frequency and δ is the damping factor. To find the solution of the above equation we define $x(t) = Ae^{-i\omega t}$ and this gives us the relation for amplitude $A(\omega)$ and position $x(t)$ as :

$$A(\omega) = -\frac{1}{m}\left(\frac{eE_0}{\omega_0^2 - \omega^2 - i\Gamma\omega}\right) \qquad 2\text{-}31$$

$$x(t) = -\frac{eE_0}{m}\left(\frac{e^{-i\omega t}}{\omega_0^2 - \omega^2 - i\Gamma\omega}\right)$$

If ex is the dipole moment of one oscillator the total polarization (dipole moment per unit volume) is given by:

$$P = N_0 ex = -\omega_p^2 \left(\frac{\varepsilon_0 E_0 e^{-i\omega t}}{\omega_0^2 - \omega^2 - i\Gamma\omega}\right) \quad 2\text{-}32$$

where N_0 is the number of oscillators per unit volume and $\omega_p^2 = \frac{N_0 e^2}{m\varepsilon_0}$ is the plasma frequency. The polarization is related to the electric field through the following relation:

$$P = \varepsilon_0 \chi E \quad 2\text{-}33$$

where χ is the electric susceptibility of the medium. Comparing Eq. 2-32 and 2-33 we get:

$$\chi = \frac{\omega_p^2}{\omega_0^2 - \omega^2 - i\Gamma\omega} \quad 2\text{-}34$$

The relative permittivity is related to χ as:

$$\varepsilon = \chi + 1 \quad 2\text{-}35$$

Inserting the value of χ from Eq 2-34 gives:

$$\varepsilon(\omega) = 1 + \frac{\omega_p^2}{\omega_0^2 - \omega^2 - i\Gamma\omega} = \varepsilon_1 + i\varepsilon_2 \quad 2\text{-}36$$

The real and imaginary part of dielectric function can be written as:

$$\varepsilon_1(\omega) = 1 + \frac{\omega_p^2(\omega_0^2 - \omega^2)}{(\omega_0^2 - \omega^2)^2 - \Gamma^2\omega^2} \quad 2\text{-}37$$

$$\varepsilon_2(\omega) = 1 + \frac{\omega_p^2 \delta\omega}{(\omega_0{}_0^2 - \omega^2)^2 - \Gamma^2\omega^2} \quad 2\text{-}38$$

The complex refractive index is related to the dielectric function as:

$$(n + ik) = \sqrt{\varepsilon_r} \qquad 2\text{-}39$$

Where $n^2 - k^2 = \varepsilon_1, \;\; 2nk = \varepsilon_2$

For multiple oscillators the dielectric function can be modified using superposition principle:

$$\varepsilon = \sum_j 1 + \frac{\omega_{pj}^2}{\omega_{0j}^2 - \omega^2 - i\Gamma\omega}$$

where ω_{0j} is the resonance frequency of each(ω) oscillator.

Drude model for metals: For metals there are free carriers (electrons), and no spring to connect electrons to ions, hence $F_s = -k_s x$=0, and since $\omega_0^2 = k_s/m$ the free electron system can be represented as zero resonance frequency i.e. $\omega_0 = 0$.

$\omega_0 = 0$. The Eq. 2-36 reduces to:

$$\varepsilon(\omega) = 1 - \frac{\omega_p^2}{\omega^2 + i\Gamma\omega} \qquad 2\text{-}40$$

and the imaginary and real parts of dielectric function $\varepsilon_r(\omega)$ can be obtained accordingly.

These above results are known as the Drude model[†]. Metals such as alkali elements allow us to use the approximation of $\omega_0 = 0$. For metals such as noble metals, that show strong plasmonic response, the contribution of bound electrons should be taken into account, which

---

[†] The above formulation of dielectric function in Lorentz and Drude model can be found in **J.D. Jackson, Classical Electrodynamics, Wiley, New York, 1975** and **MIT Open course ware (http://web.mit.edu/course/6/6.732/www/6.732-pt2.pdf).** The definitions of permittivity and the electric susceptibility can be obtained in **Introduction to electrodynamics By D.J. Griffith, Prentice Hall 2nd or 3rd edition.**

will partially polarize the positive ion core. This effect can be represented by introducing an additional constant in the dielectric function.

$$\varepsilon(\omega) = \varepsilon_\infty - \frac{\omega_p^2}{\omega^2 + i\Gamma_0\omega}$$

where damping constant $\Gamma_0 = \frac{1}{\tau}$ represents different scattering rates which includes electron-electron, electron-defect, electron-lattice ions and electron-phonon scattering in bulk materials. ε_∞ includes the contribution of bound electrons in particles polarizability and can be considered as unity if only the conduction band electrons contributes into the dielectric function[25,26]. The real and imaginary parts of the dielectric function can be obtained accordingly using Eqs. 2-37 and 2-38. When dealing with nanoparticles the presence of interfaces needs to be taken into account, for nanoparticles smaller than the mean free path of conduction electrons, electron-surface scattering is believed to be important as well. Hence an additional term needs to be added in the damping constant and the dielectric function becomes a function of the particle radius as follows [27]

$$\Gamma_i = \Gamma_0 + A\frac{v_f}{R_i} \qquad 2\text{-}41$$

Where A is a theoretical parameter which describes the loss of coherence due to different scattering events (typical values are in the range of 0.1-0.7 for Ag nanoparticles [28]) and v_f is the velocity of the electron at Fermi energy.

2.5.1 Optical properties of metal nanoparticles and surface plasmon resonance

Metal nanoparticles have some unique optical properties which are very different from the bulk solids due to their reduced dimensions. The main feature in the optical absorption of metal nanoparticles (such as Ag and Au) is the absorption band in the UV/Vis region of the electromagnetic spectrum. The absorption band is due to the resonant excitation, surface plasmon resonance (SPR). The SPR is produced by the movement of the conduction electrons in the particle. The electric field of the incident electromagnetic radiation results in a displacement of the negative charge cloud w.r.t positive nuclei in the metal nanoparticle. This displacement gives origin to the particle polarization, because the positive charge provides a restoring force to electrons to produce oscillations. Classically, the concept of SPR is described in terms of a particles polaraizability. If we consider a spherical particle of radius R under the influence of an electric field $\boldsymbol{E}$, the dipole moment of the spherical particle can be written as[25]:

$$\boldsymbol{P} = \alpha \varepsilon_m \boldsymbol{E} \qquad 2\text{-}42$$

where α is the polarizability of the metal sphere and is given by:

$$\alpha = 4\pi R^3 \frac{\varepsilon_{np} - \varepsilon_m}{\varepsilon_{np} + 2\varepsilon_m} \qquad 2\text{-}43$$

ε_{np} and ε_m are the dielectric functions of the host and the nanoparticles respectively. From the above equation, a resonance in the polarizability and hence in the dipole moment can be observed when $\varepsilon_{1np} = -2\varepsilon_m$ i.e. when the dielectric function of metal sphere is negative

which is satisfied for Ag and Au nanoparticles in the UV/Vis region of the electromagnetic spectrum. In theoretical formulation of the dipole moment and polarizability of a metal sphere the authors have used a quasi-static approximation in which the particle size is much smaller than the wavelength of light i.e. R<<λ , the retardation effect of electric field inside the metal nanoparticle can be neglected and the field inside the region of interest is constant. Eq. 2-42 describes the dipole moment of the metal nanoparticle in terms of its polarizability; however in real experiments we usually measure quantities like absorption and scattering from the nanoparticles. According to the polarizability theory, the absorption and scattering coefficients for metal spheres are given by:

$$\sigma_{abs} \cong \frac{\omega V_0}{c}\left[\frac{\varepsilon_{2np}}{(\varepsilon_{1np}+2\varepsilon_m)^2+(\varepsilon_{2np})^2}\right] \qquad 2\text{-}44$$

$$\sigma_{sc} = \left(\frac{\omega}{c}\right)^4 \frac{1}{6\pi}|\alpha|^2 \qquad 2\text{-}45$$

where V_0 is the volume of the nanoparticle, and ω and c are the angular frequency and speed of light respectively. The extinction cross section is usually taken as the sum of absorption and scattering coefficients i.e. $\sigma_{ext} = \sigma_{abs}+\sigma_{sc}$. It can be seen that the absorption coefficient depends linearly on the particles volume and the scattering coefficient quadratically. Thus the scattering cross section for small nanoparticles can be neglected. A range of < 20 nm has been suggested for that.

The exact solution for absorption and scattering of light from small nanoparticles was described by Mie[29], the theory is also known as Mie scattering theory. Mie presented an analytical solution of Maxwell's equation for the scattering of an incoming electromagnetic

plane wave from a spherical nanoparticle. The solution was obtained by introducing the electromagnetic potential and expanding it (multipole expansion) for a homogeneous isotropic sphere surrounded by a dielectric medium. The exact equations for absorption and scattering cross section for multipole expansion can be found in Ref. [25]. In the particular case, for long wavelength approximation ($\lambda > R$) only the dipolar term is non-negligible and the extinction cross section for the spherical metal nanoparticle is given by:

$$\sigma_{ext} = \left(\frac{9\omega}{c}\right) V_0 (\varepsilon_m)^{3/2} \left[\frac{\varepsilon_{np2}}{(\varepsilon_{np1}+2\varepsilon_m)^2+(\varepsilon_{np2})^2}\right] \qquad 2\text{-}46$$

where ε_m is the dielectric function of host and V_0 is the volume of metal sphere. Since we are dealing with nanoparticle films, i.e. nanoparticles deposited on a solid substrate, the equation for transmission from nanostructured thin films of equivalent thickness d is given by.

$$T = \frac{I}{I_o} = \exp(-N\sigma_{ext}) = \exp(-d\frac{\sigma_{ext}}{V_o}) \qquad 2\text{-}47$$

where I and I_0 are the transmitted and initial intensities and N is the number of nanoparticles per unit area. The resonance condition in Mie theory is similar to the dipolar model i.e. $Re\ [\varepsilon_{np}\ ] = -2(\varepsilon_m)$ which in fact shows similarity to the calculation to obtain the extinction coefficient of metal spheres[26]. Figure 2-9 is an illustration of the surface plasmon resonance of a metallic nanoparticle. The absorbance of a nanostructured film goes to maximum when the resonance condition is satisfied.

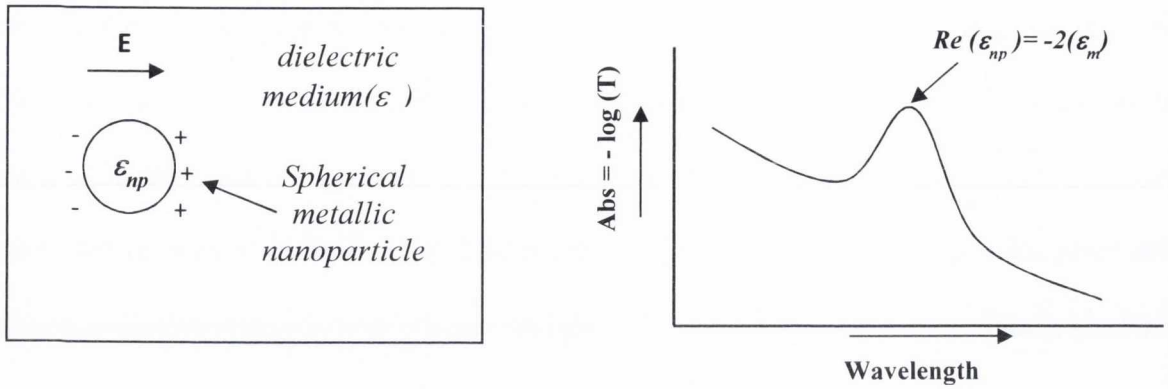

Figure 2-9 Illustration of surface plasmon resonance of a spherical metal nanoparticle

2.5.2 Maxwell-Garnet effective medium theory

The other widely used theoretical model for the calculation of the optical properties of metal nanoparticles is the Maxwell-Garnet effective medium theory, also called Maxwell-Garnet approximation[30,31]. The Maxwell-Garnet theory is one of the most widely used methods for the calculation of bulk dielectric properties of inhomogeneous materials. This theory calculates an average dielectric function which takes into account the dielectric function of each component of the film by considering a two-component layer. One component is considered as a host in which spherical inclusions of other components are embedded with the volume fraction of the inclusions kept small. Figure 2-10 shows the schematic diagram of a composite thin film in the Maxwell-Garnett (MG) framework.

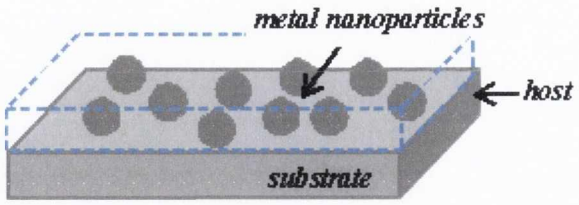

Figure 2-10 Composite thin film in which the spherical metal inclusions are embedded in a host medium.

The Maxwell-Garnet expression for calculating an effective dielectric function ε_{eff} is given by:

$$\left(\frac{\varepsilon_{eff}-\varepsilon_m}{\varepsilon_{eff}-2\varepsilon_m}\right)=f\left(\frac{\varepsilon_{np}-\varepsilon_m}{\varepsilon_{np}-2\varepsilon_m}\right) \qquad 2\text{-}48$$

where ε_m and ε_{np} are the bulk dielectric function of the host and the spherical metal inclusions, and f is the volume fraction of the inclusions. Solving for the effective dielectric function gives:

$$\varepsilon_{eff}=\varepsilon_m\left(1+\frac{3f_1\beta}{1-f_1\beta}\right) \qquad 2\text{-}49$$

Figure 2-11 shows the real and imaginary parts of the dielectric function of bulk Ag and a composite layer with a volume fraction of 0.1. The bulk dielectric function was obtained using criteria in Eq. 2-39 i.e ($n^2-k^2=\varepsilon_1, 2nk=\varepsilon_2$) where the bulk values of n and k were obtained from the tabulated data[4]. The effective dielectric function was calculated using Eq. 2-49 and the host medium was considered as ambient ($\varepsilon_m=1$). It can be seen that the

components of the effective dielectric function are significantly different to the bulk so that the optical properties of the composite layer will be very different to a bulk thin film.

$$\beta = \left(\frac{\varepsilon_{np} - \varepsilon_m}{\varepsilon_{np} - 2\varepsilon_m}\right) \qquad 2\text{-}50$$

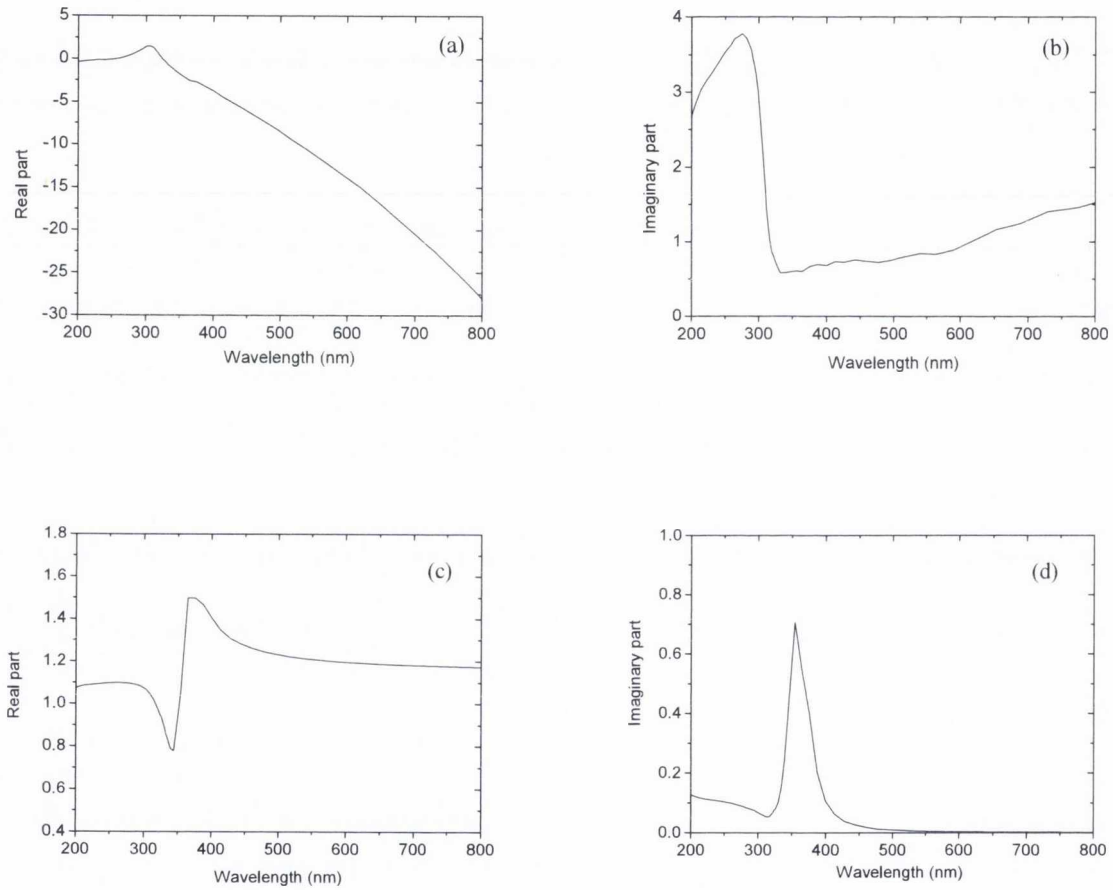

Figure 2-11 Real and imaginary parts of (a), (b) bulk Ag dielectric function and (c), (d) effective dielectric function for volume of 0.1.

With knowledge of the effective dielectric function for nanostructured thin films, the optical properties like reflectance, transmittance and absorbance of films can be calculated. The equations to calculate transmittance from nanoparticle film is as follows:

$$T = \left(\left| \frac{t_{12} + t_{23} + \exp(2i\Delta)}{1 + t_{12} + t_{23} + \exp(2i\Delta)} \right| \right)^2 \qquad 2\text{-}51$$

where r_{12} , r_{23} and t_{12}, t_{23} are Fresnel coefficients given by:

$$r_{12} = \frac{n_1 - n_2}{n_1 + n_2}, r_{23} = \frac{n_2 - n_3}{n_2 + n_3}, t_{12} = \frac{2n_1}{n_1 + n_2}, t_{23} = \frac{2n_2}{n_2 + n_3} \qquad 2\text{-}52$$

n_1, n_2 *and* n_3 are the refractive indices of ambient, host medium and the substrate respectively and $\Delta = \frac{2\pi n_2 d}{\lambda}$, which represents the phase shift as light travels through and absorbing medium of thickness *d*. The absorbance of a nanoparticle film can be calculated as *A=-log(T)*. Figure 2-12 gives absorbance of Ag composite film calculated using MG approximation for different equivalent thicknesses and volume fractions. For this calculation n_1 is taken to be ambient (i.e. = 1), n_2 is the effective refractive index ($n_2 = (\varepsilon_{eff})^{1/2}$) and n_3 is the substrate refractive index and for our example we used glass (n_3 = 1.5).

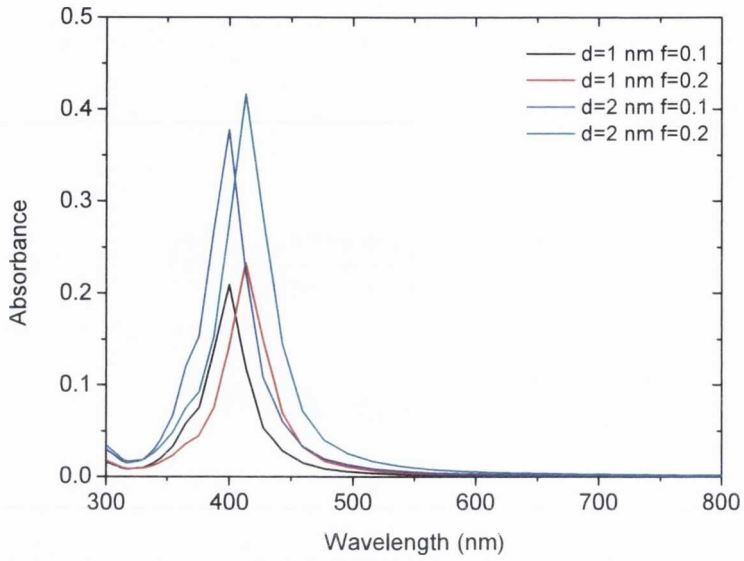

Figure 2-12 Absorbance of Ag thin films deposited on glass substrates for different equivalent thickness (d) and volume fraction (f).

The spectra show clearly the SPR feature i.e. a large peak around 400 nm and the peak position and magnitude veries with the volume fraction as well as the thickness. Hence the MG approximation provides also a simple approach to study the SPR features of noble metal nanoparticle films. Ref. [30,32] uses the Maxwell-Garnet approximation in order to calculate the absorbance of Ag nanoparticles embedded in a SiO_2 matrix and deposited on formvar grids respectively. The absorbance of Ag and Au thin films for different volume fractions and thicknesses were calculated using a computer code written in Mathematica and the results were compared with the experimental data. The detail of the Mathematica code used to calculate the transmittance and the absorbance is given in Appendix B.

It has been observed that although the MG code provides a quick and approximate method to generate the optical spectra of nanoparticle films, it has some limitations as well. One of them is that the width of the experimentally measured absorbance is quite large as compared to the simulated one. The other feature is that both the Mie and MG theories consider the nanoparticles as spherical and so does not take into account the shape of the particles sitting on the substrate which i.e. whether it is a complete or a truncated sphere. The shape of a nanoparticle sitting on the substrate in fact depends on the interface energy. For metals on dielectric substrates, the most favorable growth mode is the island growth mode. Because of the poor adhesion energy of metals on insulating substrates such as glass or silicon the growth of a thin film proceeds by the nucleation of atoms on the surface and hence formation of nanometer scale islands. Along with the shape of particle, the optical absorption spectra or the SPR depends on several other parameters including particles shape and the dielectric environment[27,33]. In order to simulate the optical absorption spectra of metal nanoisland films prepared using PLD we have used another theoretical model called Granfilm[34]. The word Granfilm originates from granulated film. The Granfilm program calculates the optical properties of nanoisland films deposited on different dielectric substrates such as Ag nanoisland films deposited on MgO and fused quartz substrates and thus gives the closest scenario to PLD films. The exact theoretical description of the software is quite complicated. The theoretical introduction and working principle is given in the following section.

2.5.3 Granfilm program

The program first calculates the surface susceptibilities of an island layer deposited on a solid substrate using appropriate boundary conditions for Maxwell's equations. The surface

susceptibilities for a continuous film of thickness d and dielectric function ε_1 deposited on a substrate of dielectric function ε_2 is given by:

$$S_1 = d(\varepsilon_1 - \varepsilon_2) \text{ and } S_2 = \frac{d(\varepsilon_1 - \varepsilon_2)}{\varepsilon_1 \varepsilon_2}$$

where S_1 and S_2 are the first-order surface suscaptabilities and describe the ability of a surface to polarize. In the case of a metal island on the substrate, the surface susceptibilities depend also on the polarisabilities of the truncated metal islands i.e.

$$S_1 = N\alpha_\perp \text{ and } S_2 = N\alpha_\parallel$$

where $\alpha_\perp, \alpha_\parallel$ are polarisabilities parallel and perpendicular to the substrate and N is the number of islands per unit area. The geometry of metal islands used by Granfilm [34] to simulate the optical response of a metal island layer is given in Figure 2-13. This shows the reflection and transmission of s and p-polarized incident waves on a surface. The surface is known as a perturbed surface of layer $d<<\lambda$ separating two media of dielectric function ε_1 and ε_2 (see Figure 2-13(b)), ε_2 is the dielectric function of the metal island. The factor t_r in Figure 2-13(b) is known as a truncation factor which defines if the particle is an emerging island ($t_r>0$) or a cap ($t_r<0$). The polarisabilites are calculated by solving the Laplace equation $\nabla^2 \Psi(\mathrm{r})$ for electrostatic potential $\Psi(\mathrm{r})$ for a spherical symmetric system (the nanoparticle). The $\Psi(\mathrm{r})$ is expanded on a mutipolar basis and the polarisabilities are given by the first coefficients of the multipolar expansion as $\alpha_\perp \cong A_{10}$, $\alpha_\parallel \cong A_{11}$ for $t_r<0$. The detailed equation for emerging island polarizabilites can be found in Ref [34]. With the knowledge of surface susceptibility and island polariaability the quantities like transmission

and reflection can be calculated using Fresnel equations. As an example the transmission coefficient for *s* polarized incoming light at $\theta i = \theta t = 0$ can be written as:

$$t_s = \frac{2n_3}{n_3 + n_2 \frac{-i\omega s_1}{c}}$$

Where n_3 and n_2 are the refractive indices for metal and the substrate.

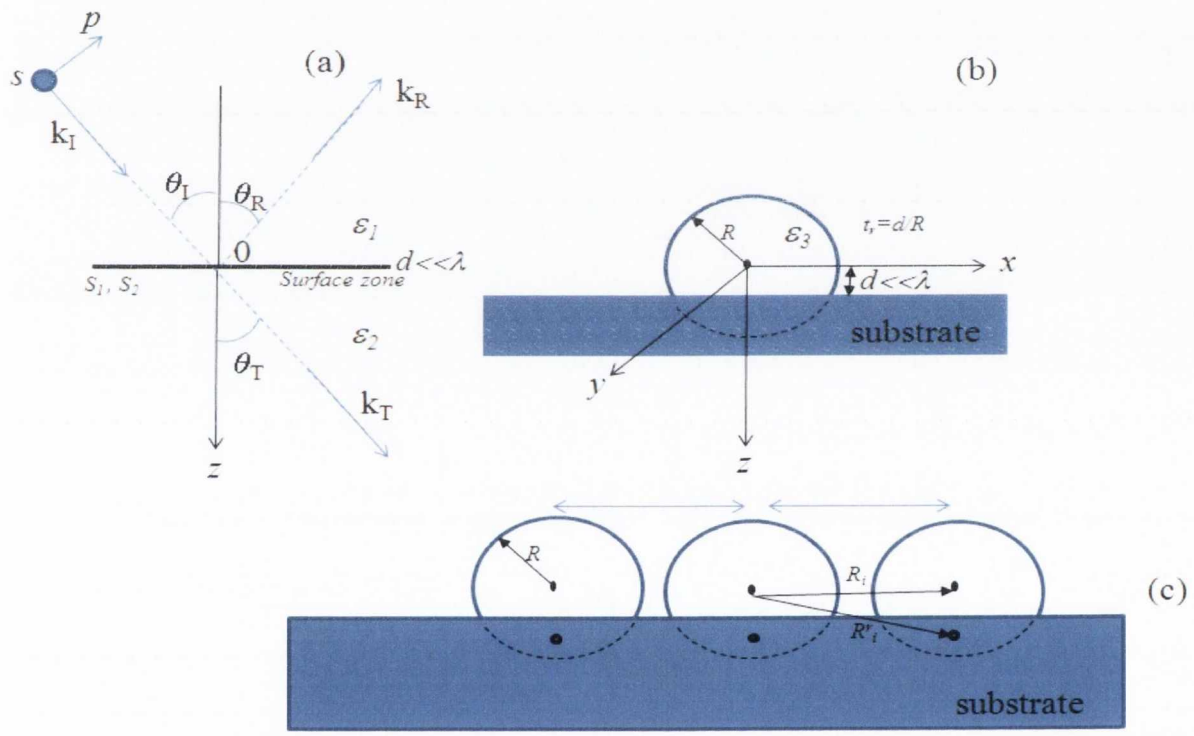

Figure 2-13 (a) Reflection and transmission of an incident wave on a surface characterised by its surface susceptibilities. The perturbed surface layer separates the two media with dielectric function ε_1, ε_2 respectively. (b) Illustration of a truncated sphere on the solid substrate showing how the truncation ratio and particle co-ordinates are defined.

Finite size approximation and inter-island interactions: Additionally the Granfilm model also takes into account the surface scattering of electrons in the metal nanoparticles

calculating their dielectric function (see Eq.2-41), which is important when the size of the nanoparticle becomes smaller than the mean free path of electrons. The program also considers the coupling between nanoparticles in a quasi-static approximation i.e. when the separation between the nanoparticles is much smaller than the exciting wavelength and the islands are excited approximately by the same amplitude. In this case the particles are considered to be excited uniformly by the incident electric field and to the local field resulting from the excited dipoles inside the particles and their image charges in the substrate.

2.6 References

1 S. I. Anisimov, B. S. Luk'yanchuk, and A. Luches, Applied Surface Science **96-98**, 24 (1996).

2 S. R. David and and F. R. Fickett, Journal of Research of the National Institute of Standards and Technology (NIST) **100** (2), 119 (1995).

3 V. N. Tokarev and F.H. Alexander Kaplan, Journal of Applied Physics **86** (5), 2836 (1999).

4 P. B. Johnson and R. W. Christy, Physical Review B **6** (12), 4370 (1972).

5 P. Winsemius, F. F. van Kampen, H. P. Lengkeek, and C. G. van Went, Journal of Physics F: Metal Physics **6** (8), 1583 (1976).

6 S. Amoruso, Applied Physics A: Materials Science & Processing **69** (3), 323 (1999).

7 J. G. Lunney and R. Jordan, Applied Surface Science **127–129** (0), 941 (1998).

8 Y. B. Zel'dovich and Y. P.Raizer, Physics of Shock Waves and High Temperature Hydrodynamic Phenomena (1966).

9 G. O'Connell, I. Tobin P, and J. G. Lunney P, 30th ICPIG, August 28th– September 2nd 2011, Belfast, Northern Ireland, UK.

10 A. De Giacomo, M. Dell'Aglio, A. Santagata, and R. Teghil, Spectrochimica Acta Part B: Atomic Spectroscopy **60** (7–8), 935 (2005).

11 R. Rozman, I. Grabec, and E. Govekar, Applied Surface Science **254** (11), 3295 (2008).

12 E. Hutter and J. H Fendler, Advanced Materials **16** (19), 1685 (2004).

13 D. Marla, V. U. Bhandarkar, and S. S. Joshi, Journal of Applied Physics **109** (2), 021101 (2011).

14 B. L. Kapelovich and T. L. Perel'man S. I. Anisimov, Zh. Eksp. Teor. Fiz **66**, 776 (1974).

15 D. S. Ivanov and and V. L. Zhigilei, Physical Review B **68** (6), 064114 (2003).

16 Zhibin Lin, Leonid V. Zhigilei, and Vittorio Celli, Physical Review B **77** (7), 075133 (2008).

17 D. Perez and J. L. Lewis, Physical Review Letters **89** (25), 255504 (2002).

18 S. Amoruso et al., Journal of Physics D: Applied Physics **40** (2), 331 (2007).

19 S. I. Anisimov, D. Bäuerle, and B. S. Luk'yanchuk, Physical Review B **48** (16), 12076 (1993).

20 B. Toftmann, J. Schou, and J. G. Lunney, Physical Review B **67** (10), 104101 (2003).

21 T. N. Hansen, J. Schou, and J. G. Lunney, Applied Physics A: Materials Science & Processing **69** (7), S601 (1999).

22 B. Doggett and J.G. Lunney, Journal of Applied Physics **105** (3), 033306 (2009).

23 T. Donnelly, J. G. Lunney, S. Amoruso, R. Bruzzese, X. Wang, and X. Ni, Journal of Applied Physics **108** (4), 043309 (2010).

24 S. Noël, J. Hermann, and T. Itina, Applied Surface Science **253** (15), 6310 (2007).

25 U. Kreibig and M. Volmer, *Optical properties of metal clusters*. (Springer, 1995).

26 C. Sonnichsen., Ludwig-Maximilians-Universit¨at M¨unchen, 2001.

27 S. Link and M. A. El-Sayed, The Journal of Physical Chemistry B **103** (21), 4212 (1999).

28 K. P. Charlé, L. König, S. Nepijko, I. Rabin, and W. Schulze, Crystal Research and Technology **33** (7-8), 1085 (1998).

29 G. Mie, Ann. Phys. (Liepzig) **25** 377 (1908).

30 R. W. Cohen, G. D. Cody, M. D. Coutts, and B. Abeles, Physical Review B **8** (8), 3689 (1973).

31 O. S. Heavens, *Optical properties of thin solid films*, 2nd ed. (Dover books on physics, 2011).

32 T. Donnelly, B. Doggett, and J. G. Lunney, Applied Surface Science **252** (13), 4445 (2006).

33 K. Lance Kelly, E. Coronado, L. L. Zhao, and G. C. Schatz, The Journal of Physical Chemistry B **107** (3), 668 (2002).

34 R. Lazzari and I. Simonsen, Thin Solid Films **419**, 124 (2002).

Chapter3 Experimental setup and characterization techniques

This chapter gives a detailed description of the PLD systems, including laser and vacuum systems. Afterwards there will be a description of the experimental techniques which we have used for the characterization of laser ablation plasmas and nanoparticle films such as electron microscopy and optical absorption spectroscopy. At the end a summary of the setups used for optical emission spectroscopy of the fs-laser ablation plume is presented.

3.1 Laser and vacuum system for nanosecond and femtosecond pulsed laser deposition

Laser ablation of metal targets and nanoparticle film growth was carried out using two different kinds of laser systems and deposition chambers. Figure 3-1 represents a general schematic diagram of the PLD setup used for nanosecond (ns) and femtosecond (fs) laser ablation. The detailed description of all components used for both ns and fs-PLD is given in the following sections.

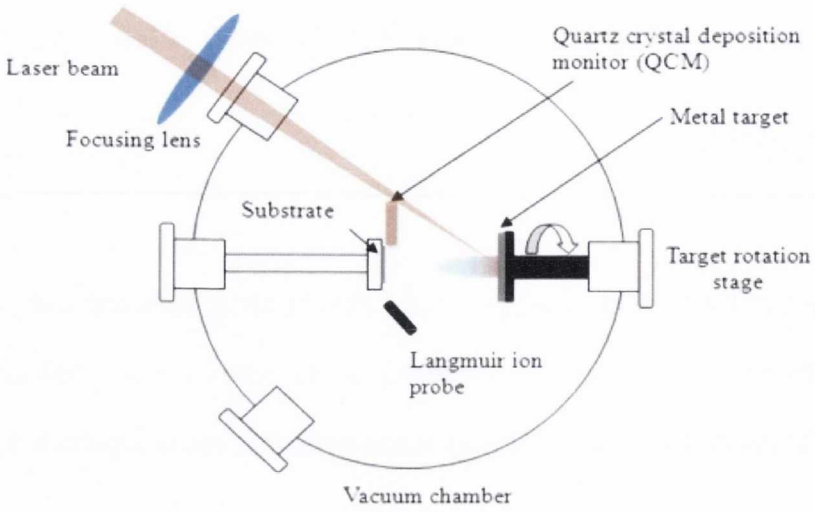

Figure 3-1 Schematic diagram of pulsed laser deposition experimental setup

3.1.1 Nanosecond PLD setup

A Lambda Physik Complex Pro 102 KrF laser, operating at 248 nm, with full width at half maximum (FWHM) of 23 ns was used to ablate the metal targets; the temporal profile of Lambda PhysiK KrF laser is given in Figure 3-2. The maximum repetition rate of the laser was 20 Hz. The laser beam was imaged on to the target surface at an incident angle of 45^0 using a 35 cm focal length quartz lens. The target was mounted on a rotation stage fitted inside the vacuum chamber and was driven externally using a stepper motor. The target was continuously rotated during the depositions in order to avoid drilling a hole in the target. The laser beam was entered the vacuum chamber through a quartz window.

The vacuum system used for nanosecond laser ablation was a high vacuum chamber with approximately 20 litres volume. A Pfeiffer Turbo molecular pump[†] with maximum rotation speed of 1000 Hz and an Edward oil rotary backing pump[‡] were used to evacuate the ns-PLD chamber. The chamber pressure was measured using a Pfeiffer vacuum

[†] Model TMU 262
[‡] Model RV12

gauge[§] (Model: PKR 251) with combined Pirani and cold cathode measurement system with measurement range from 5×10^{-9} mbar-1000 mbar. The ultimate vacuum which could be obtained for this PLD system after 8 hours pumping was 2×10^{-7} mbar. The complete PLD workstation was manufactured by Surface Systems and Technology, Hueckelhoven Germany.

Pulse width measurement for ns-laser: The temporal pulse profile of Lambda Physik Complex pro 102 KrF laser was measured using a biased Si photodiode with a rise time of 1 ns [1]. The data was collected on a Tektronix TDS 3034B oscilloscope. The temporal profile of KrF laser is given in Figure 3-2.

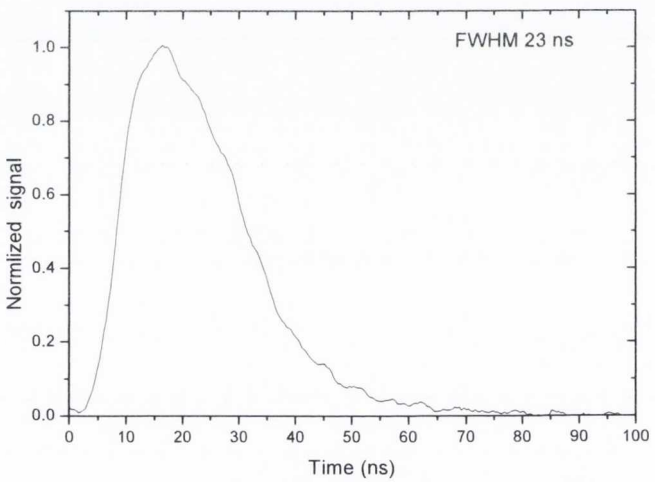

Figure 3-2 Temporal profile of KrF Excimer laser

3.1.2 Femtosecond PLD setup

For the fs-PLD setup a Coherent Legend-Elite solid state Ti-sapphire laser operating at 800 nm with a pulse duration of 130 fs was used. The maximum repetition rate of the laser was 1 kHz with a maximum energy of 1mJ/pulse. The fs-PLD chamber was pumped

[§] Model PKR251

using a Pffiefer-Balzer pumping system consisting of a turbo molecular pump (Model: TPH 050) and an oil rotary backing pump (Model: DUO 1.5A). The ultimate vacuum for the fs-PLD chamber was 2×10^{-6} mbar after approximately 5 hours pumping. A Balzers cold-cathode "Penning" gauge was used to measure the pressure below 10^{-3} mbar inside the chamber. The optical setup for fs-PLD was similar to the ns-PLD but instead uses a 20 cm focal length glass lens to focus the laser beam on the target surface. The target was placed at an angle of 45° with respect to the incident laser beam, which makes an elliptical shaped by beam spot on the target surface.

Pulse duration measurment for fs-laser system: The pulse duration of the femtosecond laser system was measured using an intensity autocorrelator from APE (Angewande Physik Elektronik GmbH). Intensity autocorrelators are used for various purposes, in particular for the measurement of duration of ultrashort laser pulse, where an apparatus based on a photodiode, with a rise time of a few nanoseconds, is too slow. A brief description about ultrashort pulse width measurement using intensity autocorrelator is given here. Figure 3-3 is the schematic diagram of the optical setup of intensity autocorrelator setup.

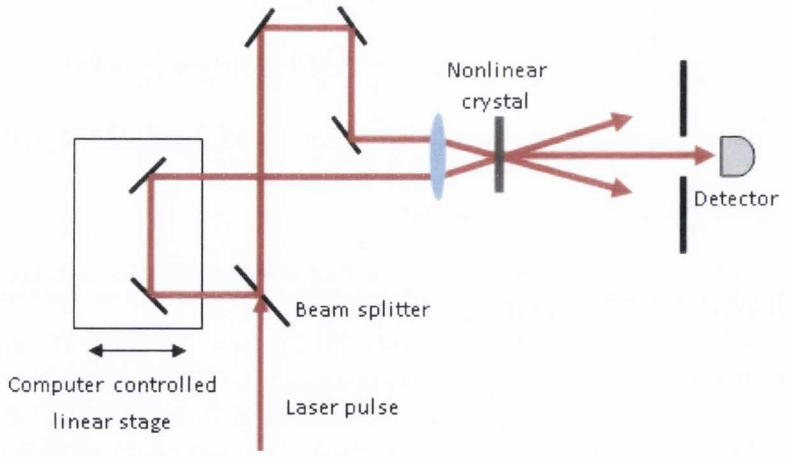

Figure 3-3 Setup of the intensity autocorrelator

In an intensity autocorrelator, a beam splitter splits the input laser pulse into two, which are then focused and sent into a non-linear crystal with χ^2 nonlinear susceptibility. The path length difference and the relative timing between the pulses are then adjusted via a variable delay line. If the path length difference is made smaller, so that the pulses meet in the non-linear crystal. Frequency sum generation in the crystal thus leads to an output at half of the wavelength. On the other hand, if the relative time delay between laser pulses increased, so that the overlap of the pulses in the non-linear crystal reduces, the mixing product becomes weaker. For the measurement of pulse duration, the power of the mixing product is recorded as a function of path length, where the path length can be changed by computer controlled motorized translation stage. The dependence of the intensity autocorrelation signal on temporal delay is given by;

$$I_{ac}(\tau) = \int_{-\infty}^{+\infty} I(t)I(t+\tau)\,dt \qquad 3\text{-}1$$

Where τ is the time delay between two pulses. After getting the autocorrelation function (ACF) trace, the full width at half maximum (FWHM) of the ACF can be measured. To get the real pulse duration one has to correct the ACF-width with a form factor depending on the pulse shape i.e.

$$\Delta\tau = FWHM\,(ACF) \times F \qquad 3\text{-}2$$

for $sech^2$ shaped pulse $F \approx 0.65$. Figure 3-4 shows ACF trace recorded using autocorrelor. The Full width at half maximum obtained using ACF of our fs-laser system was 200 fs hence the real pulse width for that system is $209 \times 0.65 = 135$ fs.

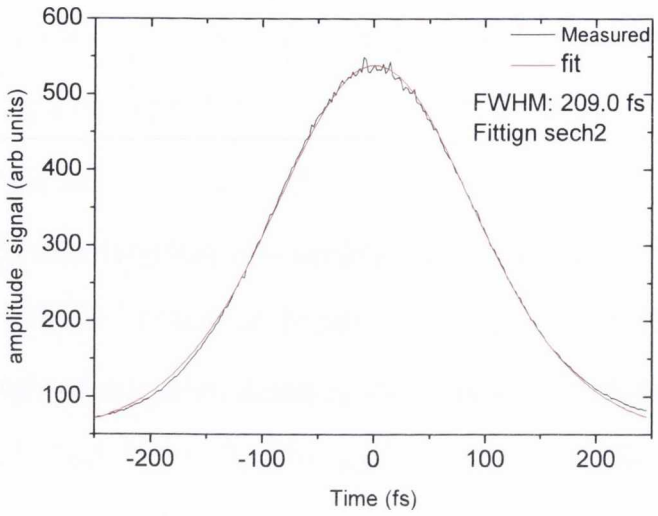

Figure 3-4. Intensity autocorrelation of fs-laser system with sech^2-shaped pulse. The actual pulse width is 135 fs in this case.

3.1.3 Deposition rate measurement

For the ns-PLD chamber the deposition rate was estimated using a Langmuir ion probe. A Langmuir ion probe measures the ion fluence per laser shot, then by knowing the atom density of the material the thickness deposited per laser shot can be estimated. The description of the ion probe is given in section 3.2.1. However the actual thickness of some of the deposited films was also measured using the x-ray reflectivity technique.

For the fs-PLD chamber, a Sycon instruments STM/100 MF quartz crystal deposition monitor (QCM) was used in to measure the thickness deposited per laser shot. A QCM consists of a resonant oscillating quartz crystal (6MHz). The resonant frequency is disturbed due to thin film deposition on the surface of the oscillating crystal. By knowing the density of the deposited material, the deposited thickness can be measured. The QCM can be used in vacuum to monitor the deposition rates in thin film deposition systems. In the fs-PLD chamber, it was situated 4.8 cm away from the target and perpendicular to the target surface.

3.1.4 Sample cleaning and preparation

The material in the laser ablation plume was deposited on 5 mm×5 mm×1 mm fused quartz substrates and SiO_2 coated transmission electron microscopy grids**, the grids were 3.2 mm in diameter with thickness of 20 μm ± 3 μm. The quartz substrates were pre-cleaned using acetone and isopropanaol in an ultrasonic bath (15 minutes each). An alkaline liquid concentrate from Helma Analytics was also used to clean the quartz and glass substrates. A 2% solution diluted with water was prepared and the substrates were cleaned in that solution using an ultrasonic bath for 30-35 minutes at ~35 C^0.

3.2 Plasma and nanoparticle thin film characterization techniques

3.2.1 Langmuir Probe

For the characterization of laser produced plasma and to monitor the ion fluence and energies, a Langmuir ion probe was used [2]. The probe consists of a conducting surface that is biased and inserted into plasma. Depending on the polarity of biasing voltage, the ion or electron component in the plasma can be studied. For a positively biased probe, current due to electrons in the plasma is measured. When the probe is biased sufficiently negative biased to prevent the electrons with highest thermal energy to reach the probe, a saturated current due ions can be recorded. This current is related to the ion density n_i by following relation[3].

$$I_i = en_iAv \qquad 3\text{-}3$$

** The grids were bought from 2spiSupplies, (www.2spi.com)

Where e is the electronic charge, A is the probe area and v is the ion velocity which can be approximated by dividing the target-to-probe distance by ion time of flight. The above equation assumes that the ions in the plasma are singly ionized. Figure 3-5 is the ion time-of-flight signal of ns-laser ablation of Ag ablation at ~ 0.8 J cm^{-2}.

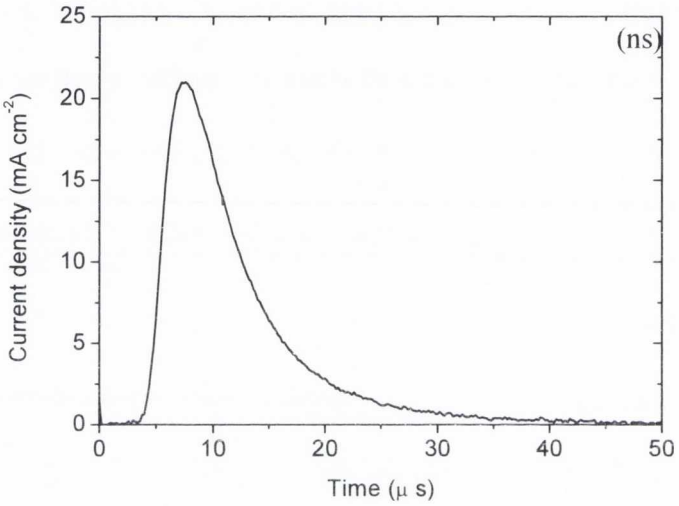

Figure 3-5 The ion time-of-flight signal for ns-laser ablation of Ag at 0.8 J cm^{-2}

The current density was calculated by dividing the ion current *I(t)* with the probe area. It can be seen from Figure 3-5 that the ion current density rises rapidly as the plume arrive at the probe and drops as the plume moves away from the target. An estimate of ion fluence (Number of ion per unit area) can also be determined from the ion signal using the following relation:

$$F_i = \frac{1}{eA}\int I(t)\,dt \qquad 3\text{-}4$$

Hence by integrating the ion current signal and dividing it by electronic charge and the probe area, one obtains the ion fluence. For instance, the ion fluence for the signal shown

above is 1.5×10^{12} cm^{-2}. The ion time-of-flight signal can also be used to obtain the energy distribution of ions in the plasma plume. This can be derived by rewriting the Eq. 3-4:

$$F_i = \frac{1}{eA}\int I(t)\,dt = \int \frac{dN}{dE}\,dE \qquad 3\text{-}5$$

Expressing the right hand side as a derivative with respect to time:

$$\frac{dN}{dE}\,dE = \frac{dN}{dE}\frac{dE}{dt}\,dt \qquad 3\text{-}6$$

By taking $E=1/2mv^2$ and ion velocity as d/t on obtains the energy distribution function dN/dE as[4].

$$\frac{dN}{dE} = \frac{I(t)t^3}{Aemd^2} \qquad 3\text{-}7$$

Where dN/dE is the number of ions per unit energy interval per unit area with units of eV^{-1} m^{-2}. The average ion energy can be calculated from the ion energy distribution using the following equation:

$$< E >= \int E\frac{dN}{dE} / \int \frac{dN}{dE} \qquad 3\text{-}8$$

A schematic diagram of the biasing circuit and an image of the Langmuir ion probe used during experiment is given in Figure 3-6. A simple RC circuit[5] was used to record the pulsed current caused by the detection of ions by the probe. The conducting part area of probe in this case is 0.09 cm^2, the bottom part of probe was covered with an insulator in

order to avoid contact of conducting part of the probe with ground via thin metal film deposition.

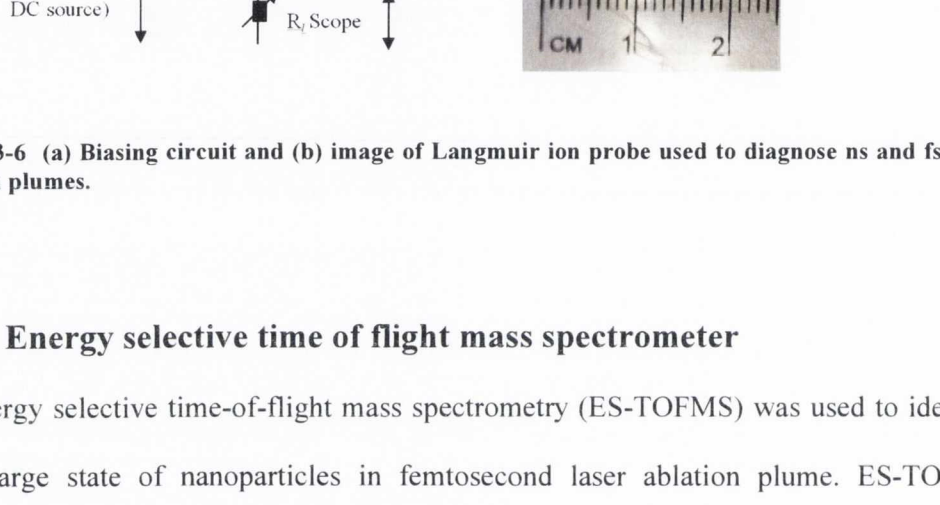

Figure 3-6 (a) Biasing circuit and (b) image of Langmuir ion probe used to diagnose ns and fs laser ablation plumes.

3.2.2 Energy selective time of flight mass spectrometer

An energy selective time-of-flight mass spectrometry (ES-TOFMS) was used to identify the charge state of nanoparticles in femtosecond laser ablation plume. ES-TOFMS achieves mass separation of charged nanoparticles by accelerating them in a constant electric field, since the kinetic energy is the same for all nanoparticles of equal charge; those of lower mass reach a higher velocity and reach the detector earlier. Figure 3-7(a) shows the schematic diagram of the top view of an ES-TOFMS.

When a voltage is applied to the plates and an electric field is established, the spectrometer acts as an energy filter, allowing only particles with certain energies to reach the detector, The pass energy of the spectrometer is given by:

$$E_{fillter} = \frac{Z\Delta VR_0}{2D} \qquad 3\text{-}9$$

Where Z is the particle charge ΔV is the voltage applied between the plates, R_o (3.5 cm) is

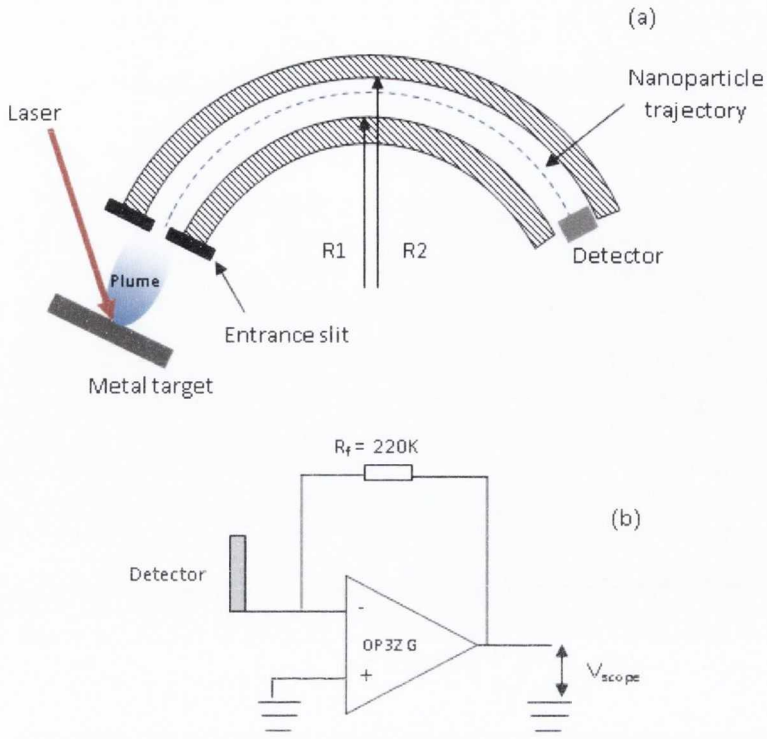

Figure 3-7 (a) The ES-TOFMS with nanoparticle trajectory and detector, R1 and R2 are the radii of two parallel electrodes. (b) Circuit diagram of the I-V converter

the centreline radius of curvature and *D* (3.25 mm) is the distance between the plates. The whole spectrometer setup was isolated in a (8×5×2 cm) grounded aluminium box with a replaceable entrance slit.

A current to voltage convertor (I-V) circuit was used to collect the detector signal. Figure 3-7(b) shows the circuit diagram of the I-V converter. The circuit essentially consists of on operational amplifier (OP37G) in inverting configuration and R_f is the feedback resistor which determines the gain. V_{scope} is the output voltage signal recorded at the oscilloscope. A more detailed description about the functionality of the ES-TOFMS and the results obtained are given in Ch 4.

3.2.3 X-ray reflectivity

The thickness of the deposited films was measured using the x-ray reflectivity (XRR) technique. XRR is a widely used tool for the measurement of thin film thickness. XRR also has the advantage of measuring the surface and interface roughness as well as the density of amorphous and crystalline thin films and multilayers.

XRR measurements for this thesis work were performed in Bruker D8 discover x-ray diffractometer. Thickness, density and roughness values were obtained by fitting the experimental reflectivity pattern to a computer simulation called LEPTOS[6]. Figure 3-8 shows a schematic diagram of the XRR setup. Following this, a brief theoretical description of the technique is given.

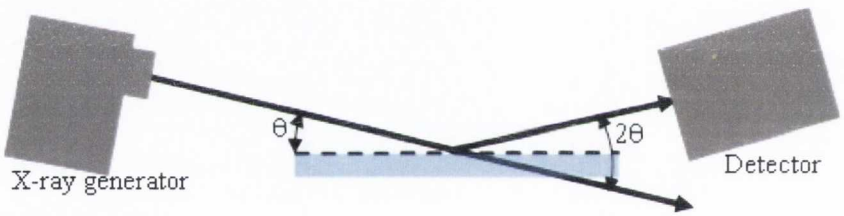

Figure 3-8 Schematic diagram of x-ray reflectivity setup.

XRR is based on the fact that for x-rays, the refractive index n is less than 1 for materials. Thus at critical angle, total internal reflection occurs for x-rays passing from ambient medium (air) into thin film. The complex refractive of material in x-ray range is given by[7]:

$$n = 1 - \delta + i\beta \qquad 3\text{-}10$$

where δ represent the deviation of the refractive index from 1 and is a positive number of the order of 10^{-5} - 10^{-6}, β is the absorption index. The quantity δ is related to the electron density n_e of the material by following relation:

$$\delta = \frac{\lambda^2 n_e r_e}{2\pi} \qquad 3\text{-}11$$

where λ is the wavelength of radiation and r_e is the classical electron radius. The electron density is given by:

$$n_e = N_A \frac{(Z - f)}{A} \rho \qquad 3\text{-}12$$

where N_A is the Avogadro number, Z is the number of electron per atom, f is the atomic scattering factor, A and ρ are the atomic weight and mass density of the material respectively. Hence, the quantity δ can be related to mass density ρ of the material and the critical angle (the angle at which the x-ray beam starts to penetrate the sample or thin film) thus can be used to determine the mass density of the film. Neglecting β in Eq.3-10 gives:

$$n \approx 1 - \delta$$

$$\cos(\theta_c) = n_1 / n_{air} \qquad 3\text{-}13$$

$$1 - \frac{{\theta_c}^2}{2} \approx 1 - \delta_c$$

Thus the value of δ at critical angle (δ_c) is given by:

$$\delta_c = \frac{{\theta_c}^2}{2} = \frac{\lambda^2 r_e}{2\pi} N_A \frac{Z - f}{A} \rho \qquad 3\text{-}14$$

Thus, we can determine the mass density of the thin film material. The Kiessig fringes which result from interference after beam has penetrated into the sample can be used to determine the thickness of thin film, using the equation:

$$\alpha_m^2 = \alpha_c^2 + m^2 \frac{\lambda^2}{4t^2} \qquad 3\text{-}15$$

Where t is the thickness of thin film m is the order of fringe and α_m is position of the fringe in radians. The surface roughness of the films can also by be determined by modelling the extinction of the reflected intensity and the attenuation of the Kiessig fringes.

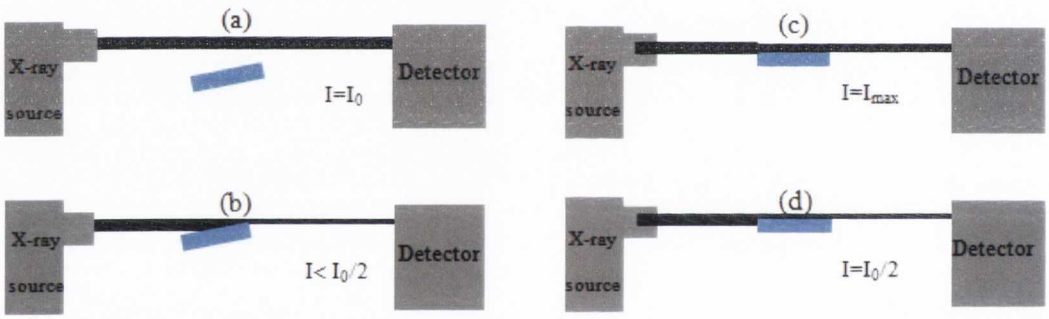

Figure 3-9 Schematic diagram explaining the method for alignment of sample for XRR measurement.

Figure 3-9 describes the step by step method for alignment of the sample for XRR measurement. The x-ray generator and the detector are first placed in a straight through position (i.e. 2θ=0) in order to measure the beam intensity Figure 3-9(a). The sample is raised so that the intensity of the x-ray beam reduced to about 1/3 of the maximum intensity (Figure 3-9(b)). The sample is then rotated through ω (the angle the sample surface makes with the beam) until the intensity is maximum (Fig. 3-8c), the sample surface is then parallel to the beam. The sample is finally raised so that the intensity is

half of the initial intensity (Figure 3-9(c)). The sample is thus aligned to the beam and bisecting it (Figure 3-9(d)). A θ - 2θ scan is then performed from $0^{o} - 6^{o}$. The reflected intensity curve are fitted using a commercial software called LEPTOS[6].

3.2.4 Scanning electron microscopy

The surface morphology of the nanoparticle films were studied using a scanning electron microscope (SEM). The scanning electron microscope accelerates electrons that have been generated by heating a tungsten filament through several (0.3-4) kV potential. These electrons are focused into a beam using a magnetic lens onto the sample surface. The electrons interact with the sample and generate secondary and back scattered electrons, these are detected to image the sample surface. The SEM used for this study was a Carl Ziess Ultra plus at the Advanced Microscopy Laboratory, CRANN, Trinity College Dublin. This microscope also has the facility to work in transmission mode; the corresponding detector is known as a scanning transmission electron microscopy detector. In order to get better contrast for size distribution analysis and higher resolution, samples were investigated using this type of detector with microscope operating at 25 kV. A built-in variable pressure tool was also used in order to avoid charging the sample surface with the electron beam, since some of the samples were insulators.

3.2.5 Atomic force microscopy

The surface morphology of nanoparticle films in some experiments was studied using an atomic force microscope (AFM). AFM is suitable to investigate a wide range of materials, including insulators and semiconductors. AFM probes the surface of a sample with a microfabricated tip (~8 nm in diameter) mounted on a flexible cantilever (about 100-200 μm long). Forces between the tip and the sample surface (van der Waals forces or Pauli exclusion forces, etc.) cause the cantilever to bend, or deflect. A detector

measures the cantilever deflection as the tip is scanned over the sample. The measured cantilever deflections allow a computer program to generate a map of the surface topography with resolutions down to nanoscale. From the stored digital information, a three-dimensional image may be manipulated and enhanced with color, filters and can be enlarged and displayed from any altitude or azimuth. The lateral and vertical movements of the tip are controlled by piezoelectric transducers and a feedback loop that produces voltage differences proportional to the movement.

The AFM can be operated via two primary modes, contact or non-contact, to produce a three-dimensional surface profile. Surface imaging by AFM with a lateral resolution down to about 3 nm can be used to determine the features on the nanoscale and resolve individual holes, and atomic clusters on the sample surface. Three-dimensional profiling probes samples in real, three-dimensional space with vertical resolutions up to 0.01 nm. In the course of this study an Asylum Research Stand Alone atomic force microscope with 90 μm x and y and > 15 μm z travel was used to study surface morphology of the nanoparticle films. The tips were made of silicon with a tip diameter < 5 nm. More information about the AFM can be found, for example, in Ref. 9.

3.2.6 Nanoparticle size distribution analysis

Digitized scanning transmission electron micrographs (STEM) were used for the nanoparticle size analysis. A commercial software called Image-J was used to process the STEM images. The image processing needs only a few steps and precautions before getting the final size distribution.

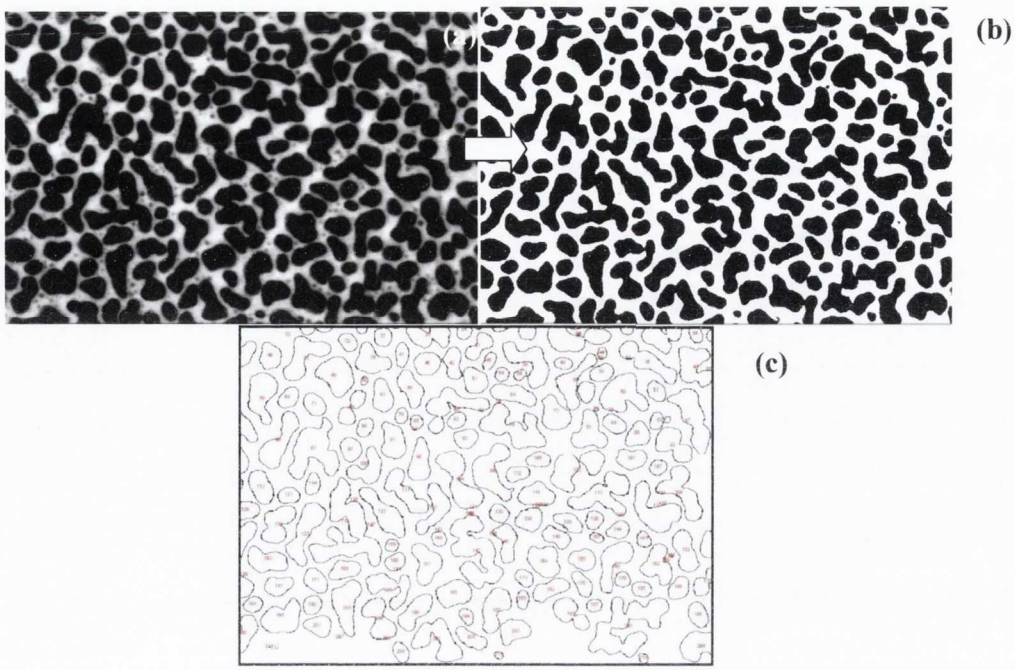

Figure 3-10 (a) original image (b) threshold image (c) final outlined particles.

A bright field STEM image is first loaded into the programme. The contrast/brightness of the images is then adjusted so that the particles stand out clearly from the background, great care has to be taken for vary small particles (< 3 nm) as they have inherently small contrast. The image is then transformed into a binary black and white image by thresholding the original image in order to have individual particles fully distinguishable (Figure 3-10 b). A good threshold image is found to be that in which all the particles are separated and show clear boundaries, sometimes, digital filters are used to improve the quality of threshold image. The image is then scaled in order to obtain the number of nanometres per pixel. The "Analyze particle" feature can finally be used to obtain a table containing geometrical information such as particle areas, perimeters and diameters including Feret diameter (the maximum distance between any two points along the selection boundary (Figure 3-10 c). An image of outlined and measured particles can be obtained in the end in order to confirm the measurement. The table containing

geometrical information about the particles can then be exported into analysis software such as Origin, where the statistical analysis such as histogram plotting and fitting the histogram using statistical distribution functions (to obtain the mean particle diameter) can be performed.

3.2.7 UV/Vis Spectroscopy

The optical absorption spectra of nanoparticle films were recorded using a Cary-50 UV/Vis single beam spectrophotometer, which can measure the transmittance ($T=I/I_0$) of the sample in the range of 190-1000 nm, where I is the intensity of light after it passes through the sample and I_0 is the intensity of light before it passes through the sample. The main parts of the spectrometer are a *Xe* discharge lamp as a UV/Vis radiation source, a sample holder compartment and a monochromator to measure a single wavelength of light.

To obtain a background reading, a blank substrate is loaded first into the sample compartment and the $T = 100\ \%$ is measured. The beam is then blocked to measure the $T = 0\ \%$. The sample is then finally loaded in the sample compartment to measure the transmittance of the sample (T). The absorbance A of the sample can then be calculated using equation:

$$A = \log(1/T) \qquad 3\text{-}16$$

3.2.8 White light interferometeric surface profiler

A white light interfermetric (WLI) surface profiler was used to analyse the ablation craters produced by nanosecond and femtosecond laser ablation, from which the total amount of material removed per laser shot from the target surface, was estimated. For the measurement of amount of material removed per laser shot, a small crater can be made on

the target surface and three dimensional profile of the crater can be obtained using the WLI surface profiler, from which the average crater volume and total ablation depth can be measured. By dividing the maximum ablation depth by number of laser shot fired, the ablation depth per pulse can be estimated.

The optical setup of the WLI surface profiler is essentially like a Michelson interferometer; a white light beam is split into two components using a beam splitter, one component goes to a reference surface inside the interferometer and the other goes to the sample or test surface. After reflection, the beams recombine, undergoing constructive and destructive interference and produce a fringe pattern. A precision translation stage and a CCD camera together generate a 3D interferogram of the sample which is stored in the computer memory. The interferogram is then transformed by frequency domain analysis into a quantitative 3D image. The crater profile in this experiment was measured using a ZYGO instruments 3D optical surface profiler. The optical setup for the ZYGO white light interferometer and 3-dimensional profile of crater is given in Figure 3-11. A more detail explanation of WLI surface profiler can be found in Ref.10.

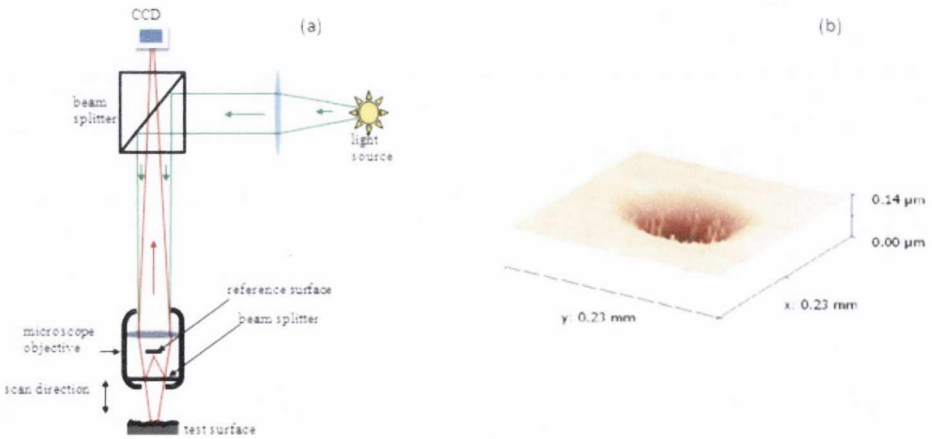

Figure 3-11 (a) Basic optical setup for WLI surface profilometer and (b) 3D surface profile of crater on a Ag target using fs-laser ablation.

3.3 Thickness distribution of the deposited material

To study the angular distribution of the overall plume in ns and fs-PLD, material from the ablation plume was deposited on a curved transparent plastic substrate and the thickness profile of thin film was obtained. This was done by measuring the optical transmission of the deposited film with the help of a calibrated flatbed scanner[††]. Figure 3-12 shows the schematic diagram of the experimental setup. The deposited substrate was scanned using the flatbed scanner operating in transmission mode. The scanned image was recorded with a resolution of 150 dots per inch (dpi) and saved in a *24 bit RGB tif* file format. The procedure to obtain the film transmission from the scanned signal is described in the following section.

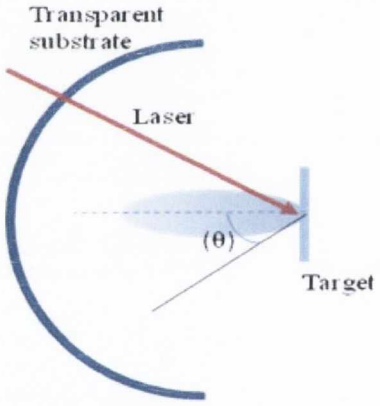

Figure 3-12 The schematic diagram of deposition setup

Scanner signal to transmission: The saved image was imported into the Matlab computer program and converted into a matrix corresponding to the green part (515 nm) of *RGB* image. The data from scanned image comes out in the form of scanner signal (as numbers from 0-255) which needs to be transformed into the film transmission. For this, a set of neutral density filters was used and the scanner signal was calibrated to obtain the

[††] Epson Perfection V700 PHOTO, 6400 dpi

relevant transmission. Figure 3-13 shows the calibration curve for the flatbed scanner for 515 nm.

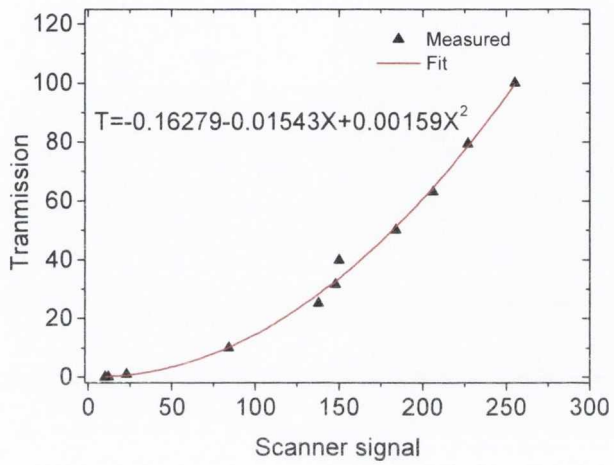

Figure 3-13 Calibration curve used to convert the scanner signal to the transmission of thin film. The red curve is the second order polynomial fit to the measured data, the equation is given in the plot.

Figure 3-14 shows the schematic diagram of the optical setup used for transmission measurements using flatbed scanner. The transmission of the film was normalized to the bare substrate by following method. The scanner was used to measure the transmission of the deposited substrate, $T_{film+subs}$, and the transmission of a bare substrate, T_{subs}. The ratio $T = T_{film+subs} / T_{subs}$ was then found. Since the glass substrate is transparent, $T_{subs} = T^2_{bare}$ where T_{bare} is the transmission across each bare glass interface thus:

$$T = \frac{T_{film}\, T_{bare}}{T_{bare}^2} = \frac{T_{film}}{T_{bare}} \qquad 3\text{-}17$$

where T_{film} is the transmission of the film into the substrate and T is the normalized transmission.

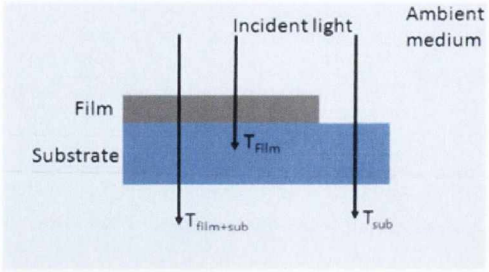

Figure 3-14 Schematic diagram of deposited substrate. The figure shows the formulism used for thickness analysis.

Transmission to thickness conversion: Thickness distribution of the deposited material was obtained by comparing the measured transmission with a calculation obtained from a commercial software called IMD/XOP[11] . The software uses bulk refractive index values and calculates the optical properties of thin metal film deposited on solid substrates using Fresnel equations. Figure 3-15 is the transmission versus thickness plot for Ag obtained using XOP software. The transmission curve was fitted using following equation.

$$T = Ae^{-d/B} + C \qquad 3\text{-}18$$

where *A*, *B* and *C* are fitting constants and *d* is the film thickness. The values of fitting constants obtained for Ag thin film are: *A=1.21403 ±0.00525, B=19.12116±0.24147* and *C=-0.0259±0.00403.* Thus the thickness profile can be obtained by rearranging Eq. 3-18 as:

$$d = -19.1211 \ln\left(\frac{T + 0.0259}{1.21403}\right) \qquad 3\text{-}19$$

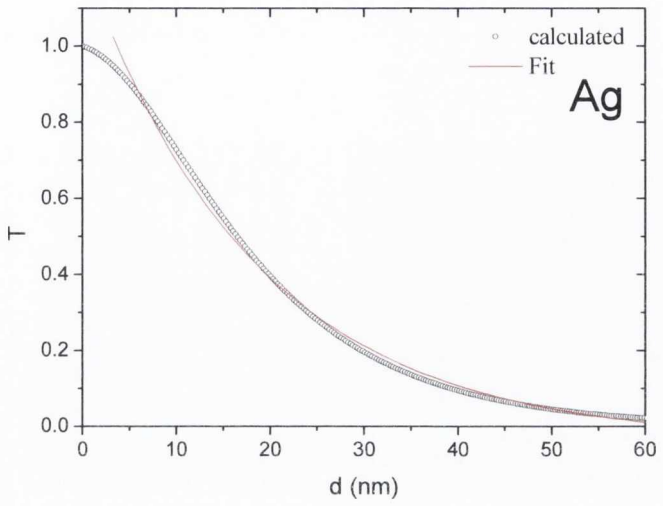

Figure 3-15 Transmittance Vs thickness of Ag film calculated using XOP/IMD software.

where T is the normalized transmission. The thickness of Ni and Au, was also obtained by the same procedure. Figure 3-16 (a) and (b) shows calculated and fitted transmission curves for Ni and Au respectively. The equation used to calculate the thickness from measured transmission is given in each plot. It should be noted that the transmission in each case was normalized by the substrate transmission (0.96) in order to take account for the reflection losses due to the bare substrate.

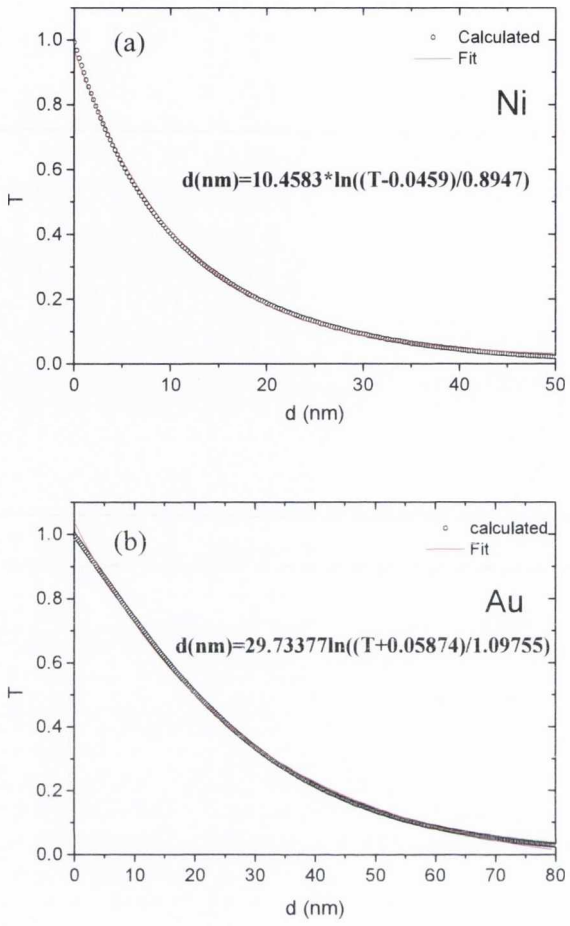

Figure 3-16 Transmittance of thin silver, nickel and Au films as a function of films thicknesses, the red curve is theoretical fit to the plot obtained by XOP software. The equation obtained after fitting to calculate the film thickness is given in each plot.

3.4 Optical emission spectroscopy and imaging of femtosecond laser ablation plume

Time and space resolved optical emission spectroscopy and imaging was used to study the dynamics of the fs-laser ablation plume the detail of which is described below.

Two intensified charged couple devices (Andor-istar DH 734 and Andor DH 520) were used to study the time resolved emission from the fs-laser ablation plume. One of these cameras was used to capture the optical emission from the plasma in imaging mode via a

1:1 camera lens, while the other camera was attached to a 0.25 m Czerny-Turner spectrometer (Oriel Cornerstone 260i) with selectable diffraction gratings (300, 600 and 1200 lines/mm). The optical configuration of the spectrometer is given in Figure 3-17. The entrance slit of the spectrometer was 50 μm×3 mm in dimensions, and the optical configuration of the spectrometer imaged the slit 1:1 in the horizontal plane and 1:1.6 magnified in the vertical plane. The Andor ICCD DH 520 which was used to record the wavelength dispersed spectra consisted of 1024×255 pixels each of size 26×26 μm. The minimum temporal gate Andor-istar DH 734 and Andor DH520 was 3 ns and 7 ns respectively.

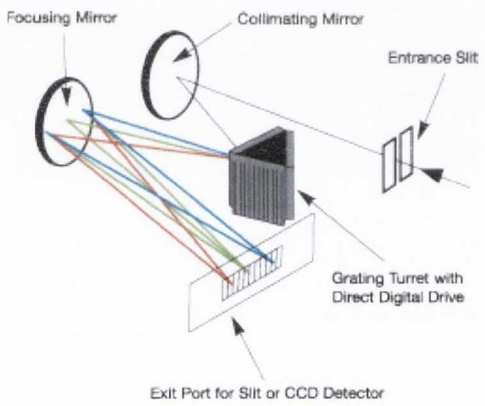

Figure 3-17 Optical configuration used in Oriel Cornerstone 260i spectrometer

The delay between the measurement and some reference time zero was adjusted using a Stanford Research DG535 delay generator. Figure 3-18 show the optical imaging setup used for optical emission spectroscopy and fast imaging of femtosecond laser ablation plume.

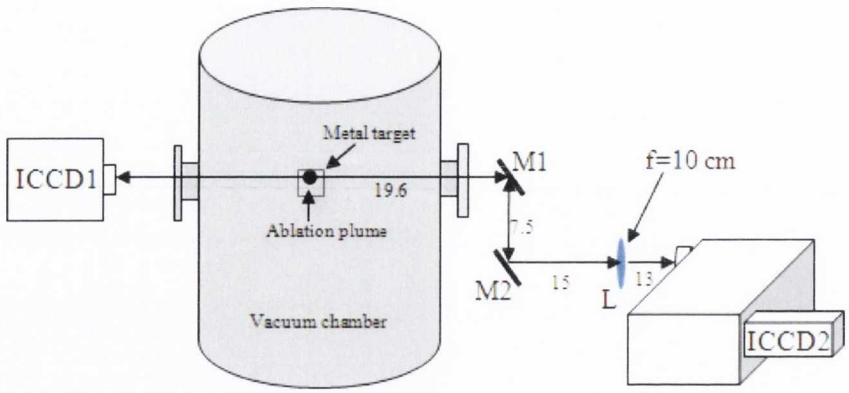

Figure 3-18 Schematic diagram of the optical setup used to study the dynamics of fs-laser ablation plume. All distances are in centimetre units.

In the above diagram M1 and M2 are two mirrors used to rotate the plume image by angle of 90^{o} so that the long axis of the plasma which is normal to the target surface is parallel to the spectrometer entrance slit and L is a 10 cm focal length achromatic glass lens used to image the plasma emission onto the spectrometer slit to deliver light into the spectrometer. An achromatic lens was used to correct any wavelength dependent aberration effects. The imaging system resulted in an overall demagnification of 3 of the optical emission area onto the spectrometer slit. ICCD1 and ICCD2 are the intensified charged coupled devices for plume imaging and optical emission spectroscopy respectively. The half-angle subtended at the entrance slit by the lens was 5.5^{o} which is smaller than the spectrometer acceptance half-angle of 7^{o}, therefore the spectrometers numerical aperture was somewhat under-filled. The will also has effect on the resolving power of the spectrometer. The resolving power or chromatic resolving power, R, of diffraction grating is defined in terms of λ and $\lambda+\Delta\lambda$, where $\lambda+\Delta\lambda$ is the closest wavelength to λ that can be resolved. Theoretically, the resolving power of the grating is given by the following equation[12,13]:

$$R = \frac{\lambda}{\Delta\lambda} = \frac{W(\sin(I) + \sin(D))}{\lambda} \qquad 3\text{-}20$$

Where W is the illumination width of grating, I and D are the angle of incident and diffracted ray of light w.r.t the grating normal. To explain grating normal and angles I and D, a schematic diagram representing diffraction of light ray (AB) from grooved diffraction grating is given in the following figure:

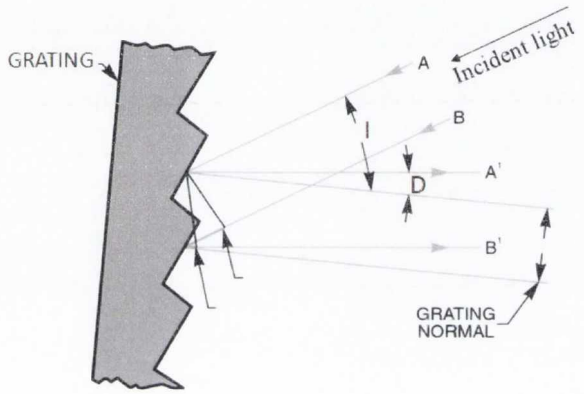

Figure 3-19 Schematic of diffraction of light ray AB from diffraction grating.

The factor of $(\sin(I) + \sin(D))$ in the above equation corresponds to the grating equation; $m\lambda=(sin(I) + sin(D))$ (the path difference equation for constructive interference), where m is the diffraction order. By under-filling the spectrometer numerical aperture means we will be reducing the illuminated width of the diffraction grating. Hence looking at Eq. 3-20 it can be seen that reducing the illumination width would reduce the resolving power of the spectrometer.

3.4.1 Spatial calibration

The spatial calibration of the spectrometer (distance measured in μm per pixel) was performed experimentally. For this, a metal grid of known separation was placed at the

plasma plane (the plane of ablation plume), and a spectrally resolved ICCD image of the grid was recorded.

Figure 3-20 shows ICCD image of the grid placed at the plasma plane. The grid separation was 3 mm and the corresponding number of pixels is 70, this gives a spatial resolution of 42.8 μm per pixel.

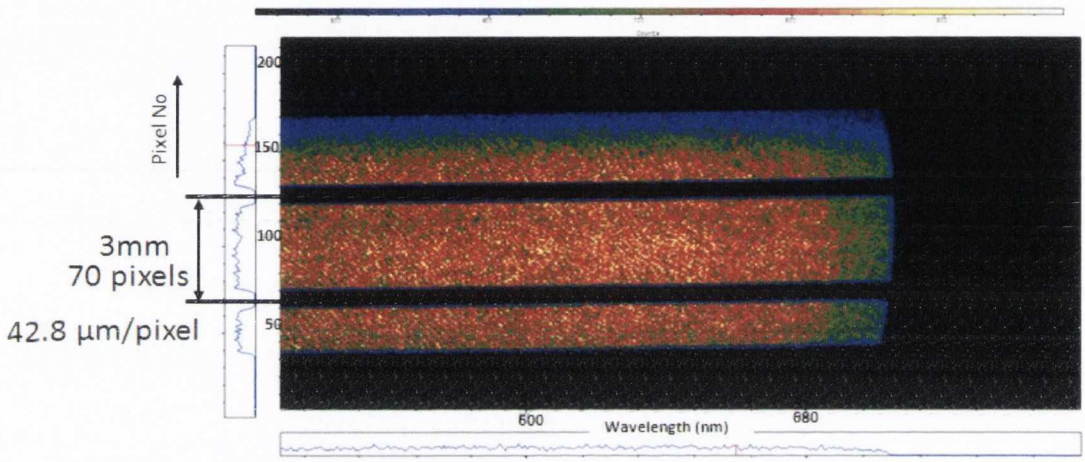

Figure 3-20 Spectrally resolved ICCD image of the grid placed at the plasma plane. The image was recorded by placing tungsten halogen lamp at the back of the grid.

3.4.2 Wavelength and intensity calibration

For the wavelength calibration of the spectrometer, a mercury (Hg) lamp and a potassium (K) lamp with known line transitions were used. As an example, Figure 3-21 shows the optical emission spectrum of the Hg lamp used for spectrometer wavelength calibration. The calibration was also corroborated using a helium neon laser and femtosecond ablation laser operating at 800 nm. For the calibration of the absolute intensity, a 100 W quartz tungsten halogen lamp (Oriel QTH 6333) with a well-defined output was used.

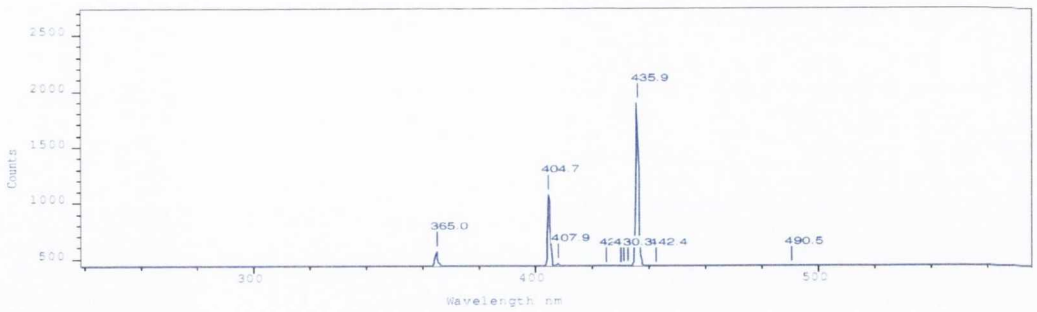

Figure 3-21 Optical emission spectrum of Hg lamp in the wavelength range of 244-500 nm, showing important transitions at 365, 404.7, 404.8 and 435.9 nm.

The halogen lamp emits like a blackbody with well-known spectral irradiance (W m^{-2} nm^{-1}) at 50 cm away from the emission source, and the output is given by the following formula:

$$I_l(\lambda) = K_{fit} 10^{-9} \frac{2\pi hc^2}{\lambda^5} \left(\frac{1}{e^{\frac{hc}{\lambda kT}} - 1} \right) \qquad 3\text{-}21$$

where $K_{fit} = 7.64 \times 10^{-6}$ is a fitting constant and the temperature T=3317.8 K. The irradiance of the calibration lamp calculated using the above equation and is plotted in Figure 3-22.

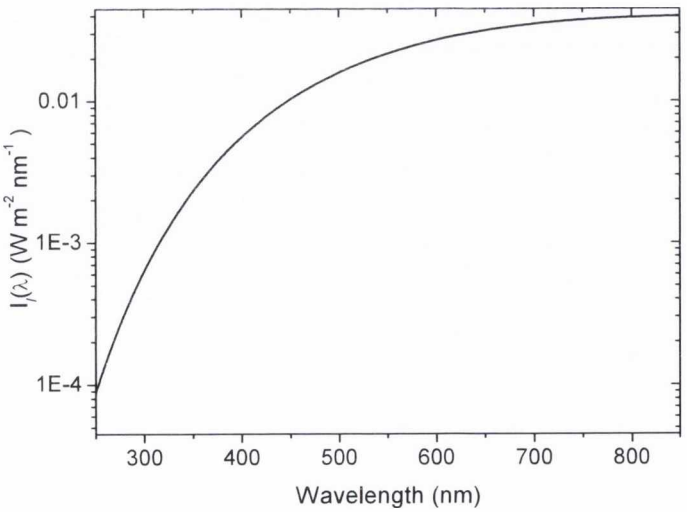

Figure 3-22 Spectral irradiance of 100 W quartz tungsten halogen lamp 50 cm away from the source.

The detector itself measures a certain number of counts $C_l(\lambda)$ from source which can be related to the spectral irradiance by following formula:

$$C_l(\lambda) = F(\lambda)\, I_l(\lambda)(n_a n_p \Delta t)_l \qquad 3\text{-}22$$

Where $F(\lambda)$ is the calibration function, n_a is the number of acquisition for collection of light from the source, n_p is number of pixel binned and Δt is the gate time of the camera. The absolute intensity of light measured by the ICCD sensor depends upon various factors, such as throughput of light collection system such as mirrors, lenses, apertures and the spectrometer (entrance slit, diffraction grating). The number of counts read by each pixel in the ICCD sensor also depends on the gain of the detector, the gate time and the number of acquisitions used to accumulate the signal. The calibration function $F(\lambda)$ takes into account all these losses or changes in the spectral energy distribution of the emitted light when it reached the ICCD detector. Rearranging the above equation for $F(\lambda)$ gives:

$$F(\lambda) = \frac{C_l(\lambda)}{I_l(\lambda) n_a n_p \Delta t} \qquad 3\text{-}23$$

Measurements of the output of spectral lamp were made by placing it 50 cm away from the plasma plane, where the radiation flux of the lamp is described by Eq. 3-21. The half angle subtended by the lamp on the spectrometer slit is 0.92^{o} which is smaller than the acceptance half angle of the spectrometer 7^{o}, this means that all the light emitted by the lamp leaving the plasma plane is collected by the spectrometer. The signal (photon counts) recorded using the calibration lamp and the calibration function for our optical setup is plotted in Figure 3-23.

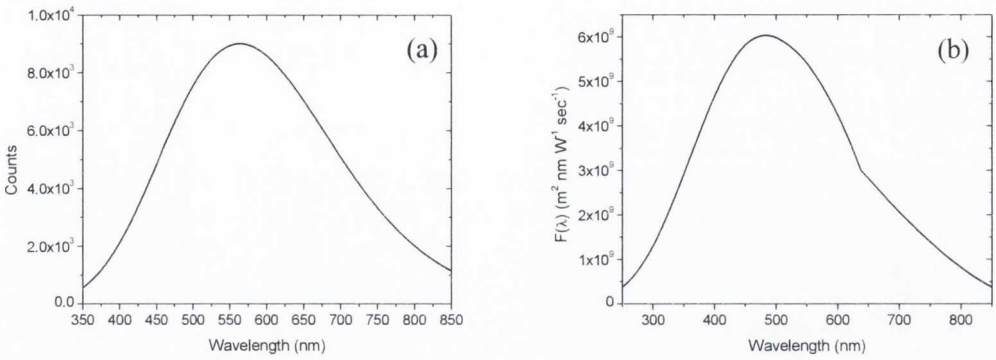

Figure 3-23 (a) Signal from the 100 W quartz tungsten halogen lamp recorded by placing it 50 cm away from the plasma plane, (b) calibration function *F(λ)* calculated using calculated using Eq 3-22.

Hence if the source of known spectral irradiance is measured, the calibration function $F(\lambda)$ can be obtained for a particular optical setup. The equation describing the counts recorded for plasma will be:

$$C_p(\lambda) = F(\lambda)L_p(\lambda)\Omega(n_a n_p \Delta t)_p \qquad 3\text{-}24$$

where $L_p(\lambda)$ [W m^2 nm^{-1} sr^{-1}] is the plasma spectral radiance and Ω is the solid angle subtended by the optical system (the lens L in Figure: 3-17) to the plasma plume.

3.5 References

1 Thorlabs 13123-S01 data sheet model DET10C, (2009).

2 I. Langmuir and H.M. Mott-Smith, Gem. Electr. Rev 26, 731 (1923).

3 B. Doggett and J.G. Lunney, Journal of Applied Physics 105 (3), 033306 (2009).

4 Y. Franghiadakis, C. Fotakis, and P. Tzanetakis, Applied Physics A: Materials Science & Processing 68 (4), 391 (1999).

5 D.W.Koopman, Physics of Fluids 8 (14) (1971).

6 http://www.bruker-axs.com/stress.html.

7 E. spiller, *Soft x-ray optics* (SPIE, 1994).

8 D. S. Su and Su-Huai Wei, Applied Physics Letters 74 (17), 2483 (1999).

9 D. Rugar and and P. Hansma, Physics Today 43 (10), 23 (1990).

10 B. Brian and T. Vincent, Optical Engineering 37, 1796 (1998).

11 http://www.esrf.eu/computing/scientific/xop2.1/extensions.html.

12 J.Michael Hollas (Ch 3), *Modern spectroscopy*. (John Wiley & sons Ltd, 2004).

13 Newport(http://www.newport.com/Grating-Physics/383720/1033/content.aspx).

Chapter 4 Investigation of ns- and fs-ablation of metals and deposition of nanoparticle films

4.1 Introduction

Nanostructured materials and surfaces show interesting novel optical, electronic, magnetic and catalytic properties which result when the dimensions of matter are reduced to the nanoscale (1-100 nm)[1,2]. There are a wide range of physical and chemical techniques that can be used for nanoparticle deposition. Among the physical methods PLD is a simple technique that can, in principle, be applied to all solid materials.

For nanoparticle growth with ns-PLD, there is much evidence that the growth takes place by surface diffusion of the deposited material. Dolbec *et al.*[3] have prepared Pt nanoparticles on highly oriented pyrolithic graphite by ns-PLD. By studying the morphology of nanoparticles at different equivalent thickness they found that the nanoparticle size varies with equivalent solid-density thickness. A similar trend has been observed in the fabrication of nano-composite films of Cu and amorphous alumina by Afonso *et al*[4]. In the fs-blation, Amoruso *et al.* observed via fast photography and OES that the nanoparticles are present in the ablation plume and can be collected on a solid substrate[5]. The investigation of fs-laser ablation plume via fast imaging and OES will be discussed in more detail in next chapter.

In this chapter we report the results of the detailed investigation of ns- and fs-laser ablation plumes. The ablation rate, ionization fraction and the energy distribution in both ns- and fs-ablation plumes have been studied. We have also explored how the morphology of nanoparticles changes with the equivalent solid-density thickness in both cases. A

quantitative theoretical description of the measured optical absorption spectra of noble metal nanoparticle films is given in the end of the section.

4.2 Determination of focused laser beam spot size

4.2.1 ns-laser

An important quantity in the pulsed laser ablation process is the laser fluence (laser pulse energy/focal spot area). For the ns-laser (KrF Excimer), the focal spot was rectangular shaped. Figure 4-1(a) shows a photograph of the burn spot made on laser burn paper using a single laser shot.

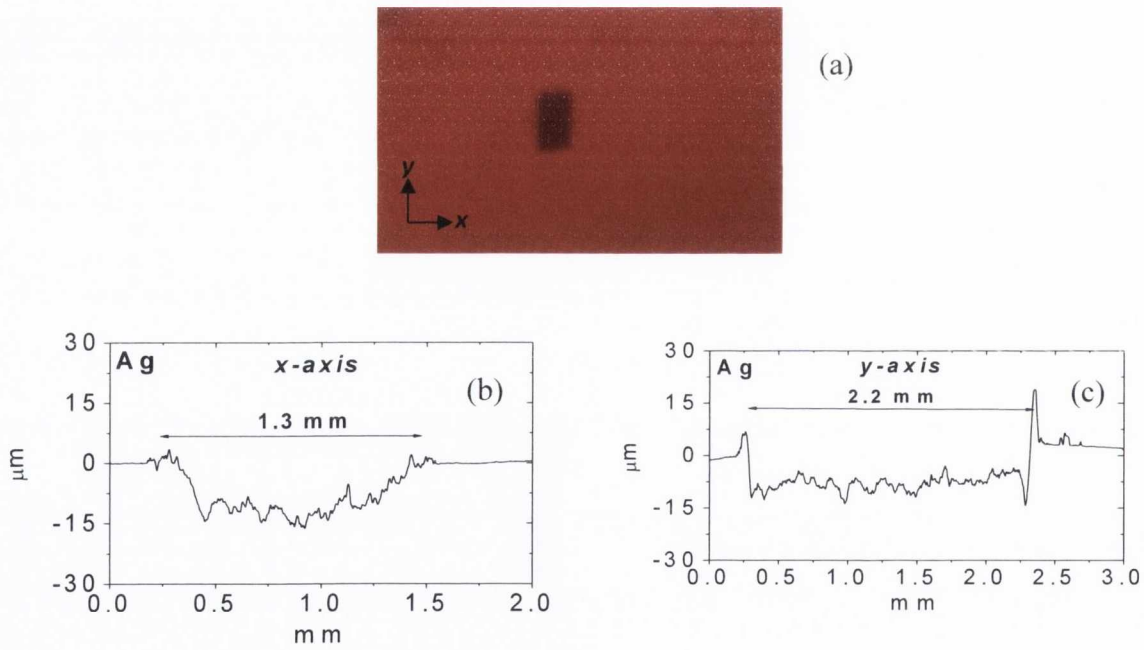

Figure 4-1(a) ns-laser focal spot shape as recorded on the laser burn paper. (b, c) Profile of the laser ablation crater along x- and y-axis respectively, made on a Ag target at 50 mJ pulse energy using 1200 laser shots.

To obtain the exact spot dimensions at focus along x and y-axis, a crater was made on a Ag target using 1200 laser shots at 50 mJ pulse energy and the dimensions of the crater along both directions were measured using a Dektak surface profiler. Figure 4-1(b) and (c) shows the crater profiles made on the Ag target along x and y-axis respectively.

The spot dimensions obtained from the profile measurements were 0.13 cm and 0.22 cm (along x- and y-axis respectively) which correspond to the spot area of 0.0286 cm^2. Considering a uniform spatial intensity distribution, the average fluence was obtained using the following relation:

$$F = \frac{P}{f_{rep}A} \qquad 4\text{-}1$$

Where f_{rep} is the laser repetition rate, P is the laser power in watts (as measured using power meter with laser running at repetition rate f_{rep}) and A is the focused laser beam spot area.

4.2.2 fs-laser

The spatial profile of the fs pulsed laser was non-uniform and Gaussian in shape. Figure 4-2 shows the profile of the unfocused laser beam recorded using a Coherent CCD laser beam profiler[†].

The focal spot size in this case was measured by considering that the spatial profile of the laser beam is Gaussian, and beam waist was measured according to the method explained in Ref. 6.

[†] Coherent Laser Cam-HR 2/3 inch, 1.3 Megapixel, CMOS camera

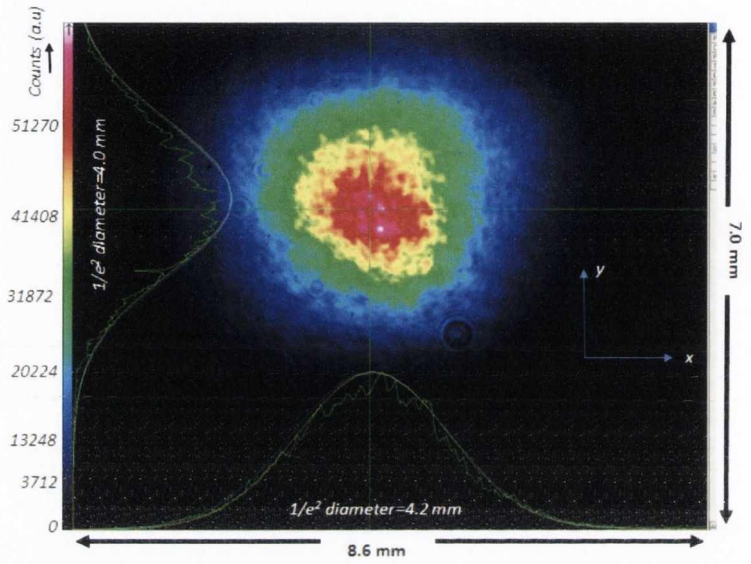

Figure 4-2 fs laser beam profile measured with the CCD beam profiler camera. The color from red to blue represents the beam intensity from maximum to minimum. The $1/e^2$ diameters of the unfocused beam along x and y axis are also given in the figure. The diameters were obtained using the software provided with the beam profiler camera.

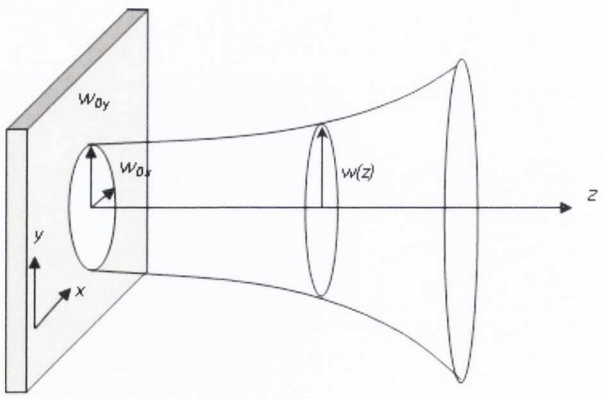

Figure 4-3 Gaussian beam waist w(z) as a function of axial distance z . w_{0x} and w_{0y} are the beam waists in x and y direction on the target surface.

In our experimental setup, the target was placed at an angle of 45° with respect to the laser beam which makes an elliptical shaped spot on the target surface. Figure 4-3 shows the propagation of a Gaussian beam and spot shape on the target surface. The fluence distribution of an elliptical Gaussian beam on the target surface placed in *xy*-plane can be written as:

$$F = F_p e^{-2\left(\frac{x}{w_{0x}}\right)^2} e^{-2\left(\frac{y}{w_{oy}}\right)^2} \qquad 4\text{-}2$$

Where F_P is the peak fluence the centre of the beam and w_{0x} and w_{0y} are the beam waists in *x* and *y* direction. Integrating the laser fluence over *xy* plane gives the energy per pulse of the laser beam.

$$E = \iint_{-\infty}^{\infty} F_p e^{-2\left(\frac{x}{w_{0x}}\right)^2} e^{-2\left(\frac{y}{w_{oy}}\right)^2} dx\, dy$$

$$E = \frac{1}{2} F_p \pi w_{0x} w_{0y}$$

hence

$$F_p = \frac{2E}{\pi w_{0x} w_{0y}} \qquad 4\text{-}3$$

which is the expression for calculating the peak fluence F_p of an elliptical Gaussian beam. The values of w_{0x} and w_{0y} can be obtained using the following method.

Considering that there exists a threshold fluence (F_{th}) for laser ablation, the points where the fluence drops below F_{th} will define an elliptical spot with radii x_{th} and y_{th} or minor and major diameters $X_{th}=2x_{th}$ and $Y_{th}=2y_{th}$ with its centre at the peak fluence. Figure 4-4 shows

this approach for $F_{th} = 0.2F_p$, the fluence distribution is plotted in this figure only along the x-axis for $F_p = 1$.

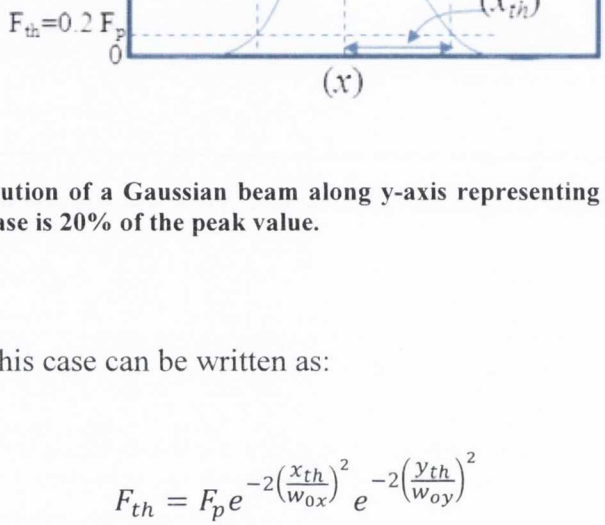

Figure 4-4 Fluence distribution of a Gaussian beam along y-axis representing the threshold radii (yth). Threshold fluence is this case is 20% of the peak value.

The relation for F_{th} in this case can be written as:

$$F_{th} = F_p e^{-2\left(\frac{x_{th}}{w_{0x}}\right)^2} e^{-2\left(\frac{y_{th}}{w_{oy}}\right)^2} \qquad 4\text{-}4$$

Since the Eq. 4-4 hold for each point in xy-plane it can be written for the coordinate $(x_{th}, 0)$ and $(0, y_{th})$, and the equations for x_{th} and y_{th} in terms of beam waist along x and y axis (w_{0x} and w_{0y}) can be obtained. Rewriting Eq. 4-4 for ($x_{th}, 0$) and working through for x_{th} gives:

$$x_{th} = \sqrt{\frac{1}{2}w_{0x}^2 \ln(F/F_{th})} = \sqrt{\frac{1}{2}w_{0x}^2 \ln(E/E_{th})} \qquad 4\text{-}5$$

In term of diameter (X_{th}):

$$X_{th} = \sqrt{2w_{0x}^2 \ln(E/E_{th})} \qquad 4\text{-}6$$

or

$$X_{th}^2 = 2w_{0x}^2(\ln(E) - \ln(E_{th})) \qquad 4\text{-}7$$

where E is the laser pulse energy and X_{th} is the diameter of the elliptical beam spot along the x-axis. The above equation can be used to fit the experimental data i.e. the plot between X_{th}^2versus *ln (E)* and the beam waist and the threshold energy can be obtained from the slope of and intercept of the graph provided that a linear relationship exists between both quantities (i.e. X_{th}^2 and ln(E)). A similar relationship can be obtained for Y_{th} and the beam spot area can be calculated as $A = \frac{\pi}{4} X_{th} Y_{th}$.

Figure 4-5 shows the optical microscope images of ablation spots or craters made on a Si substrate at different laser energies. The sample was placed at the position of target in the vacuum chamber and each crater was made using 10 laser shots. The minor and major diameters (X_{th}) and (Y_{th}) were measured by transferring the microscope images into a commercial software called Image J[7] and X_{th}^2 and y_{th}^2 were plotted versus ln(E) to obtain the beam waists along minor and the major axis.

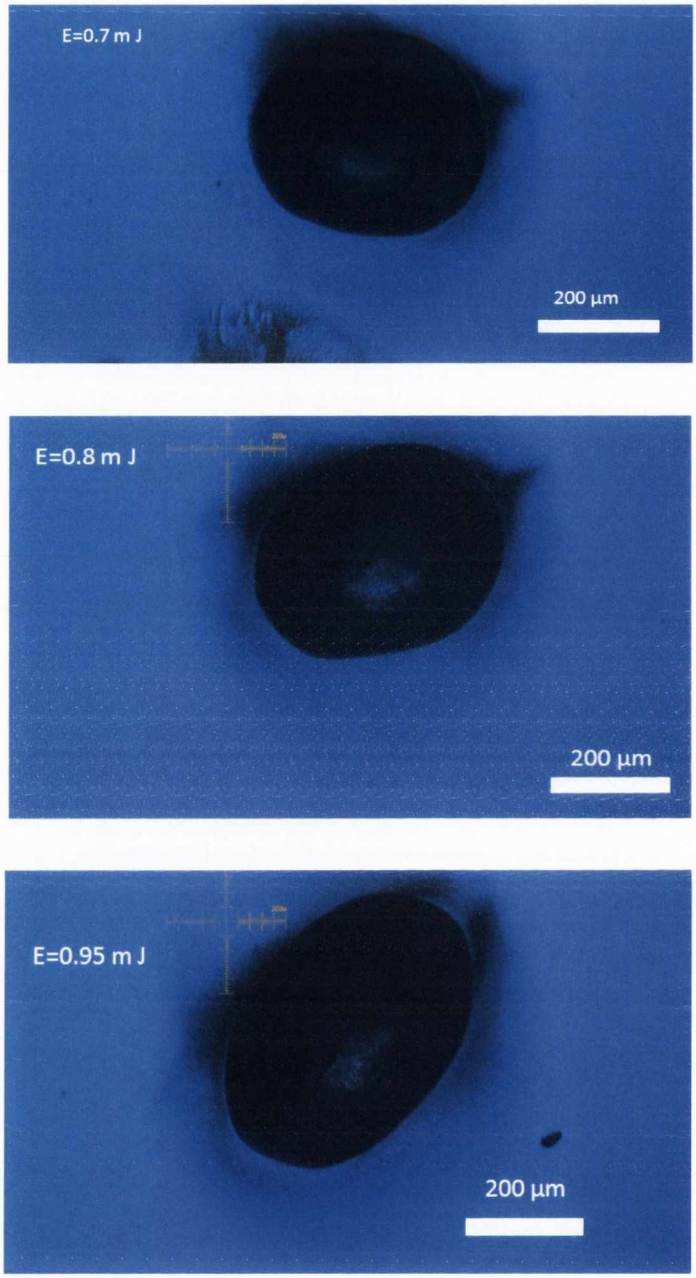

Figure 4-5 Optical microscope images of the craters made on a Si substrates, each ablation crater was made using 10 laser shots and the laser energy was changed for each crater.

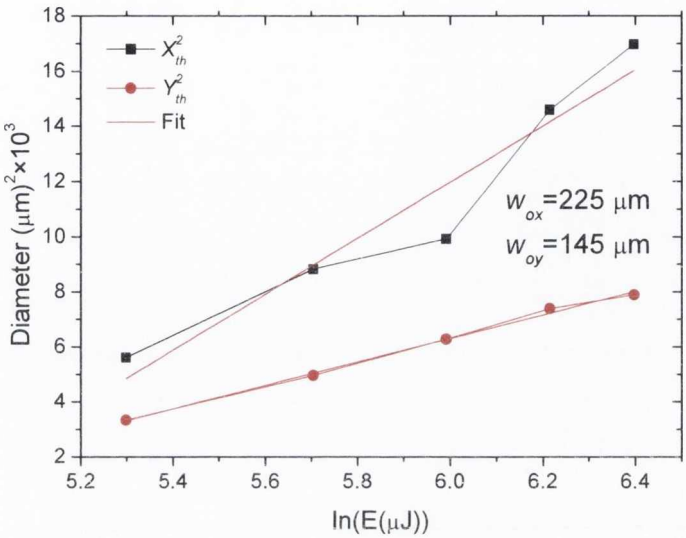

Figure 4-6 Plot of threshold diameters square (X_{th}^2 and y_{th}^2) *vs* ln (E). The minor and major waists are given in the plot.

Figure 4-6 shows the plot of the square of the minor and major diameters versus *ln (E)* for the beam waist and threshold energy calculation. The minor and major waists are: w_{0x}=145 μm and w_{0y}=225 μm in this case and the threshold energy for 10 laser shots is 109 μJ. Since the threshold energy for Si target is known it is also possible to calculate the threshold fluence. Dividing the obtained value of threshold energy with the laser spot area as $E_{th}/\pi\omega_{0x}\omega_{0y}$ gives us 0.09 J cm^{-2}, which is the threshold fluence for 10 laser shots of a Si target. Finally, from the knowledge of beam waists, the peak fluence can be calculated using Eq. 4-3 for a known value of pulse energy.

4.3 Analysis of ns- and fs-laser ablation plumes.

In this section the results of ns- and fs-laser ablation analysis are given. Laser ablation was performed for both cases in high vacuum (3×10^{-5} mbar for ns-PLD chamber and 6×10^{-5} mbar

for fs-PLD chamber). The average laser fluence was ~1.76 J cm^{-2} for ns-PLD and the peak laser fluence was ~1.4 J cm^{-2} for fs-PLD.

The range of above mentioned range of fluence was chosen to avoid particulate generation during laser ablation. For ns-laser of solids, splashing of molten material may cause generation of micron size particulates in ablation plume. One of the important mechanisms of splashing is surface boiling, where the subsurface layer is superheated before the actual surface layer has reached the vapor phase. This effect is most likely to take place in metals, because of their high conductivity. The maximum power density that a surface can absorb without splashing effect is scaled as; $P_{max} \propto 1/\rho^{1/2}$ where ρ is the electric conductivity[8]. Another factor involved in splashing is recoil pressure of the forward directed ablation plume to the liquid layer on target surface. Such effects i.e. surface boiling and magnitude of shockwave pressure can be decreases by lowering laser power density at the expense of decreasing deposition rates[8].

Experimental investigations of solid targets have shown that the ejection of such particulates or liquid droplets, are significant at laser fluence $\geq$ 2 J cm^{-2} [9,10,11]. Hence a laser fluence of $1 \leq F \leq 2$ J cm^{-2} was used in our experiments, to reduce the effect of droplet emission and to have sufficient deposition rates (nm/laser shot). However, because of constraints to adjust the laser power (since the UV attenuator was not available at this stage), and not to have very large spot size, an average fluence of 1.76 J cm^{-2} was used.

For fs-ablation, fluence value close to the ns-ablation was adjusted in order to have similar experimental conditions. The laser energy was reduced using neutral density filters to adjust the fluence. It is important to know if the above mentioned splashing effect is also present in fs-ablation. According to the experimental investigation of Ni by Liu *et al.*[12] some splashing

and particulate emission can also be observed in fs-ablation of metals. It has been suggested that this splashing can be due to the Gaussian fluence distribution on the target surface. Figure 4-7 show a schematic of Gaussian fluence distribution on target surface. Looking at the figure below, we can see that there exists a limit of fluence called F1 (well above the ablation threshold) below which the ablation takes place by emission some atoms and ions as well as direct emission of nanoparticles from the target surface (due to explosive boiling as explained in Ch1).

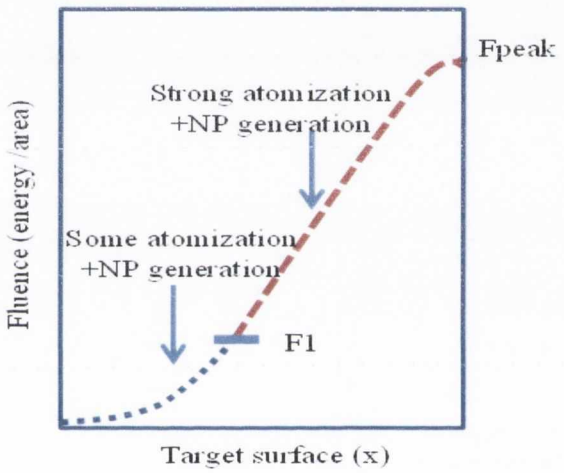

Figure 4-7 Schematic diagram of Gaussian fluence distribution and different fluence ranges in fs0laser ablation.

Above F1 direct nanoparticle emission occur along with a strong atomization (atoms and ion of the ablated material), this was observed by a rapid increase in the current density of the ablation plume using Langmuir ion probe. This strongly atomized, forward directed plume exert some recoil pressure in the region below F1 on the target surface, where the material exists in superheated liquid state. This may cause emission of few hundred nanometer (100-500 nm) size particulates.

The F1 suggested for Ni was ~ 1.0 J cm^{-2}. The peak laser fluence used in our experiments was 1.4 J cm^{-2}, hence some "large" particle emission is possible, and those particles were also observed during microscopy analysis of fs-PLD films (see e.g. Figure 4-29). The results obtained using above mentioned fluence for ns- and fs-PLD are given in the following sections.

The ion fluence and the net deposition were compared for both ablation plumes. The ion fluence was obtained by integrating the ion time of flight (TOF) signal recorded using a negatively biased Langmuir ion probe while the net deposition, in atoms cm^{-2} per laser shot, was derived from the deposition rate measured using a QCM.

The ion energy distribution $\left({}^{dN}/_{dE}\right)$ for both ns- and fs-ablation plumes was also derived from the measured ion TOF signal using the following ion energy distribution function:

$$\frac{dN}{dE} = \frac{I(t)t^3}{Aemd^2} \qquad 4\text{-}8$$

where $I(t)$ is the ion current with respect to time t, A is the area of the probe, m is the mass of an atom of the target material and d is the distance between probe and target. From this equation the average ion energy was calculated. The estimation of ion energy is important since it also gives us the information about self-sputtering of thin films during deposition with energetic ions in the ablation plume. The measured ion TOF signal and energy distribution for the ns-laser ablation case was also compared with the theoretical Anisimov model of plasma plume expansion described in Ch. 2. The results of ns- and fs-laser ablation analysis are given in the following sections.

4.4 ns-laser ablation analysis

Figure 4-8 (a) shows the Langmuir probe signal for Ag at laser fluence of ~1.76 J cm^{-2}. The probe was biased at -25 V and the target-to-probe distance was 5.8 cm. It can be seen that the ion signal rises rapidly as the plume approaches the probe and starts to drop after a few μs as the plume moves beyond the probe position. Assuming that the ions move with a constant velocity after leaving the target, it is also possible to calculate their velocity by dividing the probe distance by the TOF. Although the assumption is not strictly true, it can be seen theoretically that the initial acceleration phase of the ablation plume lasts for a few nanoseconds. The ion velocity corresponds to a peak TOF (v_p) for Ag is 13.8 km s^{-1}. It is also possible from the Anisimov model to calculate the plume front velocity (v_f) i.e. the velocity when the initial ions arrive at the probe. The relationship between the plume front velocity and the velocity corresponding to the peak TOF is given by[13] (for γ=1.25):

$$\frac{d}{v_f t_{peak}} = 0.577 \qquad 4\text{-}9$$

where d is the probe-to-target distance, which shows that the plume front velocity is almost twice the value of v_p. The value of v_p is this case is 23.9 km s^{-1}. Figure 4-8 (b) shows the corresponding ion energy distribution curve. The energy distribution extends up to few hundreds of eV with an average energy of 85 eV.

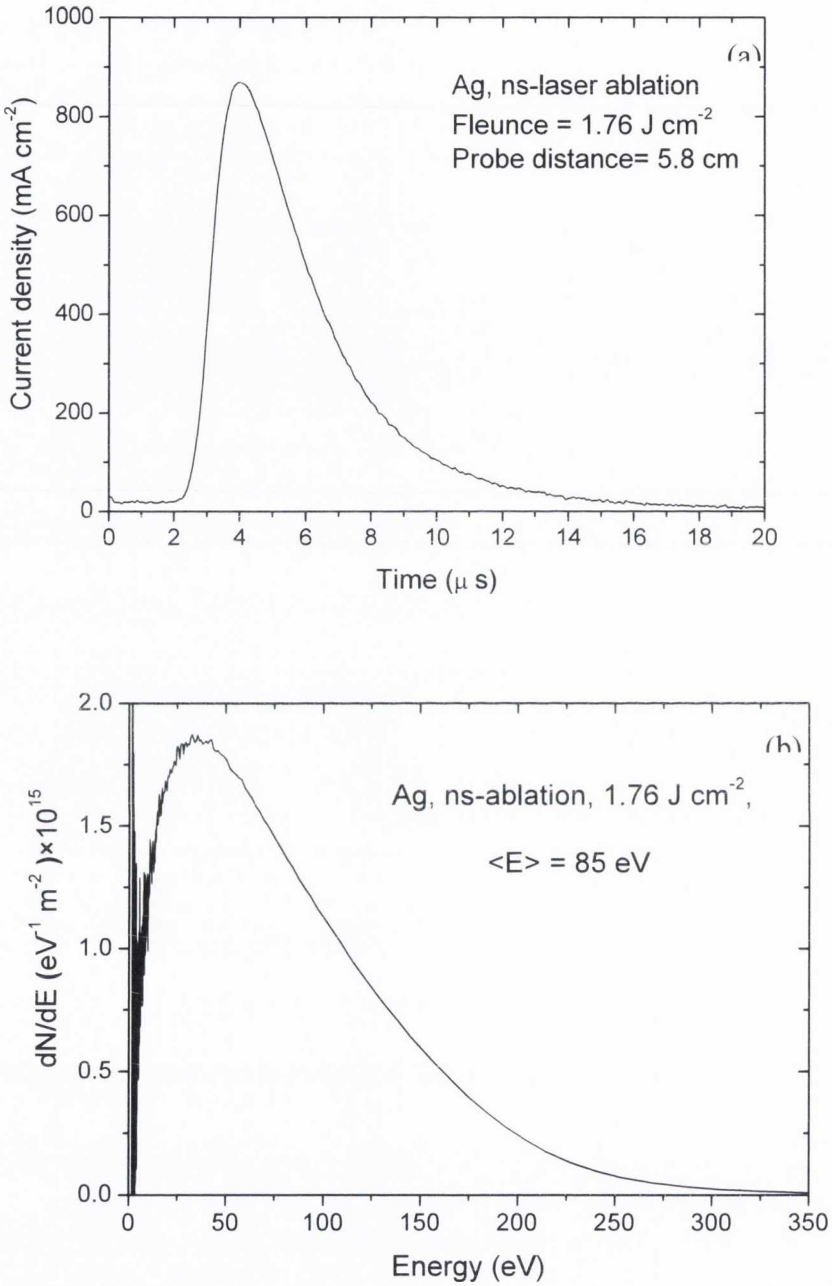

Figure 4-8 (a) Ion time-of-flight signal recorded using Langmuir probe placed at a distance of 5.8 cm away from the target at laser fluence of 1.76 J cm-2. (b) Corresponding ion energy distribution curve.

The experimentally measured probe signal and the energy distribution were also compared with the Anisimov plume expansion model.

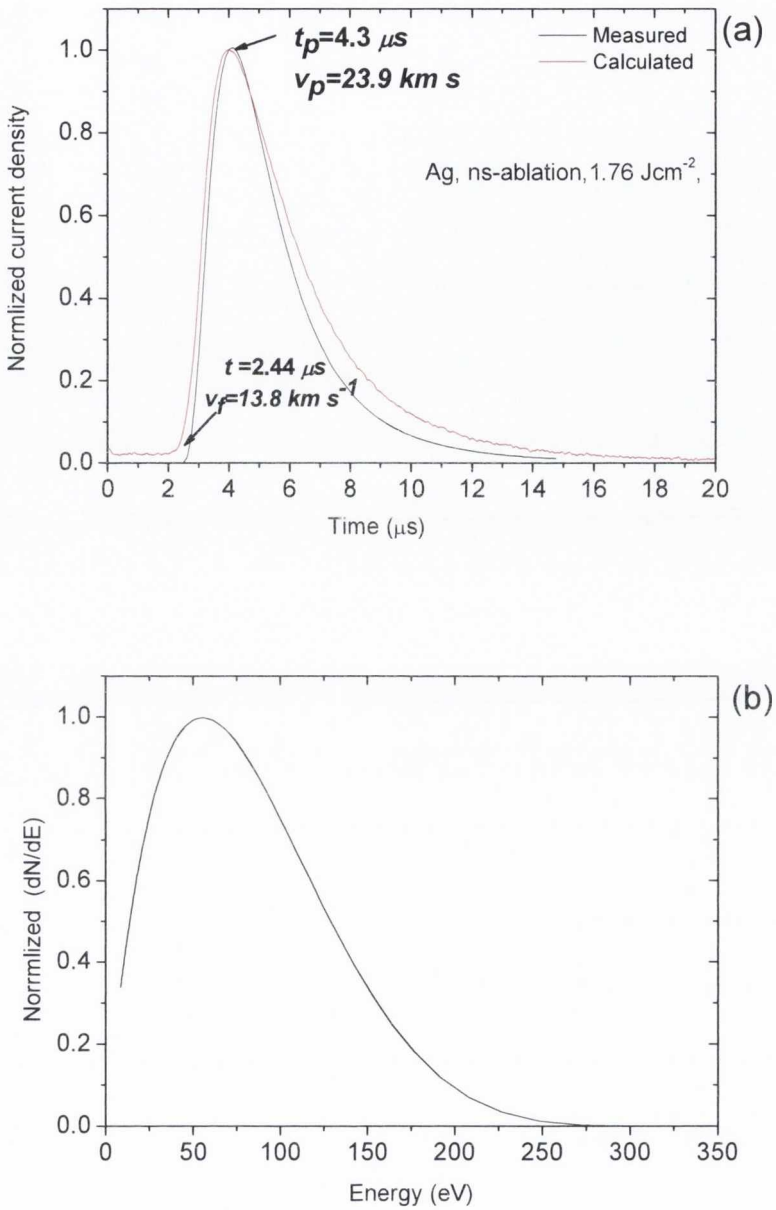

Figure 4-9 (a) Measured and calculated (for γ=1.10) ion current density signal of ns-laser ablation of Ag at 1.76 J cm^{-2}. The plume front and peak velocity was calculated from measured probe signal (b) Ion energy distribution function (dN/dE) calculated using Anisimov model.

The calculations were performed using a computer code written in Mathematica. The parameters which are required to run the code are initial plasma plume radii i.e. X_0 , Y_0 *and* Z_0 , the average energy per particle ε_p and the mass of particle m_p in the plume.

The initial plume dimensions in the *xy*-plane were taken as the laser spot dimensions on the target i.e. X_0*=2.5/2 mm*, Y_0*=1.5/2 mm*. The value of Z_0 was calculated using relation $Z_0 \approx c_s \tau_\ell$, where $c_s = (\gamma(\gamma-1)\varepsilon_p/m_p)^{1/2}$ is the speed of sound and τ_ℓ is the laser pulse width which is 23 ns in our case.

The average energy per particle ε_p was initially calculated to be 28 eV using the following equation[14]:

$$v_f = \left(\frac{dz}{dt}\right)^2 = \frac{\varepsilon_p}{m_p}\frac{2}{\gamma-1}\frac{5\gamma-3}{(1+2/k^2)} \qquad 4\text{-}10$$

where $\boldsymbol{v_f}$ is the plume front velocity and was obtained from the measured probe signal, γ is the adiabatic index which was set to 1.25, and m_p = 107.86 amu is the atomic mass of Ag, $k^2 = k_{zx}k_{zy}$ are the plume aspect ratios in *zx* and *zy* planes, k_{zx} =3.7 was obtained from the angular variation of the probe signal and k_{zy}=3.0 was estimated from the Anisimov model. The best fit was obtained for ε_p = 30 eV and Z_0 = 72.9 μm. Figure 4-9 (a) shows the measured and calculated normalized ion probe signals. It can be seen that the calculated probe signal agrees well with the theoretical model of the plasma plume expansion in vacuum. Figure 4-9 (b) shows the ion energy distribution obtained from the fitted probe signal, the shape of the distribution is similar to the measured one. The average energy in this case is 80 eV and the energy distribution extends up to 300 eV which is also in agreement with the measured energy distribution (see Figure 4-8 (b)).

The ion TOF signal of Au and Ni for ns-laser ablation was also recorded using a Langmuir ion probe. Figure 4-10 (a) shows the ion current density versus TOF signal for Au ablation. The velocity of ions correspond to the maximum of the probe signal (peak TOF) is 6.6 km s^{-1} and the plume front velocity calculated using Eq. 4-9 is 11.5 km s^{-1}. The ion energy distribution of the Au ablation plume is plotted in Figure 4-10 (b) the average ion energy is 36 eV in this case. Similarly Figure 4-10 (c, d) shows the ion current density and the energy distribution curve for Ni. The velocity of ions corresponding to the plume front and the peak of the current density signal are 26 km s^{-1} and 15 km s^{-1} which are higher compared to Ag and Au because of its lower atomic mass.

Looking at the ion energy distribution for all three metals we can see that in all cases, the ion energy extends up to a few hundred eV. Thus it can be seen that PLD is an energetic processes where high energy ions in the ablation plume may cause some self-sputtering of the deposited film[15]. However a more detailed description of the ion beam sputtering has been described by P.C. Zalm *et al*[16]. According to Zalm the sputtering yield of thin films, (Y_F), by a certain ion energy (E_P) depends on both the cohesive energy of the film species and the ion energy. The relation for $Y_F(E_P)$ is given by:

$$Y_F(E_P) = \frac{1.9}{U_0}\sqrt{\frac{Z_F}{f}}\left(\sqrt{E_P} - 0.09\sqrt{U_0}\right) \qquad 4\text{-}11$$

Where U_0 is the cohesive energy of the film species, E_P is the ion energy measured in keV, Z_F is the target mass and f is a function which is related to the ratio of the masses of target and the ion species. Along with the self-sputtering it has also been observed that the high kinetic energy (K.E) species (ions or atoms) also influence the morphology of the

nanoparticle films by making new nucleation sites, whose density increases with the K.E of the incident ions or

atoms in the ablation plume[3].

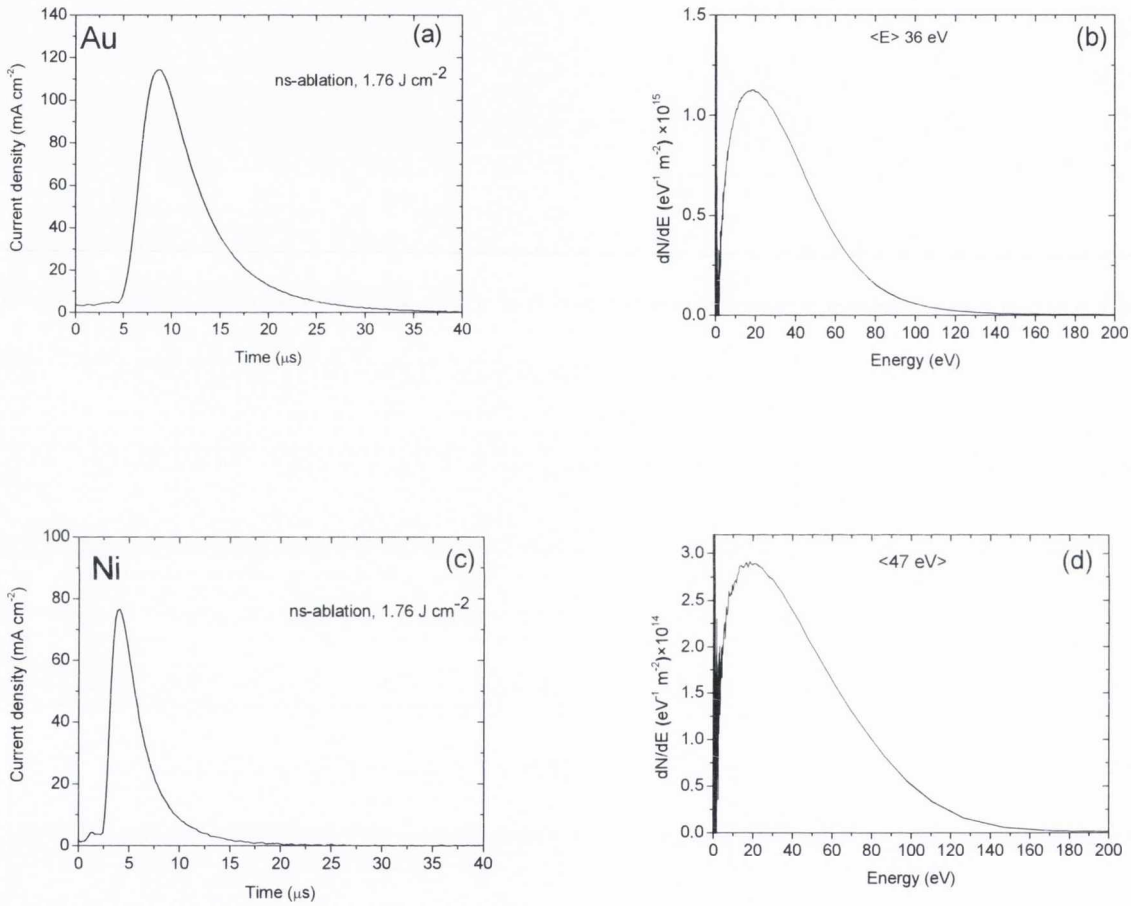

Figure 4-10 Transient ion current density and ion energy distribution for (a), (b) Au and (c, d) for Ni at laser fluence of 1.76 J cm^{-2}.

4.4.1 Comparison of ion and the atom fluence in ns-laser ablation plume

In order to obtain the ionization fraction in the ns-ablation plume, the ion and the total particle (ion+atoms) fluence was compared. We will call the total particle fluence the atom fluence throughout in the following section.

The ion fluence (ions cm^{-2}) was obtained by integrating the ion TOF signal for each metal and the atom fluence was calculated from the deposition rate measured using a QCM. In order to take into account the difference in the position of the probe, the QCM and the substrate in the vacuum chamber we have used the $1/d^2$ dependence of the ion and the atom fluence in the ablation plume, where d is the distance of the probe or QCM and all the results were obtained at the position of substrate.

Figure 4-11 explains further the experimental setup of the ns-PLD chamber. The target-to-probe distance is 5.8 cm, target-to-QCM distance is 6.5 cm and target-to-substrate distance is 8 cm.

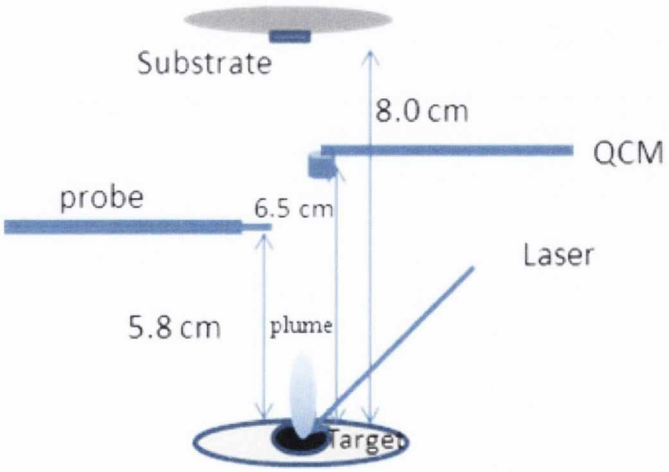

Figure 4-11 Schematic diagram of the experimental setup in ns-PLD chamber.

The ion fluence was obtained by integrating the probe signal in Figure 4-8 (a) and is 2.24×10^{13} ions cm^{-2}. Using $1/d^2$ scaling law, the fluence at the position of the substrate is 1.16×10^{13} ions cm^{-2}. The ion and the atom fluence for Au and Ni were obtained in a similar way, where the ion fluence was obtained by integrating the probe signal given in Figure 4-10 (a and c) and the atom fluence was obtained from QCM. Figure 4-12 shows the integrated ion and the atom fluence for Ag, Au and Ni at 1.76 J cm^{-2}. The deposition rates or the atom fluence and the ion fluence of Ag was found to be much higher (~8-10 times) as compared to Au and Ni which could be due to the difference in the latent heat of vaporization of three materials ΔH_{Vap} . The ablation threshold of materials is related to ΔH_{Vap} by[17]:

$$F_{th} = \rho\Delta H_{Vap}/\alpha(1-R) \qquad 4\text{-}12$$

where ρ is the mass density, α is the optical absorption coefficient, ΔH_{Vap} is the latent heat of vaporization and R reflectivity of the target material. The values for Ag, Au and Ni are 250.5, 335.0, 370.0 in units of kJ/mol[17] which shows lower ΔH_{Vap} and hence lower F_{th} for Ag as compared to the other metals.

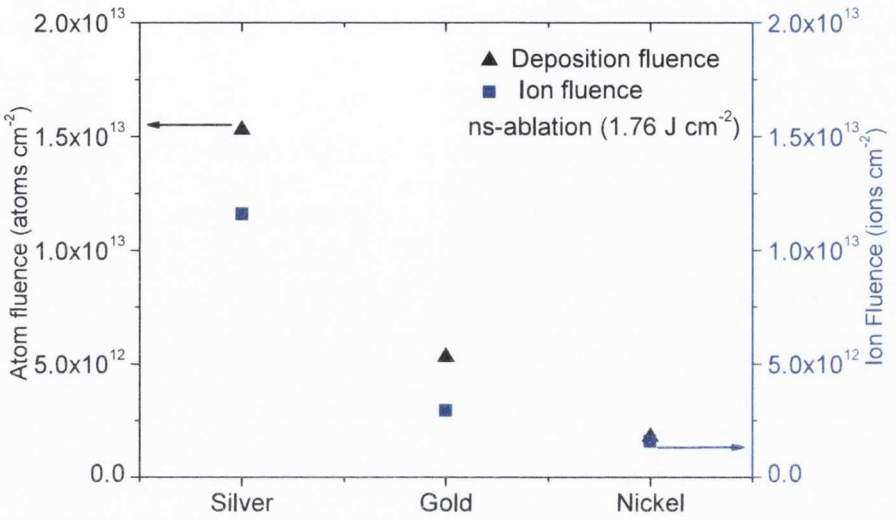

Figure 4-12 Integrated ion fluence and the atom fluence for Ag, Ni and Au at laser fluence of 1.76 J cm^{-2}.

Comparing ion and the atom fluence it can be seen that for all three metals the plume is nearly fully ionized, i.e. the atom fluence is just 1.3 and 1.5 times higher than the ion fluence for Ag and Au respectively. This can be understood in term of long pulse duration and ablation mechanism involved. In ns-ablation, the pulse duration is much higher than the electron-phonon relaxation time (5-20 ps for most metals). Hence after the absorption of laser energy by the target surface and thermal evaporation in the first few nanoseocnds, the laser-plume interaction starts. This leads to heating and ionization of vapor plume through inverse bremsstrahlung, bound-bound, bound-free excitations (see Section 2.2, Ch. 2). However it can also be seen that the atom fluence is nearly equal to the ion fluence for Ni (atom fluence is just 1.1 times higher than the ion fluence). A valid mechanism for this not available at this stage, however it can due to the less strong heating of the Ni plume.

4.4.2 Angular distribution of the ion fluence and net deposition

It is also of interest to study the angular distribution of the plasma plume and net (ion+atom) deposition flux for ns-ablation plume dynamics study. The angular distribution of ion fluence was obtained by rotating the probe around the ablation spot and recording the ion signal at small steps of angles. Figure 4-13 (a) shows ion TOF probe signal for few different angles with respect to the normal to the target surface, the current density is maximum and the peak TOF is minimum when the probe is at normal to the target surface [13].

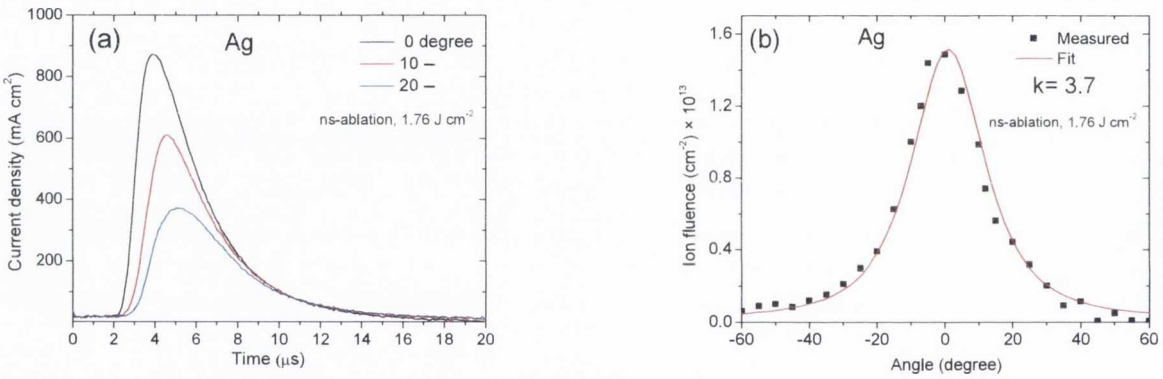

Figure 4-13 (a) Ion TOF signal at different angles w.r.t the normal to the target surface for Ag. (b) Angular variation of the ion fluence.

The angular variation of ion fluence was plotted by integrating the ion TOF signal at different angles. The integrated ion signals were fitted to the angular distribution $F(\theta)$ derived from the gas dynamical expansion model of ablation plume[18] using the following equation.

$$F(\theta) = F(0)\left(\frac{1+tan^2(\theta)}{1+k^2tan^2(\theta)}\right)^{3/2} \qquad 4\text{-}13$$

where k is the plume aspect ratio, a larger k value means a more forward directed plume. Figure 4-14 shows the angular variation of the net deposition for a Ag film deposited using ~ 7700 shots on a hemispherical transparent plastic sheet. The thickness distribution was obtained using the technique described in Ch3. Fitting the angular distribution of the net deposition to Eq. 4-13 yields k=2.8. Comparing the aspect ratio of ion fluence (k=3.7) to the net deposition it can be seen that the plasma part of the ns-ablation plume is narrower than the overall plume. A similar behavior was observed for Au and Ni. It can also be observed from Figure 4-14 that the film thickness has been reduced from the central part which might be due to the self-sputtering of the deposited film by energetic ions in the ablation plume.

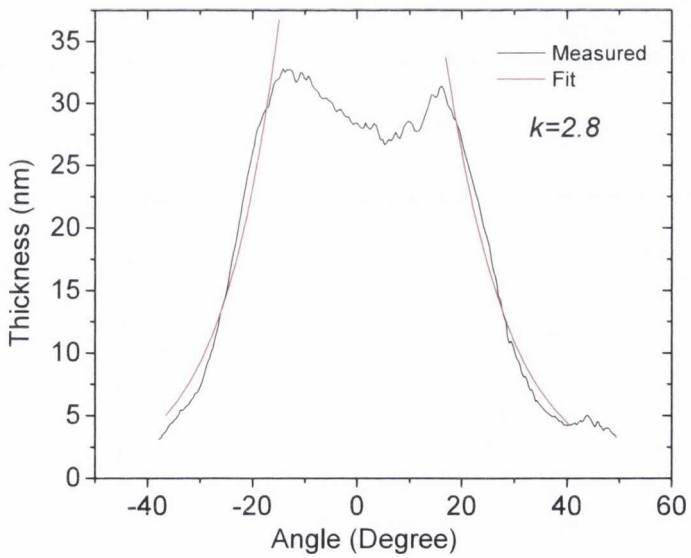

Figure 4-14 Angular variation of the net deposition of Ag on a circular surface of radius 5.8 cm centered on the ablation spot.

Figure 4-15 shows the angular variation of the ions and the total deposition for Au. Similar to Ag the k value in this case of plasma part (k=2.74) is larger than the net deposition (k=1.9). Similar results were obtained for Ni, with k=3.1 for ion fluence and 2.1 for the net deposition.

It can also be seen in the angular distribution of the deposited material for Au that the calculated thickness show unexpected shoulders around ± 30°). To identify the reason we investigated the Au deposited curved plastic substrate from which the angular distribution of deposited material was calculated.

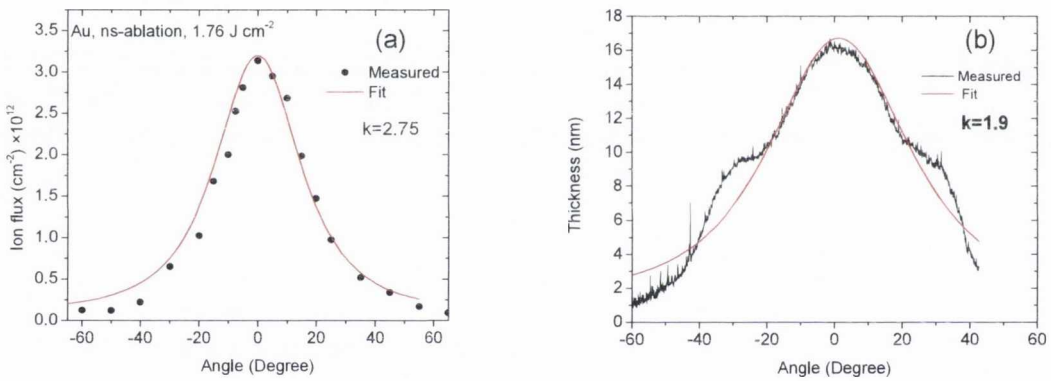

Figure 4-15 Angular distribution of (a) ion fluence and (b) net deposition for Au ns-ablation plume.

Figure 4-16(a) shows a photograph of an approximately 18 nm thick Au film deposited on a transparent plastic sheet. The photograph shows that the film is yellowish in the middle at position 1 which turns into blue close to the edges at very thin (< 10 nm) part of the film. Figure 4-16 (b, c) show the absorption spectra recorded at position 1 where the film thickness is approximately 18 nm and at position 2 where film thickness is < 10 nm. Figure 4-16 (b)

also shows theoretically calculated spectra of a 18 nm thick continuous Au film. The spectra was calculated using IMD/XOP software[19].

It can be seen that the recorded absorption spectra in the middle part of the film in the wavelength range of 350-550 nm is similar to a continuous Au thin film, however the optical absorption at longer wavelength, beyond 550 nm, do not match with the theoretically calculation. It is possible that the measured optical absorption spectra show a combined behavior of continuous and nanostructured film. The surface plasmon resonance (SPR) peak of Au nanoparticles films deposited on silica or quartz lies around 575 nm[20]. It has been observed experimentally that the SPR peak of noble metal nanoparticle films (Ag and Au) shift to the longer wavelength (red shift) as the nanoparticle size increases and the separation between them decreases[21,22] which is usually the case of ns-PLD films at higher equivalent thickness. It has been suggested that the red shift is due to increased dipole-dipole interaction between nanoparticles (see sec. 4.8). Hence it can be concluded that the thin film in Figure 4-16 (a) is not perfectly continuous or smooth in the middle but rather contain large granular Au nanostructures which cause excitation of SPR with peak position shifted towards longer wavelength. The absorption spectra at the edge (at position 2) is shown in Figure 4-16 (c), the spectra show a peak around 575 nm which is the surface plasmon resonance position for Au nanoparticles [20].

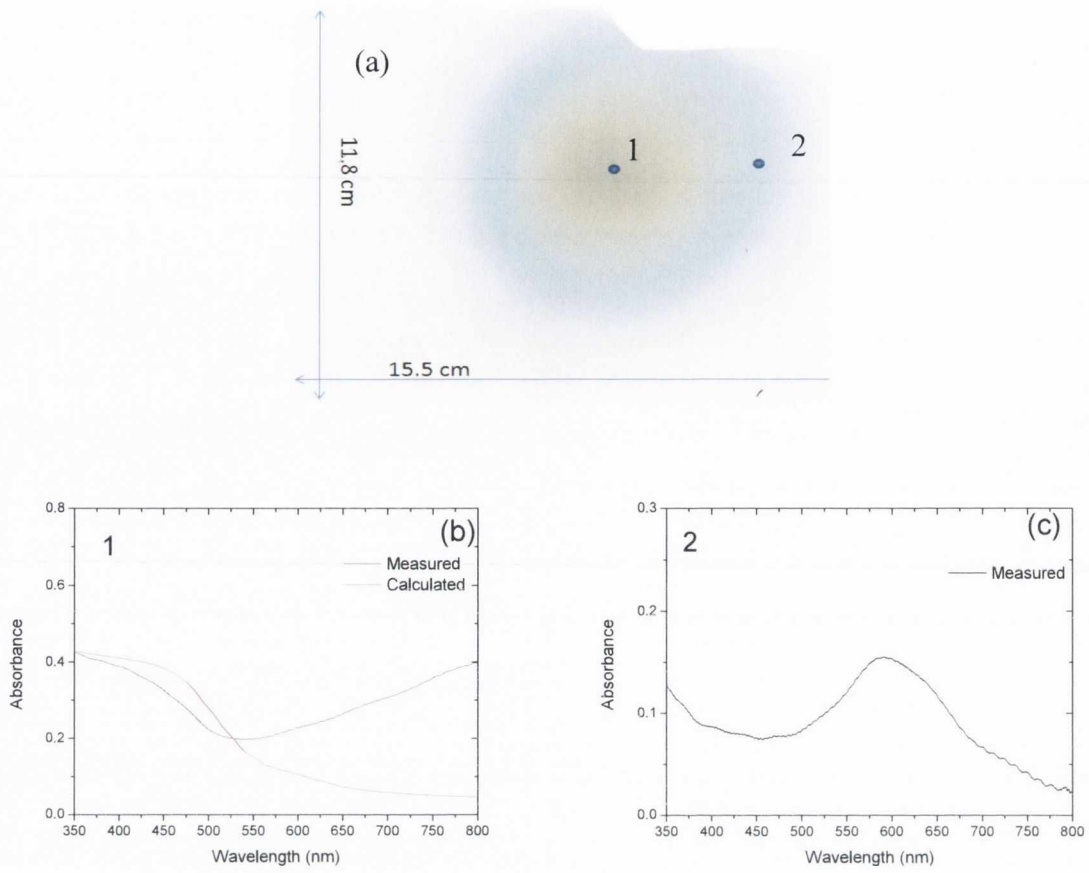

Figure 4-16 (a) Photograph of a 18 nm thick Au film deposited on a plastic sheet using ns-PLD. (b) Measured and calculated optical absorption spectra at the central part of the Au film at position 1. (c) Measured optical absorption spectra of Au film at the edge at position 2.

This shows that film is composed of Au nanoparticles at the edges. Recalling the technique in Ch 3, we calculated the film thickness from the optical transmission measurement, assuming that the film is continuous. However the above analysis shows that this method is not so reliable for nanoparticle films.

4.5 fs-laser ablation analysis

The ion and the atom fluence for fs-laser ablation were also obtained from Langmuir ion probe signals and QCM. The target-to-probe and the target-to-QCM distance was 5.2 cm in this 4.6 cm in this case. Using $1/d^2$ scaling law, all the fluence values were calculated at 6 cm

i.e, at the position of substrate. Figure 4-17 (a) shows the ion time-of-flight spectrum of Ag fs-ablation plume recorded on the ion probe at peak laser fluence of ~1.4 J cm^{-2}. A single peak TOF flight spectra similar to the ns-laser ablation was observed. The nature of the fast peak at about 1 μs is however less clear at this stage, but the peak has been observed in previous experiments and assigned to the low Z contamination on the target surface[23,24]. This will be discussed in more detail in the next section. Figure 4-17 (b) shows corresponding energy distribution, the average energy in this case is 60 eV. Thus it can be seen that fs-PLD also leads to the generation of energetic ions which may cause self-sputtering of deposited films[15].

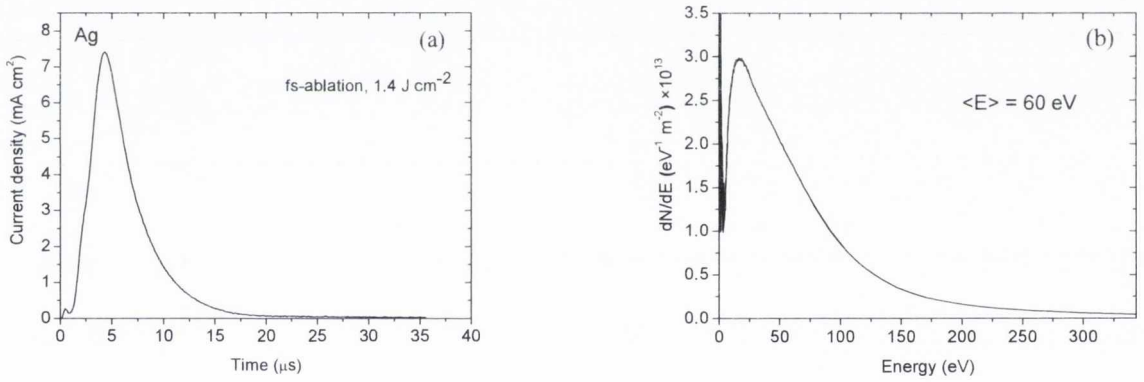

Figure 4-17 (a) Ion time-of-flight signal for Ag fs-laser ablation at F_p=1.4 J cm^{-2}, the target-to-probe distance is 4.6 cm. (b) Corresponding ion energy distribution plot.

The deposition rate was measured to be 2×10^{-3} nm per laser shot using QCM, which corresponds to 1.17×10^{13} atoms cm^{-2}. The ion dose obtained from the integrated ion signal is 1.7×10^{11} ions cm^{-2}, which is about 1.4 % the total deposition rate. Figure 4-18 (a) and (b) shows a probe signal for Au fs-laser ablation and the ion energy distribution respectively.

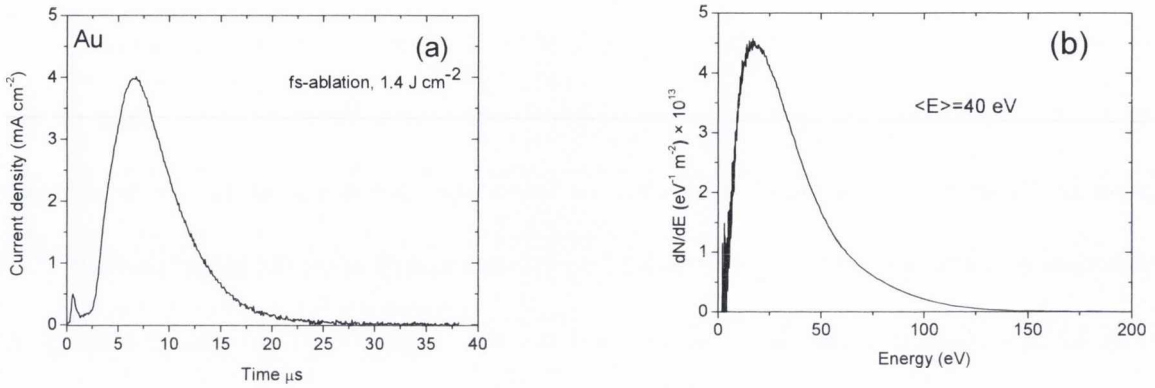

Figure 4-18 (a) Ion TOF signal for Au and (b) the corresponding energy distribution at peak fluence of 1.4 J cm^{-2}

The atom fluence (measured from QCM deposition rate data) for Au is 4.6×10^{12} ions cm^{-2} and corresponding ion fluence (measured from the integrated ion signal) is 1.0×10^{11} ions cm^{-2} which is about 2 % of the overall deposition. Similarly the values found for Ni are 3.1×10^{12} atoms cm^{-2} and 7.5×10^{10} ions cm^{-2} which is again approximately 2 % of the atom fluence. Finally, the ion and the atom fluence comparison for Ag, Ni, and Au is shown in the following figure. Both ion and the atom fluence is plotted in in $\log_{10}$ scale in the range of 1×10^{10}-3×10^{13} cm^{-2} to view a clear difference between them.

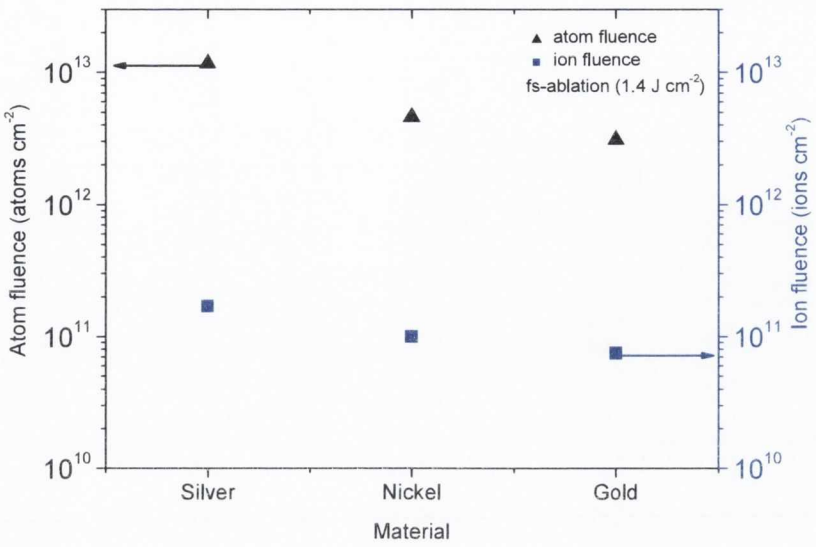

Figure 4-19 Ion and the atom fluence of Ag, Au and Ni fs-PLD measured at peak fluence of 1.4 J cm^{-2}.

The total ion and the atom yield for all three materials were also measured to obtain the ion fraction in fs-ablation plume. The ion yield per pulse was calculated from Anisimov model using following equation:

$$F(0) = \frac{2\pi d^2 F(0)}{k_{xz} k_{yz}} \qquad 4\text{-}14$$

Where d is the probe distance in cm, $F(0)$ is the ion fluence normal to the target surface. The value of k_{xz} and k_{yz} was obtained from the angular distribution of ions in the ablation plume.

To obtain the total number of atoms ablated per laser shot, a small crater was formed on the stationary target surface by fixed number of laser shots. By measuring the volume of the crater and dividing it with the number of laser shots, the mass or the total atoms ablated per

pulse can be calculated. Figure 4-20 shows the angular distribution of ions in the Ag fs-ablation plume. Fitting the angular distribution using Eq. 4-13 yields k_{xz}=3.0.

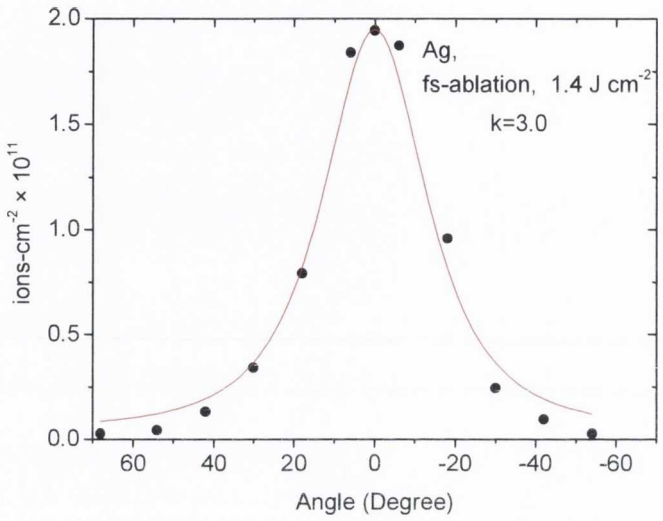

Figure 4-20 Ion Angular distribution of Ag fs-ablation plume at peak laser fluence of 1.4 J cm^{-2}. Red curve is the fit to the experimental data using Anisimov model (Eq. 4-13).

The focused laser beam spot was measured to be almost circular in this experiment with minor and major waists of 100 and 107 μm hence the value k_{yz} was taken to be similar to k_{xz}. Putting the values of *F(0), d* and the plume aspect ratios in Eq. 4-14 gives the ion yield obtained of 3.5 ×10^{12} ions per pulse.

Figure 4-21 (a) and (b) shows two- and three-dimensional maps of a crater formed by firing 50 laser shots on the stationary Ag target. Due to a technical fault in the laser the intensity profile of the beam was inhomogeneous; this can be seen in the crater profile (Figure 4-21 (c)). The maximum ablation depth is approximately 15 μm and the total volume removed is 3.42 ×10^{5} μm^{3} which corresponds to 4×10^{14} atoms per pulse. The total volume removed was

obtained using a nano- and microscale image processing software called SPIP™ (available at //www.imagemet.com/) provided with the white light interferometer. The software computes the volume by integrating the pixel data of the crater image, where each pixel contains information about depth or height of the area under observation. Comparing total ablation yield with the ion yield confirms that the ion yield is just 1% of the total ablated material. The total ion and the atom yield results for Ni and Au are given in Table 4-1.

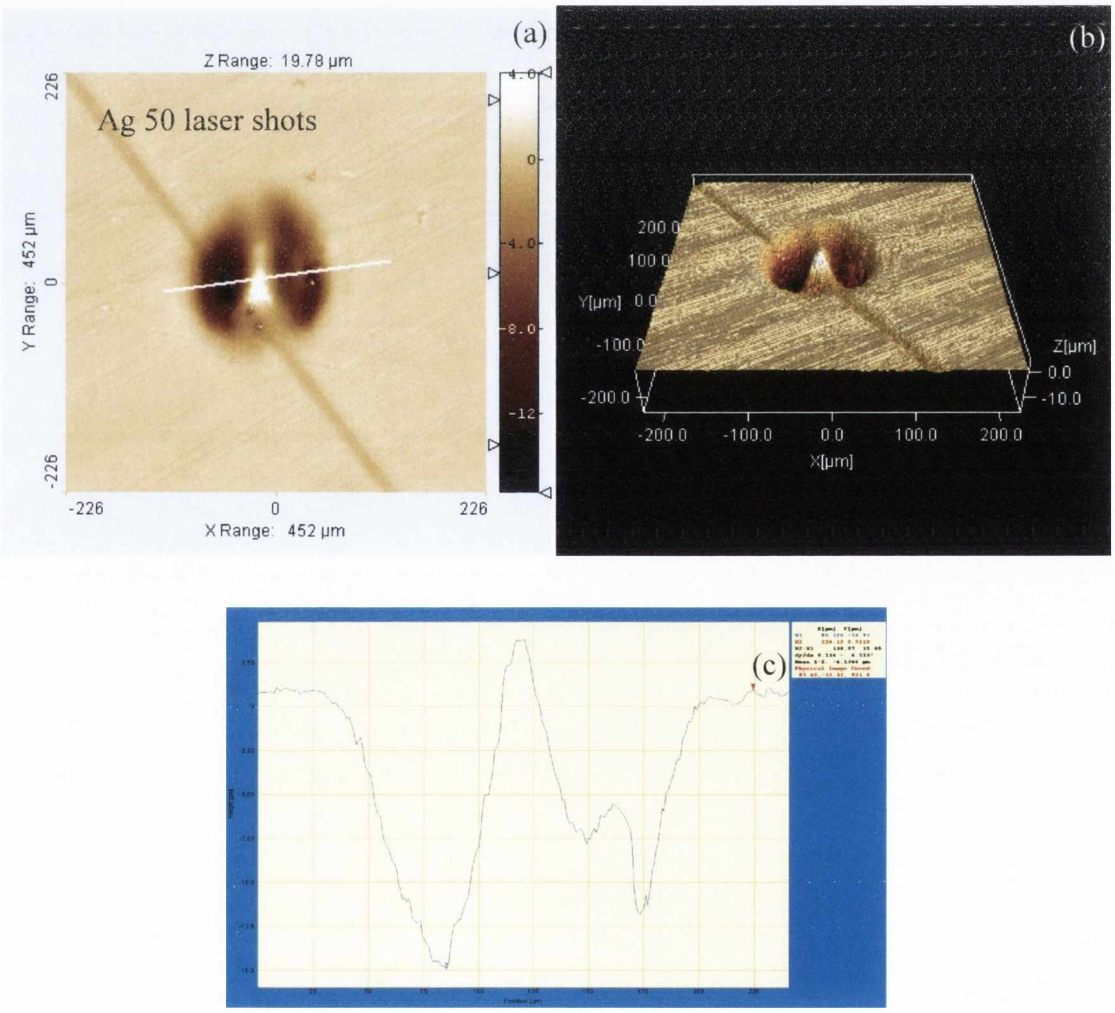

Figure 4-21 (a) Two dimensional and (b) three dimensional profile of the crater made by 50 laser shots on stationary Ag target at peak laser fluence of 1.4 J cm^2. (c) 2D-plot of crater profile along line drawn in part (a).

Table 4-1 Ion and Atom yield for Au and Ni found from crater depth measurements

	Ion yield	Atom yield	Ion fraction
Au	2.65×10^{12}	2.30×10^{14}	1.2 %
Ni	3.30×10^{12}	1.20×10^{14}	2.7%

The comparison of ion and the atoms fluence and total yield clearly shows that for all metals, the fs-ablation plume contains a small fraction (1-2 %) of ionized material, and most of the material is ablated in the form of either neutrals or the nanoparticles of the target material similar to findings of other authors[24,25]. The results of our experiments about time and space resolved OES and fast photography of fs-ablation plume also show a strong nanoparticle plume emission from Au and Ni targets. The results will be discussed in more detail in the next chapter.

It is of also interest to confirm the charge state of emitted species in the fs-ablation plume. For that purpose we used an energy selective TOF mass spectrometer (ES-TOFMS). The following section provides the results of TOF mass spectrometry of the fs-ablation plume.

4.6 TOF mass spectrometry of fs-ablation plume

The ES-TOFMS allows us to measure the kinetic energy distribution as well as the mass spectrum of ions in the LPP through the measurement of their time-of-flight[26,27]. An introduction and the setup of ES-TOFMS has been given in Ch 3. The device essentially consists of two curved metal plates separated by a few mm. By applying a certain potential

difference ΔV between the plates, a suitable pass energy of the ions can be set. The pass energy of the spectrometer is related to the applied potential difference by:

$$E(eV) = \frac{Z\Delta V R_0}{2d} \qquad 4\text{-}15$$

where Z is the charge state of the ion, ΔV is the potential difference applied between the metal plates, R_0 (3.5 cm) is the centerline radius and d (3.25 mm) is the distance between the plates. The voltage on the plates could be varied from (0-60 V) which gives an energy range of 0-320 eV assuming singly charged species (Z=1) in the plasma plume. This covers most of the measured ion energy distribution range in the fs-ablation plume (see Figure 4-17 (b)). The spectrometer was placed at 23.5 cm along the target normal. The mass-to-charge ratio of the ions can be determined as:

$$\frac{E}{z} = \frac{e\Delta V R_0}{2d} \qquad 4\text{-}16$$

hence

$$\frac{m}{z} = \frac{e\Delta V R_0}{2dv_i^2} \qquad 4\text{-}17$$

where v_i is the ion velocity which can be calculated from the TOF spectrum. We first investigated the Ag ablation plume to test the functionality of the device. Figure 4-22 (a) shows the TOF mass spectrum of ions during Ag fs-ablation at a peak laser fluence of 1.4 J cm^{-2}. The spectrum show the presence of both singly and doubly ionized Ag atoms (Ag^+ and Ag^{++}). The pass energy is 97 eV for Ag^+ and 194 eV for Ag^{++}.

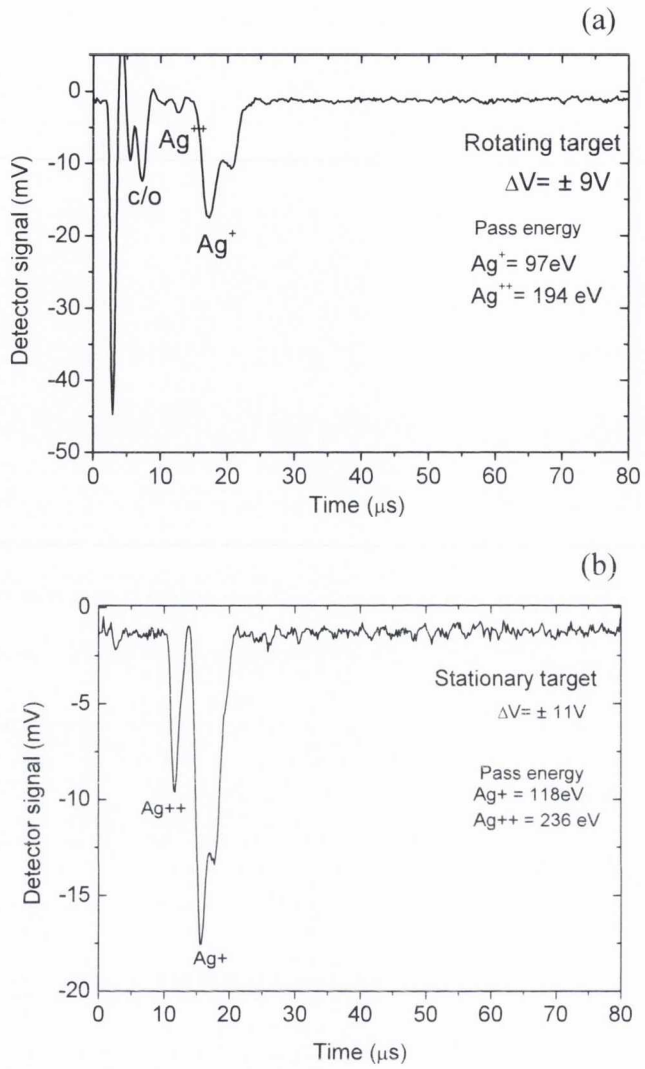

Figure 4-22 (a) Ion TOF mass spectrum of rotating Ag target at F_p=1.4 J cm^{-2}. The spectrometer was placed at 23.5 cm away from the target surface; the potential difference between the plates is ±9V. (b) The output of the spectrometer for stationary Ag target at potential difference of ±11V in this case, the pass energy for single and doubly ionized Ag atoms are given in the plots

The spectrum also shows some fast peaks before 10 μs along with the singly and doubly ionized Ag peaks. Calculating the charge to mass ratio for these signals, we identified that the peaks are due to O and C impurity atoms. However the nature of very fast peak at about 2.6 μs is not clear. These impurity peaks have also been identified in other laser ablation experiments and it has been suggested that ablating the target surface with few laser shots

can remove the contamination locally[27]. This can be seen in our case as well when the target is stationary (Figure 4-22 (b)). The laser was running at 10 Hz and spectrum was recorded as an average of 32 laser shots. However it was observed during experiments that the peak reappears when the laser was blocked for few seconds and was unblocked again, which shows that the origin of the peaks could also be due to the poor quality of vacuum.

One of the limitations of the device is the space-charge effect at low transmission energies. The space-charge effect deflects the peak position and cause a corresponding error in measurement of peak TOF, which could be the case of distortion of Ag^+ ion peak in the measured TOF mass spectrum. The magnitude of space charge field can be given by:

$$E_{space} = \frac{wn_i e}{2\varepsilon_0} \qquad 4\text{-}18$$

Where w is the entrance slit width, e is the electronic charge, n_i is the ion density and ε_0 is the permittivity of free space. From the probe signal in Figure 4-23 the maximum ion density ($n_i = J/ev$) is $\approx 10^{10}$ cm^{-3}, a slit width of 500 μm gives E_{space}= 50 $\times 10^3$ V/m. The applied bias voltage of ±11 V (E_{pass} = 118 eV) correspond to the field of 7.5 × 10^3 V/m, which shows that the space charge can have a significant effect on the measured spectra.

The optimum voltage at which the spectrometer should be operated to reduce the space charge effects would then be ± 90 V (≈ 60×10^3 V/m) which corresponds to E_{pass} ≈ 950 eV. The pass energy seems to be very high under the experimental conditions used for this experiment. Infact this energy is very high for the usual PLD experiments. Our experimental investigations has shown that for metal ablation in the fluence range of 1-2 J cm^{-2}, the ion

energy distribution extends just upto few hundred of eV (~100-200 eV). Hence detecting ions with such a high energy would not be trivial.

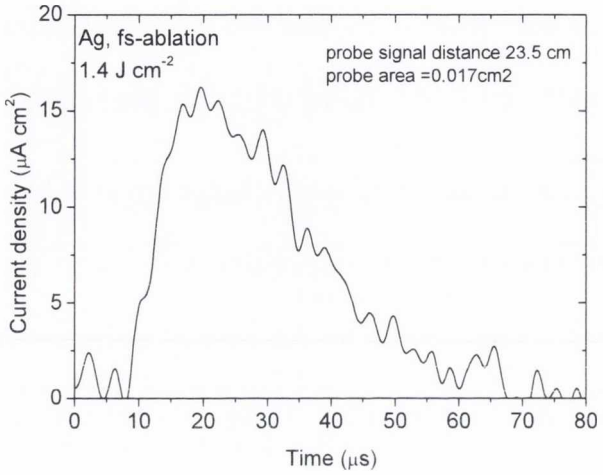

Figure 4-23 Ion TOF signal at 23.5 cm away from the target surface.

The other possibility is to reduce the spectrometer slit width. Currently a 500 μm slit width was used. Looking at Eq. 4-18 it can be seen that by reducing the slit width by a factor of for example 10 (i.e. 50 μm slit) the space charge field can also be reduced by the same factor. Hence for a 50 μm slit width the space charge field would be 5×10^3 V/m which is smaller than the applied field for E_{pass}=118 eV i.e. 7.5×10^3 V/m.

One of the aims of the experiment was to identify the charge state of the nanoparticles in the fs-laser ablation plume. In some of our earlier experiments we investigated the fs-ablation plume of Ag using Langmuir ion probe. Figure 4-24 shows the signal for positively biased probe. The first peak at 13 μ-sec is the electron signal, the signal also shows a second peak at about 25 μ-sec which was thought to be due to the arrival of charged nanoparticles at the probe, but the velocity of the species seems to be very high.

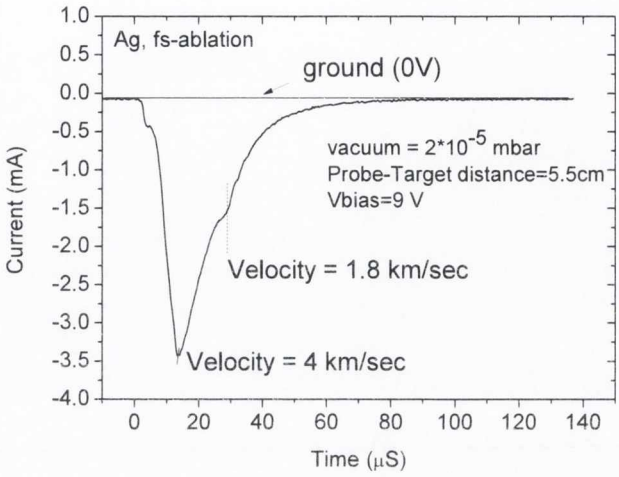

Figure 4-24 Electron signal for positively biased (+9V) Langmuir ion probe

It has been observed via fast imaging that in fs-ablation the nanoparticle plume leaves the target with velocity approximately 10 times smaller than the ions or atoms (~100-200 m s^{-1})[25] and the time of arrival should be of the order of milliseconds.

Investigating the plume using ES-TOFMS the following assumptions were made.

Considering a 5 nm diameter particle leaving the target surface with the velocity of about 200 m s^{-1}, the particle would have K.E of 16.5 eV. Assuming Z=1 (single charged particle) and adjusting $\Delta V \pm 3$ eV , the pass energy of 16.5 eV of the spectrometer can be obtained. Adjusting these parameters a few signals were recorded for Ag ablation at ~ 1.4 J cm^{-2}; however no sign of charged nanoparticle arrival was observed. In order to see if the nanoparticle plume can be charged, a target biasing technique for future experiments was

considered. The detail of experimental setup and the biasing circuit for that technique are given in Ch 8 and in Appendix C.

4.7 Morphology of nanoparticle films prepared using ns- and fs-PLD

To study the morphology of nanoparticle films prepared using ns- and fs-PLD, thin films with equivalent solid-density thickness of 1, 3, 5 and 7 nm were prepared on carbon coated TEM grids and fused quartz substrate. The morphology of the film prepared on TEM grids was examined using scanning transmission electron microscopy. Films prepared on quartz substrates were used for thickness measurements and in some cases to record their optical absorption spectra using a UV/Vis spectrophotometer. The microscopy results of ns- and fs-PLD films are given in the following section.

4.7.1 Ag nanoparticle films prepared using ns-PLD

Prior to the fabrication of Ag thin films, the deposition rate per laser shot was obtained using x-ray reflection (XRR) technique since the QCM was not available in the vacuum chamber at this stage. For that, a Ag film was deposited on quartz substrate with known number of laser shots and thickness and the average density of the film was measured using XRR. Figure 4-25 show an XRR curve for a film prepared using ≈ 73,000 laser shots on fused quartz substrate. The measured reflectivity curve was fitted using commercial software called LEPTOS[28]. The film thickness and density obtained by fitting the XRR curve are 13.8 nm and 10 g cm^{-3}, which gives an equivalent thickness of 13 nm. Dividing the equivalent thickness with the number of laser shots fired gives 1.78×10^{-4} nm per laser shots.

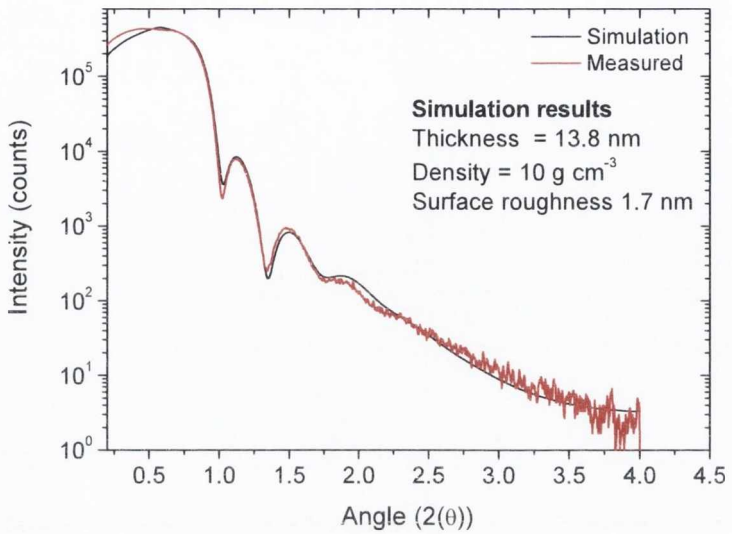

Figure 4-25 XRR curve for Ag films prepared using 73,000 shots at laser fluence of ~ 0.8 J cm^{-2}

This deposition rate was used to prepare the Ag films with varying thickness for microscopy analysis. It should be noted that a 2.8 nm Ag_2S (silver sulphide) layer with an average density of 6 g cm^{-3} was added on the top of Ag film during the fitting procedure to obtain the best fit to the measured XRR curve, since Ag thin films are reactive and show sulfidation when exposed to air[29]. For the confirmation of deposition rate, the film with the equivalent thickness of 7nm deposited on quartz substrate was also analysed using XRR. For ≈ 37,600 pulses the film thickness was 10.2 nm and the density was 6.8 g cm^{-3} which is 65 % of solid density (10.5 g cm^{-3}) and hence indicate the porous nature of the deposited film[30] . Taking into account the average density; the film thus has an equivalent solid density thickness of ~ 6.7 nm which agrees well with the deposited thickness.

Figure 4-26 (a-d) shows scanning transmission electron micrographs (STEM) of Ag nanoparticle films with equivalent thickness of 1, 3, 5 and 7 nm prepared using ns-PLD on

Carbon (C) coated TEM grids. The Feret diameter distribution of 1, 3 and 5 nm thick films are shown in

Figure 4-26 (e-g). These distributions were fitted with a log-normal distribution function to find mean value (μ) and the standard deviation (σ).

$$f(x) = \frac{1}{x\sigma\sqrt{2\pi}} e^{-\frac{(ln(x)-\mu)^2}{2\sigma^2}} \qquad 4\text{-}19$$

A description of Feret diameter and lognormal distribution is given in appendix D. From STEM it can be seen that the films with equivalent thickness of 1 and 3 nm show well separated, round shaped nanoparticle. However as the equivalent thickness is increased to 5 nm, the nanoparticle begin to coalesce and make elongated structures. These elongated structures grow even more and connect with each other to form percolated nanostructures when the film thickness increases to 7 nm. This shows that the metal film prepared using ns-PLD show similar growth behavior to that obtained using thermal evaporation and sputtering where the nanoparticles grow by surface diffusion of adatoms[31,32]. The coalescence and percolation of thin metal films can be understood more in terms of growth of metals on the insulating substrates.

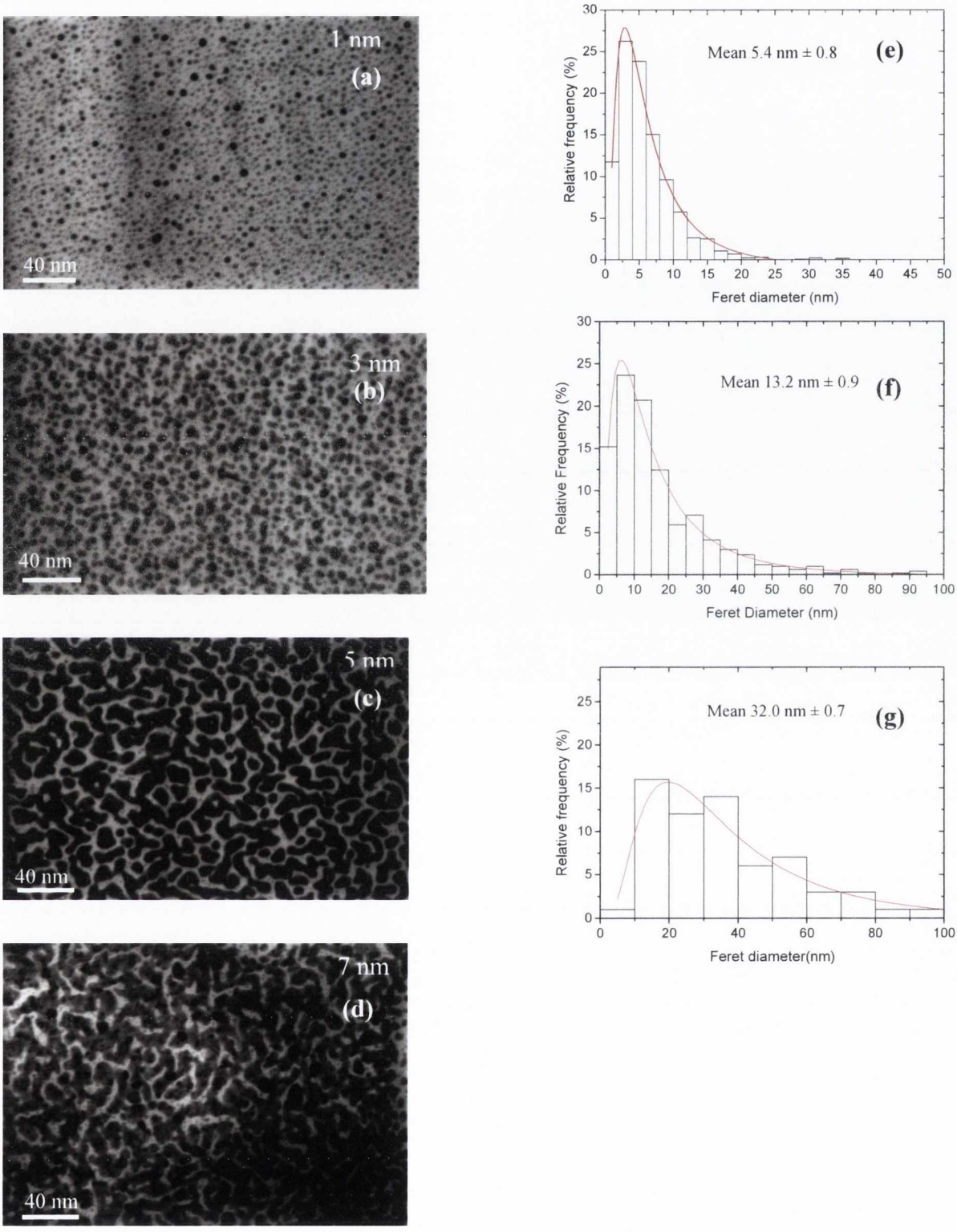

Figure 4-26 STEM (a-d) and corresponding size distribution histogram (e-g) of 1, 3, 5 nm thick Ag films prepared using ns-PLD in vacuum. The red curve is represents log-normal distribution. The error in the given Feret diameter corresponds to the standard deviation in the measured data.

Since most metals do not wet to insulating substrates such as Si and glass[33], thin films grown on such substrates proceed through several morphological changes. In the initial stage, the film consists of compact and isolated islands, as more material is deposited the islands grow and coalesce into larger groups and become elongated. At a particular film thickness or surface coverage, which is known as the critical surface coverage these elongated structures connect to form a percolating structure. The critical surface coverage however varies for different metals[32]. The most favorable growth mode which has been suggested for metals on insulating substrate is the Volmer-Weber growth mode where the atoms (or molecules) are more strongly bounded to each other than to the substrate[34]. In the above example we have shown the results of Ag deposited on C-coated TEM grids. In order to make sure that the growth of nanoparticles follows similar behavior on insulating substrate like glass, thin Ag films with equivalent thickness of 7 nm were deposited on C and SiO_2 coated TEM grids.

Figure 4-27 shows STEM of Ag thin films prepared on both kind of TEM grids or substrates. It can be seen that films prepared on SiO_2 substrates show coalescence behavior similar to the carbon coated substrates; however the film prepared on C grid show more connected nono-islands or a percolated structure while the film prepared on SiO_2 grids show elongated but separated nano-island. The evolution sequence of separate nanoparticles to elongated nanoisland can be understood by a theoretical model called the interrupted coalescence (ICM) model[31,35].

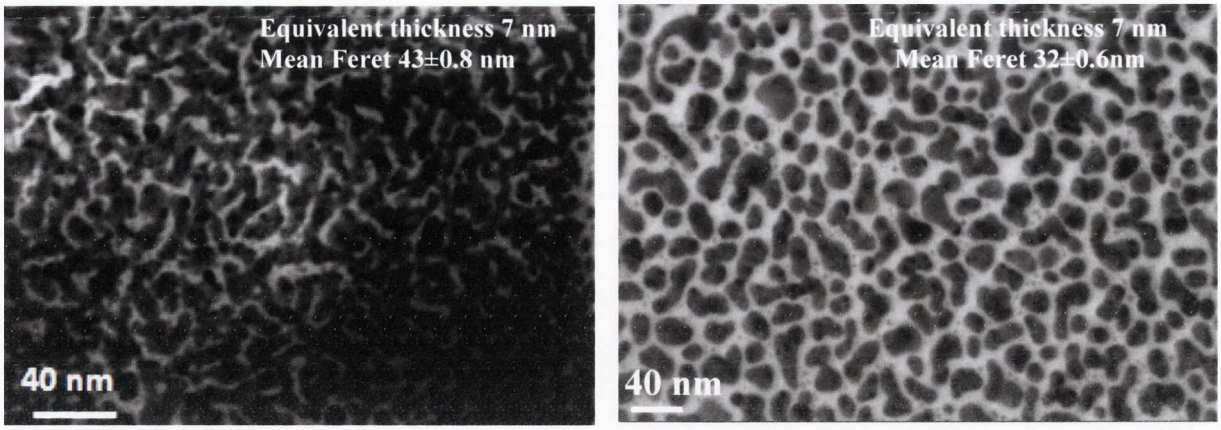

Figure 4-27 STEM of Ag nanoparticle films with equivalent thickness of (a) 7 nm film prepared on C-coated TEM grid and (b) 7 nm prepared on SiO_2 coated TEM grid.

According to this model at the early stages metal particles may grow on the surface through homogeneous nucleation (i.e., island formation due to nucleation on defect-free terraces) and heterogeneous nucleation (island formation at steps and other defects)[31,36]. In order for islands to form on the substrate, atoms deposited from the vapour phase undergo a series of kinetic processes, including thermal accommodation onto the substrate, surface diffusion of the adatoms to initiate nucleation, island formation and thin film growth[36]. As more and more atoms are deposited, small islands may grow, contact each other, and then fully coalesce (i.e., two islands merge into larger) but are still compact islands.

This description was first described by M. Volmer in 1939[37] for metal thin films on nonweting substrates. In terms of the ICM model, at a later stage of growth, when the island radius reaches a critical size R_c, full coalescence does not occur, instead, islands coalesce partially to form elongated structures with wormlike features. With continued deposition these elongated nanoislands undergo further partial coalescence and form continuous but irregular nanoislads. This connectivity of elongated nanoislands also causes a rapid increase in the electric conductivity of the metal nanostructured film.

The transition from full coalescence (compact islands) to wormlike structures is defined by a critical nanoisland radius R_c[35] and is given by:

$$R_c^4 \approx \frac{D_s t_c \gamma_f \Omega^{4/3}}{k_B T} \qquad 4\text{-}20$$

Where R_c is the critical radius for percolation, D_s is the surface diffusion coefficient of metal on substrate, t_c is the critical time at which the radius is formed, γ_f is the metal surface free energy Ω is the atom density of metal, k_B is the Boltzmann constant and T is the absolute temperature. It can be seen that the critical radius for percolation depends on several factors including the surface diffusion coefficient of adatoms and the temperature.

Now according to equation Eq. 4-20, it can also be observed that the higher diffusion coefficient leads to a higher value of critical radius for SiO_2, since the deposition was performed under the same experimental conditions at room temperature. On the bases of available data[38,39] the surface diffusion coefficient of metals on SiO_2 and carbon based substrates are of the order of 10^{-6}-10^{-7} cm^2 s^{-1}, which are close to each other and does not give a clear description of continuous nanoislands on C substrates. It should also be noted that these values are not specifically for PLD. Secondly, it could also be the case that the amorphous carbon coated TEM grids contain a larger amount of defects than SiO_2 coated grids, and hence provide higher density of nucleation sites for the growth of nanoislands and may contribute to lower value of critical radius for partial coalescence and percolation.

4.7.2 Ag nanoparticle films prepared using fs-PLD

Similar to the ns-PLD experiment thin films with equivalent thickness of 1, 3, 5 and 7 nm were prepared on TEM grids and quartz substrates by fs-PLD. The deposition rate as

measured using QCM was 4.2×10^{-4} nm per laser shot for this experiment. The deposition rate was also confirmed using XRR. Figure 4-28 is the XRR curve for a nanoparticle film which was deposited after 27.5 minutes with the laser running at 10 Hz. The film had an equivalent solid-density-thickness of 7 nm as measured by the a QCM. The XRR curve was fitted to obtain the following parameters for the nanoparticle film: thickness = 10.0 nm, density = 7.8 g cm^{-2} and root mean squared (rms) surface roughness = 2.3 nm. Hence the XRR measurement yields a value of 7.8 nm for the equivalent solid-density thickness, which compares quite well with the value from the QCM.

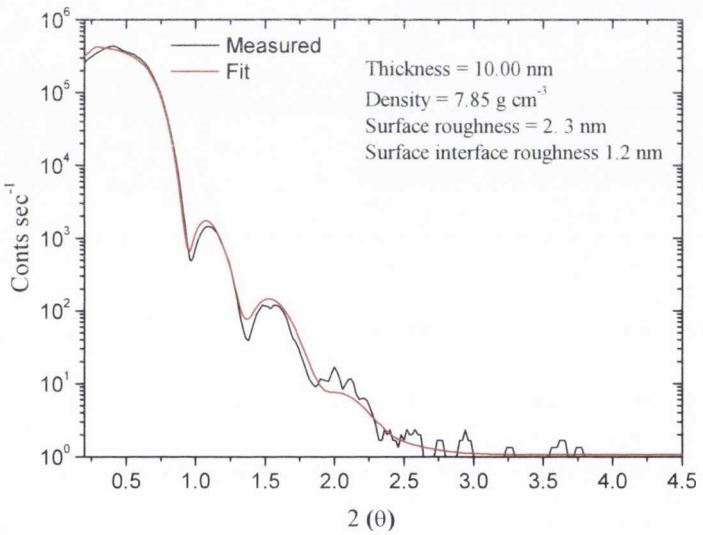

Figure 4-28 XRR curve for Ag film deposited on quartz substrate for approximately 27.5 minutes at 10 Hz laser repetition rate.

Figure 4-29 (a-d) shows STEM of Ag nanoparticle films prepared using fs-PLD at a laser fluence of ~ 0.82 J cm^{-2}. The micrographs show that the nanoparticles are well separated and can be analysed to obtain the Feret diameter distributions which are shown in Figure 4-29 (e – h).

We observed in that case that the nanoparticle size increases with the equivalent thickness.

Figure 4-30 (a) shows that mean Feret diameter increases from about 3 – 11 nm as equivalent thickness increased from 1 – 7 nm. This can also be seen from

Figure 4-30 (b) which shows that both, the areal density of nanoparticles and the surface coverage depend on the film thickness.

This behavior is different to that seen in fs-PLD of Ni[40] where the nanoparticles accumulate as a loosely packed film without coalescing. The reason for the different behavior for Ag and Ni is not clear at this stage. We also observe a small number of mesoscale particles having diameters greater than ~15 nm which were not included in the size distribution histogram. The mesoscale particles have been observed before in fs-PLD of nickel nanoparticle films[12], and it was found that the density of mesoscale particles increases with increasing the laser fluence.

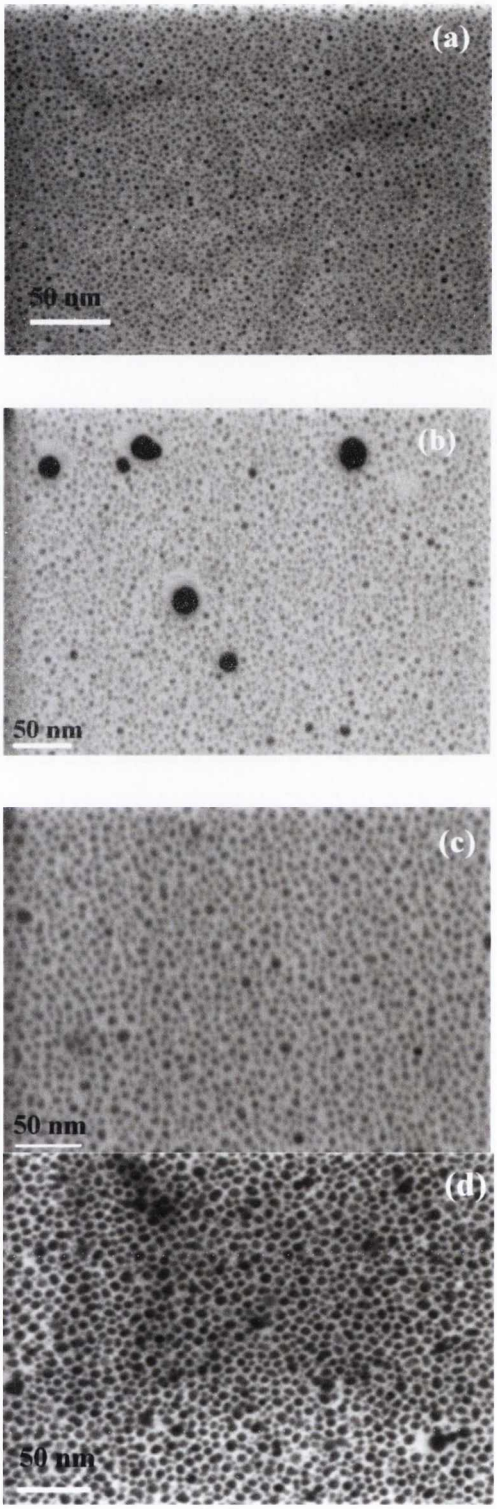

Figure 4-29 STEM (a-d) and corresponding size distribution histogram (g-h) of 1, 3, 5 and 7 nm thick Ag films prepared using fs-PLD in vacuum. The description of Feret diameter and lognormal distribution is given in appendix D.

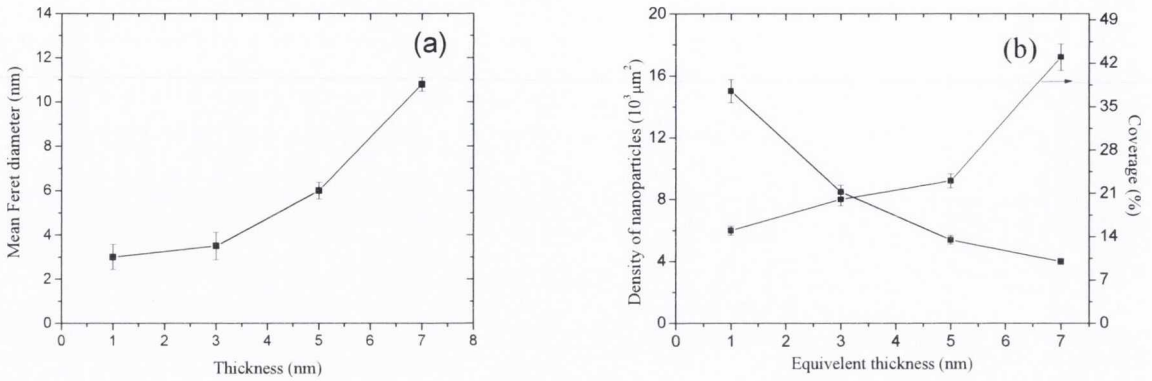

Figure 4-30.(a) Plot of mean Feret diameter of the Ag nanoparticles as a function equivalent film thickness, the error bars corresponds to the standard deviation in the measured data (b) Density and the surface coverage of nanoparticles as a function of equivalent thickness of Ag thin films.

4.7.3 Morphology of Au and Ni films

The morphology of Au and Ni films prepared using ns and fs-PLD on C-coated TEM grids was also studied. Figure 4-31 (a,b) shows STEM of Au nanoparticle films with equivalent thickness of 3 and 5 nm. Looking at the shape of nanoparticles it can be seen that the films show the usual thin film growth behavior. Initially the film is comprised of small and isolated nano-islands which, in the later stage, coalesce due to the surface diffusion of deposited atoms and form elongated and connected nanostructure. The mean Feret diameter is 4.8 nm for films with equivalent thickness of 3 nm which increases to 9.5 nm for 5 nm thick film. The STEM of Ni films with equivalent thickness of 3 and 5 nm is shown in Figure 4-31 (c,d).

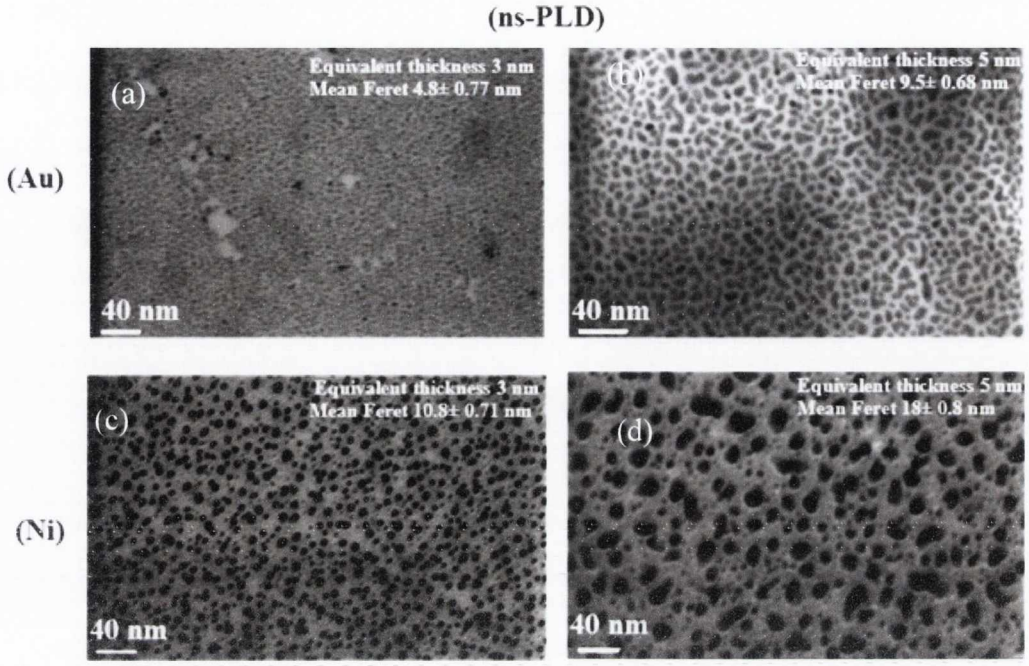

Figure 4-31 STEM of nanoparticle films prepared using ns-PLD of (a, b) Au and (c,d) Ni . The equivalent thickness of the films and mean Feret diameter is given in each micrograph.

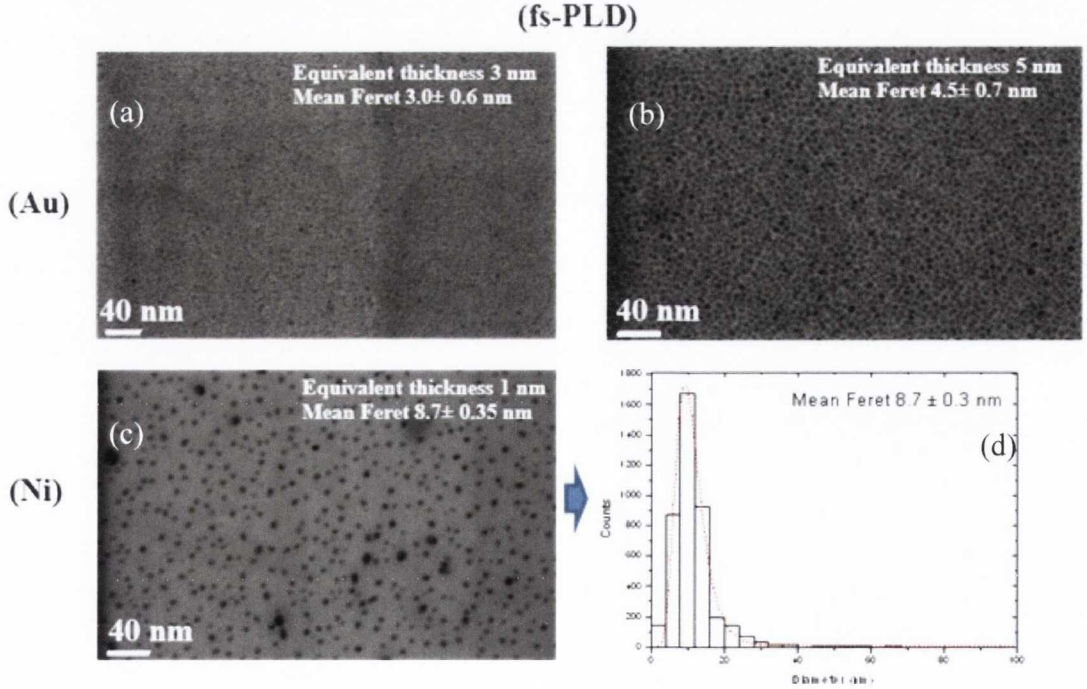

Figure 4-32 STEM of nanoparticle films prepared using ns-PLD of (a, b) Au and (c) Ni. (d) The Feret diameter distribution histogram of Ni thin film. The equivalent thickness of the films and mean Feret diameter is given in each micrograph.

The films are nanostrucred with mean Feret of 10.8 and 18 nm for equivalent thickness of 3 and 5 nm. However the percolation threshold for Ni is seem to be higher for Ni as compared to Au. It is of also interest to study the morphology of Au and Ni nanoparticle films prepared using fs-PLD. Figure 4-32(a, b) show STEM of Au nanoparticle films with equivalent thickness of 1 and 3 nm. The corresponding mean Feret diameters are 3 and 4.5 nm respectively. We have observed in our experiments via fast photography and optical emission spectroscopy that Au show strong nanoparticle emission during ultrafast laser ablation. A similar behavior for Au was observed by other authors via optical emission spectroscopy experiments[25]. Hence one can expect accumulation of nanoparticles on the substrate surface in case of Au. Looking at the micrographs of nanoparticles for different equivalent thickness it seems like that the nanoparticle are growing as a consequence of nucleation and coalescence of deposited atoms. It can also be possible that both the accumulation of emitted nanoparticles and growth via deposited atomic material are present at the same time. However the exact mechanism of Au nanoparticle growth needs further microscopy analysis. Figure 4-32(c, d) shows STEM of Ni nanoparticle film with equivalent thickness of 1 nm prepared using fs-PLD, the film show well separated nanoparticle with mean diameter of 8.7 nm, but it was difficult to obtain well resolved STEM for thick films. A further analysis of nanoparticle emission from Ag, Au and Ni targets is given in Ch. 5.

4.8 Optical properties of Ag nanoparticle films

Since we are dealing with noble metal nanoparticles, it is also of interest to study the optical absorption properties of such nano-materials. The main feature in the optical absorption spectra of noble metal nanoparticles is an absorption band in the visible region of electromagnetic spectrum due to the surface plasmon resonance (SPR). SPR is a collective

oscillation of conduction band electrons confined to the metal nanoparticle in response to the incident electromagnetic field. We have mainly studied the optical absorption properties of Ag here and compared the experimental results with the existing theoretical models.

Figure 4-33 shows the absorbance spectra of Ag nanoparticle films prepared using ns- and fs-PLD on fused quartz substrates with different equivalent thickness. The SPR peak around 500 nm can clearly be seen in both ns- and fs-PLD films and the magnitude of the peak absorption is increasing with the film thickness. It can also be observed that some of the spectra show small peaks around 350 nm which may be due to the presence of oblong nanostructures which show different resonance frequencies due to the electric field vector being oriented along the long and short axis of the particles[41].

The absorbance spectra show several other interesting features such as the SPR peak shifting to the longer wavelength in both cases as the film thickness increases. A similar behavior has been observed in case of Ag nanoparticles of various sizes deposited and embedded in SiO_2 substrates[42,43]. The exact nature of the red shift in the SPR peak with increasing film thickness is not completely understood. However the effect has been attributed to the dipole-dipole interaction between the particles. We can see from STEM of ns- and fs- PLD films that the average particle size increases and the separation between particles decrease with increasing equivalent thickness.

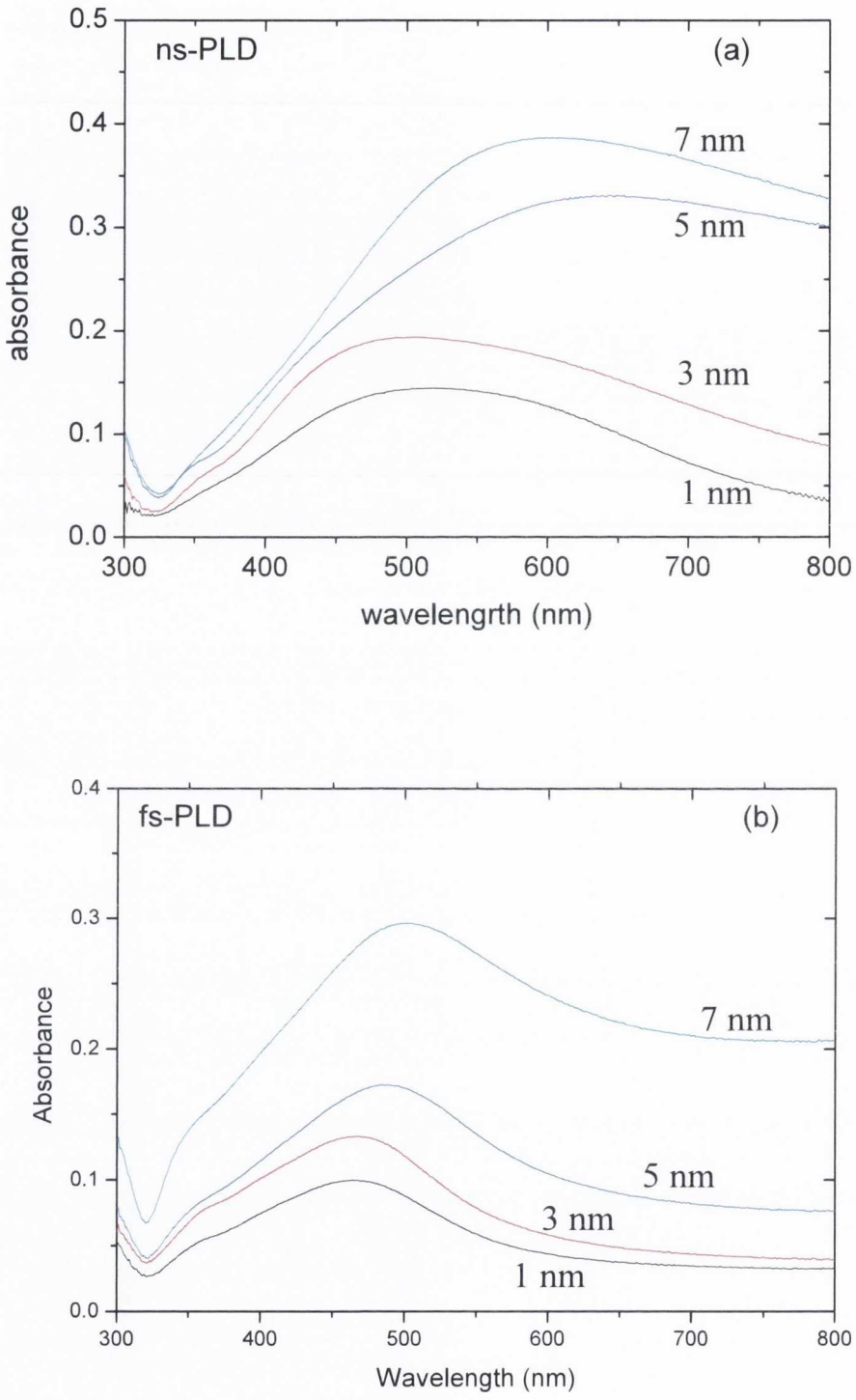

Figure 4-33 UV/Vis optical absorption spectra of Ag nanoparticle films with equivalent thickness of 1-7 nm for (a) ns-PLD (b) fs-PLD.

The exact nature of the red shift and the broadening of the SPR peak with increasing film thickness is not completely understood at this stage. However these effects have been attributed to several physical parameters such as size dependence of the dielectric function in Drude theory. According to that, when the particle size becomes smaller than the electrons mean free path (~ 60 nm for Ag) the damping of electron from the surface of metal nanoparticles becomes important [44] and an additional, size dependent term need to be added in the damping constant (see Eq. (2.50)). Hence, the enhanced damping for small nanoparticles leads to a broader SPR. For our PLD films, the width of the SPR broadens as the average particle size increases. Thus it seems that size dependence of the dielectric function is not the cause of that behavior of SPR. Another possible cause of broadening might be the size distribution. As we can see that the size distribution of nanoparticles gets broader as the equivalent thickness increases. It has been observed experimentally that the SPR depends on size as well as the shape of the particles[44], hence if the measured sample has a broad nanoparticle size distribution, the SPR represent a convolution effect for different size nanoparticles[45] which probably is the case for the PLD films.

From a general solution of Maxwell's equation for aggregates of metal spheres[46], the dipole-dipole interaction between the particle is proportional to $(R/d)^{2L+1}$ where R is radius of the particle , d is the separation between the particles and L is the multipole order (L=1 for dipole, L=2 for quadrupole, etc.). Clearly with increasing particle size and decreasing separation between the particles (which is the case of PLD films) the dipole-dipole interaction increases, which may cause a red-shift in the SPR wavelength[42].

The exact theoretical calculation of the absorbance of metal nanoparticles films is a complicated procedure and needs a few assumptions. However it will be useful to see up to

what extent the measured absorption spectra can be explained by existing simple theoretical models. We simulated the absorption spectra of Ag nanoparticle films using Mie theory, Maxwell-Garnett (MG) effective medium theory and using a commercial program called Granfilm. The simulation results are given in the following section.

Figure 4-34 shows calculated optical absorbance spectra of Ag nanoparticle films with equivalent thickness of 1 and 3 nm using Mie theory according to the method explained in Ch 2 (Eq. 2-46). The films contain 5 nm diameter, non-interacting spherical nanoparticles. Since the films are deposited on fused quartz, the dielectric function of medium was taken as an average of quartz and air (1.625)[43,47].

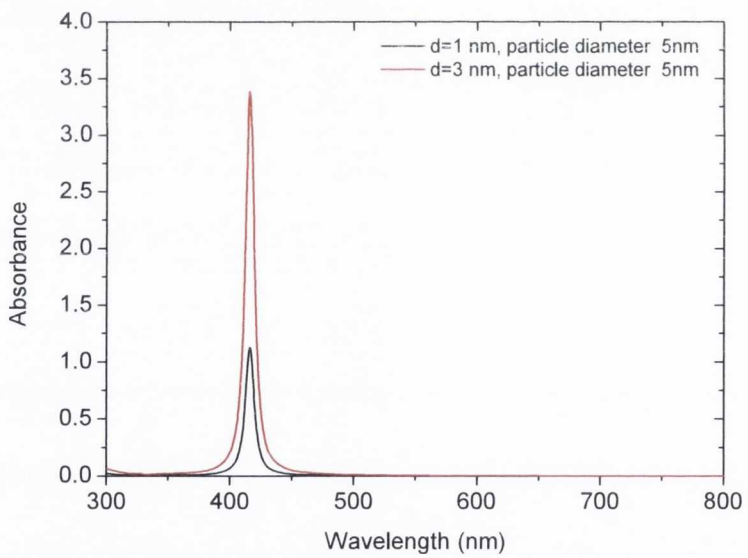

Figure 4-35 Optical absorption spectra of Ag nanoparticle films with equivalent thickness (d) of 1 and 3 nm calculated using Mie Theory.

The simulation results show a narrow absorption band compared to the experimentally measured spectra with peak centered at 415 nm. The peak position could be tuned by

changing the dielectric function of the medium but the size of the nanoparticle does not have any effect on the position or broadening of SPR peak. Figure 4-36 show the optical absorbance spectra of Ag nanoparticle films calculated according to the MG approximation. It can be seen that increasing the volume fraction *(f)* shifts the peak position towards longer wavelength and at $f = 0.35$ gives the peak position at 450 nm, close to the experimentally measured spectra. It should be noted that the MG approximation is valid only if the nanoparticles occupy a small fraction of the composite film and theory becomes invalid if $f > 0.5$[4848]. The width of the peaks in this case is also narrow as compared to the measured spectra and is not dependent on the volume fraction.

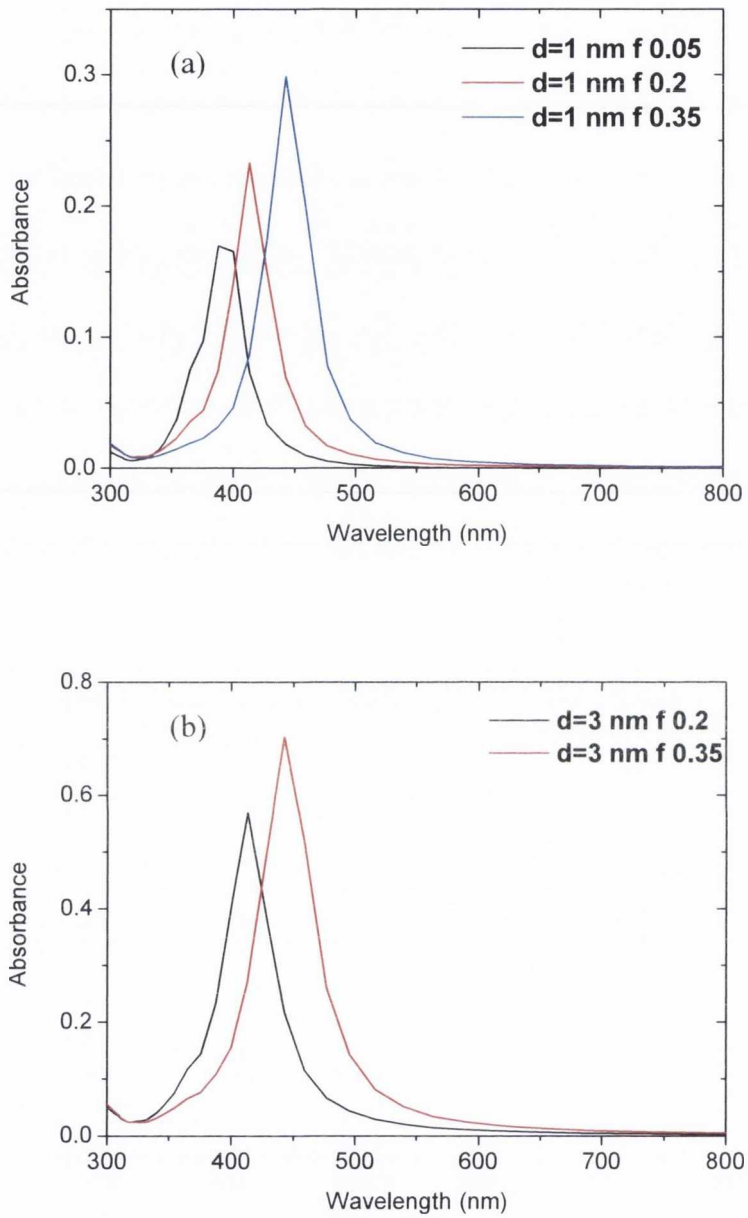

Figure 4-36 Absorbance of Ag nanoparticle films with equivalent thickness (d) of (a) 1 nm and (b) 3 nm calculated using MG effective medium theory.

Finally the optical absorbance of Ag nanoparticle films was calculated using the Granfilm software. The main parameters which are required to simulate the optical absorbance of a nanoparticle film in Granfilm software are the particle diameter and the particle height from

the surface which is given as a truncation factor. It also requires the surface coverage of the nanoparticle film to take into account the interaction between particles. We took here the example of Ag nanoparticle films prepared using fs-PLD with equivalent thickness of 3 and 5 nm and particle diameter and surface coverage was obtained from data in

Figure 4-30. The particles were considered as nanoislands sitting on the substrate surface with truncation factor of 0.2 (height of the centre of spherical nanoparticle from substrate surface / the radius of nanoparticle), since the AFM analysis showed that the nanoparticles were not perfectly hemispheres in shape. The finite size approximation was also introduced in the simulation process to take into account the surface scattering of electrons in the metal nanoparticles. Figure 4-37 (a) shows optical absorbance of Ag nanoparticle films calculated using the Granfilm software.

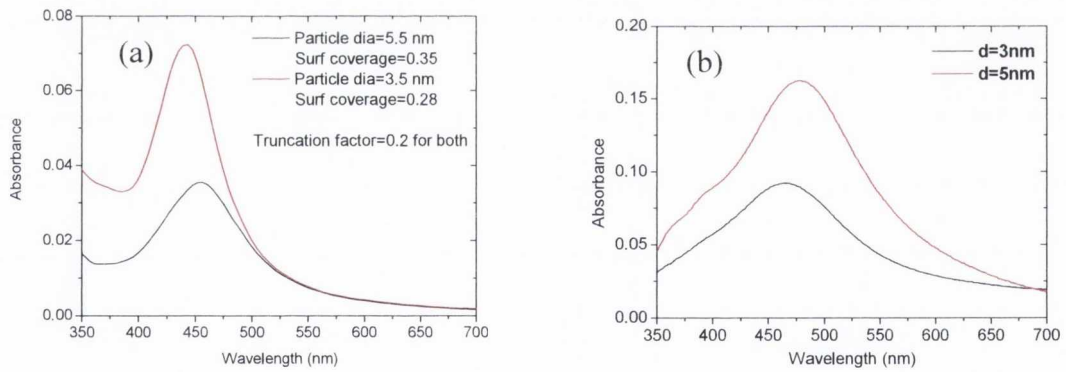

Figure 4-37 (a) Calculated optical absorbance of films with equivalent thickness of 3 and 5 nm. The particle diameter and surface coverage used for the simulation is given in the plot. (b) Measured absorbance of Ag nanoparticle films prepared using fs-PLD with similar thickness.

The simulation shows an SPR peak around 450 nm close to the experimentally measured value (Figure 4-37 (b)). The broadening of the calculated spectra is also comparable to the measured one, the magnitude of the absorbance is however approximately half of the

measured value. It was observed that increasing the surface coverage and particle size primarily increases the magnitude of absorbance. Also the red shift in the absorption spectra was not observed although the island-island interaction (dipole-dipole) was introduced during simulation. These factors indicates that one might have to consider the exact particle shape on the substrate surface and may need to account for the higher order modes, such as quadrupole interaction between particles to simulate the spectra. Nevertheless, compared to the Maxwell-Garnett and Mie theory, it can be seen from simulation results that the Granfilm model gives a better quantitative description of the measured absorption spectra.

4.9 Conclusion

In conclusion, a comprehensive study of ns and fs-laser ablation of some noble and transition metals was presented in this chapter. The metals are particularly of interest for the different material science and optical applications given in Ch.8. The laser beam spots were first characterized to obtain the value of fluence (J cm^{-2}) in both cases. The applicability of Anisimov model of plasma plume expansion in vacuum was also demonstrated for ns-ablation case. The model was also used to describe well the angular distribution of ablation plume and net deposition for both ns- and fs-ablation. Several other aspects of ns- and fs-ablation were examined; the summary for them is given in the following sections.

Langmuir probe analysis: The ablation plume for both ns- and fs-ablation was analysed using an electrostatic Langmuir ion probe. The description of probe geometry and working principle can be found in Ch 3. The analysis showed that the TOF signals were similar; both ns- and fs- ablation showed a singly peaked time-of-flight distribution for laser fluence well above threshold value. The comparison of net deposition fluence measured using QCM and

ion fluence obtained from Langmuir probe analysis showed that for all metals the fs-ablation plume contain a small fraction (1-2 %) of ionized material. This was also confirmed from total ablation and ion yields. Furthermore, the ns- and fs-ablation efficiencies in terms of material removal and ion production per mJ of laser energy were also calculated and compared. For the ns-ablation the ablation efficiency was 2.4×10^{13} atoms mJ^{-1} of incident laser energy, while the ion production efficiency is 4.8×10^{12} ions mJ^{-1}. For fs-ablation; efficiency is 5.9×10^{14} atoms mJ^{-1} and the ion production efficiency is 5.1×10^{12} ions mJ^{-1}. It can be seen that the material removal efficiency of fs-ablation is substantially higher (about 25 times) as compared to ns, while the ion ablation is of the same order. Several aspects can be responsible for higher fs-ablation efficiency.

As has been described before that the mechanisms of ns- and fs-ablation are quite different. In ns-ablation, the pulse width is substantially longer than the electron-phonon (e-ph) coupling time and the material is removed from the target surface by thermal evaporation. While in fs-ablation, the pulse width is significantly shorter then e-ph coupling time and the heat diffusion depth is smaller. As a result, most of the material in fs-ablation is removed in the form of nanofragments during a relaxation process of the extreme material state. Also in ns-ablation, the laser energy gets absorbed by the evaporated material and forms a plasma plume due to longer pulse duration. While in fs case, because of the short pulse duration, a significant amount of laser energy can be coupled to the lattice.

Morphology of nanoparticle films: The morphology of nanoparticle films with equivalent thickness of 1, 3, 5 and 7 nm showed that the film produced using ns-PLD show normal nanoparticle growth behavior i.e. the growth of particle size with increasing equivalent thickness due to surface diffusion and coalescence between small nanoclusters. However

some increase in the particle size was observed at least in the case of fs-PLD of Ag nanoparticle films. This indicates that instead that the nanoparticles are emitted directly from the target during laser ablation, some surface diffusion and coalescence involved in the growth process.

Optical properties: The optical absorption of Ag nanoparticle films prepared by both ns- and fs-PLD was observed. The SPR peak was clearly observed, however the peak seem to be broad for ns-PLD and this fact was related to the size distributions of nanoparticles. The red-shift in SPR peak was observed in both cases, this red-shift is likely due to enhanced dipole-dipole interaction between particles. Finally, the measured optical absorption was compared with the existing theoretical models, including Mie theory. From the simulation results it was concluded that although MG can be used to obtain information about magnitude and peak position, the Granfilm model gives a better quantitative description of the nanoparticle films absorption spectra.

In addition to the above conclusion, The PLD parameters used during experiments and main experimental findings have also been summarized in Table 4-2.

Table 4-2 Main parameters used for the laser ablation and some of the important experimental findings.

	ns-PLD	**fs-PLD**
Pulse energy	50 mJ per pulse	0.7 mJ per pulse
Pulse width	23 ns	130 fs
Repatition rate	10 Hz (max 20 Hz)	10 Hz (max 1 kHz)
Beam waist	28.6×10^{-3} cm^2	1×10^{-3} cm^2
Laser fluence	≈ 1.76 J cm^{-2} (Avg fluence)	≈ 1.4 J cm^{-2} (Peak fluence)
Ion fluence (cm^{-2})	Ag: 1.16×10^{13} Au: 2.94×10^{12} Ni: 1.60×10^{12}	Ag: 1.7×10^{11} Au: 1.10×10^{11} Ni: 7.0×10^{10}
Net deposition fluence (cm^{-2})	Ag: 1.53×10^{13} Au: 5.31×10^{12} Ni: 1.80×10^{12}	Ag: 1.17×10^{13} Au: 4.6×10^{12} Ni: 3.1×10^{12}
Ion ablation efficiency (for Ag)	4.8×10^{12} ions mJ^{-1}	5.1×10^{12} ions mJ^{-1}
Atom ablation efficiency (for Ag)	2.4×10^{13} atoms mJ^{-1}	5.9×10^{14} atoms mJ^{-1}

4.10 References

[1] W. Eberhardt, Surface Science **500** (1-3), 242 (2002).

[2] F. Rosei, Journal of Physics: Condensed Matter **16** (17), S1373 (2004).

[3] R. Dolbec, E. Irissou, M. Chaker, D. Guay, F. Rosei, and M. A. El Khakani, Physical Review B **70** (20), 201406 (2004).

[4] C. N. Afonso et al, Applied Physics A: Materials Science & Processing **69** (7), S201 (1999).

[5] S. Amoruso et al., Journal of Physics D: Applied Physics **40** (2), 331 (2007).

[6] J. M. Liu, Opt. Lett. **7** (5), 196 (1982); Tonney donnelly, Trinity college Dublin, 2009.

[7] W. S. Rasband, (1997).

[8] D.B. Chrisey and G.K. Hubler, *Pulsed laser deposition of thin film.* (John Wiley & Sons, Inc., New York, 1994).

[9] Seong Shan Yap, Wee Ong Siew, Cecile Ladam, Turid Worren Reenaas, and Teck Yong Tou, AIP Conference Proceedings **1328** (1), 305 (2011).

[10] E. Agostinelli, S. Kaciulis, and M. Vittori-Antisari, Applied Surface Science **156** (1–4), 143 (2000).

[11] R. Jordan, D. Cole, and J. G. Lunney, Applied Surface Science **109–110** (0), 403 (1997).

[12] L. Bing, H. Zhendong, C. Yong, C. Yanbin, and P. Xiaoqing, Applied Physics Letters **90** (4), 044103 (2007).

[13] B. Doggett and J.G. Lunney, Journal of Applied Physics **105** (3), 033306 (2009).

[14] B. Doggett, Trinity College Dublin, 2006.

[15] R. Jordan, D. Cole, J. G. Lunney, K. Mackay, and D. Givord, Applied Surface Science **86** (1-4), 24 (1995).

[16] P. C. Zalm, Journal of Vacuum Science & Technology B: Microelectronics and Nanometer Structures **2** (2), 151 (1984).

[17] L. M. Cabalín and J. J. Laserna, Spectrochimica Acta Part B: Atomic Spectroscopy **53** (5), 723 (1998).

[18] B. Toftmann, J. Schou, and J. G. Lunney, Physical Review B **67** (10), 104101 (2003).

[19] http://www.esrf.eu/computing/scientific/xop2.1/extensions.html.

[20] R. W. Cohen, G. D. Cody, M. D. Coutts, and B. Abeles, Physical Review B **8** (8), 3689 (1973).

[21] J. C. Alonso, R. Diamant, P. Castillo, M. C. Acosta–García, N. Batina, and E. Haro-Poniatowski, Appl Surf Sci **255** (9), 4933 (2009).

[22] T. Donnelly, S. Krishnamurthy, K. Carney, N. McEvoy, and J. G. Lunney, Applied Surface Science **254** (4), 1303 (2007).

[23] S. Fahler, K. Sturm, and H. U. Krebs, Applied Physics Letters **75** (24), 3766 (1999).

[24] T. Donnelly, J. G. Lunney, S. Amoruso, R. Bruzzese, X. Wang, and X. Ni, Journal of Applied Physics **108** (4), 043309 (2010).

[25] S. Noël, J. Hermann, and T. Itina, Applied Surface Science **253** (15), 6310 (2007).

[26] S. Amoruso, V. Berardi, R. Bruzzese, R. Velotta, N. Spinelli, and X. Wang, Applied Surface Science **138–139** (0), 250 (1999).

[27] R. Dinger, K. Rohr, and H. Weber, Journal of Physics D: Applied Physics **17** (8), 1707 (1984).

[28] Bruker (http://www.bruker-axs.com/stress.html).

[29] T. E. Graedel, J. P. Franey, G. J. Gualtieri, G. W. Kammlott, and D. L. Malm, Corrosion Science **25** (12), 1163 (1985).

[30] S. Banerjee and et al., Journal of Physics D: Applied Physics **34** (15), L87 (2001).

[31] X. Yu, P. M. Duxbury, G. Jeffers, and M. A. Dubson, Physical Review B **44** (23), 13163 (1991).

[32] F. Ruffino and M. G. Grimaldi, Journal of Applied Physics **107** (7), 074301 (2010).

[33] B.Lewis and J.C. Anderson, *Nucleation and Growth of Thin Films*. (Acadamic Newyork, 1978).

[34] G D T Spiller and M Hanbucken J A Venables, Rep. Prog. Phys. **47**, 399.

[35] G. Jeffers, M. A. Dubson, and P. M. Duxbury, Journal of Applied Physics **75** (10), 5016 (1994).

[36] G. D. Spiller and M. Hanbucken J. A. Venables, Rep. Prog. Phys. **47**, 399.

[37] M. Volmer, Dresden (1939).

[38] V.V. Dick, I.A. Solov'yov, and A.V. Solov'yov, AIP confrence proceedings **76** (2009).

[39] R. Gommer, Rep.Prog.Phys, 917 (1990).

[40] S. Amoruso et al., Journal of Physics: Condensed Matter **18** (4), L49 (2006).

[41] U. Kreibig and M. Volmer, *Optical properties of metal clusters*. (Springer, 1995).

[42] Zhengxin Liu, Honghong Wang, Hao Li, and Xuemei Wang, Applied Physics Letters **72** (15), 1823 (1998).

[43] T. Donnelly, B. Doggett, and J. G. Lunney, Applied Surface Science **252** (13), 4445 (2006).

[44] K. Lance Kelly, E. Coronado, L. L. Zhao, and G. C. Schatz, The Journal of Physical Chemistry B **107** (3), 668 (2002).

[45] S.Link and M. A. EL-sayed, INT Review in Physical Chemistry **19** (3), 409 (2000).

[46] J. M. Gérardy and M. Ausloos, Physical Review B **27** (10), 6446 (1983).

[47] G. Xu, M. Tazawa, P. Jin, and S. Nakao, Applied Physics A: Materials Science & Processing **80** (7), 1535 (2005).

[48] T. C. Choy, *Effective medium theory: principles and applications, Clarendon Pres*. (oxford, 1999).

Chapter 5. Optical emission spectroscopy of femtosecond laser ablation plume

5.1. Introduction

In recent years it has been observed that ablation of solid materials using fs-laser pulses leads to material blow off composed of fast ions and atoms as well as clusters and nanoparticles of the target material, and the size and surface morphology of nanoparticle films depends on the processing parameters[1]. Hence, fs-laser ablation in vacuum has been suggested as a powerful and versatile tool for the production of metal and semiconductor nanoparticles, showing several experimental advantages with respect to other more standard techniques. The process of fs-laser ablation of some solid prototype materials has been subjected to several experimental and theoretical investigations[2,3]. The theoretical approach to model the fs-laser ablation process is quite complicated since the material properties as well as the laser processing conditions need to be considered. The quantities which need to be taken into account are the optical absorption of the material, the heat conduction, electron-lattice thermalisation, evaporation kinetics, and fluid dynamics of the ablation plume during expansion.

In this experiment we carried out an analysis of fs-laser ablation of Ni, Au and Ag, three metals with different electron-phonon coupling times. The atomic mass, atom density, the electron-phonon coupling time and the absorption coefficient are given in Table 5-1. We have used fast imaging along with time- and space-resolved optical emission spectroscopy (OES) techniques to characterize the main features of the ablation plume. A detailed

experimental setup of fast imaging and OES has been given in Ch. 3. The ablation was performed in vacuum using a fs-pulsed laser (800 nm, 130 fs). The laser pulse was incident at 45° to the target normal and the optical emission was measured perpendicular to the target normal. The results of OES and fast imaging for all three metals are given in this chapter.

Table 5-1 Atomic mass (m_A), atom density and electron lattice thermalization time (τ_{e-p}) for Ag, Au and Ni.

	Ag	**Au**	**Ni**
$m_{A\ (amu)}$	107.86	196.96	58.69
Atom density (cm^{-3})	5.86×10^{22}	5.92×10^{22}	9.13×10^{22}
$\tau_{e-p\ (ps)}$	~ 20 [4,5]	~ 15 [6]	~ 9 [3]
Optical absorption coefficient; α (cm^{-1}) *for* λ=800 nm [7]	7.86×10^{5}	4.70×10^{5}	7.42×10^{5}

In the first stage of the experiment, the optical emission from a fs-laser ablation plume was studied by imaging it in the direction perpendicular to the target surface (z-direction). The images were recorded at various time delays from 50 ns to ~ 10 μs. The zero time was taken as the onset of plasma emission from the target surface. For higher time delays (≥ 400 ns) the gate width was increased to a quarter of the delay time to record more light from the nanoparticle ablation plume. In the second stage of the experiment the optical emission from the ablation plume was measured with the aid of a 0.25 m focal length imaging spectrometer. The emission intensity for OES was measured using an ICCD camera coupled to the spectrometer.

5.2. ICCD imaging and spectroscopy of Ni femtosecond ablation plume

Figure 5-1 shows plume images recorded during laser ablation of a Ni target at different time delays, the corresponding gate widths and delay times are given for each of the images. Each image was recorded by accumulating the signal over 70 laser shots on a rotating Ni target to get a better signal-to-noise ratio.

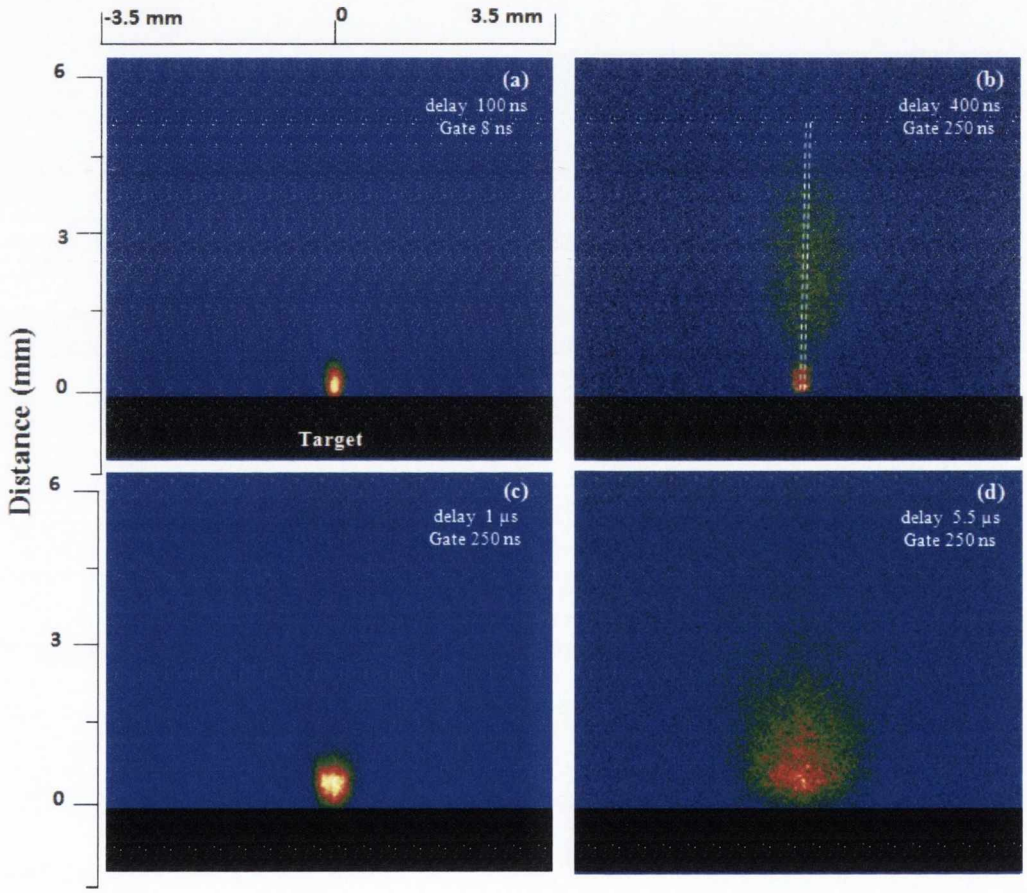

Figure 5-1 Selected ICCD images for different delay times for fs- laser ablation plume of Ni. The scale on left hand side represents the distance from the target surface.

The image at 400 ns delay time shows two plume components, a slow component located close to the target, and a fast component located a few millimetres away from the target

surface. The two components have different expansion dynamics. It was observed that the slow component remains close to the target even after a few microseconds delay. The dynamics of the fs-laser ablation plume has been investigated experimentally and theoretically (MD simulation coupled to the two temperature heat diffusion model)[1,8]. Both give evidence of the ablation plume splitting into two main components, a fast atomic cloud which leaves the target with expansion velocity of few tens of km/s and a slow component mainly composed of nanoparticles of the ablated material with expansion velocity almost ten times smaller than the atomic plume[8]. The expansion behaviour of the slow component is also dependent on the nanoparticle size and temperature. Numerical simulation also predicts that the evolution of large sized particles is affected by collisions and that they are located in the colder part of the plume closest to the target[9] surface.

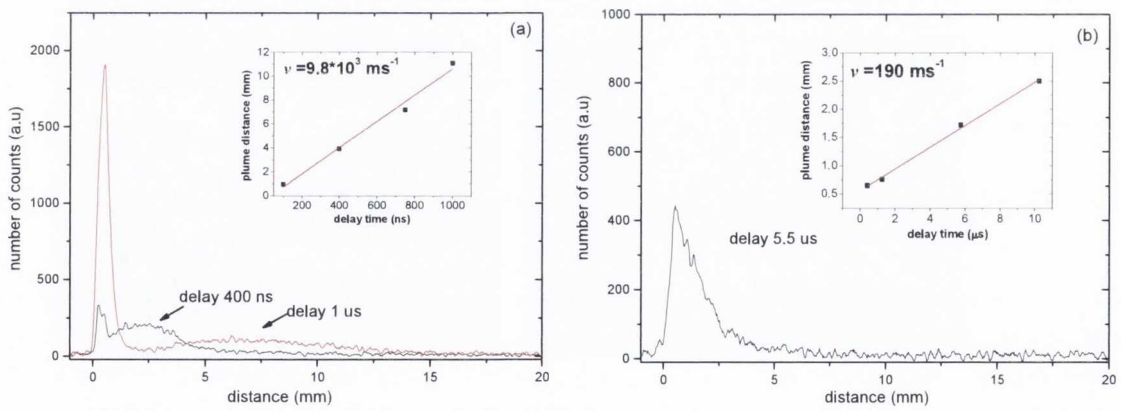

Figure 5-2 Spatial profile of Ni ablation plume at different time delay of (a) 400 ns and 1 µs and (b) 5.5 µs along the direction normal to the target surface. The insets show the centre-of-mass distance versus time delay plots at different time delay from (a)100 ns -1 µs and (b) 1-10 µs, from which the velocities of atomic and nanoparticle plumes were obtained.

Since the ICCD images are symmetric around the surface normal, this allows us to analyze them by taking a slice of the central part of the image in the direction normal to the target surface to plot signal versus distance. The early stage emission of slow plume component and progression of fast atomic plume can be seen from Figure 5-2 (a), after few microseconds, the fast atomic component moves further away and second slow component stay close to the target surface (see Figure 5-2 (b)). The plots in Figure 5-2 also enable us to define a distance $\bar{d}$ of centre-of-mass intensity to calculate the characteristic expansion velocity of each ablation plume where:

$$\bar{d} = \frac{\int zI(z)dz}{\int I(z)dz} \qquad 5\text{-}1$$

The distance of centre-of-mass ($\bar{d}$) and time plots are given in insets of Figure 5-2, the velocities obtained for atomic and slow nanoparticle plume are ~10 km s^{-1} and 200 m s^{-1} .

Figure 5-3 shows the ICCD images of spectral emission from Ni fs-laser ablation plume in the region of 300-540 nm and 400-640 nm at time delays of 400 ns and 1 μs respectively. Each ICCD image was recorded by accumulating spectra from 700 laser shots on a rotating Ni target. Prior to that, the background spectrum with the same number of acquisition was also recorded, which was then subtracted from the spectral emission of the ablation plume. Neverthaless some noise along with the spectral lines in the ICCD images can be seen.

Several kinds of electronic noise can be present in image sensor devices; one of the common types is called readout noise. In readout noise, when the accumulated charge is shifted on CCD chips, some of electrons are left behind or jump around which may cause a static

charge effect[10]. This effect can even be enhanced when the ICCD is used in acquisition mode and may have caused noise in the recorded spectra.

The image at 400 ns delay time shows only atomic line emission due to the plasma component of the plume, where the spectra at 1 μs delay shows continuum emission close to the target surface (z=0) due to the hot nanoparticle plume (see Figure 5-3(b)).

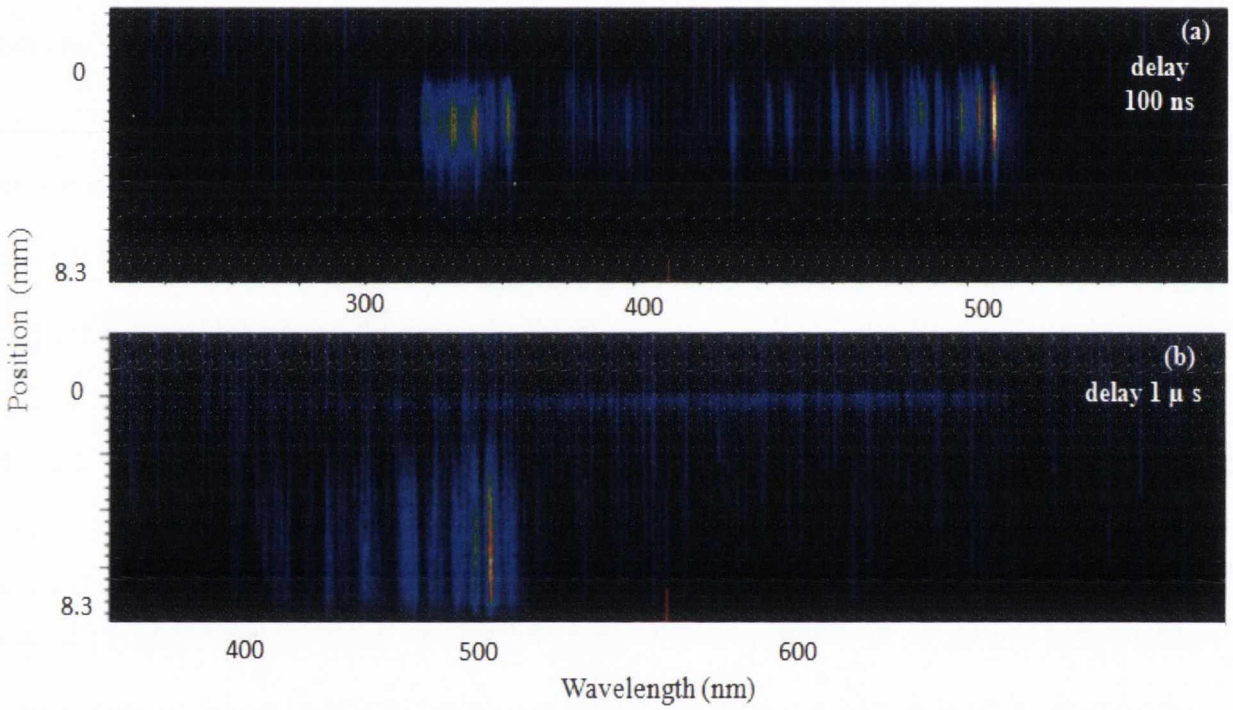

Figure 5-3 ICCD images of the spectral emission from Ni femtosecond laser ablation plume at (a) 100 ns and (b) 1 μs delay with respect to the laser emission, the gate width is 40 ns and 250 ns respectively. Zero in position axis represents the target surface.

For a clear view, we plotted the spectral emission from both the fast and slow plume components. Figure 5-4 (a) shows the emission spectra of the fast component in the range of 300-550 nm, it can be seen that the spectrum is dominated by the transition lines of neutral Ni I and Ni II (Ni^+), which indicates that the fast component is mainly composed of atoms

and ions of the target material. The lines at 341.4 nm, 352.4 nm and 361.9 nm are due to transitions between $3d^9 4s(^3D_3) \rightarrow 3d^9 4p(^3F_4)$, $3d^9 4s(^3D_3) \rightarrow 3d^9 4p(^3P_2)$, $3d^9 4s(^1D_2) \rightarrow 3d^9 4p(^1F_3)$ energy levels of neutral Ni (Ni I). Whereas the lines at 429.4 nm and 508.3 nm are due to $3p^6 3d^9(^2D_{3/2}) \rightarrow 3p^6 3d^8(^4P_{3/2})$ and $3d^8 4d(^4G_{11/2}) \rightarrow 3d^8 4f(^4I_{11/2})$ energy levels of neutral Ni, where $3d^8 4s^2(^3F_4)$ is the ground state configuration of (Ni I) and the ionization is 7.6398 eV. The energy level configuration for atomic transitions was taken from Ref. 11. Figure 5-4 (b) shows the spectral emission from the slow plume component, the spectrum shows a structure-less, broad continuum in the spectral range of

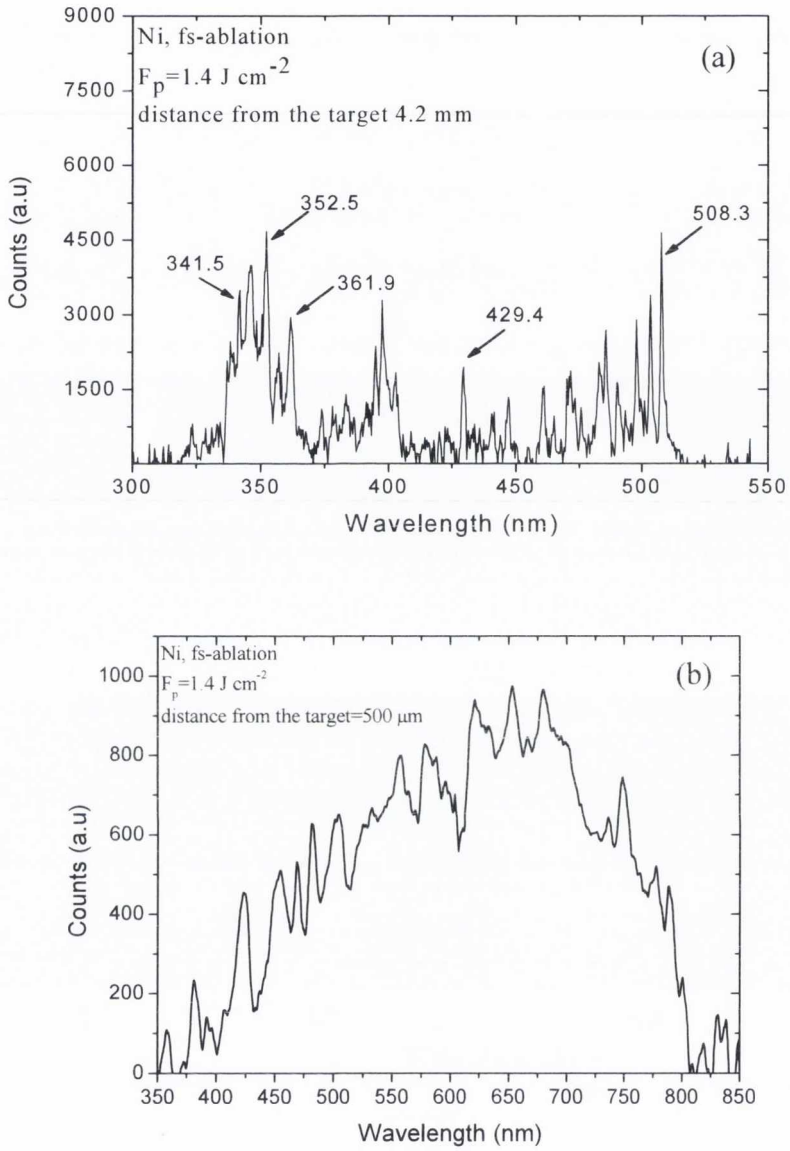

Figure 5-4 Background corrected optical emission spectra of Ni for (a) fast and (b) slow plume component at time delay of 400 ns and 1 μs respectively. The laser fluence used for the fs-ablation of Ni and distance from the target surface at which the spectra is plotted are given in the respective plots.

350-750 nm. Similar observations of continuum emission from the slow plume in the fs-laser ablation of other metals has been reported by other authors[1,8]. It was suggested that the blackbody-type continuum emission from the slow component is because of the presence of hot nanoparticles of the target material.

However, for the quantitative analysis of emitting species in the laser ablation plume (plasma and nanoparticle) it is necessary to perform absolute intensity calibration of the optical emission spectra. The spectra in Figure 5-4 are spectrally calibrated using known line emission from a mercury lamp. For the intensity calibration, a 100 watt quartz halogen lamp (Oriel 6333) was used, as it has a characteristic irradiance when placed 50 cm away from the imaging plane. Once calibrated the relative transfer function of our optical detection system can be obtained and the measured spectra can then be corrected using this transfer function. The complete process of intensity and wavelength calibration is given Ch. 3. Figure 5-5 shows the intensity calibrated optical emission spectra of fast atomic and slow nanoparticle plume.

The continuum emission from the nanoparticle plume was used to estimate the temperature of the hot nanoparticles, the results for the temperature measurement will be presented in Sec 6.5. It was observed that the intensity of optical line emission from the fs atomic plume was approximately 100 times lower as compared to the ns-laser ablation plasmas of metals in the same fluence range ($\approx$ 1 J cm^{-2}). This might be because the laser focal spot size is about 24 times smaller than the ns-ablation which makes the plasma volume under observation significantly smaller. It should also be considered that the laser pulse duration in fs-ablation case is a few hundred times less than the electron-phonon coupling time (few ps for metals), and the interaction of laser pulse with the emitted atomic species can be very small as compared to the ns-ablation case.

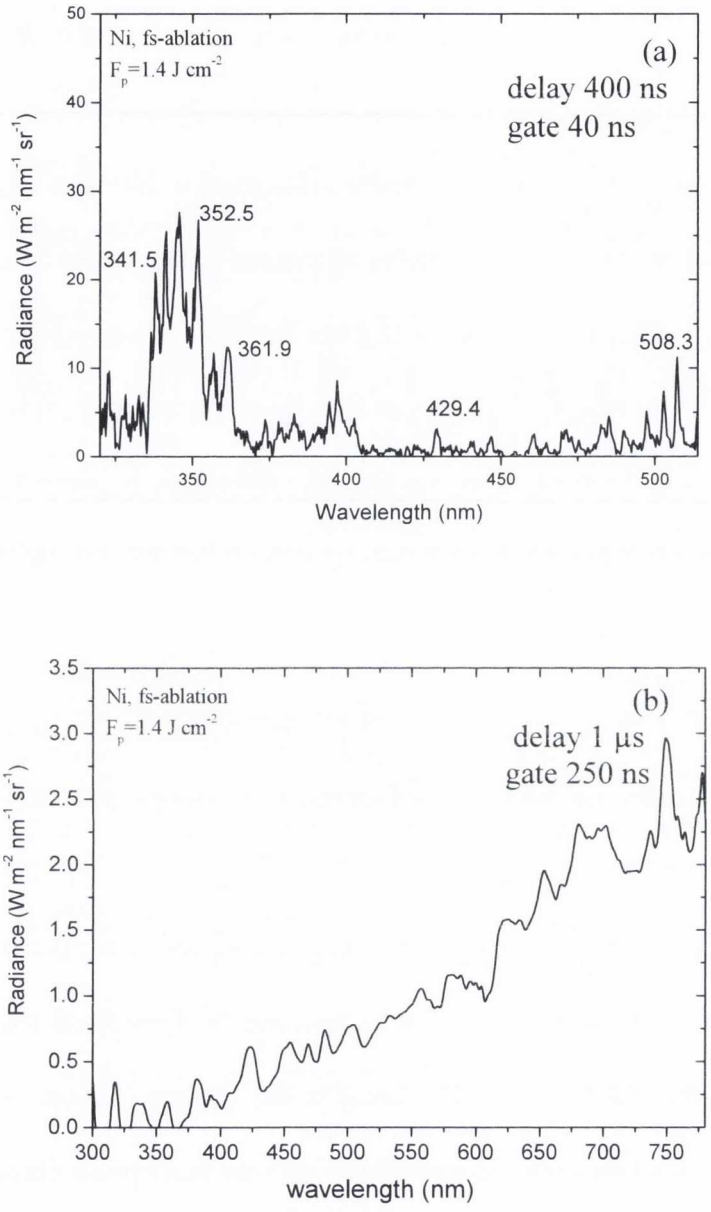

Figure 5-5 Intensity calibrated optical emission spectra of (a) atomic and (b) nanoparticle plume for fs-laser ablation of Ni.

5.2.1. Analysis of optical emission spectra of Nickel atomic plume

The emission spectra in Figure 5-5 (a) can also be used to extract the parameters such as temperature and ion/atom density of plasma produced by fs-laser ablation. These parameters can be obtained by well-established techniques in spectroscopic plasma diagnosis[12]; the electron temperature is related to the relative intensity of the lines from different energy levels which are in local thermodynamic equilibrium and the energy level population is distributed according to the Boltzmann law. For our case a commercial software package called PrismSPECT[13] was used to simulate the emission spectra. PrismSPECT calculates the collisional-radiative ionization and excitation and emitted spectrum for plasma at given temperature, density and size or thickness. Along with the emission spectrum the software also calculates the transmission spectrum, plasma opacity and the ionization fraction. Prism SPECT was mainly used to obtain the temperature, density and the ionization fraction of the fs-laser ablation plasma.

The approximate initial plasma thickness and density for the calculation was obtained from the ICCD plume image at 400 ns delay and the Langmuir probe signal[14] respectively. The spectrum was then further calculated for a few different values of temperature and densities. Figure 5-6 (a) shows the simplified energy level diagram representing all the mentioned optical emission lines.

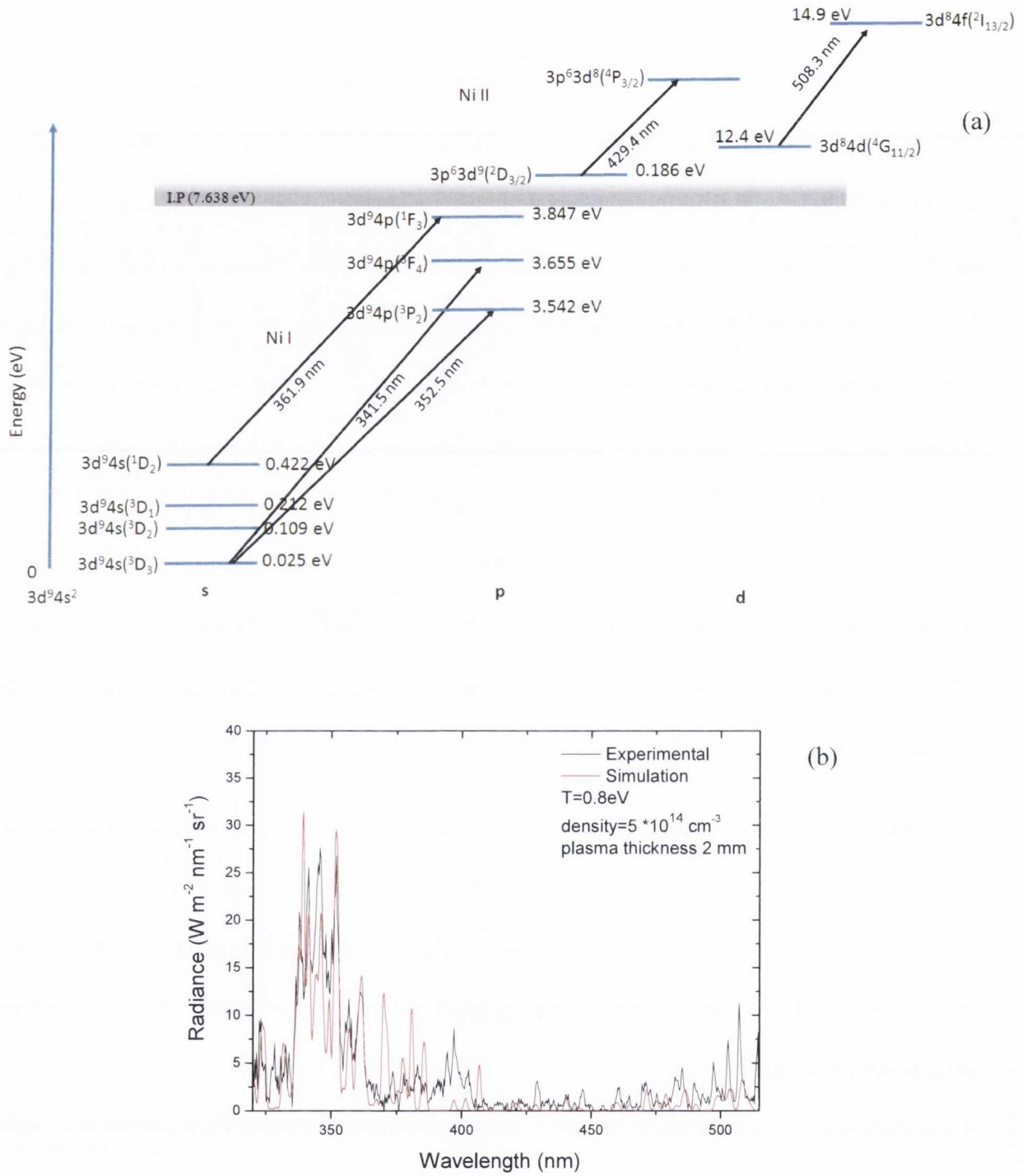

Figure 5-6 (a) Energy level diagram of Ni I and Ni II showing important radiatively linked levels. The shaded line represents the ionization limit of Ni I (b) Experimental and simulated optical emission spectra of nickel atomic plume at 400 ns delay.

The lines at 429.4 and 508.3 nm due to Ni^+ are also given in the energy level diagram. Figure 5-6 (b) shows the best possible fit to the experimentally obtained spectra of Ni atomic plume. The plasma temperature and density obtained from the simulation are 0.8 eV and 5×10^{14} cm^{-3}. The fraction of Ni I and Ni II or (Ni^+) was 0.4 % and 99 % respectively.

5.3. ICCD imaging and spectroscopy of Au ablation plume

Figure 5-7 shows the ICCD images of Au ablation plume at four different time delays. It can be seen that initially, at 100 ns delay the atomic plume has expanded about a mm in front of target surface in vacuum and a few mm at 400 ns delay. The emergence of a slow and intense nanoparticle plume can also be seen close to the target surface at 400 ns delay (see Figure 5-7 (b)) which evolves further in vacuum at later time. Similar to the Ni ICCD images, the intensity profile of atomic and nanoparticle plume was plotted as a function of distance from target surface for different time delays. The velocity of the slow nanoparticle plume was calculated from the distance of center-of-mass intensity at different time delays (see plots in Figure 5-8). The velocities of the fast and slow plumes in this case were found to be 4 km/s and about 100 m/s respectively. Figure 5-9 shows the ICCD images of spectral emission of the Au ablation plume recorded at 400 ns and 1 μs after the laser pulse, a weak continuum emission from the nanoparticle plume can be seen close to the target surface at 400 ns delay. In Figure 5-9 (a), the atomic lines are also evident a few millimeters further away from the target. Figure 5-9 (b) shows a clear continuum emission from the nanoparticle plume and by looking at the space resolved atomic line spectra, the atomic plume have moved further away from the target surface.

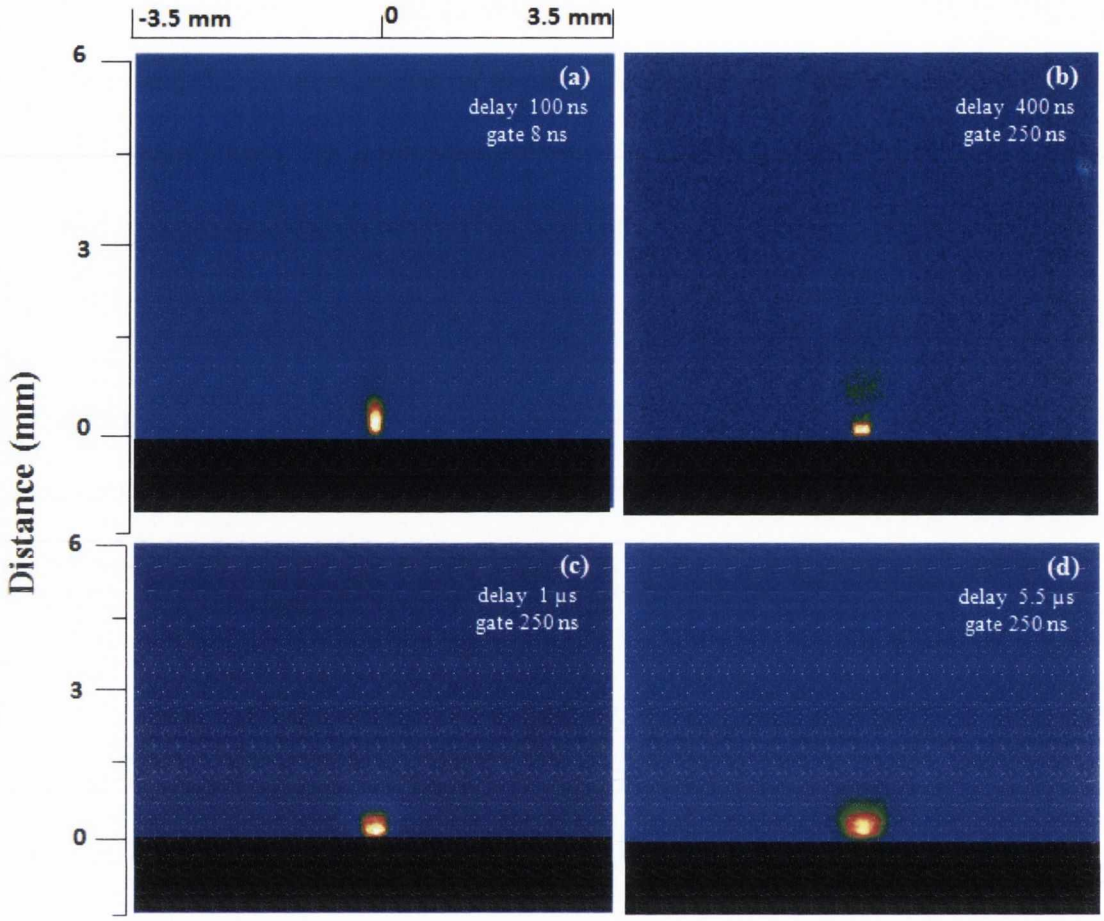

Figure 5-7 Selected ICCD images of the Au fs-laser at 1.4 J cm-2 ablation plume for different delay times.

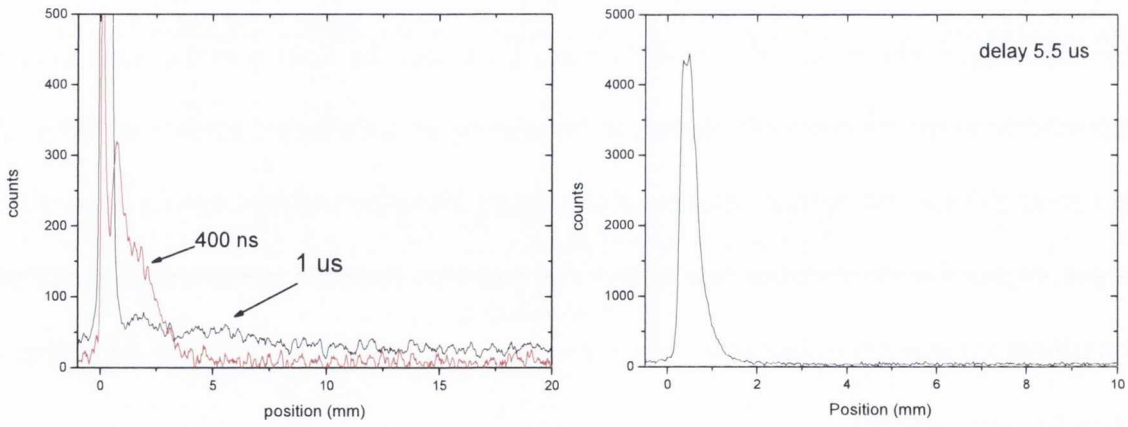

Figure 5-8 Cuts through the central part of ICCD plume images of Au fs-ablation along the direction normal to the target surface at different time delay.

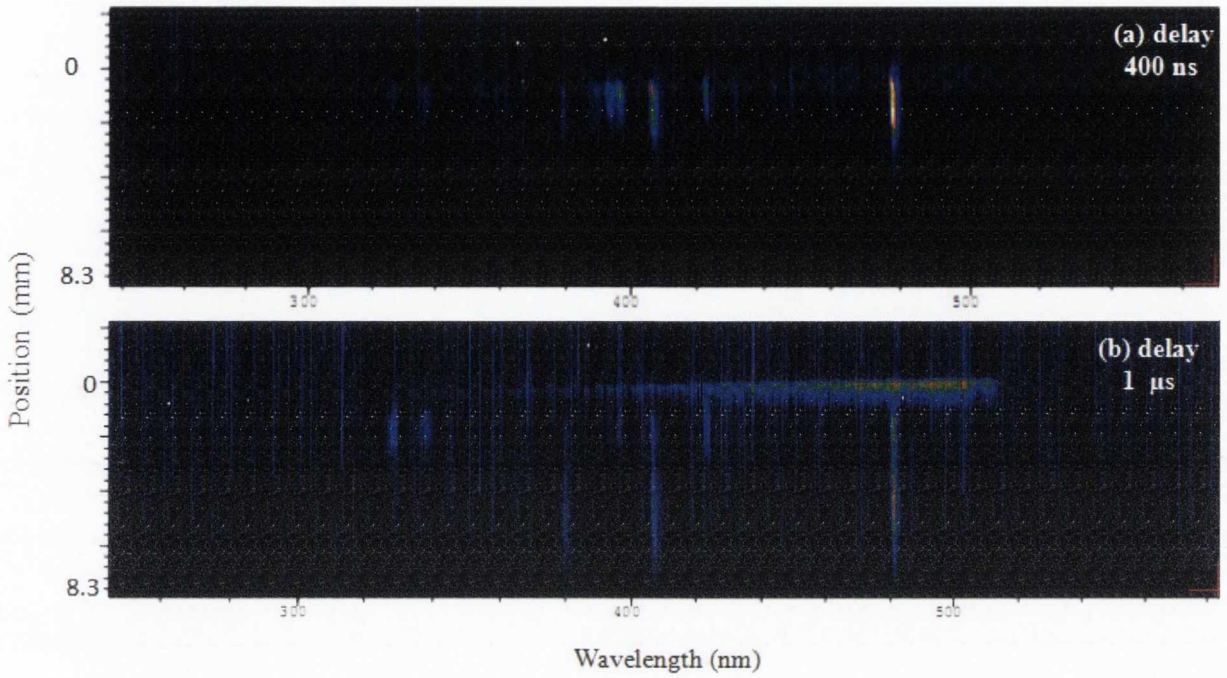

Figure 5-9 ICCD images of spectral emission from Au fs-laser ablation plume at (a) 400 ns and (b) 1 µs delay with respect to the laser emission, the gate width is 40 ns and 250 ns respectively.

The lines at 406.2 nm and 422.7 nm are neutral Au (Au I) lines obtained from Ref. 11. The spectra for Au was not studied and simulated in detail since a very limited spectroscopy database is available for Au also the PrismSPECT atomic database for Au was not available at this stage. Figure 5-10 (a) show the intensity calibrated atomic plume spectra of Au ablation plume. Figure 5-10 (b) shows the intensity calibrated continuum emission spectrum of the Au nanoparticle plume in the range of 350-750 nm. The continuum emission from the Au nanoparticle plume seems to differ from the Ni in terms of intensity and shape. It can be seen that the radiance of the Au nanoparticle plume is ~ 5.6 times higher than the Ni nanoparticle plume and the spectra show a slight enhancement peak between 550-600 nm.

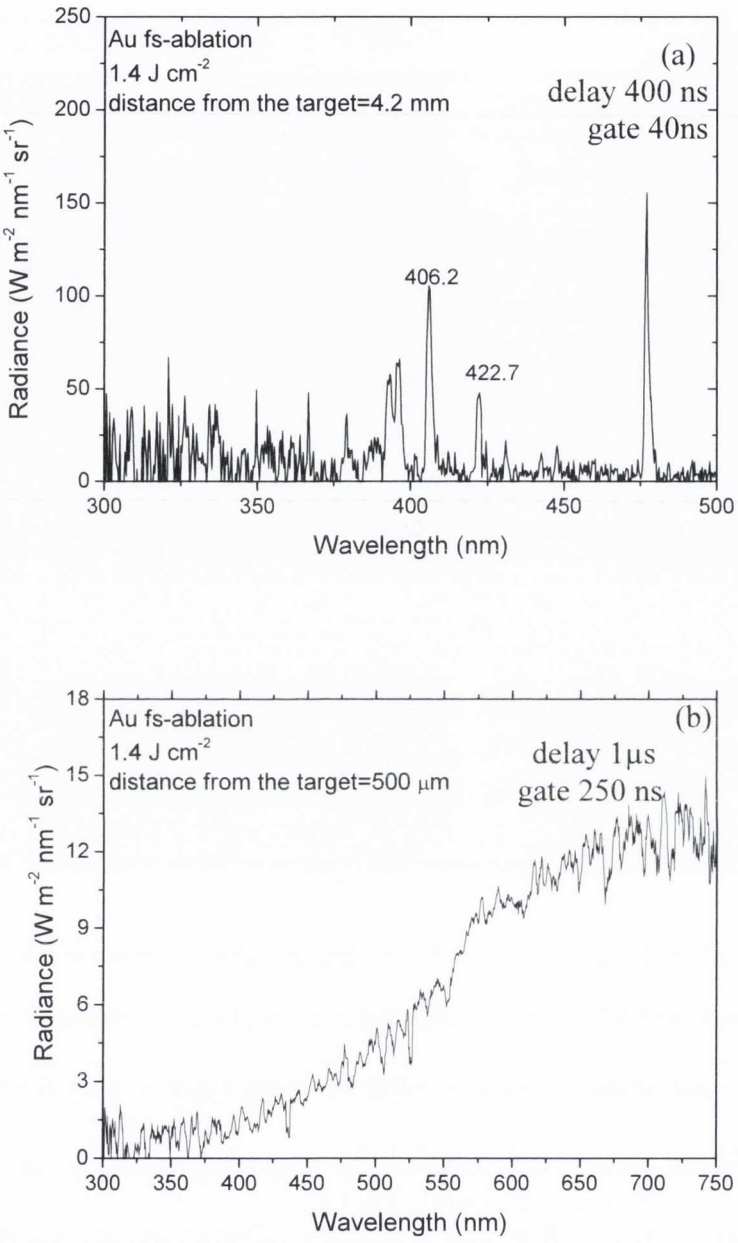

Figure 5-10 Intensity calibrated (a) line emission and (b) continuum emission spectra of the Au ablation plumes at 400 ns and 1μs delay respectively. The fluence value and the distance from the target at which the spectra was plotted is given in each plot.

Since Au is a noble metal and the optical properties of such materials are strongly dependent on their dielectric function, hence we can expect a different optical response from the Au

nanoparticles in the ablation plume. An explanation of the enhancement in optical emission of Au nanoparticle plume in terms of the nanoparticles emissivity is given in Sec 5.5.

5.4. ICCD imaging and spectroscopy results for Ag ablation plume

The temporal and spatial evolution of Ag fs-ablation plume was also investigated under the same experimental conditions (i.e. same peak fluence, vacuum and ICCD electronic settings). Figure 5-11 show the spatial evolution of the Ag ablation plume at different time delays.

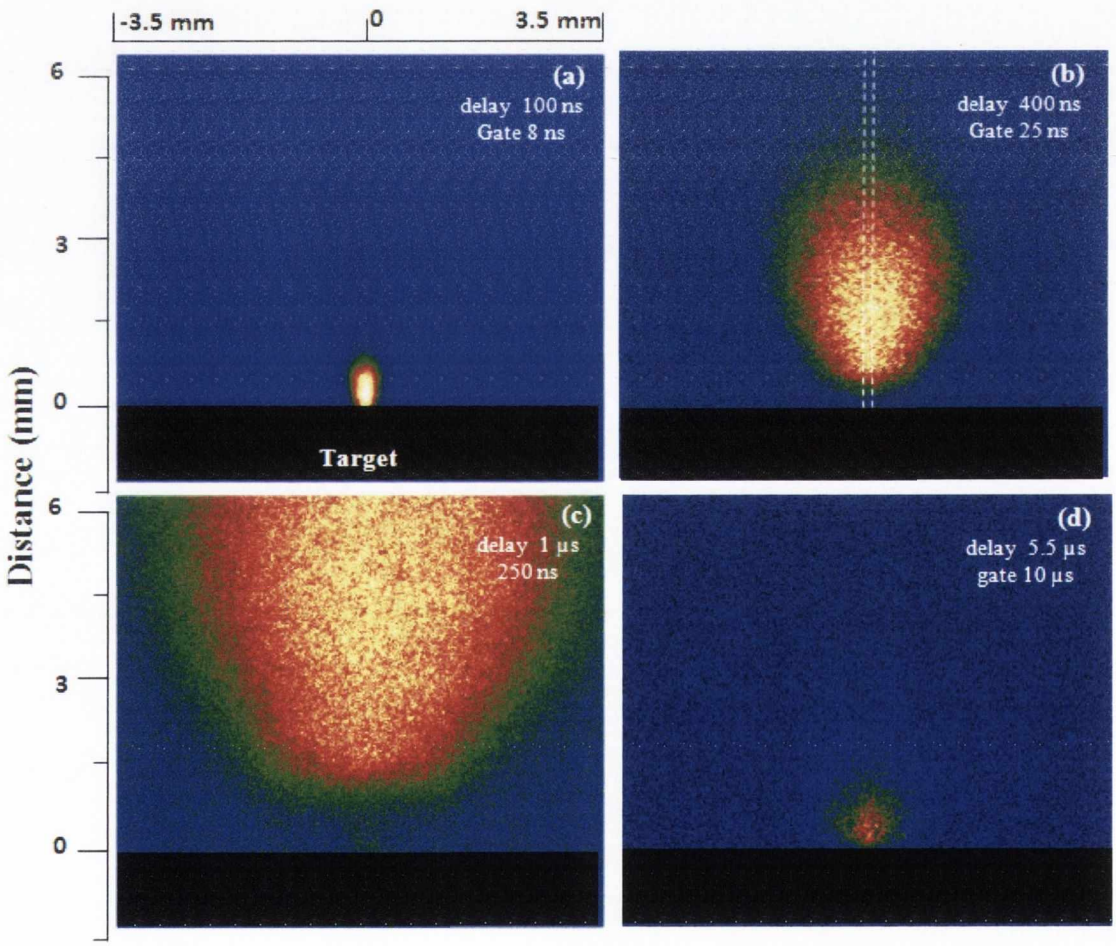

Figure 5-11 ICCD images of the Ag fs-laser ablation plume at different time delays. The laser fluence if 1.4 J cm^{-2}.

Unlike Ni and Au the image at 400 ns delay does not show any emission from a slow nanoparticle plume; however a slight emission can be seen at 1μs delay (see Figure 5-11(c)) very close to the target surface. In order to see further evolution of slow plume component, the images were recorded at 5.5 μs delay with 1.3 μs gate width (quarter of delay time). As the photon counts were found to be very small in this case, a large gate time was used to capture more light and to have a clear image of the slow ablation plume. Figure 5-11 (d) shows an ICCD image of the slow plume component at 5.5 μs with 10 μs gate. The emission from the slow nanoparticle plume is thus evident from this image but the light emission of the plume seems to be very small as compared to the Ni and Au slow nanoparticle ablation plumes. An explanation of the lower light emission from the Ag nanoparticle plume is given in last section of the chapter in terms of the emissivity of nanoparticles. It has been suggested that in order to calculate incandescence it is important to take into account wavelength dependent emissivity[15]. The calculated emissivity of Ni, Au and Ag nanoparticles has also been given in Sec 5.5 . Figure 5-12 shows the intensity distribution of the Ag ablation plume in the direction normal to the target surface, from which the velocity of both atomic and nanoparticle (i.e. ionized and neutral) plumes were calculated. The velocities of all three (Ni, Ag, Au) elements are summarized in Table 5-2, the difference in the velocities of all three elements is due to the difference in their relative atomic masses (see Table 5-1).

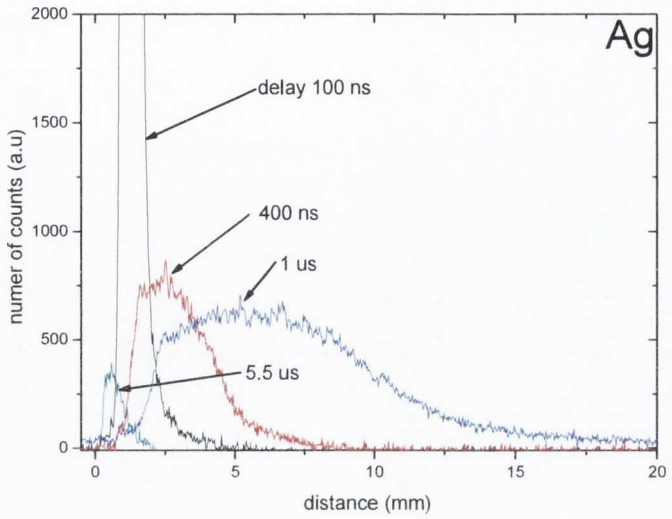

Figure 5-12 Cuts through the central part of Ag fs-ablation plume at 1.4 J cm^{-2} showing intensity distribution normal to the target surface.

Table 5-2 Velocities of atomic and nanoparticle plume for fs-laser ablation of Ni, Au and Ag at peak laser fluence of ≈ 1.4 J cm^{-2}. The error correspond to the standard deviation in the measured values.

	Ni	Ag	Au
v_{np} (m/s)	200 ± 6.7	160±2.5	100±2.0
v_{atomic} (km/s)	10±0.1	8.0 ±0.25	4±0.20

Figure 5-13 (a,b) show ICCD spectral images of the Ag ablation plume at different time delays. The spectra show well separated atomic transition lines, the photon counts from the very low light emitting nanoparticle plume was not detectable in spectroscopy as we detected in the ICCD imaging, since in spectroscopy each pixel array of the ICCD gets photons of a certain energy or wavelength while in imaging each pixel gets photons of all energies or wavelengths. Figure 5-13(c) is the intensity calibrated line emission spectra of the Ag

ablation plume showing the most prominent optical emission lines in the range of 300-550 nm.

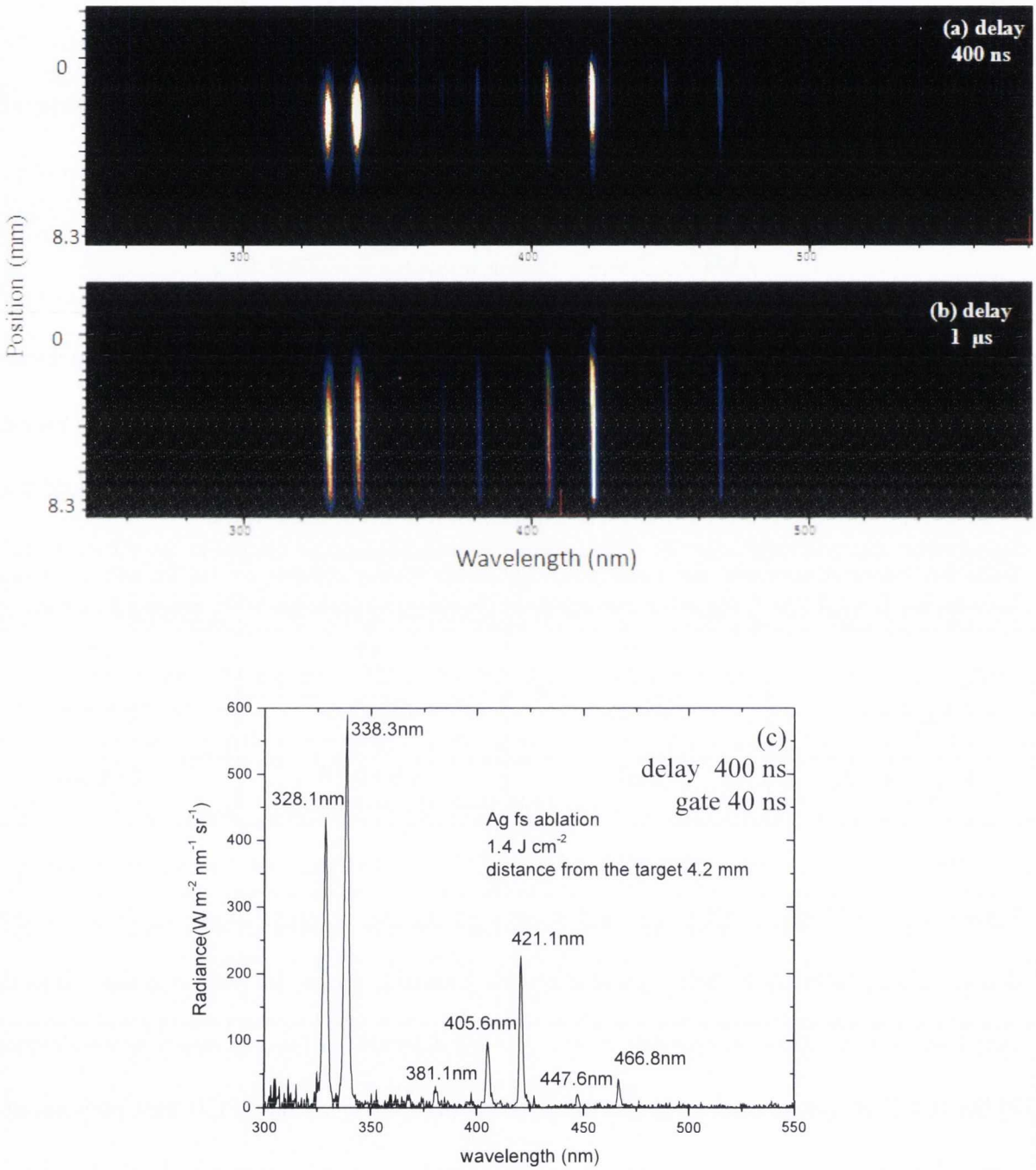

Figure 5-13 ICCD images of spectral emission from Ag fs-laser ablation plume at (a) 400 ns and (b) 1 µs delay. (c) Intensity calibrated optical emission spectra of Ag atomic plume at 400 ns delay.

5.4.1. Optical emission spectra of Ag atomic plume:

The energy level configurations of the above line transitions are given in table below.

Table 5-3 Energy level configurations of Ag I radiative transitions shown in Figure 5-13.

Wavelength (nm)	Upper level	Lower level
328.1	$4d^{10}5s: {}^2S_{1/2}$	$4d^{10}5p: {}^2P_{3/2}$
338.3	$4d^{10}5s: {}^2S_{1/2}$	$4d^{10}5p: {}^2P_{1/2}$
381.1	$4d^{10}5p: {}^2P_{3/2}$	$4d^{10}7d: {}^2D_{5/2}$
405.6	$4d^{10}5p: {}^2P_{1/2}$	$4d^{10}6d: {}^2D_{3/2}$
421.1	$4d^{10}5p: {}^2P_{3/2}$	$4d^{10}6d: {}^2D_{3/2}$
447.6	$4d^{10}5p: {}^2P_{1/2}$	$4d^{10}7s: {}^2S_{1/2}$
466.8	$4d^{10}5p: {}^2P_{3/2}$	$4d^{10}7s: {}^2S_{1/2}$

Figure 5-14 (a) shows the energy level diagram showing the strongest lines for Ag I. Figure 5-14 (b) shows the experimentally measured and simulated spectra of Ag atomic plume in the range of 300-500 nm. For a plasma temperature of 0.65 eV the density was measured to be 2×10^{15} cm^{-3}, the distinct lines at 405.6, 421.1 447.6 and 466.8 nm agree well with the simulated spectra for the mentioned plasma temperature and density. The position and energy level configuration for the lines was taken from NIST and Ref.11 . However the calculated intensity of the lines at 328 and 338 is higher as compared to the measured one. The spectra was also calculated for higher temperatures in order to adjust the relative intensity of lines[16], but for that case the intensity of lines above 350 nm was found to be very different from the measured one along with some additional lines due to population of higher energy states. It

might be that the absorption coefficients for these particular transitions are different in the code and it is not appropriate to adjust the relative intensity of lines by adjusting the plasma temperature. The energy level data was obtained from NIST and from Ref. 11 and was also compared with data available from the PrismSPECT code However the line at 381.1 nm due to Ag I seem to be missing in the code. This can also be seen in Figure 5-14 (b) the ion fractions obtained from the PrismSPECT code for Ag fs-laser ablation plasma is Ag I 12% and Ag II 87 % which shows that plume is not fully ionized as we found for Ni.

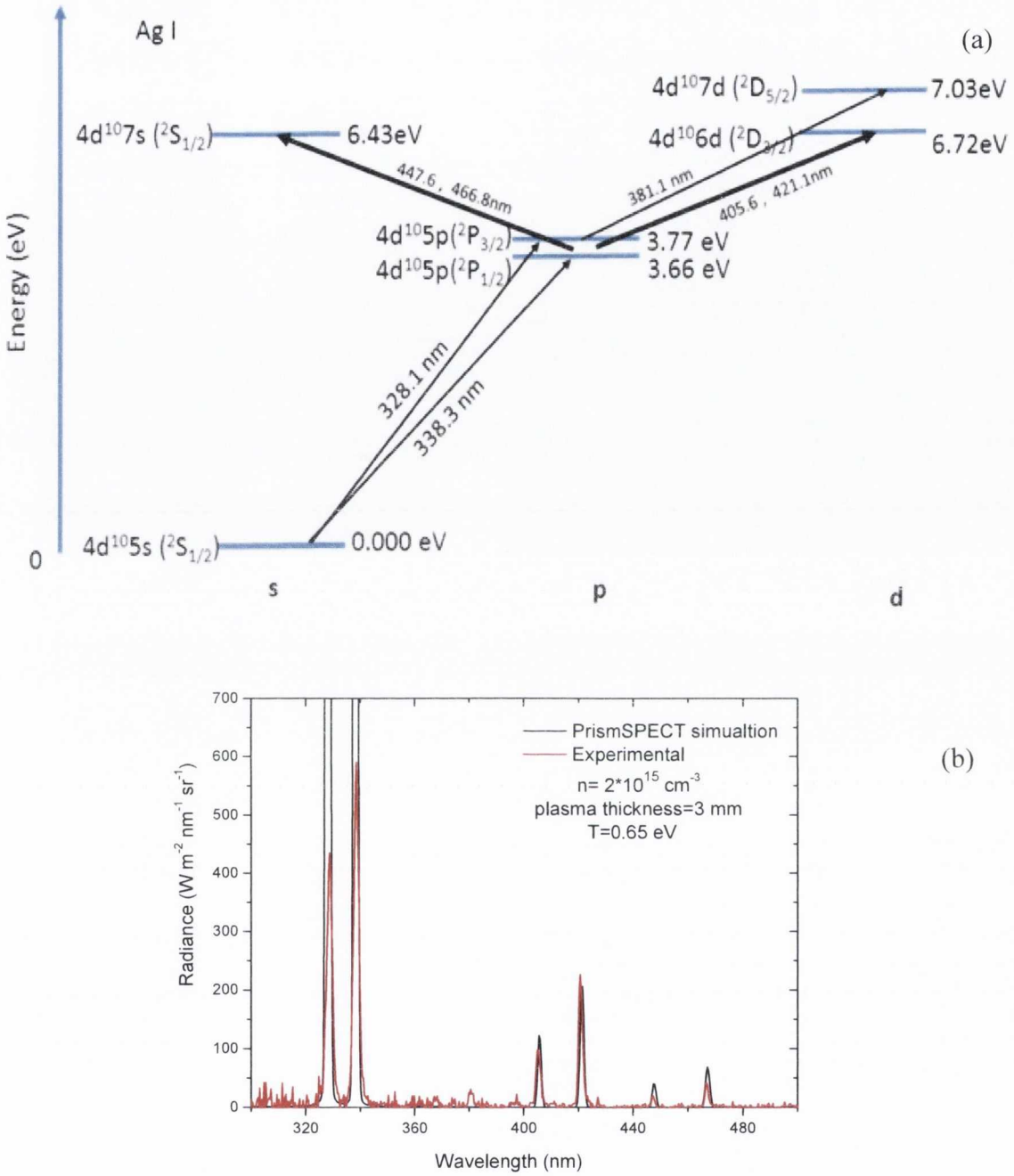

Figure 5-14 (a) Simplified energy level diagram for Ag I. (b) Measured and simulated spectra of Ag fs-laser ablation plume at 400 ns time delay.

5.5. Temperature determination of nanoparticles in slow ablation plume

By fitting the structure-less, broad continuum emission as Planck's radiation spectrum, it is also possible to estimate the temperature of the hot nanoparticles in the slow ablation plume. However the usual blackbody intensity distribution function needs to be modified for this case. The important quantity which needs to be taken into account is the spectral emissivity which depends on the dielectric properties of the nanoparticles, since we are dealing with the noble and transition metal nanoparticles, the dielectric function for those nanoparticles is strongly dependent on incident wavelength. The spectral radiance [W m^{-2} nm^{-1} sr^{-1}] from hot nanoparticles in this case is given by:

$$L_{np}(a,\lambda) \propto \epsilon(a,\lambda)\frac{2hc^2}{\lambda^5}\left(\frac{1}{e^{\frac{hc}{\lambda kT}}-1}\right) \qquad 5\text{-}2$$

Where $\epsilon(a,\lambda)$ is the emissivity of nanoparticles of radius a and is a function of wavelength, T is temperature of the nanoparticles, and h, k and c are Planks and Boltzmann constant and velocity of light respectively. The emissivity of a nanoparticle is identical to its absorption efficiency, which is equals to the ratio of absorption cross section C_{abs} to the projected area of nanoparticles, i.e.

$$\epsilon(a,\lambda) = C_{abs}/(\pi a^2) \qquad 5\text{-}3$$

The absorption efficiency can readily be calculated from the refractive index data of the nanoparticles. According to Mie theory for scattering of light from small nanoparticles

satisfying the Reyleigh criterion i.e. ($2\pi a \ll \lambda$ usually $2\pi a \ll 0.3\,\lambda$), the absorption efficiency (or emissivity) is given by:

$$\epsilon(a,\lambda) = \frac{8\pi n_m a}{\lambda} Im\left\{\frac{(n_p/n_m)^2 - 1}{(n_p/n_m)^2 + 2}\right\} \qquad 5\text{-}4$$

Where n_p and n_m are the refractive index of nanoparticle and medium respectively. It can be seen from the above equation that for particles obeying the Rayleigh criterion and with weak dependence of refractive indices on wavelength, the emissivity can be approximated as $\epsilon(a,\lambda) \propto \frac{1}{\lambda}$ and a factor of λ^6 can be introduced in Eq. 5-2. This approximation has been successfully used in determining the temperature of Ni nanoparticles produced by fs-laser ablation[17].

Figure 5-15 (a) shows the emissivity curve for a 10 nm diameter W nanoparticle in the range of 400-700 nm, Figure 5-15 (b) is the data from Ref. 18. The curve was fitted using λ^{-x} function in order to see the 1/λ dependence of emissivity, the value of *x* obtained was 1.43 which is similar to one obtained before. Clearly there is a significant deviation from the 1/λ rule for W nanoparticles.

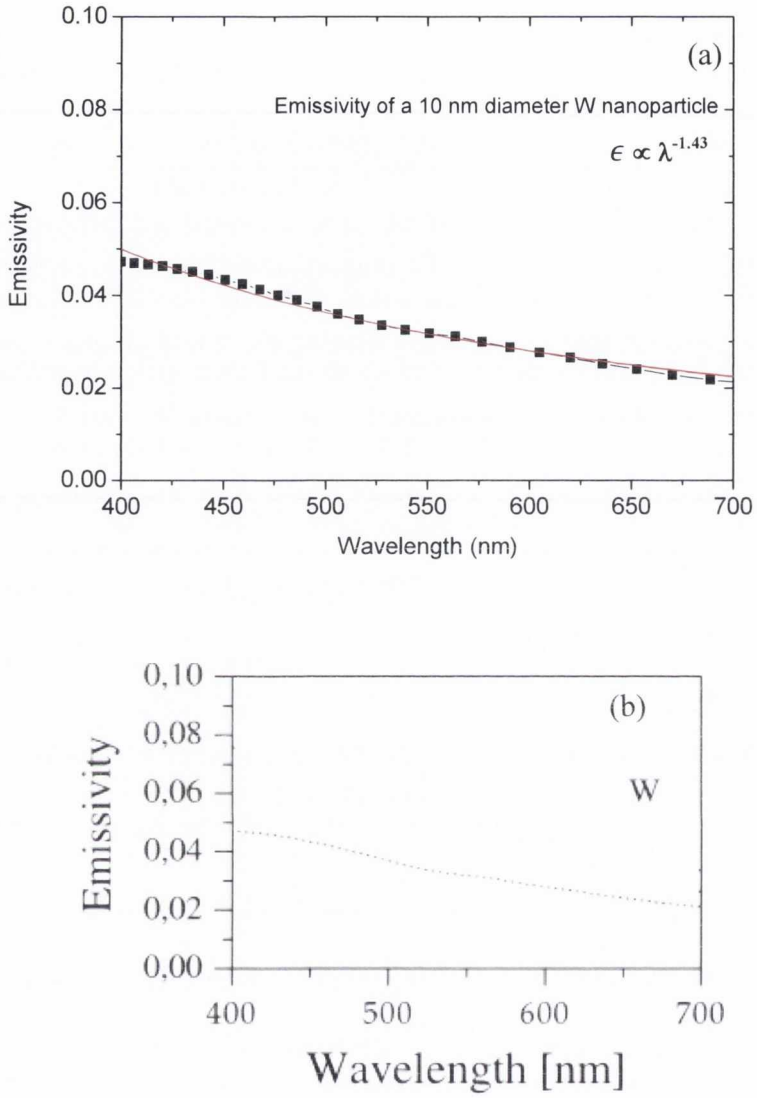

Figure 5-15 (a) Calculated emissivity for a 10 nm diameter tungsten (W) nanoparticle. (b) Emissivity curve for a 10 nm diameter W nanoparticle from Ref. 18.

The reason for this can be understood in terms of wavelength dependence of dielectric constants. Looking at Eq. 5-4 we can see that $\epsilon(a,\lambda)$ contain a $1/\lambda$ term as well as the nanoparticle and medium refractive index (n_p and n_m). Now if the dielectric contestants would be weakly dependent on the wavelength then $\epsilon(a,\lambda)$ could just be scaled as $1/\lambda$. But

from fitting the previous plot using $1/(\lambda)^x$ function we can see that there is significant deviation from this rule (i.e. $x=1.43$) which shows that there is wavelength dependence on the dielectric constants for W nanoparticles. We can expect a stronger dependence for the case of noble metal nanoparticles such as Au and Ag nanoparticles which show strong variation optical properties in the visible region of the electromagnetic spectrum. Hence it is necessary to take into account the dielectric function dependent emissivity to estimate the temperature of hot metal nanoparticles.

Figure 5-16 shows the spectral emissivity of Ni, Au and Ag nanoparticles calculated using Eq. 5-4. The emissivity of tungsten nanoparticles was also calculated in order to compare our calculation with one obtained by P. Hazsler *et al*[18]. The data for Ni and Ag in Figure 5-16 was also fitted using λ^{-x} function in order to obtain the value of x and values of 2.6 and 12 were found for both materials respectively which again show a significant deviation from the $1/\lambda$ approximation.

It can be seen from Figure 5-16 that the spectral emissivity of Au nanoparticles shows a peak around the surface plasmon resonance (SPR) position which indicates enhanced emission of Au nanoparticles at this particular wavelength. A similar peak behavior was observed for Ag nanoparticles below 400 nm at the position of its SPR wavelength (see Figure 5-17 (b)). The extinction cross-section of Ag and Au nanoparticles in Figure 5-17 was calculated using a commercial software[19] the program calculates the absorption and scattering properties of nanoparticles of different materials using the Mie extinction cross section:

$$\sigma_{ext} = \left(\frac{9\omega}{c}\right) V_o \varepsilon_o^{3/2} \left[\frac{\varepsilon_2}{(\varepsilon_1 + 2\varepsilon_o)^2 + \varepsilon_2^2}\right] \qquad 5\text{-}5$$

Where ω and c is the frequency and speed of light respectively, V_o is the volume of the

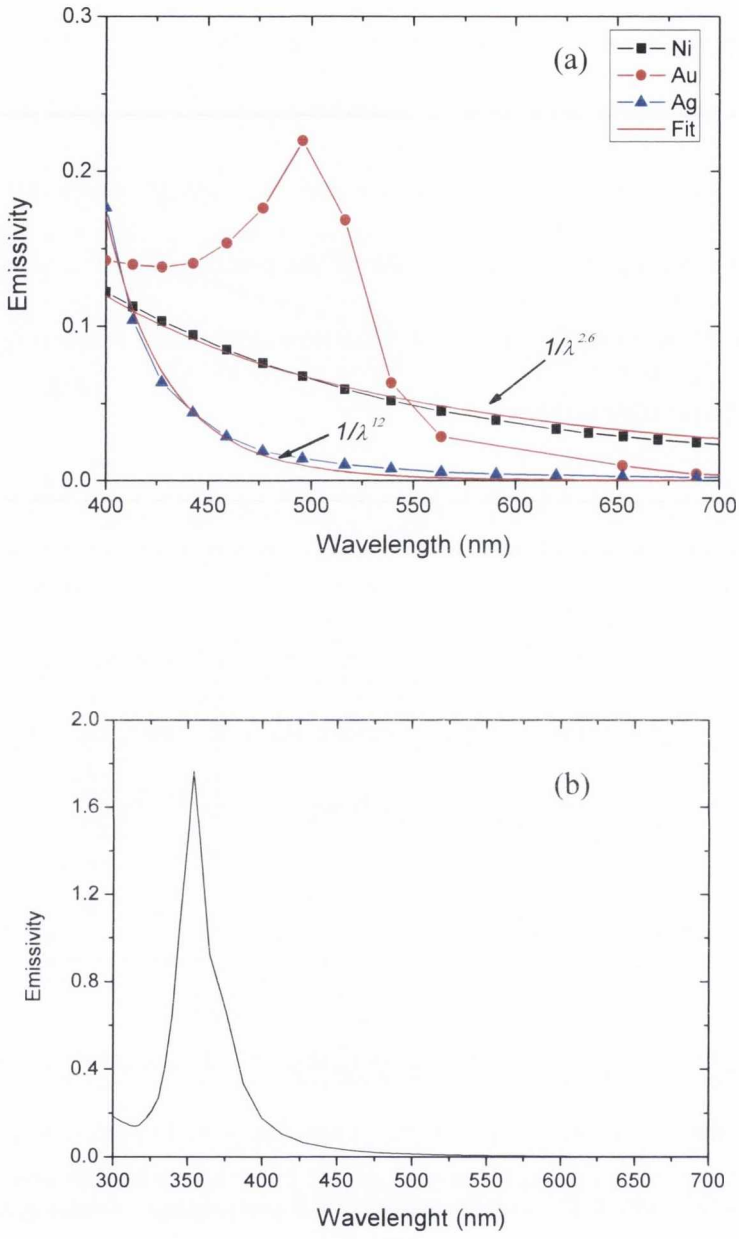

Figure 5-16 (a) Calculated spectral emissivity of Ni, Au and Ag 10 nm diameter nanoparticles in the range of 400-700 nm, the solid red line in Ni and Ag data is the fit using $1/\lambda^x$ where x is fitting constant. (b) spectral emissivity for Ag nanoparticle in the range of 300-700 nm depicting peak around SPR.

nanoparticle, ε_o is the dielectric constant of the medium and ε_1 and ε_2 are the real and imaginary parts of the dielectric function of the nanoparticle.

Figure 5-16 (a) shows that emissivity of Ni nanoparticles varies approximately like $1/\lambda^{2.6}$. However it should be noted that the theoretical emissivity of Ag nanoparticles is lower by more than a factor 10 as compared to Ni and even more as compared to Au, which explains the lower incandescence from the Ag nanoparticle ablation plume mostly in the visible region of electromagnetic spectrum in OES and ICCD imaging experiments.

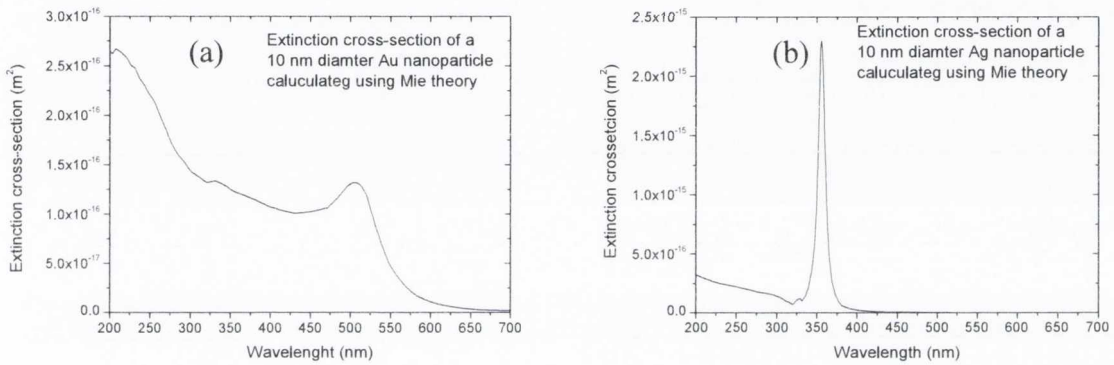

Figure 5-17 Extinction cross-section of 10 nm (a) Au and (b) Ag nanoparticles calculated using Mie theory.

For the exact measurement of temperature from the incandescence of the hot metal nanoparticles it is important to take into account the surface area of the particle, in this case the spectral power per unit wavelength [W nm^{-1}] emitted by a hot nanoparticle of radius a will be:

$$P_{np}(a,\lambda) = \epsilon(a,\lambda)\frac{2\pi hc^2}{\lambda^5}\left(\frac{1}{e^{\frac{hc}{\lambda kT}}-1}\right)4\pi a^2 \qquad 5\text{-}6$$

The above equation can also be used to derive the spectral radiance in terms of atom density

$N_{a,np}$ in the nanoparticle plume as:

$$L_{np}(a,\lambda) = \frac{12\pi hc^2}{\lambda^6} Im\left\{\frac{(n_p/n_m)^2 - 1}{(n_p/n_m)^2 + 2}\right\}\left(\frac{1}{e^{\frac{hc}{\lambda kT}} - 1}\right) N_{a,np}\frac{\ell}{N_s} \qquad 5\text{-}7$$

Where $N_{a,np}$ is the atom density in the nanoparticle layer of thickness ℓ and N_s is the solid density of the target material. We have compared the experimentally measured spectral radiance from hot nanoparticles in the fs-ablation plume with the theoretical one (Eq. 5-7) to estimate the temperature of nanoparticles. Figure 5-18 (a) and (b) shows the intensity calibrated optical emission spectra of the Ni nanoparticle ablation plume at 1 μs and 5.5 μs delay respectively.

The smooth red curves are theoretically calculated spectral radiance using Eq. 5-7. For the calculation, the thickness of the nanoparticle layer ℓ was set to 0.9 mm for 1μs delay and 2.3 mm for 5.5 μs delay (as estimated from ICCD image of nanoparticle plume). The temperature and the atom density in nanoparticle layer ($N_{a,np}$) were allowed to vary to match with the experimental data. The best fits were obtained at T= 2390 K, $N_{a,np} = 2.3\times10^{17}$ atoms cm^{-3} for 1 μs delay and at T= 2240 K, $N_{a,np} = 4.5\times10^{16}$ cm^{-3} for 5.5 μs delay.

Since we know the atom density in the nanoparticle plume, it is of also interest to compare the total number of atoms in the plume with the total ablated atoms (the atom yield) as obtained from the crater volume measurements in Ch. 4. The total atoms in the plume can be calculated if the shape or the volume of the plume is known. Considering a semi ellipsoid shaped nanoparticle plume, the volume can be calculated as $V=2/3\pi XYZ$, where XYZ are the plume radii. The approximate radii obtained from the ICCD image of Ni nanoparticle plume at 1 μs delay are 450 μm, 404 μm and 1800 μm which correspond to $V=0.6\times10^{-3}$ cm^3.

Multiplying this with the atom density ($N_{a,np}$ = 2.3×10^{17} atoms cm^{-3}) gives 1.38×10^{14} atoms in the plume.

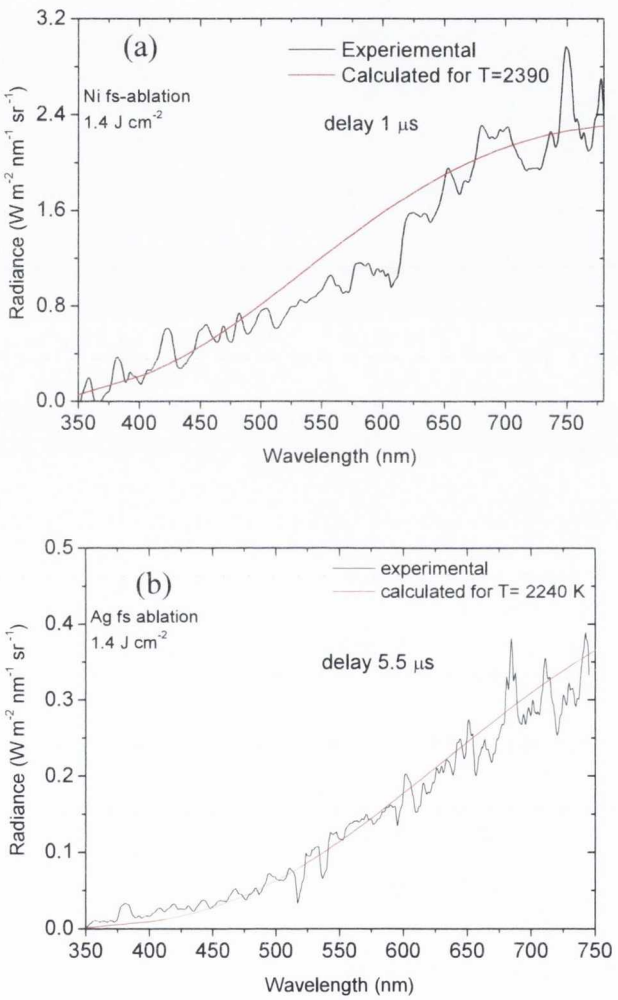

Figure 5-18 Calibrated spectra of Ni nanoparticle ablation plume at (a) 1.0 μs and (b) 5.5 μs delay with respect to the laser pulse. The smooth red curves represent the calculated data using Eq. 5-7.

The atom yield for the same peak laser fluence (1.4 J cm^{-2}) as obtained from the crater volume measurements using WLI is 1.2×10^{14}, which agrees well with the total number of

atoms in the plume. It can also be seen that the calculated initial temperature (2390 K) is also higher than the temperature obtained at a later time (2240 K at 5.5 μs) which shows cooling of nanoparticles during their vacuum expansion. A similar decrease in the temperature of Fe and Si nanoparticles was observed in other fs-laser ablation experiments[17,20]. It was suggested that the cooling rate however is not linear with the delay time which indicates that that different energy relaxation processes are involved at different stages of plume expansion such as thermionic emission and or evaporation of nanoparticles. Figure 5-19 (a) shows the

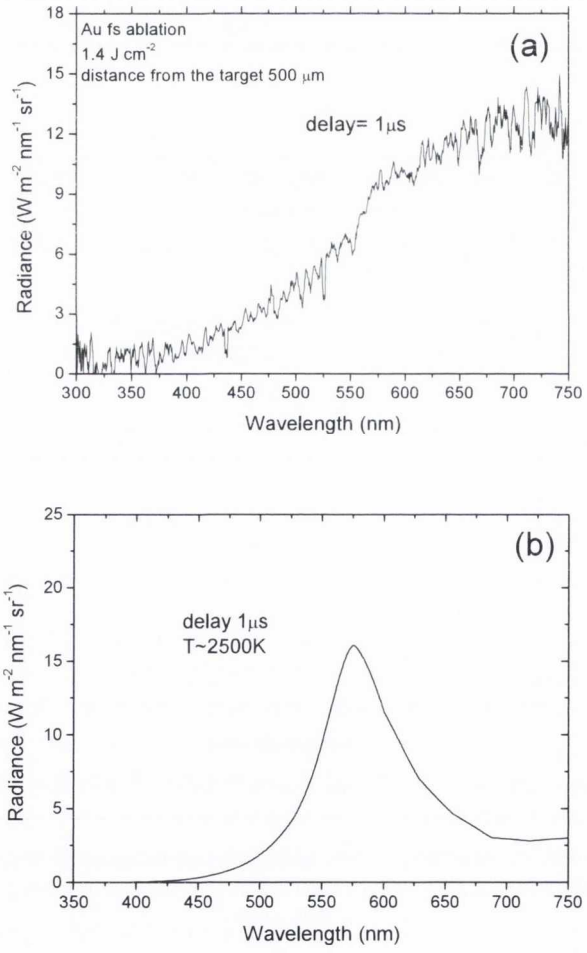

Figure 5-19 (a) Experimental and (b) theoretical optical emission spectrum for the Au nanoparticle fs-laser ablation at 1 μs delay.

intensity calibrated spectra of the Au ablation plume at 1 μs delay after the laser pulse. The spectrum in this case shows a slightly enhanced radiance around 575 nm (see Figure 5-19 (a)) and hence indicates some enhancement in the optical emission around SPR peak of Au nanoparticles. Figure 5-19 (b) shows the theoretically calculated optical emission spectra for a Au nanoparticle ablation plume calculated using ℓ=1mm, T=2500 K and $N_{a,np} = 1.0\times10^{18}$ cm^{-3}.

5.6. Conclusion

In conclusion, the fs-ablation of three metals (Ni, Ag and Au) with different thermophysical properties was studied using fast imaging and time- and space- resolved OES. For each metal, it was observed that the overall ablation plume consists of two distinct components, a fast atomic plume followed by the slow nanoparticle plume. The ICCD images taken at different time delay were used to calculate the velocities of each component. The optical emission spectra of atomic and nanoparticle plume was further subjected to spectroscopy studies and the corresponding density and temperature values were obtained.

The spectral radiance of the fs-ablation plume was observed to be less when compared to ns-ablation. Furthermore the spectral radiance of Ag nanoparticle plume was observed to be weak as compared to the other metal under similar experimental conditions. In contrast to that the plasma part of Ag ablation plume showed a strong optical emission. The weak optical emission of Ag nanoparticle plume was described in terms of spectral emissivity of Ag nanoparticles. However further spectroscopy study and theoretical calculations are required to understand the unexpected behavior of the Ag fs-ablation plume. The arrangement for the future experiment to study further the fs-ablation plume, specifically the nanoparticle emission plume is given in Ch. 8.

A commercial software called PrismSPECT was used to fit the line emission spectra from which the temperature and density of laser produced plasma was obtained. The continuum emission spectrum from slow plume was fitted using following modified Plank's blackbody relation:

$$P(a,\lambda) = \epsilon(a,\lambda)I(a,\lambda)4\pi a^2$$

Where $P(a,\lambda)$ is the spectral power emitted by a spherical nanoparticle of surface area $4\pi a^2$ (a nanoparticle radius) per unit wavelength (W nm^{-1}), $\epsilon(a,\lambda)$ is the spectral emissivity, $I(a,\lambda)$ is the spectral irradiance (W m^2 nm^{-1}). The above formula was also used to estimate nanoparticle temperature. The low nanoparticle optical emission may be understood in term of theoretical emissivity $\epsilon(a,\lambda)$ of Ag nanoparticles. Some principal findings of our experiments are given in the following table.

Table 5-4 Some of the principle findings of fs-ablation plume analysis of Ni, Ag and Au for F_p~ 1.4 j cm^{-2}

	Ni	**Ag**	**Au**
v_{np} (m s^{-1})	200 ± 6.7	160±2.5	100±2.0
v_{atomic} (km s^{-1})	10±0.1	8.0 ±0.25	4.0±0.20
Density of atomic plume (cm^{-3}) (using PrisSPECT)	5×10^{14}	2×10^{15} cm^{-3}	-
Plasma thickness (mm)	2	3	-
Plasma temperature (eV) (prismSPECT)	0.8	0.65	-
NP temperature (K) (at 1 μs delay after laser pulse)	2390	-	2500

5.7. References

1 S. Amoruso and et al., Journal of Physics B: Atomic, Molecular and Optical Physics **38** (20), L329 (2005).

2 D. Perez and J. L. Lewis, Physical Review Letters **89** (25), 255504 (2002).

3 D. S. Ivanov and and V. L. Zhigilei, Physical Review B **68** (6), 064114 (2003).

4 P. T. Mannion, S. Favre, C. Mullan, D. S. Ivanov, G. M. O' Connor, T. J. Glynn, B. Doggett, and J. G. Lunney, Journal of Physics: Conference Series **59** (1), 753 (2007).

5 J. Demsar, R. D. Averitt, K. H. Ahn, M. J. Graf, S. A. Trugman, V. V. Kabanov, J. L. Sarrao, and A. J. Taylor, Physical Review Letters **91** (2), 027401 (2003).

6 Z. Lin and L.V. Zhigilei, Physical Review B **73** (18), 184113 (2006).

7 P. B. Johnson and R. W. Christy, Physical Review B **6** (12), 4370 (1972).

8 S. Amoruso et al., Journal of Physics D: Applied Physics **40** (2), 331 (2007).

9 K. Gouriet, Proc. of SPIE 70050T (2005).

10 D.Dussault and P.Hoess, Proc. SPIE, Infrared Systems and Photoelectronic Technology(October 21) **5563** (2004).

11 J. E. Sansonetti and W.C.Martin, J. Phys. Chem. **34** (4), 1559 (2005).

12 S. Amoruso, R. Bruzzese, N. Spinelli, and R. Velotta, Journal of Physics B: Atomic, Molecular and Optical Physics **32** (14), R131 (1999).

13 www.prism-cs.com/Software/PrismSpect/PrismSPECT.htm.

14 C. Pagano, S. Hafeez, and J. G. Lunney, Journal of Physics D: Applied Physics **42** (15), 155205 (2009).

15 E. A. Rohlfing, The Journal of Chemical Physics **89** (10), 6103 (1988).

16 D. Doria, K. D. Kavanagh, J. T. Costello, and H. Luna, Measurement Science and Technology **17** (4), 670 (2006).

17 S. Amoruso, R. Bruzzese, N. Spinelli, R. Velotta, M. Vitiello, X. Wang, G. Ausanio, V. Iannotti, and L. Lanotte, Applied Physics Letters **84** (22), 4502 (2004).

18 P. Heszler, K. Elihn, L. Landström, and M. Boman, Smart Materials and Structures **11** (5), 631 (2002).

19 Philiplaven, p. software to calculate Mie extinction coeffecient.

20 G. Claes, K. Laszlo, and M. William, *Gas phase nanoparticle synthesis of nanoparticles*. (Springer, 2005).

Chapter 6 Nonlinear optical properties of metal nanoparticle films

6.1 Introduction

Materials with large third order and fast nonlinear optical response are considered as promising candidates for several optical applications such as optical telecommunication, optical data storage and digital information processing where light controlled refractive index and phase controlled modulations are required[1,2]. Together with a high nonlinear optical response, the major requirement of such material is good optical quality, low loss at desired wavelength and easy preparation procedures. In this experiment we have studied third order nonlinear optical properties of Au nanoparticle films prepared on fused quartz substrates using ns and fs-PLD, in the infrared region of electromagnetic spectrum.

6.1.1 Theory of nonlinear optics

The beginning of the field of nonlinear optics is often taken to be the discovery of second harmonic generation in 1961 by Franken *et al.*[3] shortly after the demonstration of first working laser by Miaman in 1960[4]. Nonlinear phenomena are 'nonlinear' in a sense that the response of the material system depends in a nonlinear manner on the strength of the optical field, for example, second harmonic generation occur as a result of the part of the material for which the atomic response depends quadratically on the strength of the applied optical field. The intensity of light generated at second harmonic frequency tends to increases as a square of the intensity of the applied laser light.

To understand the nonlinear optical response of materials more precisely, it is important to understand first the response of the dipole moment per unit volume or electric polarization $\boldsymbol{P}(t)$ upon the strength of the electric field $\boldsymbol{E}(t)$ of the applied optical field. In the case of conventional i.e. linear optics, the electric polarization vector is assumed to be linearly proportional to the incident electric field strength i.e.

$$\boldsymbol{P}(t) = \epsilon_0 \chi^{(1)} \boldsymbol{E}(t) \qquad 6\text{-}1$$

Where ε_0 is permittivity of free space and $\chi^{(1)}$ is the linear susceptibility of a given medium. After the demonstration of first laser device, it was found that the simple linear assumption was no longer adequate for circumstances in which an intense laser beam was incident on certain types of optical. In this case, the non-linear optical response of materials can be described in terms of a generalised relation which expresses the polarization $\boldsymbol{P}(t)$ as a power series expansion in the electric field strength $\boldsymbol{E}(t)$.

$$\boldsymbol{P}(t) = \epsilon_0(\chi^{(1)} \boldsymbol{E}(t) + \chi^{(2)} \boldsymbol{E}^2(t) + \chi^{(3)} \boldsymbol{E}^3(t)... \qquad 6\text{-}2$$

hence

$$\boldsymbol{P}(t) = \boldsymbol{P}^{(1)} + \boldsymbol{P}^{(2)} + \boldsymbol{P}^{(3)} \qquad 6\text{-}3$$

Where $\chi^{(2)}$ and $\chi^{(3)}$, and $\boldsymbol{P}^{(1)}$ and $\boldsymbol{P}^{(2)}$ are second and third order nonlinear susceptibilities and polarizations respectively. More precisely the above equation can also be written in tensor notation as:

$$P_i(\omega) = \epsilon_0(\chi_{ij}^{(1)}(\omega_m)\,\vec{E}_j(\omega_m) + \chi_{ijk}^{(2)}(\omega_m, \omega_n)\,E_j(\omega_m)E_k(\omega_n) + \quad 6\text{-}4$$

$$\chi_{ijkl}^{(3)}(\omega_m, \omega_n, \omega_o\,)E_j(\omega_m)E_k(\omega_n)E_l(\omega_o)...$$

Where *i, j, k* and *l* represent Cartesian indices, P_i is the *ith* Cartesian coordinate of the polarization. *m, n , o* denote different frequency components. Also $\boldsymbol{\chi_{ij}^{(1)}}$ is a second rank tensor (9 components *xx, xy, xz, yx, yy, yz* and so on such that $P_x=\chi_{xx}E_x$ and $P_y=\chi y_yE_y$ ...) , $\boldsymbol{\chi_{ijk}^{(2)}}$ is a third rank (nonlinear) tensor (27 components xxx, *xxy, xxz xyz,* ...) and $\boldsymbol{\chi_{ijkl}^{(3)}}$ is a third rank (nonlinear) tensor (81 components *xxxx, xxxy, xxxz, xxyx,* ....)[5]. A proper transformation of these tensor results in different nonlinear effect e.g. the term $\boldsymbol{\chi_{ijk}^{(2)}(\omega_m, \omega_n)\,E_j(\omega_m)E_k(\omega_n)}$ is responsible for all two wave effects. This include second harmonic generation (SHG) (two fields at frequency ω to create one at 2ω) sum and difference frequency generation (two fields at frequency ω_m *and* ω_n to create frequencies at $\omega_m+\omega_n$ and $\omega_m-\omega_n$). The example of SHG is also given in the next section. Though for the sake of simplicity, the tensor nature of second and third order nonlinear susceptibilities has not been used in the following discussions.

6.1.2 Second order nonlinear optical processes

Different nonlinear processes involving second order susceptibility $\chi^{(2)}$ can be understood by nonlinear polarization $P^{(2)}$, let us consider the example of second harmonic generation. For a laser beam the electric field strength is given by $E(t)=Ee^{-i\omega t}$, the second order contribution to the nonlinear polarization can be represented by[6]:

$$P^{(2)}(t) = 2\epsilon_o \chi^{(2)} EE^* + \epsilon_o \chi^{(2)} E^2 e^{-i2\omega t} \qquad 6\text{-}5$$

It can be seen that the second order polarization consists of a contribution at zero frequency and a contribution at frequency 2ω (the second term in the above equation) this contribution leads to the generation of second harmonic generation (SHG). Figure 6-1 illustrate the process of SHG, in that case two photons of frequency ω are destroyed and a photon of frequency 2ω is simultaneously created

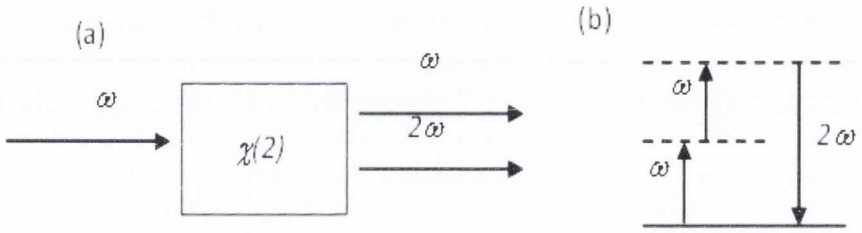

Figure 6-1 (a) Geometry and (b) energy level diagram for second harmonic generation process.

The solid line in the Figure 6-1 (b) represents the atomic ground state, and the dashed lines represent what are known as virtual levels. These levels do not correspond to the energy eigenstates of the free atom. One common use of SHG is to convert the output of a fixed-frequency laser to a different spectral region. For example, the Nd:YAG laser operates in the near infrared at a wavelength of 1.06 μm and SHG is routinely used to convert the wavelength of the radiation to 0.53 μm. However SHG can only be observed in materials with certain crystal structure called non-centrosymmetric but not in the centrosymmetric system like cubic crystal structure. The description of centrosymmetric crystal structure and reason of absence of SHG in such structures is given in the following section.

6.1.2.1 SHG in centrosymetric and non-centrosymetric crystal structures

The SHG process depends on the symmetry of the materials crystal structure. Depending on the crystallographic point groups, crystal structure can be divided into two classes, centrosymmetric and non-centrosymmetric. The centrosymmetric type is the one with inversion symmetry. In inversion symmetry, any line drawn from the origin passing through the centre of the crystal will connect to an identical feature on the opposite side. In centrosymmetric media which have inversion symmetry, the properties of the media are not changed by parity transformation $\wp$: $r(x,y,z) \rightarrow -r(-x,-y,-z)$.

For a medium with second order nonlinear optical properties, the net polarization can be represented as:

$$P_i = A_{ij} E_j + B_{ijk} E_j E_k \qquad 6\text{-}6$$

Where A and B here represents the first and the second order nonlinear susceptibilities respectively. Under the parity symmetry, the vectors are transformed as: $Pi \rightarrow -Pi$ and $Ei \rightarrow -Ei$ i.e. odd parity, because they have odd number of indices and they are polar vectors. The parity transformation applied to nonlinear coefficients as $A_{ij} \rightarrow A_{ij}$ *and* $B_{ijk} \rightarrow B_{ijk}$, It should be noted that there is no change in sign of B_{ijk} despite of odd number of indices. This is because, we literally get the same crystal back due to parity symmetry in centrosymmetric crystal, and there is no change in the material constants even in the tensor values. When the parity transformation is applied to the polarization P_i (Eq. 6-6), the original equation transforms to:

$$-P_i = -A_{ij}E_j + B_{ijk}E_jE_k \qquad 6\text{-}7$$

Which contradicts the original equation unless $B_{ijk}=0$, so the second order nonlinear coefficient term must vanish because of the transformation rule under parity.

It can also be seen from the above equation that only odd power of E_i with nonzero nonlinear coefficient e.g. the terms which are cubic in E_i are as allowed as terms which are linear in E_i under parity transformation. So the lowest order nonlinearity is third order in such crystals. This concludes that SHG cannot be observed in centrosymetric crystal structures such as cubic or face centred cubic (FCC) like Au because of inversion symmetry. Similar results were observed during investigation of Au nanoparticle films. The nanoparticle films showed strong third order nonlinear optical properties but no sign of SHG was observed in their optical transmission spectra recorded using spectrometer.

6.1.3 Third order nonlinear optical processes

We next consider third order contribution to the nonlinear polarization

$$\vec{P}^{(3)}(t) = \epsilon_o \chi^{(3)} \vec{E}(t)^3 \qquad 6\text{-}8$$

(i) Third harmonic generation

We first consider the general case in which the applied field is given by $E(t) = E_o cos(\omega t)$. By using the trigonometric identity $cos^3(\omega t) = 1/4\ cos\ (3\omega t) + 3/4\ cos\ (\omega t)$, the third order nonlinear polarization can be expressed as:

$$P^{(3)}(t) = \frac{1}{4}\epsilon_o \chi^{(3)} E_o^3 \cos(3\omega t) + \frac{3}{4}\epsilon_o \chi^{(3)} E_o^3 \cos(\omega t) \qquad 6\text{-}9$$

The first term in the above equation describes a response at frequency 3ω that is created by single frequency ω of the applied field which is called third harmonic generation.

(ii) Nonlinear refraction

For material with third order optical response, the total electric polarization at frequency ω can be written as

$$P(t) = \epsilon_o \chi^{(1)} E(t) + \frac{3\epsilon_o \chi^{(3)}}{4} E_o^2 E(t) \qquad 6\text{-}10$$

Or $$P(t) = \epsilon_o E \left(\chi^{(1)} E + \frac{3\varepsilon_o \chi^{(3)}}{4} E_o^2 \right) = \epsilon_o \chi_{eff} E \qquad 6\text{-}11$$

where $\chi_{eff} = \chi^{(1)} E + \frac{3\varepsilon_o \chi^{(3)}}{4} E_o^2$. Using relation $n^2 = (1+\chi_{eff})$, n^2 can be written as.

$$n^2 = 1 + \chi^{(1)} E(t) + \frac{3\varepsilon_o \chi^{(3)}}{4} E_o^2 \qquad 6\text{-}12$$

Since $I = \frac{1}{2}\sqrt{\frac{\epsilon}{\mu_o}} E_o^2$, the refractive index n seems to be intensity dependent and the above equation can be written as:

$$n = n_0 + n_2 I \qquad 6\text{-}13$$

Where n_o is the usual i.e. low intensity and n_2 is the intensity dependent nonlinear refractive index, taking the square of both sides of Eq. 6-10.

$$n^2 = n_o^2 + 2 n_0 n_2 I + n_2^2 I^2 \qquad 6\text{-}14$$

Neglecting the higher order last term for $n_2 << n_0$ the above equation can be written as

$$n^2 = n_o^2 + 2 n_0 n_2 I = n_o^2 + 2 n_0 n_2 \frac{1}{2}\sqrt{\frac{\epsilon}{\mu_o}} E_o^2 \qquad 6\text{-}15$$

Since

$$n^2 = 1 + \chi_{eff} = 1 + \chi^{(1)} E(t) + \frac{3\varepsilon_o \chi^{(3)}}{4} E_o^2 \qquad 6\text{-}16$$

Eq. 6-12 and 6-13 can be compared for L.H.S and R.H S

$$\frac{3\varepsilon_o \chi^{(3)}}{4} E_o^2 = n_0 n_2 \sqrt{\frac{\epsilon}{\mu_o}} E_o^2 \qquad 6\text{-}17$$

hence

$$n_2 = \frac{3\chi^{(3)}}{4n_o^2} \sqrt{\frac{\mu_o}{\varepsilon_o}} \qquad 6\text{-}18$$

One of the effects that can occur as a result of an intensity dependent refractive index is self-focusing of light, this effect is also known as Kerr lensing. This process can occur when a beam of light having non uniform transverse intensity (a Gaussian beam) propagates through a material for which n_2 is positive. Under these conditions, the material effectively acts as a positive lens, which causes the rays to curve toward each other. The beam intensity at focal spot can be sufficiently large in this case to cause optical damage of the medium. Figure 6-2 is an illustration of self-focusing of light in nonlinear medium.

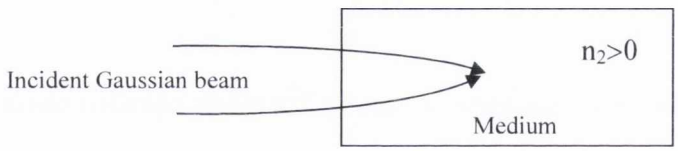

Figure 6-2 Self focusing of light in medium with positive value of intensity dependent refractive index (n2).

(iii) Nonlinear absorption (NLA)

Nonlinear optical effects can also cause materials that are strongly absorbing at low laser light intensities to become transparent at high intensities, a phenomenon known as *saturable absorption* or they can cause materials that are transparent at low intensities to become absorbing at high intensities in an effect termed *multiphoton absorption* or

reverse saturable absorption. The multi-photon absorption can occur through absorption of two, three or more photons. The photons can be of same or different frequencies. When the frequencies are different the effect is termed sum frequency absorption. The dependence of absorption coefficient on laser intensity for materials showing saturable absorption is given by the expression

$$\alpha = \frac{\alpha_o}{1 + I/I_s} \qquad 6\text{-}19$$

Where α_0 is the low intensity absorption coefficient and I_s is the saturation intensity, and for the materials showing multiphoton or reverse saturable absorption, the absorption coefficient is given by

$$\alpha = \alpha_o + \beta I \qquad 6\text{-}20$$

where β is the multiphoton absorption coefficient.

6.2 Z-scan technique

Z-scan technique has now been accepted as a standard method for determining the nonlinear change in refractive index and optical absorption coefficient mainly because the method is quite simple, and in most experiments the change in refractive index and absorption can be obtained directly from the experimental data without using a computer fit.

In Z-scan the transmission through the sample is measured as the sample move along the direction of propagation of a focused Gaussian laser beam. Two different transmission measurements can be performed, *closed aperture* and the *open aperture* Z-scan. In the standard *closed aperture* scan the transmission through the sample is measured as a function of position *Z*. The required scan range for an experiment depends on the sample

length *(L)* and laser beam parameters. A critical parameter is the diffraction length Z_0 of the focused laser beam defined as ($Z_0 = \pi\omega_0^2/\lambda$) for a Gaussian beam where w_0 is the focal spot size (half width at the $1/e^2$ of maximum irradiance). For thin samples $(L << Z_0)$ it is preferable to scan in the range of $\pm 5Z_0$[7]. The position of the aperture is rather arbitrary as long as its distance from the aperture is $d >> Z_0$, however typical values range from $20\ Z_0$ to $100\ Z_0$. The size of the aperture is signified by its transmittance S in linear regime, i.e. when the sample is far away from the focus. In most reported experiments $0.1<S<0.5$ has been used for determining the value of nonlinear refractive index. $S=1$ represents 100 % transmission i.e. *open aperture* scan, and is suitable for measuring the value of the NLA coefficient of the sample. Figure 6-3 shows the experimental setup which we have used in this experiment. BS is the beam splitter and D1 and D2 are two detectors (photodiodes). D1 is the reference detector which takes into account the fluctuation of the laser power and D2 is the probe detector, A description of both closed and open aperture scans which can be performed using this setup is given below.

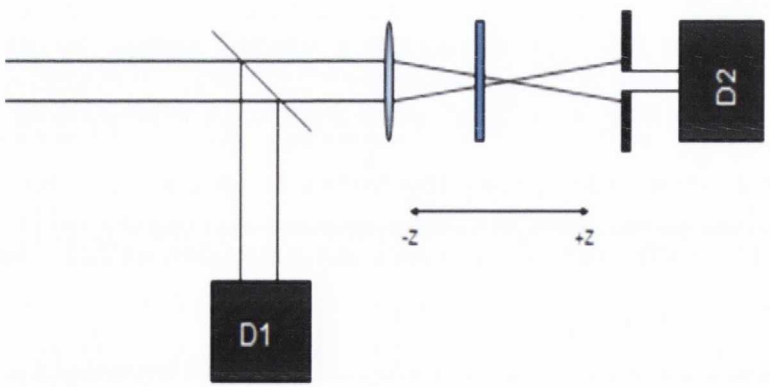

Figure 6-3 Optical setup for Z-scan measurement, D1 and D2 are detectors

During a closed aperture scan, the aperture in front of the detector D2 makes the measurement sensitive to the laser beam spreading and focusing when a sample

displaying non-linear refraction will act as lens of variable focal length. An example of this is as following: Consider a sample with negative value of nonlinear refractive index; the sample will appear to have a negligible non-linear refraction because of the low intensity of laser beam at this position. The sample starts acting as a negative lens as it moves towards the focus, collimating the beam and shifting the beam waist of the Gaussian beam, the result is the smaller spot size at the aperture and higher transmittance (See Figure 6-4 (a)). This effect increases as the sample moves towards the focus. A maximum transmittance occurs when the sample is just in front of the focus. This maximum transmittance (peak) will drop to a minimum (valley) as the sample moves away from the sample and beam diverges as a result of negative lensing of the sample. The transmittance becomes linear again when the sample moves further away from the focus. The inverse happens for a sample with positive value of non-linear index of refraction, and the graph is inverted (see Figure 6-4 (b)). It should be noted that in some cases the nonlinear absorption is present in conjunction with nonlinear refraction. In order to get the information about non-linear absorption coefficient, it is necessary to perform a scan with the aperture removed. In this case the, the z scan shows a valley or a peak (depends upon the kind of non-linear absorption).

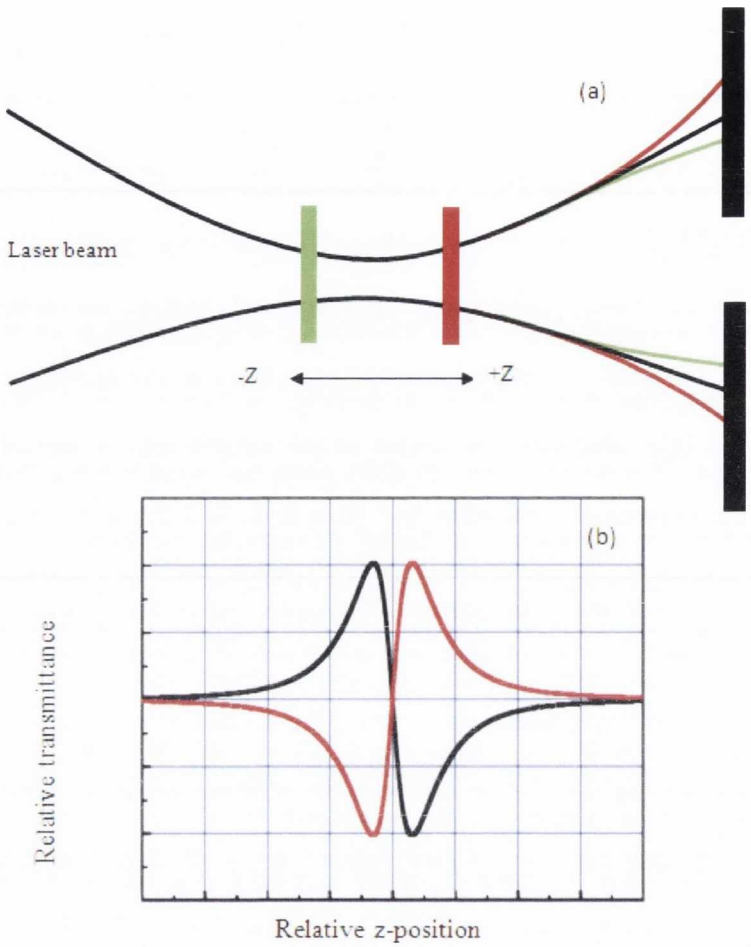

Figure 6-4 (a) Illustration of influence of a sample having negative non-linear index on Gaussian beam spot size. Black line represents the un-attenuated Gaussian beam profile, green line is for sample before the beam focus and red is for sample after the focus position. (b) Theoratical plot of a closed aperture z-scan, the black curve is for a sample with a negative value of non-linear refractive index and the red curve is for a sample with a positive value of refractive index.

The open aperture z-scan is used to extract the value of nonlinear absorption coefficient. The Non-linear index of refraction in this case can be obtained by dividing the closed aperture scan with corresponding open aperture scan. The theoretical curves for both a open and a closed aperture scan for such sample and the corresponding divide are given in Figure 6-5.

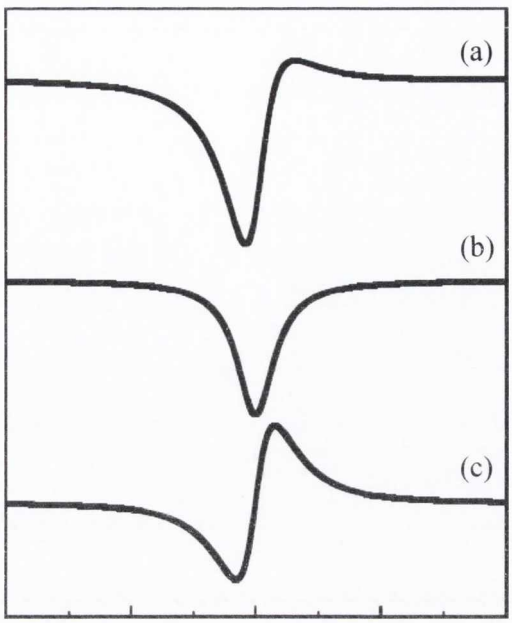

Figure 6-5 (a) close aperture scan (b) open aperture scan and (c) the resulted divide scan.

6.2.1 Measurement of nonlinear absorption coefficient and refractive index from z scan.

For a pulse of Gaussian temporal profile laser beam the effective nonlinear absorption coefficient can be obtained from the normalized transmittance for the *open aperture* z-scan by the following relation[8]

$$T(Z,S=1) = 1 - \frac{\beta I_o L_{eff}}{2\sqrt{2}\left(1+\frac{z^2}{z_o^2}\right)} \qquad 6\text{-}21$$

Where

$$L_{eff} = \frac{(1-\exp(-\alpha L))}{\alpha} \qquad 6\text{-}22$$

In the above equations, T is the sample transmittance, β *(m* W^{-1}*)* is the effective nonlinear absorption coefficient, L_{eff} is the effective thickness of the film, α is the linear absorption

coefficient, $Z_0 = \pi\omega_0^2/\lambda$ is the diffraction length and L is the actual (or equivalent) thickness of thin film. The relationship between the imaginary part of $\chi^{(3)}$ and β is as follows:

$$Im(\chi^3)(esu) = \frac{\beta c^2 n_0^2}{120\pi^2\omega} mW^{-1} \qquad 6\text{-}23$$

Where *esu* stands for electrostatic units. The normalized transmittance in the *closed-aperture* case can be approximated as:

$$T(Z) \approx 1 + \frac{4\Delta\phi_0 x}{(9+x^2)(1+x^2)} \qquad 6\text{-}24$$

And the transmission difference between peak-to-valley is given by

$$\Delta T_{p-t} = 0.406\,(1-S)^{0.25}\,|\Delta\phi_0| \qquad 6\text{-}25$$

$\Delta\phi_0$ in the above equations is the on-axis phase change at the focus caused by the third-order non-linearity[8], $x=z/z_0$. The nonlinear optical refractive index n_2 (m^2W^{-1}) can be calculated using the equations $\Delta\varphi_0 = kn_2I_0L_{eff}$ where $I_o = 2P/\pi\omega_0^2$ is the peak intensity of pulsed Gaussian laser beam. The value of $\Delta\varphi_0$ was calculated from the experimental data. The real part of $\chi^{(3)}$ was obtained using following equation.

$$Re(\chi^3)(esu) = \frac{cn_0^2 n_2^2}{120\pi^2} mW^{-1} \qquad 6\text{-}26$$

Where n_o is the linear refractive index.

6.3 Experimental details

In order to obtain the value of the third order nonlinear suscaptability, $\chi^{(3)}$, of Au nanoparticle films in the infrared region of the electromagnetic spectrum, a

synchronously-pumped optical parametric oscillator pumped with the solid state Ti-sapphire pulsed laser (130 fs, 76 MHz, 1480 nm) was used. A set of neutral density filter was used to reduce the laser output energy. Au films with different equivalent thicknesses (< 10 nm range) were deposited on 5mm×5mm×1mm quartz substrate and SiO_2 TEM grid for microscopy analysis using ns and fs PLD. The optical absorption of metal nanoparticle films in the wavelength range of 200-1700 nm was recorded using a UV/Vis/NIR double beam spectrophotometer. The linear absorption coefficient (α_0) was calculated using following equation.

$$\alpha_o = \frac{A}{t} \qquad 6\text{-}27$$

where A is the absorbance of the nanoparticle film at a particular wavelength λ, and t is the thickness of the nanoparticle film. The Gaussian beam waist ω_o at focus was measured to be 55 μm by imaging the beam on to the CCD camera[†]. Prior to study, the Au nanoparticle films, the measurement system was tested using a C_{60} sample as a reference sample. A 0.64 mM C_{60}–toluene solution was prepared similar to the concentration described in Ref.9. For Z-scan measurements the solution was placed in a 1 mm path length quartz cuvette. The value of nonlinear absorption coefficient for C_{60} was found to be β=1.6×10^{-9} cmW^{-1} at 1480 nm wavelength. Figure 6-6 (a) shows the open aperture Z-scan curves of C_{60} solution obtained by S. Couris *et al.*[9] at for laser intensity of 354 MW cm^{-2} and laser wavelength of 520 nm, Figure 6-6 (b) shows the data obtained for similar concentration solution at ~300 MW cm^{-2} . Both the curves in Figure 6-6 show reverse saturable absorption (RSA) behaviour and reveal optical limiting properties of C_{60} solution and also show that the optical properties of this material does not change much

[†] Coherent Laser Cam HR, digital USB CMOS camera.(P.No 1098577)

with wavelength. The value of absorption coefficient found by S. Couris *et al.* for 354 MW cm^{-2} and 520 nm is 6.28×10^{-9} cmW^{-1} which is higher as compared to one obtained at 1480 nm which could be due to higher laser intensity in their case.

Both open and closed aperture Z scan methods were used to obtain the value of NL refractive index and absorption coefficient for Au nanoparticle films. The closed aperture scan was divided by corresponding open aperture scan for each sample in order to eliminate the effect of nonlinear absorption from closed aperture data.

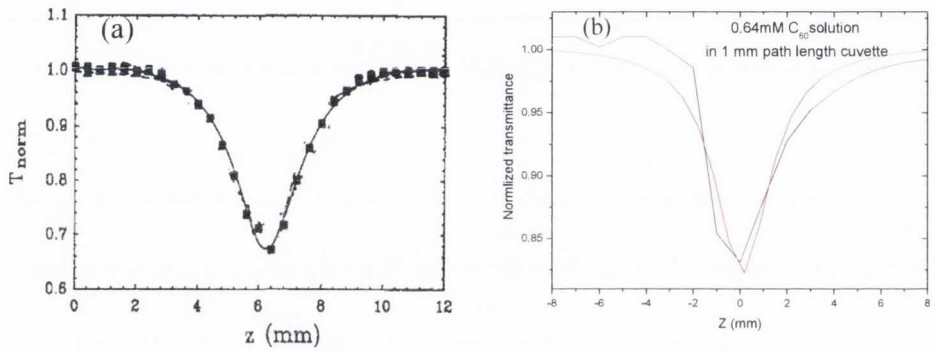

Figure 6-6 (a) Open aperture Z-scan for C_{60} solution from Ref. 9 at laser intensity of 354 MW cm^{-2} at 520 nm, the solid curve is the best fit to the experimental data. (b) Open aperture Z-scan curve of a 0.64mM C_{60}-toulene solution at incident laser intensity of 300 MW cm^{-2} at 1480 nm. The red curve is the best fit to the experimental data.

6.4 Results and discussion

Au nanoparticle films with 1, 3, 5 and 7 nm equivalent thickness were studied for this experiment. We found that not all the films show third order nonlinearity, the best results were found for 5 nm thick Au nanoparticle films prepared using ns-PLD and for 7 nm thick film prepared using fs-PLD, the Z-scan curves obtained for other thicknesses were not consistent from scan to scan and hence data from those films has not been included here. Figure 6-7 is the optical absorption spectra of 5nm thick ns-PLD and 7nm thick fs-PLD Au nanoparticle films in the wavelength range of 250 nm to 1800 nm, the linear

absorption coefficient was calculated from the absorption spectra. Figure 6-8 is the scanning transmission micrographs (STEM) of Au films equivalent thickness of 5 and 7 nm prepared using ns and fs-PLD respectively, STEM shows that both the films are nanostrctured, the film prepared using ns-PLD shows a more percolated structure similar to the initial phase structure of metal thin film growth[10], while the fs-PLD film show very small Au nanoparticles with diameter in the range of 2-8 nm.

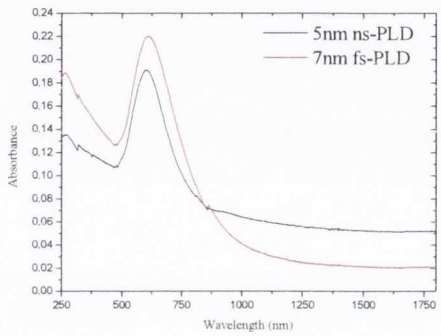

Figure 6-7 Optical absorption spectra of 5nm ns-PLD and 7nm fs-PLD Au nanoparticle films.

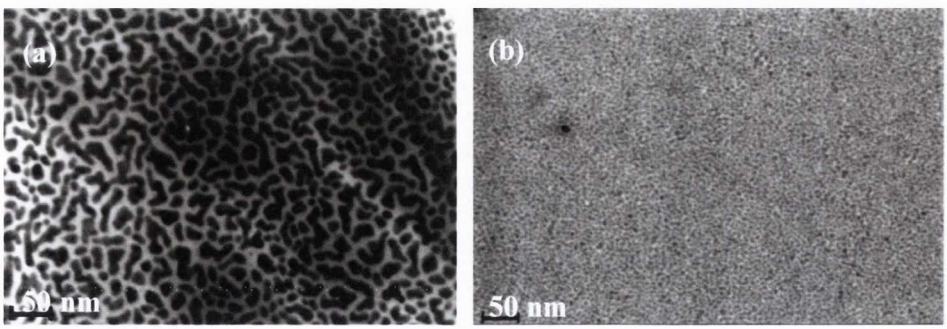

Figure 6-8 STEM of (a) 5nm ns-PLD and (b) 7nm fs-PLD Au thin films

Figure 6-9 is the open and the closed aperture Z-scans for the 5 nm and 7 nm thick Au nanoparticle films prepared using ns- and fs-PLD. The closed aperture scan show a pre-focal transmission peak, followed by transmission valley which reveals the negative sign of Re χ^3 which corresponds to negative lensing.

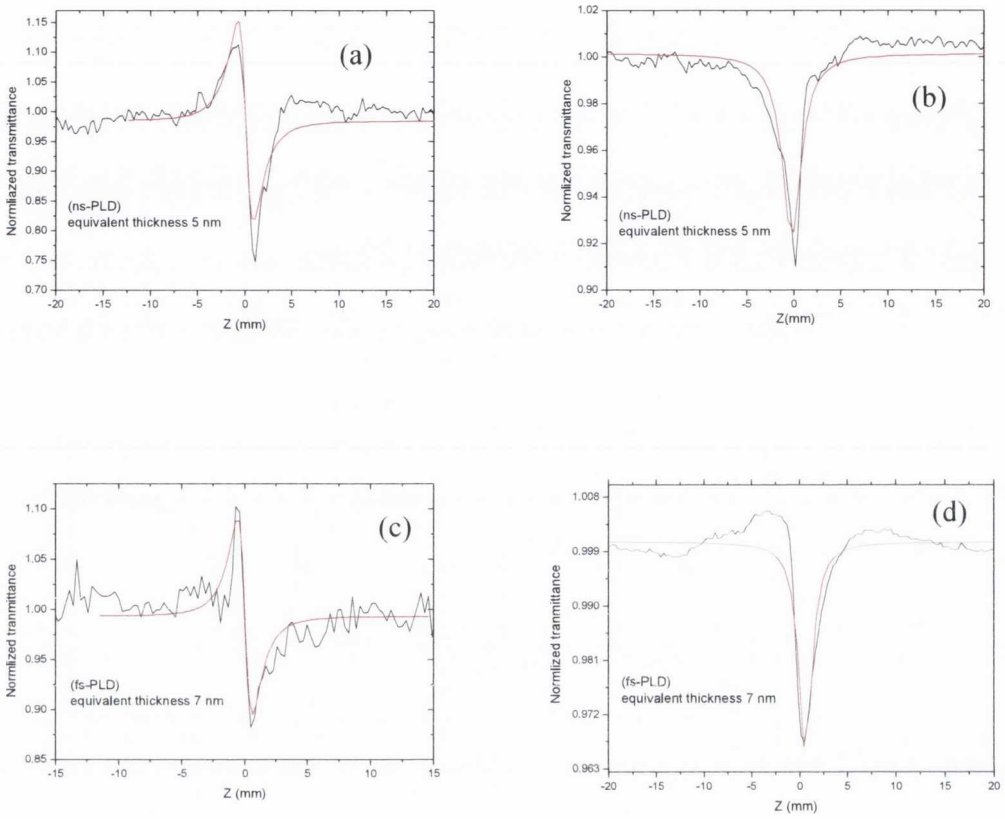

Figure 6-9 Z-scan measured curves for (a,b) 5 nm thick, Au nanoparticle film prepared using ns-PLD and (c,d) 7 nm thick, Au nanoparticle film prepared using fs-PLD. The nonlinear refractive index and absorption coefficient was obtained from the curves (a,c) and (b,d) respectively, the solid red line is the theoretical fit to the experimental data. The peak laser intensity in this case is 8×10^{7} W cm^{-2}.

The open aperture Z-scan trace for both films is found to exhibit a transmission valley, suggesting the RSA effect and hence reveal the optical limiting property of Au nanoparticle films. The RSA behaviour suggests a positive value of nonlinear absorption coefficient β and Im χ^{3}.

The plain quartz substrates were also studied for nonlinear effects under same experimental conditions. Figure 6-10 are the Z scan curves for a fused quartz substrate, the open and closed aperture scans are nearly flat and the signal strength for substrates is

< 5 % as compared to the signal for Au coated substrates, which suggest that the nonlinear effect produced by the substrate can be neglected.

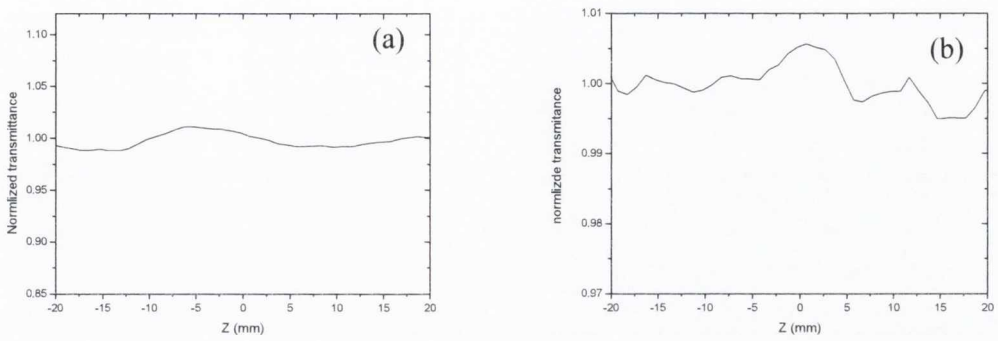

Figure 6-10 (a) Close and (b) open aperture scan of quartz substrates at peak laser intensity of 8×10^{7} W cm^{-2}.

Table 6-1 represents the values of nonlinear refractive index, absorption coefficient and corresponding values of real and imaginary part of third order nonlinear susceptibilities for 5 nm thick ns-PLD and 7nm thick fs-PLD film.

Table 6-1 Values of nonlinear refractive index, absorption coefficient and corresponding values of real and imaginary part of $\chi^{(3)}$ for Au nanoparticle films.

	5 nm ns-PLD	**7 nm fs-PLD**
β (m W^{-1})	4.3×10^{-5}	1.8×10^{-5}
n_2 (m^2 W^{-1})	4.2×10^{-11}	7.4×10^{-11}
$\chi^{(3)}_{(real)}$ (esu)	-1.9×10^{-4}	-1.1×10^{-4}
$\chi^{(3)}_{(imaginary)}$ (esu)	6.9×10^{-6}	2.9×10^{-6}

It should be noted that both Au nanoparticle films show a positive value of nonlinear absorption coefficient which represent RSA and hence an optical limiting effect from the nanoparticle Au films. Au based nanomaterials i.e. nanoparticle suspensions and embedded thin films have already been studied for the optical limiting mechanism. However, only a limited literature is available about the investigation of third order nonlinear optical properties of Au based nanomaterials in the infrared region of electromagnetic spectrum. F.Cui *et al.*[11] have observed the negative lensing effect for Au and TiO_2 composite thin films using a picosecond excitation laser with a negligible amount of nonlinear absorption and Re(χ^3) of the order of 10^{-6} esu. Handry *et al.*[12] observed an optical limiting effect for Au nanorods for 800 nm and 220 fs laser pulses. In their study, they also found that this RSA has a power density dependence, for power density above ~ 1 GW/cm^2 the nanorod aggregate shows a strong optical limiting effect or RSA. Several different mechanisms have been proposed for the nonlinear optical response for Au based nanomaterials. The review article by J. Wang and W. J. Blau[13] gives a summary of the possible mechanisms involved for Au based nanomaterials and the most common mechanism involved in ultrashort pulse excitation of Au nanoparticle is heating and vaporization of nanoparticles and scattering of light from vaporised material. In order to confirm if this is the case in our experiment, we calculated the initial rise in temperature of the nanoparticle when they absorb energy from the fs-laser pulse. The change in temperature of nanoparticle w.r.t to the ambient temp (300 K) can be related to the energy absorbed by the particle through the relation:

$$\Delta T_{np} = \frac{E_a}{m_{np}\, c_p} \qquad 6\text{-}28$$

where E_a is the energy absorbed by the nanoparticle, m_{np} is the mass of nanoparticle and c_p is the specific heat capacity of solid Au. The energy absorbed by the nanoparticle

can be written in terms of its absorption cross section and the peak laser fluence as $E_a = F_p\, \sigma_{abs}$, where F_p is the peak laser fluence and σ_{abs} is the optical absorption cross section, rewriting the equation for ΔT_{np}

$$\Delta T_{np} = \frac{F_p\, \sigma_{abs}}{m_{np}\, c_p} \qquad 6\text{-}29$$

The absorption cross section of a nanoparticle is given by:

$$\sigma_{abs} = \epsilon \times \pi r^2 \qquad 6\text{-}30$$

where ϵ is the absorption efficiency (as explained in Ch. 5, Eq. 5-3) and πr^2 is the projected area of the nanoparticle. The absorption efficiency of a 10 nm diameter Au nanoparticle for λ=1480 nm was calculated to be $\epsilon = 3.33 \times 10^{-4}$ and the projected area is $7.85 \times 10^{-13} cm^2$, which gives the value of absorption cross section for a 10 nm Au nanoparticle as:

$$\sigma_{abs} = 2.61 \times 10^{-16} cm^2$$

The peak laser fluence for a pulsed Gaussian beam can be calculated using the relation$F_p = 2E_p/\pi\omega_o^2$, where E_p is the energy per pulse and ω_o is the Gaussian beam waist. The energy per pulse E_p in our case is 150 nJ and ω_o is 55 μm which gives $F_p = 26\ mJ/cm^2$.

Substituting the values of F_p , σ_{abs} and the value of specific heat capacity, c_p=0.129 J g^{-1} K^{-1} [14] into equation Eq. 6-26, we obtained:

$$\Delta T_{np} = 5.2\ K$$

Hence, heating and vaporization of nanoparticles does not seem to occur in our experiments, and some more assumptions and explanations are required to explain the

cause of nonlinear optical response of Au nanoparticle films in the infrared region of electromagnetic spectrum. We also investigated third harmonic generation from Au nanoparticle films by studying the spectra[‡] of only emitted radiation from the sample (see Figure 6-11). The sample was placed at the focal point of the focusing lens and the output was observed at different input laser intensities ranging from 10^4 - 10^8 W cm^{-2}.

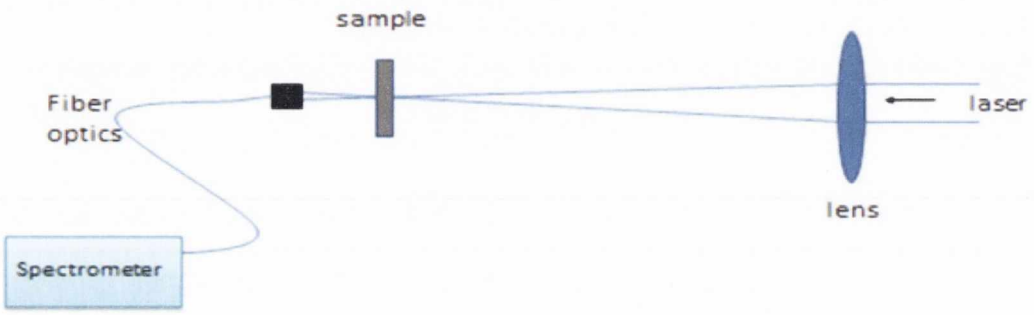

Figure 6-11 Optical setup for the investigation of third harmonic generation from Au nanoparticle films.

The sample was also moved a few microns back and forth in the direction of laser to change the intensity. We did not observe any 3ω from the nanoparticle sample for this experiment. We also studied the sample in the dark room to observe the light at the output of the sample but no green light emission was observed in this case as well. One of the reasons could be that the emitted photons are below the detection limit. According to an estimate, the human eye can detect as low as 2.35×10^{-18} J of green light. The energy of a single green light photon can be calculated as $E = h\nu$ where h is the Planks constant, ν is frequency of light and is given by $\nu = c/\lambda$ where λ is the wavelength. So the energy E can be written as $E = hc/\lambda$, hence we can find the energy in one photon at that wavelength as:

[‡] The spectrum from Au nanoparticle was recorded by an Ocean Optics Spectra suit HR2000 spectrometer.

$$E = (6.62\times10^{-34} \times 3\times10^{8})/(493\times10^{-9}) = 4.06\times10^{-19}\ J$$

Dividing the minimum amount of energy detected by human eye by the energy of one photon gives:

$$2.35\times10^{-18}/4.06\times10^{-19} \cong 6$$

Which is the minimum photon emission required to be detected.

6.5 Conclusion

In conclusion, third nonlinear optical properties of Au nanoparticle films prepared by ns- and fs-PLD were studied. In the beginning, a detailed theoretical description of second and third order nonlinear optical effects including second harmonic generation, optical Kerr effect, and third harmonic generation was given. A brief explanation of second harmonic generation of centrosymmetric and non-centrosymmetric lattice structure was also given.

Our experimental results show that both, ns- and fs-PLD films show negative value of nonlinear susceptibility and optical limiting effect. No third harmonic generation was observed in their optical transmission spectra. Regarding SHG, since the material of interest (Au) has centrosymmetric lattice structure, no SHG can be observed in such materials. From the temperature calculations it was shown that the nonlinear effects are not related to the increase in temperature of nanoparticle. Also It would be advantageous to study composite films such as Au-$BaTiO_3$ prepared by both PLD methods, since such materials have shown to be more appropriate for higher order nonlinear optical properties[15].

6.6 References

1 D. Cotter, R. J. Manning, K. J. Blow, A. D. Ellis, A. E. Kelly, D. Nesset, I. D. Phillips, A. J. Poustie, and D. C. Rogers, Science **286** (5444), 1523 (1999).

2 U. Kreibig and M. Volmer, *Optical properties of metal clusters*. (Springer, 1995).

3 P. A. Franken, A. E. Hill, C. W. Peters, and G. Weinreich, Physical Review Letters **7** (4), 118 (1961).

4 T. H. Maiman, Nature **187** (4736), 493 (1960).

5 K. Semwal and S. C. Bhatt, International Journal of Optics and Applications **2** (3), 20 (2012).

6 R. W. Boyd, *Nonlinear optics*. (Academic Press, San Diego, CA, 2003).

7 M. G. Kuzyk and C. W. Dirk, (Marcel Dekker, Inc, 1998).

8 M. Said, T. H. Wei, D. J. Hagan, and E. W. V. Stryland, IEEE Journal of Quantum Electronics **26** (4) (1990).

9 S. Couris, E. Koudoumas, and A. A. Rutht and S. Leach, J. Phys. B, At. Mol. Opt. Phys **28**, 45374554 (1995).

10 Y. Li and T. R. Yang, The Journal of Physical Chemistry C **111** (29), 11086 (2007).

11 F. Cui et al, J. Opt. Soc. Am. B **26** (1), 107 (2009).

12 I. H. Elim, J. Yang, J. Lee, J. Mi, and W. Ji, Applied Physics Letters **88** (8), 083107 (2006).

13 J. Wang and W. J. Blau, Journal of Optics A: Pure and Applied Optics **11** (2), 024001 (2009).

14 L. R. David, *CRC Handbook of chemistry and physics* (Taylor & Francis, 2008).

15 C. Cong, N. Tingyin, Z. Yueliang, Z. Dongxiang, W. Pei, M. Hai, and Y. Guozhen, Journal of Physics D: Applied Physics **41** (22), 225301 (2008).

Chapter 7 Applications of metal nanoparticle films prepared using PLD

7.1 Introduction

Nanoparticle films of some noble and transition metals are of potential interest due to the exploitation of their optical properties in fields such as surface enhanced spectroscopy (SERS). The catalytic properties of metal nanoparticle films are also of great interest in catalytic carbon nanotube (CNT) growth. In this chapter we present the experimental results of some of these applications of metal nanoparticle films. In the first experiment SERS activity was studied using a silver nanoparticle film prepared on glass substrates using PLD. The SERS performance of PLD prepared films was compared with that of commercial metal nanostructured substrates and silver colloidal nanoparticles in solution. Section 7.2 provides the experimental results of this experiment.

Supported transition metal nanoparticles like Ni and Co deposited on alumina or silica substrates are of special interest for catalytic growth of CNT using chemical vapor deposition[1]. Some practical applications of CNT require high quality single walled CNT synthesis on a large scale. It is possible to gain control on the types of the nanotube growth by controlling various parameters in CVD, including size and distribution of nanoparticles used for catalysis. In our second experiment, we have used Ni nanoparticle films with different equivalent thicknesses prepared using ns and fs-PLD for the catalytic growth of carbon nanotubes. The nanoparticle films were characterized by atomic force microscopy. The experimental results of this experiment have been given in section 7.3

Metal alloys with eutectic composition are key enabling materials for nanotechnology. The alloys are composed of two or more materials with a eutectic composition, such that the alloy melts at a common temperature which is much lower than the melting point of its ingredients. Conversely when a eutectic alloy solidifies it does so at a common or single temperature.

The metal-semiconductor alloy of gold and germanium show deep eutectic above 350 C^0. Figure 7-1 is the phase diagram of the Au-Ge system. The intersection of eutectic temperature and composition is known as the eutectic point. It can be seen from the phase diagram that Au-Ge system have deep eutectic at 361 C^o where the atomic percentage of germanium is 27 %. At this temperature the material can melt and recrystallize although this temperature is much lower then the meting point of both Au and Ge (1064 C^o for Au and 938 C^o for Ge). The low temperature crystallization of an amorphous semiconductor in the presence of a metal is well known as metal enhanced crystallization of semiconductors. This behavior in the Au-Ge alloy is vary applicable in e.g. crystallization of amorphous semiconductor (a-Si)[†2] and metal (Au) nanowire fabrication[3]. For metal nanowire fabrication, the bilayer of Au and Ge deposited on a single crystal Si substrate is heated above the eutectic temperature to obtain the eutectic liquid of Au and Ge, the eutectic liquid opens up a diffusion path way for both materials. Because of the difference in the surface energy of both materials, the higher surface energy material (Au) extrudes as a single crystal Au nanowire. In this experiment a few nanometer thick Au-Ge multilayers were fabricated using ns-PLD and sputter deposition. The surface morphologies of Au-Ge bilayers and individual Au and Ge thin films were studied using TEM. The thin films were annealed to

[†] a-Si is non-crystalline form of silicon. In Si the atoms are tetraherdrally bounded to 4-niegbouring Si atoms. In crystalline Si (c-Si) this tetrahedral structure continues over a large range, thus forming a well-ordered crystal lattice. In a-Si, this long range order is not present. Rather, the atoms form a continuous random network.

achieve eutectic temperature and nanostructure growth. Section 7.4 provides the experimental procedure and results of this experiment.

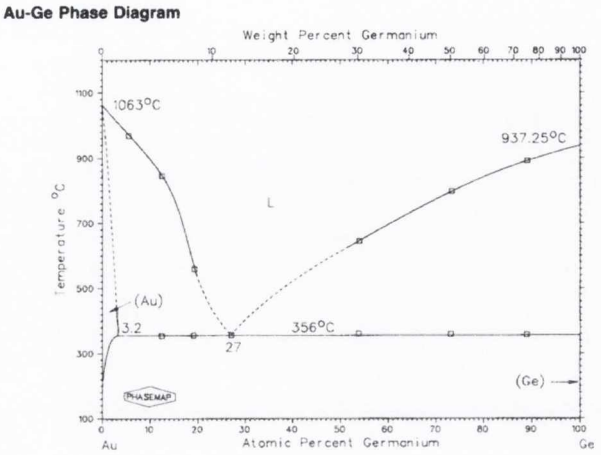

Figure 7-1 Au-Ge phase diagram from Ref. 4

7.2 Experiment 1: Silver nanoparticle films for SERS application

Surface enhanced Raman spectroscopy is a general technique with a wide range of application in fields such as bioscience, solid state physics, analytic chemistry and pharmaceutical studies. Since the discovery of SERS in the latter half of the 1970s, there has been a lot of effort and focus in terms of explaining its origins, maximising its applicability for different chemical analysis and enhancing its scattering efficiency by factor as high as 10^{10} [5]. However its progress has often been hampered with issues regarding reproducibility. The enhancement in the Raman signal is thought to be due to two main mechanisms. One of them is plasmonic enhancement of the incident radiation intensity in the neighbourhood of nanoscale features on the surface, and the other is due to chemical enhancements arising from adsorption of the target material on the nanostructured metal substrate[6]. The chemical

enhancement involves a charge transfer mechanism in which there can be an indirect coupling or charge transfer between molecule and metal surface. However in both cases metallic nanostructure substrates, such as Ag nanoparticles supported on a solid substrate like glass, provide a reasonably good solution for Raman signal enhancement.

Nanostructured Ag substrates prepared using ns-PLD in a background gas have proven to be a promising candidate for SERS[7], and have previously performed well in comparison with commercial substrates[8]. Raman enhancement can also be obtained by using colloidal particles in solution, where their nanoscale dimensions lead to the excitation of localised plasmon oscillations. In this work we use Rhodamine 6G, a dye commonly used in SERS characterisation studies, to investigate the relative SERS sensitivity of Ag nanoparticle film prepared by ns-PLD, a solution of silver colloids and a commercial substrate. Statistical analysis was used to quantify the SERS performance of each of the three approaches.

7.2.1 Experimental procedure

PLD of Ag nanoparticle films and preparation of colloidal nanoparticle synthesis: The Ag films were deposited on thin microscope glass slides and SiO_2 coated transmission electron microscopy (TEM) grids both placed 8 cm away from the target. The PLD was done in a high vacuum environment (5×10^{-5} mbar) at room temperature. Glass slides were pre-cleaned using acetone and isopropanol in an ultrasonic bath (10 minutes each) and were rinsed later with deionized water. A Ag target was ablated using a 248 nm, 25 ns KrF excimer laser operating at 10 Hz. The target was continuously rotated in order to avoid drilling a hole in the target surface. The laser was focused on the target to yield an average fluence of 0.8 J cm^{-2} over a spot area 0.0375 cm^2. A planar Langmuir ion probe with an area of 0.09 cm^2 and biased at -25 V, to reject plasma electrons, was placed at 6.5 cm from the

ablation spot. The integral of the ion probe signal may be used to obtain an estimate of the deposition per pulse since, at constant ablation conditions the ratio of the ion fluence to the atom fluence per pulse will be constant. The actual deposition rate was found by grazing incidence x-ray reflectivity (XRR) to measure the film thickness and density after a given number of laser shots. The surface morphology of PLD films and Klarite substrates was studied using scanning transmission electron microscope (STEM) operating at 30 kV. The absorption of the nanoparticle films was also measured using a UV-Vis spectrophotometer.

The colloidal silver nanoparticles were synthesised according to a method developed by Leopold and Lendl[9]. Briefly, silver nitrate was reduced using an alkaline hydroxylamine hydrochloride solution, the alkalinity of which was obtained through addition of sodium hydroxide. A final pH of 7 is obtained from the resultant nanoparticle solution. 10 mL of a 10^{-2} M (MOLAR) solution of silver nitrate was added drop wise to 90 mL of a 1.67×10^{-3} M hydroxylamine hydrochloride solution, containing $3.33\text{x}10^{-3}$ M sodium hydroxide. Immediately after preparation, the nanoparticles in solution were aggregated with 1×10^{-2} M sodium chloride, which resulted in the eventual formation of the colloidal aggregates. All the chemicals were obtained from Sigma Aldrich.

Klartie substrates: The commercial SERS substrate Klarite® was obtained from Renishaw Diagnostics. This silicon substrate is patterned with micron scale pyramidal indentations and is coated with a thin layer of gold.

SERS measurements: The system used in the Raman analysis was a Horiba Jobin Yvon LamRAM HR using 633 nm laser excitation with a power of up to 12 mW, a diffraction grating of 600 lines/mm and a charge coupled device detector. A 10x objective lens was used

and an exposure time of 5 seconds was implemented for all of the spectra acquired, with the typical sample volume consisting of a 6 μL droplet.

7.2.2 Results and discussion

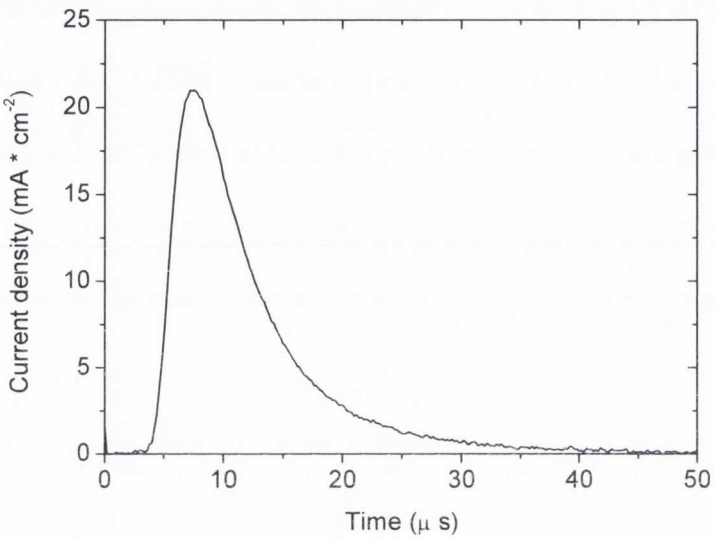

Figure 7-2 The ion time-of-flight signal for the ablation of Ag at 0.8 J cm^{-2}.

Figure 7-2 shows the ion time-of-flight signal of the laser ablation plume. The ion flux rises rapidly as the plume arrives at the probe and falls as the plume expands beyond the probe position. Integrating the ion signal yields an ion fluence of 1.5×10^{12} ions cm^{-2} per ablation pulse. Using a $1/d^2$ scaling to account for the difference in the position of the Langmuir ion probe and the substrate yields an ion fluence of 1.0×10^{12} cm^{-2} pulse at the substrate. The actual deposition rate was found by using XRR to measure the film thickness and density after a given number of laser pulses. For 37,000 pulses the film thickness was 10.2 nm and the density was 6.8 g cm^{-3} which is 65 % of solid density. Thus this film has an equivalent solid density thickness of 6.6 nm. The deposited atomic fluence per pulse is 1.0×10^{12} cm^{-2}, which is similar to ion fluence, indicating that the plume is nearly fully ionized. Figure 7-3

(a) shows a STEM image of a 7 nm Ag film prepared at a laser fluence of 0.8 Jcm^{-2}. STEM shows that the film contains well-separated nanoparticles with diameters in the range of 5-20 nm with a mean diameter of 6.5 ± 0.5nm. The mean diameter was obtained by fitting the size distribution to the log-normal distribution function.

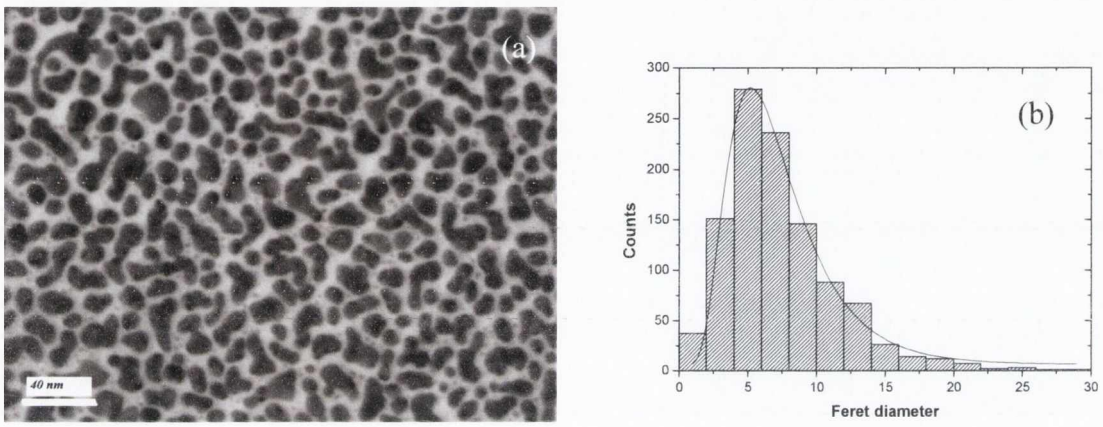

Figure 7-3 (a) STEM and (b) size histogram of Ag nanoparticle-film with equivalent thickness 7 nm prepared at a laser fluence of 0.8 J cm^{-2} using fs-PLD. The solid black line in figure (b) is log-normal fit of the experimental data.

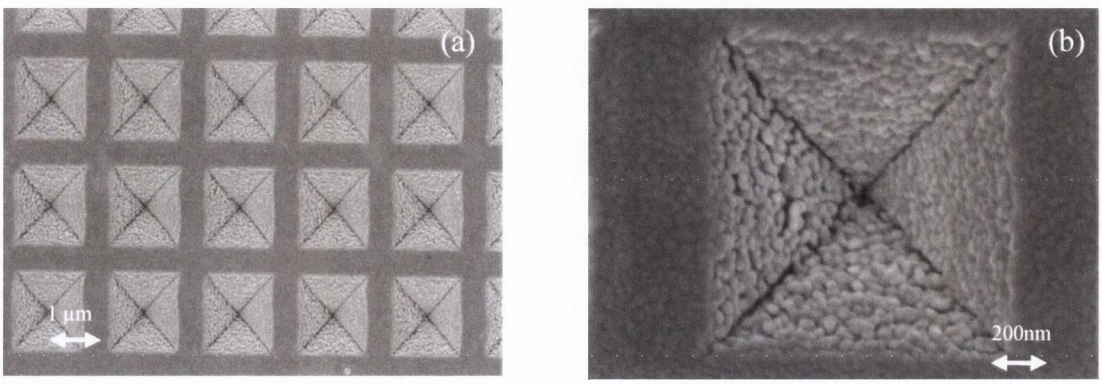

Figure 7-4 (a) SEM image of the Klarite films, showing a low-magnification view of an array of the surface features on the films. (b) Shows a high-magnification image of one of these features.

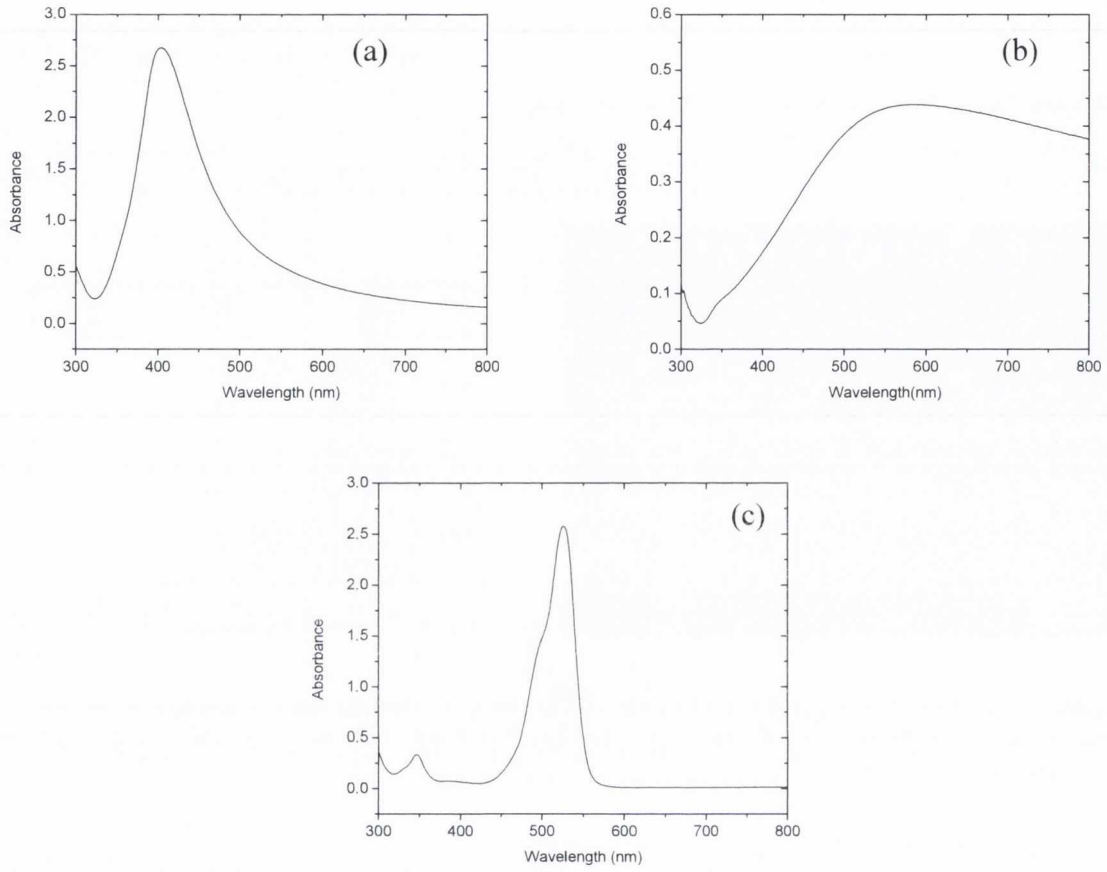

Figure 7-5 Absorption spectra of (a) the colloidal Ag nanoparticles, (b) the 7 nm Ag nanoparticle film and (c) a 3.13×10^{-5} M solution of the Rhodamine 6G dye. The spectra (a) and (c) in solution were taken using a 1 cm thick cell.

Scanning Electron Microscopy (SEM) was used to characterize the commercial Klarite films. The images in Figure 7-4 show details of the periodic distribution of the pyramid structures on the Klarite films and also a close-up of one of these structures. The images show the structures to measure about 1.2 μm along the base. In Figure 7-5 the absorption plot of silver colloidal solution, the Ag nanoparticle film and the Rhodamine 6G dye is shown. The silver colloid absorption in Figure 7-5 (a) shows a plasmonic absorption band centred at about 410 nm, while the 7 nm film shows a surface plasmon resonance (SPR) peak at the longer

wavelength of about 550 nm (see Figure 7-5 (b)), with a much broader profile than that measured for the colloidal suspension. Figure 7-5 (c) shows the absorption spectrum of Rhodamine 6G, the Raman probe used for the surface-enhanced Raman spectroscopy measurements (SERS) for characterizing various media.

7.2.3 SERS analysis

We performed SERS analysis on a solution of 6.63×10^{-5} M Rhodamine 6G using three different enhancing media, the results shown in Figure 7-6.

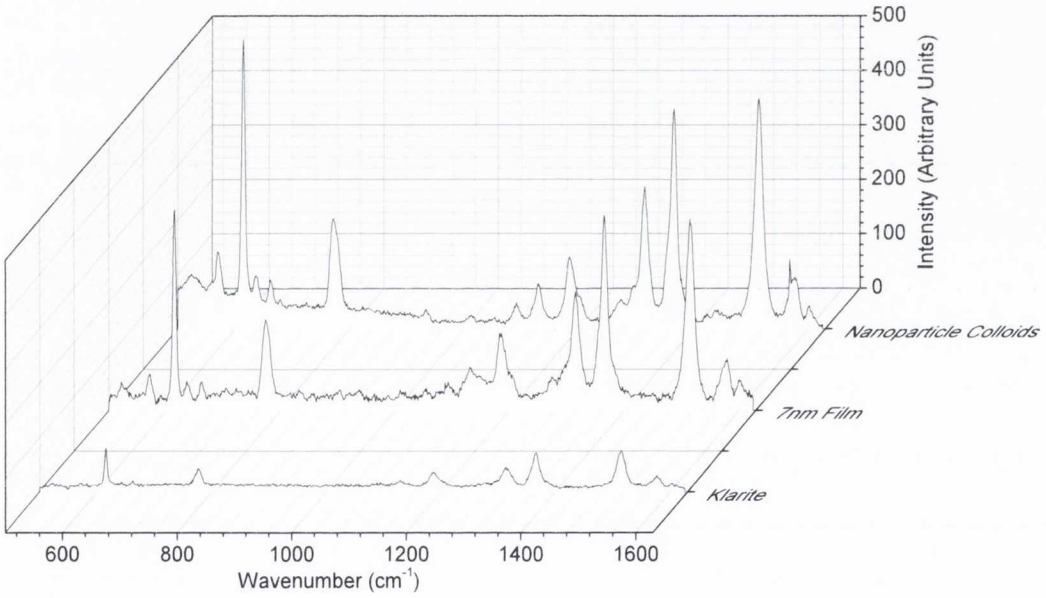

Figure 7-6 SERS spectra of 6.63×10^{-5} M Rhodamine 6G using three different enhancing media.

The Rhodamine 6G dye shows some well-defined peaks within the region examined between 500 and 1625 cm^{-1}. By comparing the obtained signals from each of the three SERS-active media, the Klarite substrate is seen to perform significantly worse in terms of the magnitude of the signal recorded. The PLD film and the nanoparticle suspension are seen to show a

similar level of SERS response, with the colloidal nanoparticle suspension performing slightly better.

The three media were further examined to test for reproducible performance. This was done by calculating the standard deviations of the six principal peaks at 616, 771, 1183, 1315 1367, 1514 cm^{-1} of Rhodamine 6G, using ten spectra taken at separate areas within the deposited droplet. The %RSD (Percentage Relative Standard Deviation) was used to examine the reproducibility of the three media, Figure 7-7 shows the % RSD data calculated using the following formula:

$$\%RSD = 100\left(\frac{\sigma}{\mu}\right)$$

Where σ is the standard deviation and μ is the average value. It can be seen that % RSD value is low for Klarite substrate, and in the case of the nanoparticle colloids used for this comparison is very high at 51%. This is somewhat of an extreme example for the colloids as this value has been observed to be only 18% for different 10-value data sets. Unfortunately, this level of unpredictability, even within its own distribution data between samples, only serves to highlight the unreliability of using the colloidal suspension without some further measure of the data spread.

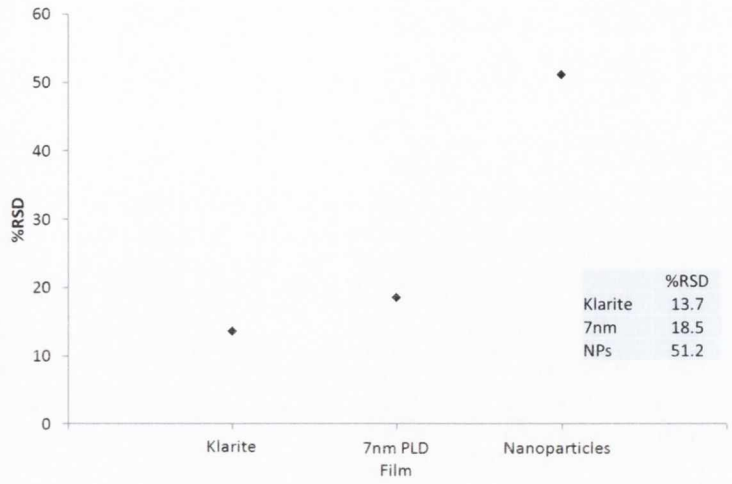

Figure 7-7 %RSD values for the various enhancing media.

7.2.4 Comparison between Ag films prepared using ns and fs-PLD.

The results of SERS measurment were also compared to nanoparticle films prepared using fs-PLD. The laser ablation in this case was carried out using solid state Ti-sapphire fs pulsed laser system (λ=800 nm, pulse width 130 fs , 10 Hz) in vacuum at peak laser fluence of 0.8 J cm^{-2}. A 4.2×10^{-4}M benzotriazole solution was used as the SERS probe to test a series of thicknesses of ns-PLD films, ranging from 1-10 nm. The results are presented in Figure 7-8 and show no detectable signal for the 1 and 3 nm films. However from 5nm thickness through to 10 nm the expected spectrum for benzotriazole is observed. Moving from the 5nm film to the 7 and 10nm films the signal was observed to increase, though not significantly between the latter two thicknesses.

The same relationship was assumed to occur for the fs-PLD films, with only films of the higher thicknesses prepared using the fs-PLD films. The SERS spectra obtained from using the two 10nm films, one representing each preparation technique were compared for

4.2×10^{-4}M benzotriazole and the results are shown in Figure 7-9 (c), the morphology of ns- and fs-PLD films are also shown in Figure 7-9 (a, b). Comparison between the two films shows the fs-PLD film to perform slightly better as compared to the ns films.

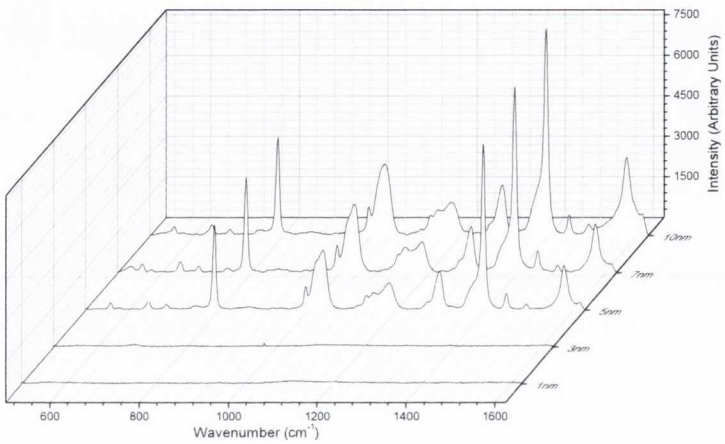

Figure 7-8 SERS spectra of 4.2×10^{-4}M benzotriazole using ns-PLD films of varying thicknesses from 1-10nm.

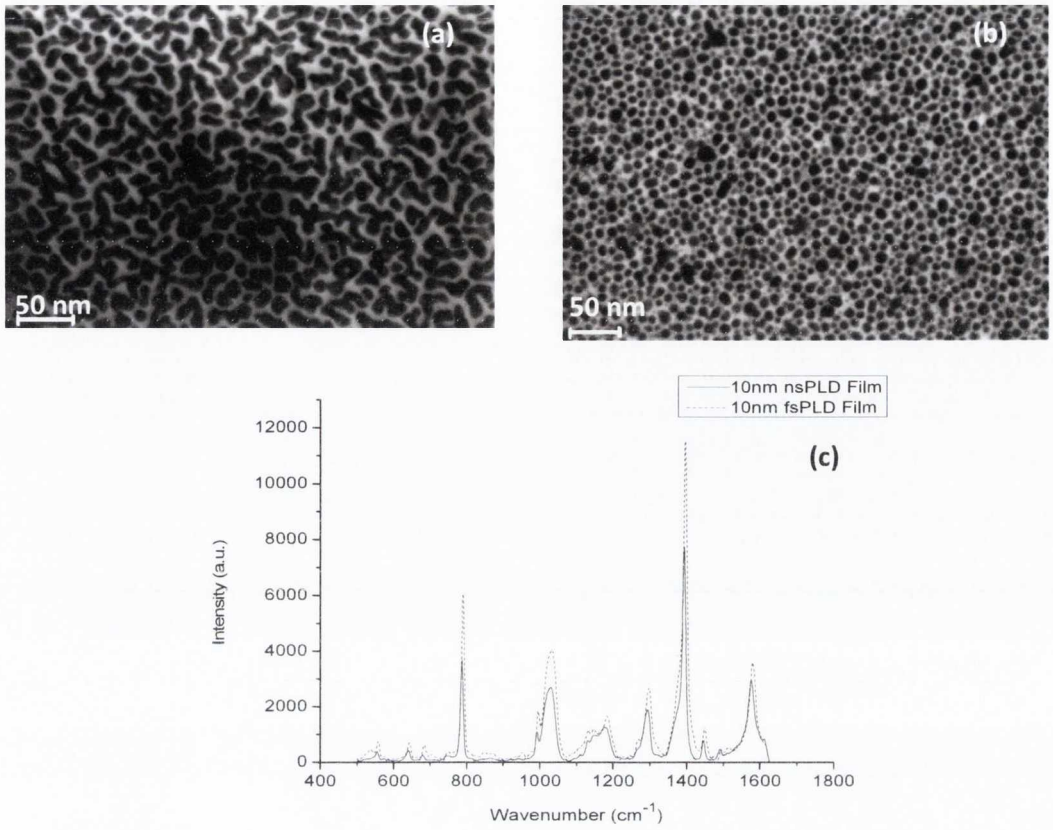

Figure 7-9 STEM of 10 nm thick (a) ns (b) fs-PLD substrates and (c) SERS spectra of benzotriazole using 10nm thick nsPLD and fsPLD films.

The same behaviour was observed for the fs-PLD films, only with films of the higher thicknesses prepared using the fs pulsed laser. The SERS spectra obtained from two 10 nm films (see Figure 7-9 (a) and (b)), one representing each preparation technique, are compared in Figure 7-9, again using benzotriazole as the probe. From these spectra it is apparent that the fs-PLD film performs better, though not by a huge amount.

Investigation of data spread for ns- and fs-PLD films comparison: In terms of substrate reproducibility the relative standard deviation (%RSD) was calculated for the various data sets. The data sets refer to ten measurements being made for each sample, with the mean and

standard deviation data deriving from measurements made of various peak heights for this data.

Table 7-1%RSD values for a range of peaks corresponding to benzotriazole (BTA) solution for ns and fs PLD films and colloidal Ag nanoparticle solution.

Spectral peak (cm^{-1}) →	792	1396
10 nm ns-PLD	23	25
10 nm fs-PLD	15	19
colloids	13	14

The reproducible performance of both the films and the nanoparticles are shown in Table 7-1, with the fs-PLD films and the colloids seen to perform better than the ns-PLD films.

7.2.5 Conclusions

In conclusion the commercial Klarite substrate offers very small SERS signal levels, which may limit their application at low analyte concentrations. The PLD substrates offer a very useful compromise of good distribution statistics alongside good SERS signal levels. According to the investigation performed for films produced by two different PLD methods i.e. ns and fs-PLD with a range of thicknesses, it was found that thicker samples produce better SERS responses using benzotriazole as the probe. Films of 10 nm thickness, prepared using ns-PLD and fs-PLD were further investigated, and it was found that the fs-PLD films performed slightly better for the benzotriazole probe.

7.3 Experiment 2: Growth of carbon nanotubes using Ni catalysts prepared by ns-PLD.

Chemical vapor deposition (CVD) is a widely used technique to produce high quality solid materials from gaseous phase and has often been used in the semiconductor industry to produce thin films for integrated circuit applications. In the CVD technique, precursor gases are delivered into the reaction chamber containing substrates at a high temperature (≈ 700 C^0). As they pass over, or come into contact, with the heated substrate, they react, or decompose, to form a solid phase which is deposited onto the substrate. The substrate temperature is a critical parameter in such experiments and can influence the reactions which need to be taken place CVD coatings are usually a few microns thick. For the catalytic growth of CNT using CVD, a carbon rich gas such as methane (C_2H_2) is used as a carbon feedstock in the reaction chamber. Briefly, the carbon-bearing molecules catalytically decompose on the surface of catalysts which is supposed to be in the liquid phase, resulting in dissolution on the catalyst nanoparticle. Upon supersaturation of carbon concentration on a particle, carbon atoms precipitate from the catalyst, leading to the formation of tubular carbon networks around or on the catalyst. The typical growth temperature for transition metal catalysts is in the range of 750-800 C^o

7.3.1 Experimental procedure

Thin Ni films with equivalent thickness of 1 and 3 nm were produced using ns-PLD at laser fluence of ~ 1 J cm^{-2}. The substrate was a Si wafer with an approximately 30 nm thick SiO_2 thermal oxide layer[‡] on it. The substrates were pre cleaned via sonication in acetone and

[‡] The substrates are custom made and the thermal oxide layer thickness was provided by the manufacturer.

isopropanol. The ablation procedure was also monitored using a Langmuir ion probe in order to obtain the ion fluence and to check reproducibility of the ablation process.

For the methane CVD experiment, the Ni-coated Si substrates were placed in a quartz tube mounted in a tube furnace. The argon gas was first passed from the quartz tube at 2.5 torr for about 10 minutes and the quartz tube was heated to the temperature of about 750 C^{o}. The argon flow was then replaced by methane (99 % purity) at 5 torr. The methane flow was lasted for 10 minutes and was replaced by argon and furnace was cooled down to room temperature. The substrates were later investigated using scanning electron microscope.

7.3.2 Result and discussion

Figure 7-10 shows atomic force micrographs of Ni nanoparticle films prepared on Si substrates with different equivalent thickness. It can be seen that the nanoparticle size increases with the equivalent thickness.

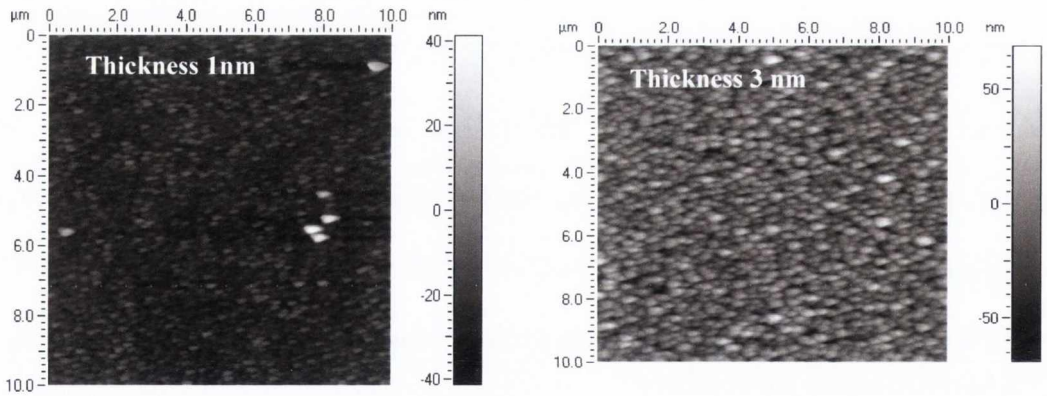

Figure 7-10 Atomic force microscope image of 1 and 3 nm Ni nanoparticle films deposited on Si substrates with 30 nm SiO_2 thermal oxide layer using nanosecond pulsed laser deposition.

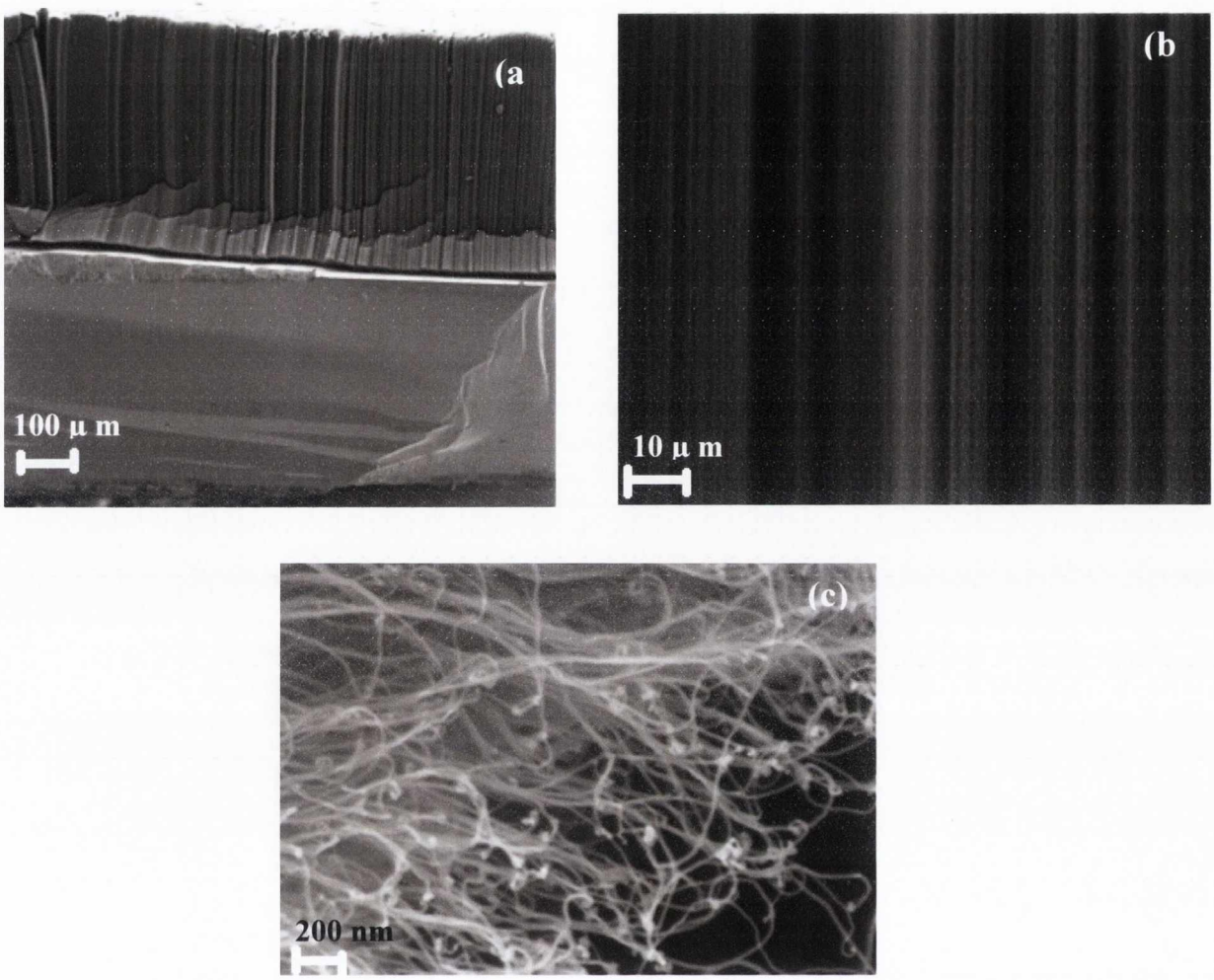

Figure 7-11 (a), (b) Scanning electron microscope image of carbon nanotubes (CNT) grown on Ni catalysts, (c) a zoomed in image at the top side of vertically aligned CNTs, the average diameter of CNTs is 10 nm.

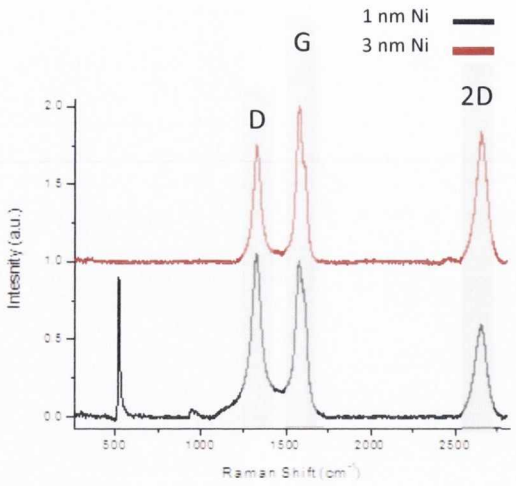

Figure 7-12 Raman spectra of multiwalled CNTs grown using Ni catalyst.

Figure 7-11 is the scanning electron micrographs of carbon nanotubes grown by chemical vapour deposition using nickel nanoparticle films as catalysts. From SEM image we can see vertically aligned growth of carbon nanotubes with diameter in the range of 10-20 nm (see figure Figure 7-11 c). Raman spectra of carbon nanotubes grown using 1 and 3 nm thick Ni catalysts are given in Figure 7-12 . The Raman spectra of CNTs show three characteristic peaks: the *D* band (~1350 cm^{-1}), the *G* band (~1580 cm^{-1}), and the *2D* (~2700 cm^{-1}). The *D* band is indicative of defects in the sample (i.e., carbonaceous impurities with sp^3 bonding, broken sp^2 bonds in the sidewalls). The *G* band results from the graphitic nature of the sample (i.e., crystallinity of the sample) and the *2D* band is indicative of long-range order in a sample and arises from the two-phonon scattering process which results in creation of an inelastic phonon[10]. Also from the low frequency Raman spectra (100-350 cm^{-1}), we do not see the radial breathing mode (RBM) which appears in the case of single walled carbon nanotubes (SWCNT).

RBMs are the characteristic phonon modes which correspond to radial expansion and contraction of a SWCNT. In this mode all atoms of the tube vibrate in phase in the radial direction (see Figure below).

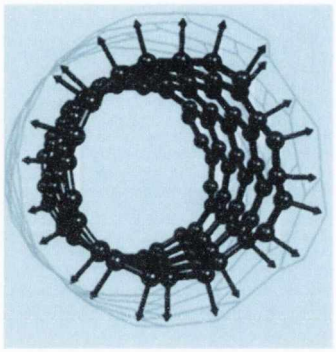

Figure 7-13 A schematic diagram of RBM from Ref. 11, the arrow indicate the phonon eignvector. The RBM leads to a periodically increase and decrease in the CNT diameter (as shown by the wire model of CNT).

Therefore the frequency of the RBM depends on the CNT diameter and is given by (in cm^{-1})[12]:

$$v_{RBM}=(c_1/d)+c_2$$

The reported values of coefficients c_1 and c_2 (from experimental and theoretical investigations) vary between 220-260 cm^{-1} nm and 0-20 cm^{-1} respectively[11,12]. The coefficient c_2 was originally introduced to account for additional external forces, e.g. interaction between CNT and substrates and between other CNT in a bundle. Depending on the diameter, the typical RBM frequency (in cm^{-1}) is in the range of 100-350 cm^{-1}.

The peaks at ~ 520 and 950 cm^{-1} are due to Si the SiO_2 substrate. The absence of RBM show that that the carbon nanotubes are muti-walled; multi-walled carbon nanotubes (MWCNT) are made of concentric graphene sheets rolled in a cylindrical form with diameters of few tens of nanometers.

7.3.3 Comparison with Ni nanoparticle films prepared using fs-PLD

The results of CNT produced by ns-PLD were also compared with one produced by the fs-PLD. Thin Ni film with equivalent thickness of 1 and 3 nm were prepared on Si substrates at peak laser fluence of ~ 1.3 J cm^{-2} at the deposition rate of 3.8×10^{-4} nm/laser shot measured using a quartz crystal deposition monitor fitted in the vaccum chamber. The Langmuir ion probe was also used to monitor the reproducibility of laser ablation process. Figure 7-14 is the AFM of Ni nanoparticle films produced using fs-PLD

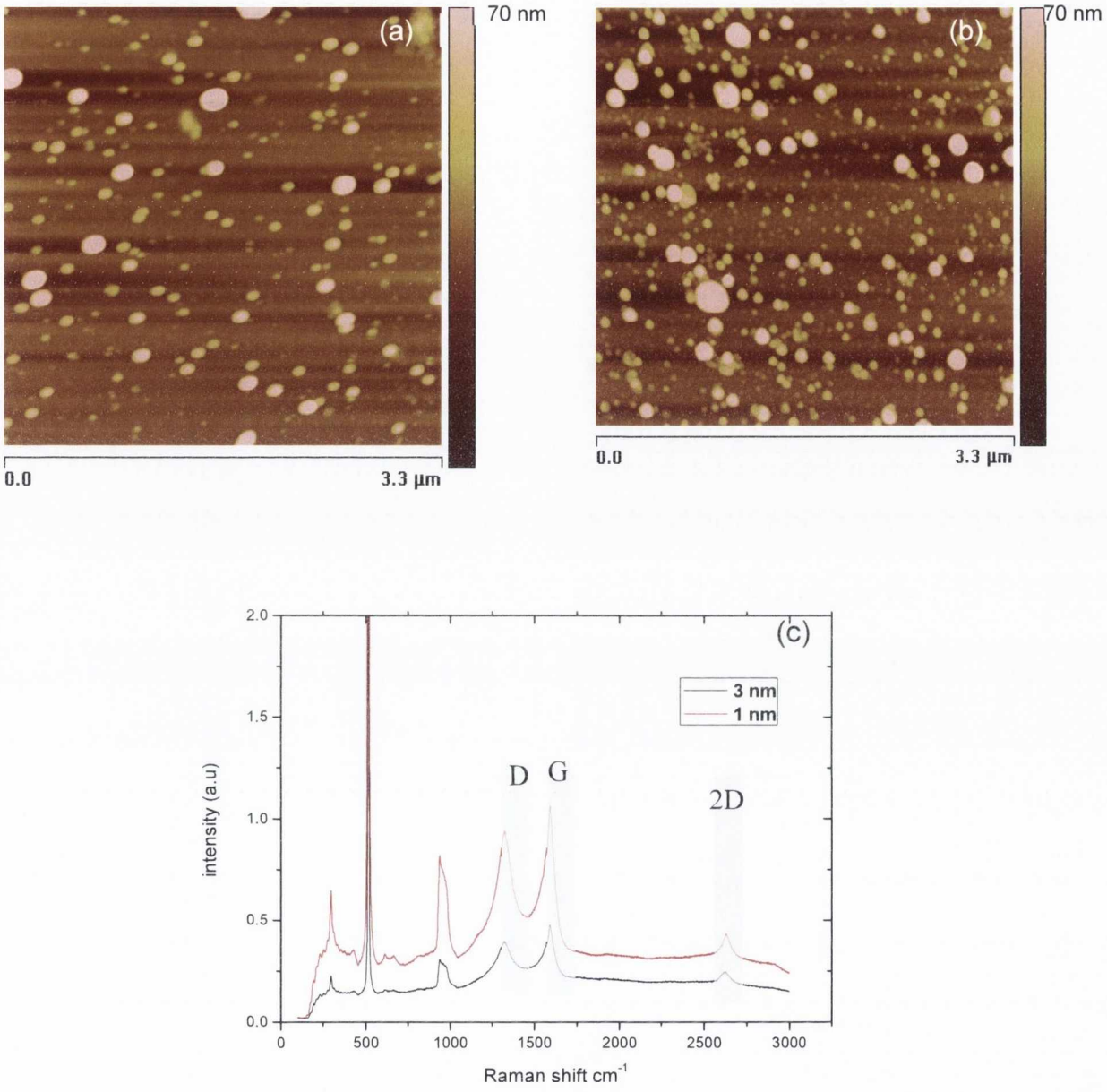

Figure 7-14 AFM of Ni nanoparticle films prepared on Si substrates using fs-PLD with equivalent thickness of (a) 1nm and (b) 3nm. (c) The corresponding Raman spectra.

It can be seen from micrographs that the areal density of particles increases with equivalent thickness and the film contains some large (aprox 100 nm in diameter) particles which are formed as a consequence of the laser fluence being well above the threshold value for fs-

laser ablation [13]. After the growth of CNT using CVD under conditions as described in section 7.3.1, the sample was characterized using Raman spectroscopy. Figure 7-15 (c) is the Raman spectra of CNT sample prepared using fs-PLD Ni catalysts. The characteristic *D*, *G* and *2D* band at 1350 cm^{-1}, 1580 cm^{-1} and 2700 cm^{-1} are clearly visible in both samples along with the substrate peaks at 520 and 950 cm^{-1} . However some additional peaks were also observed in those samples at about 300 cm^{-1} which are most likely due to fraction of single walled CNT contained in the sample. As has been described before, several parameters in the CVD experiment are responsible for the quality and types of CNT growth, one of them is size and distribution of nanoparticles. It has been observed in our experiments that fs-PLD produced narrow nanoparticle size distribution with small average nanoparticles for the same amount of deposited material, hence the smaller seed catalysts ($\leq$ 5 nm) produced in fs-PLD are potentially the origin of SWCNT. However it requires further in-depth study of Raman spectra to see if the signal is caused by the SWCNT present in the sample.

7.4 Experiment 3: Au nanostructure and single crystal nanowire growth

In this experimet, metal-semiconductor (Au-Ge) bilayer films were prepared using fs-PLD. The films were used for growth of Au nanowires and nanostructures. The nanowire and nanostructure growth technique is based on simple heating the Au-Ge bilayers and taking the advantage of different surface energies of substrate and film component. An introduction to this technique has already been given earlier. Here, the experimental procedure and results are given.

7.4.1 Experimental procedure

Au-Ge bilayers were prepared on a 275±25 μm thick, n-type Si(100) substrate by fs-PLD and sputter deposition[§]. The Si (100) substrate has a 30-40 nm thick oxide layer on it. Bi-layer samples were annealed for typically 12 h at 400 C^{o} in a 10:90 atmospheric of hydrogen and argon at a flow rate of 60 sccm and reaction pressure of 350 mTorr, with heating and cooling rates of 100 C^{o}/h. These conditions were chosen because the Au-Ge eutectic comprised of 27.0 atom % Ge melts at 356 C^{o}[4]. All characterisations were performed after the sample was cooled to room temperature. The surface morphology, crystal structure, and composition were characterized by a scanning electron microscope (SEM, Carl Zeiss, Ultra) which also works in transmission mode (STEM), energy dispersive analysis (EDX, Carl Zeiss, Ultra), and transmission electron microscopy (TEM, FEI Titan).

7.4.2 Results and discussion

10 nm thick bilayer Au and Ge films were prepared on Si (100) substrates via fs-PLD and sputter deposition. The morphology of films was studied after anealing the deposited substrate to 400 C^{o} for about 12 hours. Figure 7-16 is the SEM of a Au 10 nm/Ge 10 nm bilayer films prepared using (a) sputter deposition (b) fs-PLD. The insets show a schematic diagram of bilayer films prepared on Si before annealing

[§] 208 HR high reolution sputter coater from Tedpella Inc.

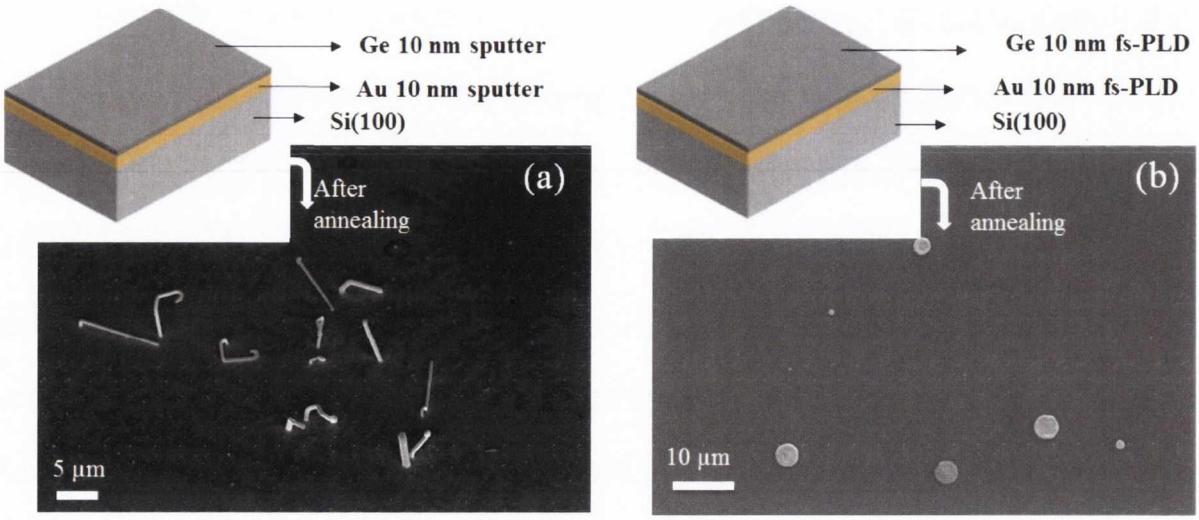

Figure 7-16 Morphology of (a) Au 10 nm sputter/Ge 10 nm sputter (b) Au 10 nm PLD/Ge 10 nm PLD films after annealing at 400 C^0 for 12 hours. The insets show a schematic diagram of bilayer films prepared on Si before annealing.

It can be seen that the sputtered films contain micrometer long nanowires, EDAX analysis show that the nanowire consists of pure Au. The nanowire growth has been understood as a surface energy driven phenomenon[3]. The surface energy** of Au (1.33 J cm^{-2}) is higher then the Ge (1.00 J cm^{-2}) so that Au tends to dewet the SiO_2 substrate with higher curvature as compared to the Ge. What follows is the explanation of the nanowire growth procedure.

The growth mechanisim of Au nanowires in this experiment was observed for different amounts of Au on Ge deposited substrates. When only 10 nm Ge was deposited on Si substrate, the sample was unchanged for 12 hour anealing layer. After increasing the amount of Au from 1 to 5 nm on Ge deposited substrate and anealing above eutectic temperature, a disordered sample surafce containing connected clusters of Au particles or a fractal like Au structure were observed, which resulted from melting and recrystallizing of the sample. Also the fractal structure was observed to be similer to well known diffusion limited aggragation

** Surface energy across the interface of Au and SiO_2 or Ge and SiO_2.

model explained by Sander *et al*[14]. After further increase in the thickness of Au (Au 10 nm / Ge 10 nm) the fractal like structure disappeared and ball shaped droplet structure and crystalline Au structures were observed. It was observed via EDAX maping and cross-cut observation of the ball-shaped eutectic nanostructures that enhanced concentration of Au on Ge leads to diffusion and supersaturation of Au inside the eutectic nanostructures and ultimately growth of Au nanowires. A similer experiment was performed using a film prepared by fs-PLD. Figure 7-16 (b) is the SEM of 10 nm thick anealed Au/Ge film prepared using PLD. In this sample, no particular nanostructure or nanowire growth was observed. Big droplet-like nanoparticles of Au were observed on the surface which may have been produced during PLD process when hot molten material in the form of liquid droplets arrive the substrate. The analysis was extended to observe films produced by a combination of fs-PLD and sputter deposition. Figure 7-17 (a) is the SEM of 10 nm thick film produced by fs-PLD of Au and sputtering of Ge.

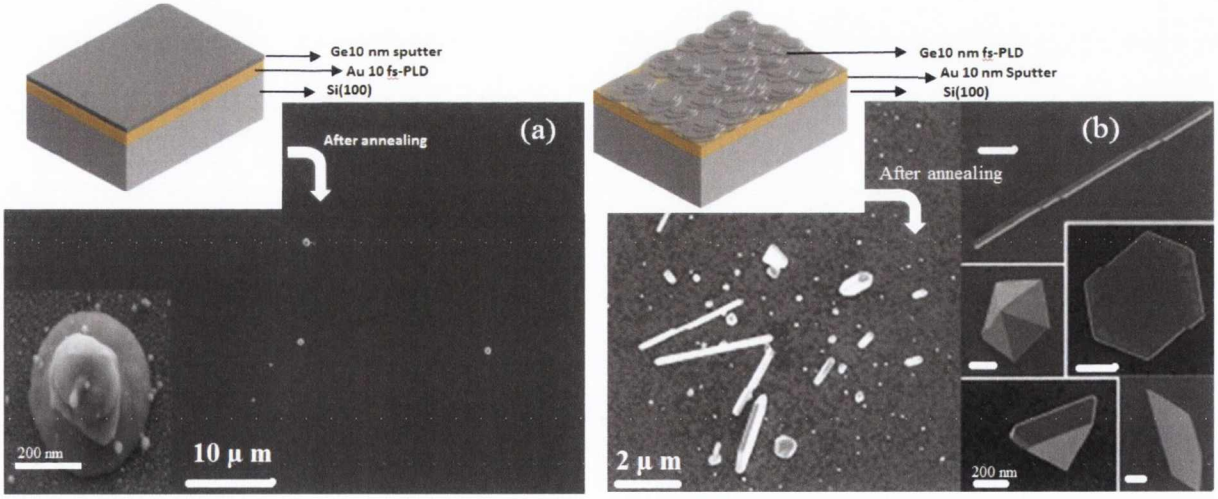

Figure 7-17 Morphology of (a) Au 10 nm PLD/Ge 10 nm sputter (b) Au 10 nm sputter/Ge 10 nm PLD sample after annealing at 400 C^0 for 12 hours, the scale bar on all sub images is of 200 nm. The insets show a schematic diagram of bilayer films prepared on Si before annealing.

In that combination some extruded micron size Au droplet were observed on the surface but no nanowires were observed. Figure 7-17 (b) is the SEM of film prepared under same condition. In this sample, Au nanowires as long as 10 μm with different thicknesses and several different shape and size nanostructures were observed. The morphology of sputtered Au and Ge PLD films prepared on SiO_2 TEM grid was also studied before anealing using the TEM. It was observed that the bilayer film contains polycrystalline Au and droplets of polycrystalline Ge (see Figure below). The possible mechanism of Au nanostructure growth at certain localized place in this case can be explained as follows:

Upon anealing, the big Ge droplets sitting on the Au (sputtered) thin film forms Au-Ge eutectic composition at different Ge rich places. Furthermore, the diffusion and nucleation supersaturates Au concentration inside these eutectic droplets (depending on the Ge particle size).

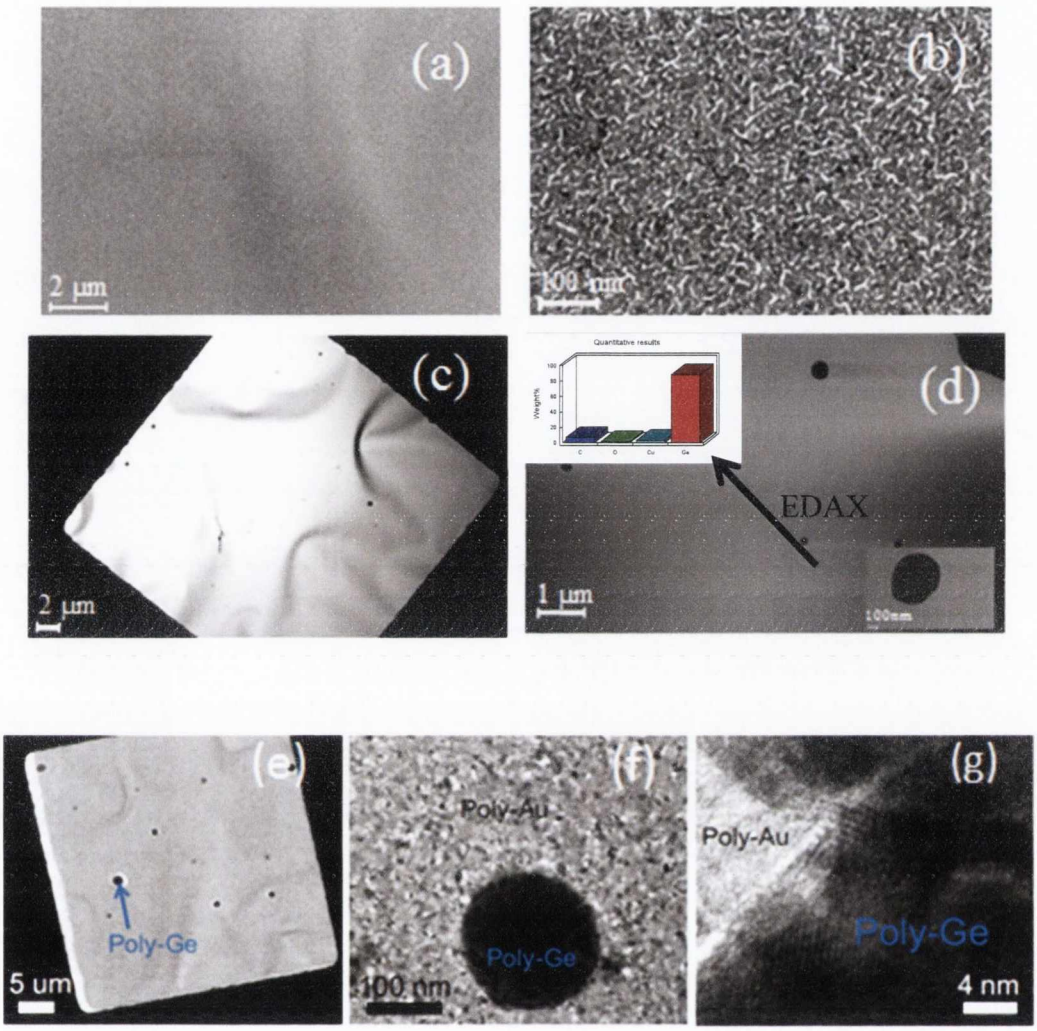

Figure 7-18 STEM of 10 nm thick (a, b) Au and (c, d) Ge at different magnifications. The material was deposited on SiO_2 coated TEM grid. The inset of (d) shows EDAX on one of big nanoparticle showing the main Ge content. (e-g) are the TEM (transmission electron micrographs) of the Au-Ge bilayer where (f) and (g) are high resolution TEM showing big polycrystalline Ge nanoparticle on polycrystalline Au layer.

This leads to the growth of Au nanowires and differnt shaped Au nanostructures at localized places on the substrates. However invesitgation of five fold Au structures needs further in-depth study.

7.5 References:

1 J. Kong, A. M. Cassell, and H. Dai, Chemical Physics Letters **292**, 567 (1998).

2 T. J. Konno and R. Sinclair, Materials Science and Engineering: A **179–180, Part 1** (0), 426 (1994).

3 S. Jung, T. Lutz, M. Boese, J. D. Holmes, and J. Boland, Nano Letters **11** (3), 1294 (2011).

4 R. Elliott and F. J. Shunk, J. Phase Equilib **1**, 51 (1980).

5 E. C. Le Ru, E. Blackie, M. Meyer, and P. G. Etchegoin, The Journal of Physical Chemistry C **111** (37), 13794 (2007).

6 Eric C. Le Ru and Pablo G. Etchegoin, (Elsevier, 2009).

7 C. D'Andrea, F. Neri, P. M. Ossi, N. Santo, and S. Trusso, Nanotechnology **20** (24) (2009).

8 N.R. Agarwal, F. Neri, S. Trusso, A. Lucotti, and P. M. Ossi, Appl Surf Sci, doi:10.1016/j.apsusc.2011.12.030 (2011).

9 N. Leopold and B. Lendl, J Phys Chem B **107** (24), 5723 (2003).

10 R. A. DiLeo, B. J. Landi, and R. P. Raffaelle, Journal of Applied Physics **101** (6), 064307 (2007).

11 J. Maultzsch, H. Telg, S. Reich, and C. Thomsen, Physical Review B **72** (20), 205438 (2005).

12 A. G. Souza Filho, S. G. Chou, Ge G. Samsonidze, G. Dresselhaus, M. S. Dresselhaus, Lei An, J. Liu, Anna K. Swan, M. S. Ünlü, B. B. Goldberg, A. Jorio, A. Grüneis, and R. Saito, Physical Review B **69** (11), 115428 (2004).

13 B. Liu et al, Applied Physics Letters **90** (4), 044103 (2007).

14 T. A. Witten and L. M. Sander, Physical Review Letters **47** (19), 1400 (1981).

Chapter 8. Conclusions and the future work

This chapter described the main conclusions resulting from the experimental work in this thesis and possibilities of future work.

8.1. Conclusions

- The ablation plume of metals (Ag, Au and Ni) produced by two laser sources, a 23 ns KrF laser (248 nm), and a 130 fs solid state Ti:saphhire laser (800 nm) was studied using an electrostatic Langmuir ion probe. The TOF ion spectrum of ns and fs laser ablation are similar; in both cases the ion signal rises when the plume front arrives at the probe and decreases as the plume expands away from the probe position. The ion fluence and net deposition were compared for two ablation regimes. The ion fluence was obtained by integrating the ion TOF signal while net deposition, in atoms per cm^2 per laser shot, was derived from the deposition rates measured on the QCM. The comparison of ion and the atom fluence at laser fluences well above ablation threshold show that the ns-laser ablation plumes are strongly ionized. In fs-ablation however, only a small fraction (~1-2 %) of material is removed as plasma. The ns- and fs- ablation efficiencies in terms of material removed and ion production per mJ of laser energy were also calculated. The calculation shows that the ion production efficiency is similar in both cases, while the material removal efficiency of fs-ablation is approximately 25 times higher than ns-ablation. From the measured ion TOF signals, the ion energy distribution was also derived, it was observed that both the ns-

and fs- ablation plumes are energetic and the distribution extends up to a few hundred of eV.

- The fs-ablation plume was also investigated using an energy selective time of flight mass spectrometer (ES-TOFMS). Depending on the charge state, the spectrometer can detect species with different energies in the ablation plume. The analysis of the Ag fs-ablation plume showed that the plume contains both singly and doubly ionized Ag with energies up to a few hundred eV. The device was also used to study the charge state of nanoparticles in the fs-ablation plume. However charged nanoparticles were not observed in a preliminary experiment.

- It has been shown that both ns- and fs-PLD can be used to fabricate nanoparticle films of different noble and transition metals. In ns-PLD the nanoparticles are formed by nucleation and surface diffusion of deposited material on non-wetting substrates. The particle size grows with the equivalent thickness since the coalescence and agglomeration between small nanoparticles play an important role. However a similar behavior was observed for Ag films prepared using fs-PLD which indicates some similarity in the nanoparticle growth mode. This similarity was also observed in a recent experiment of Ag nanoparticle film by fs-PLD [1]. In addition to microscopy analysis, the nanoparticle films were also characterized using a unique technique called X-ray reflectivity (XRR). The XRR has an advantage of simultaneously measuring equivalent thickness, density and surface and interface roughness of thin films[2]. In our experiments it was applied to nanoparticle films. The measured equivalent thickness was in accordance with QCM results. The average density of

both ns- and fs- films was observed to be less than the material solid density. Also the RMS surface roughness was observed to be higher for fs-PLD films which indicate that the fs-PLD grown films contains more nanoisland structures which might be stacked on each other.

- Optical absorption of both ns and fs-PLD Ag films increases with the equivalent thickness. The absorption spectra also show a characteristic surface plasmon resonance (SPR) peak around 400-500 nm. The measured spectra were also compared with theoretical models. Results show that the Maxwell-Garnett effective medium theory and a commercial package called Granfilm can be used to describe the main features of SPR.

- Space- and time-resolved fast photography and OES of fs-ablation of metals show that the plume is composed of two main components; a fast atomic cloud leaving the target with velocity of few km s^{-1} followed by a slow component moving perpendicular to the target surface with velocity approximately 10 times smaller than the fast component. OES results confirm that the fast component is composed of atoms or ions of the ablated material and the slow component is due to hot nanoparticles of the ablated material.

- The intensity calibrated optical emission spectra of hot nanoparticles were used to obtain their temperature. It was observed that the spectral radiance of the Ag nanoparticles plume was lower as compared to Au and Ni, but its atomic plume still shows a strong optical emission. Hence further OES study is required to understand the unexpected behaviour of Ag fs-ablation plumes. Theoretical calculations show that the spectral emissivity of Ag nanoparticle is approximately 10 times smaller than

Au and Ni. Hence the lower optical emission can be related to the optical properties of the materials.

- In chapter 6, third order nonlinear optical properties of pure Au nanoparticle films prepared using ns and fs-PLD were studied using a Z-scan technique. The obtained closed aperture scans of films prepared by both methods show a pre-focal transmission peak, followed by transmission valley which reveals that the negative sign of Re (χ^3) corresponds to negative lensing. The corresponding open aperture scans show a positive value of the nonlinear absorption coefficient which represents the reverse saturable absorption (RSA) and hence the optical limiting effect of the nanoparticles. The experimental findings agree with the available results for Au based nanomaterials for a similar excitation laser[3,4]. However it is not clear if these effects are due to light scattering or some heating effects of nanoparticles. Some initial calculations show that the heating and vapourization of nanoparticles may not be the dominant process under the experimental conditions used. Looking at the spectrum of at the emitted radiation from the nanoparticle sample, no sign of third harmonic generation was observed.

- In chapter 7, the application of Ag, Ni and Au nanoparticle films were used for SERS, catalytic growth of CNT and Au nanowire growth. The SERS results of ns-PLD films were also compared with commercially available Klarite and those prepared with the fs-PLD. It was observed that the ns-PLD films give better SERS signal level as compared to the commercial substrates. Also the comparison between ns- and fs-PLD films showed that the fs-PLD films performed slightly better.

However looking at the statistical analysis (% RSD) further optimization is required for PLD films. We are already working in collaboration with other groups in TCD for the optimization and reproducibility experiments for SERS using nanoparticle films prepared by both PLD methods. The Ni films with varying equivalent thickness prepared by ns- and fs-PLD were successfully used for catalytic growth of CNTs. The morphology of films was studied using AFM. The CNTs were characterized by Raman spectroscopy. AFM images showed that the films are nanostructured. The Raman analysis showed that both the samples contain multi walled carbon nanotubes (MWCNTs).

- In the final experiment, Au nanowires and nanostructures were fabricated. The technique is based on annealing Au-Ge bilayer thin films (10 nm each) to achieve the eutectic temperature (360 C^0) and taking advantage of surface energy of both materials. Different combinations of Au-Ge bilayer thin films were prepared using sputter deposition and fs-PLD. The Au 10 nm sputter/Ge 10 nm sputter system leads to growth of few μm long crystalline Au nanowires, where the Au 10 nm sputter/Ge 10 nm fs-PLD films leads to growth of polycrystalline Au nanostructures. The reason for the growth of Au nanostructures is supposed to be due to (100-200 nm size) Ge particulates sitting on the sputtered Au films which super saturates the Au concentration upon annealing, and leads to growth of different shaped Au nanostructures.

8.2. Future work

- **Size selection of nanoparticle experiment:**

  For future experiments, a target bias technique is suggested to produce charged nanoparticles. If the nanoparticles acquire charge, it should also be possible to make size selection via electrostatic deflection. The technique is based on charging metal nanoparticles immersed in plasma to a floating potential. The experimental setup of the technique is shown in Figure 8-1. The target can be biased up to a few 100 V potential using the circuit shown in the figure. The experiment can be performed in a low pressure (0.1-1 torr) argon gas pressure. In this way a DC-glow discharge and hence plasma can be formed through which the nanoparticle plume can flow. Since the electrons are more mobile than the ions in the plasma the particle can become negatively charged by collecting electrons on its surface. The magnitude of the charge can be estimated from the electron temperature ($\phi_s \approx z T_e/e$)[5] where ϕ_s is the floating potential on the surface of spherical metal particle, e is elementary charge and z is the coefficient of proportionality.

  The above described method is plasma based charging. It has also been suggested that laser ablated nanoparticles can be charged via photoionization. In this method the ablation plume is subjected to a pressure-reducing differential, there, the irradiation of the plume via secondary laser leads to photoionization. Ehbrecht *et al.* applied this technique for SiH_4, the detail can be found in Ref. 6. For the size selection of charged nanoparticles, the electrostatic deflection can be used. The theoretical description of the deflection of a charged nanoparticle in the electric field between two metal plates is given in Appendix C. However, the energy selective time-of-flight mass

spectrometry can also be used to analyze the charge state of nanoparticles and to record their energy spectrum.

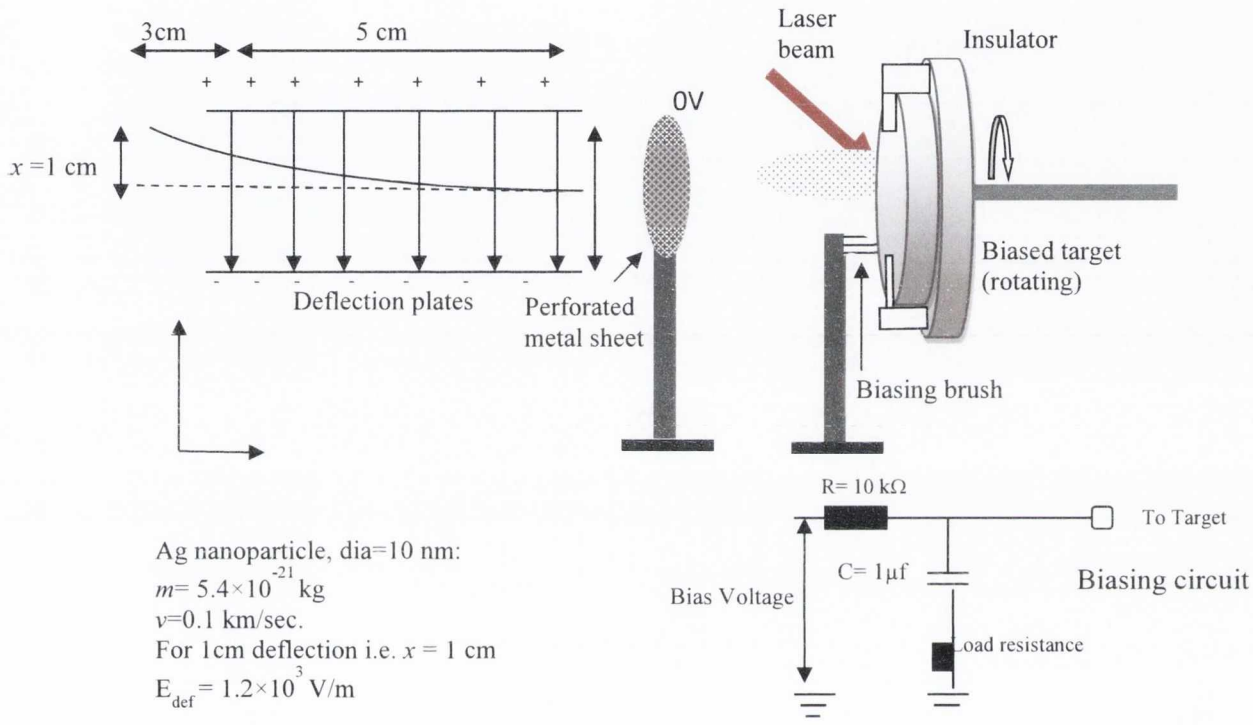

Figure 8-1 Experimental setup of charged nanoparticle deflection

- **Emissivity calculation of hot metal nanoparticles:**

The current calculation for spectral emissivity was performed using room temperature dielectric constants. However it would be more appropriate for future experiments to use high temperature values of optical constants for emissivity calculations. Also a controlled fs-ablation experiment for Ag should also be performed to obtain the atom and the ion yields to calculate the ionization fraction. The spectral emissivity and the ionization fraction measurements would be helpful to understand better the

phenomenon like growth dynamics of Ag nanoparticles on the solid substrates and reduced optical emission from the Ag nanoparticle plume.

- Furthermore, it will also be useful to do a direct measurement of the optical absorption through the nanoparticle plume of Ag as well as of Au and Ni for comparison. The schematic diagram of the experimental setup is shown in Figure 8-2. The laser ablation is performed by a fs-laser (130 fs, 800 nm). A secondary laser (the detection laser) aligned parallel to the target surface; passing through the ablation plume can be used to study the optical absorption of the nanoparticles. The output of the laser can be monitored via a fast photodiode (the detector) and the detector signal can be recorded using oscilloscope. The absorption of the secondary laser by the nanoparticle plume will give a transient signal and hence will give information about the optical absorption of the nanoparticle plume.

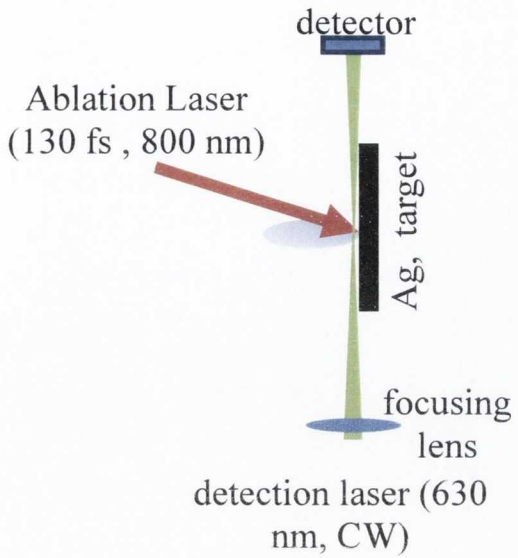

Figure 8-2 Schematic diagram of the experimental setup for nanoparticle plume absorption measurements.

- **Further investigation of nonlinear optical properties of Au nanoparticle films:**

  It will be interesting for future experiments to do a controlled florescence measurement experiment along with the Z-scan to look at how the fluorescence of the sample changes with laser intensity. This will be useful to learn more about two or three photon absorption mechanisms. It will also be interesting to fabricate nanocomposite films by ns- and fs-PLD such as $Au/BaTiO_3$ and Au/TiO_2 to study the enchantment factor in the nonlinearity, as these materials are appropriate and have shown large nonlinear absorption cross sections as compared to the pure metal films[7,8].

8.1 References

1 A. De Bonis, A. Galasso, N. Ibris, M. Sansone, A. Santagata, and R. Teghil, Surface and Coatings Technology 207 (0), 279 (2012).

2 T. C. Huang and W. Parrish, Adv in X-ray Anal 35A, 137 (1992).

3 F. Cui et al, J. Opt. Soc. Am. B 26 (1), 107 (2009).

4 I. H. Elim, J. Yang, J. Lee, J. Mi, and W. Ji, Applied Physics Letters 88 (8), 083107 (2006).

5 S. Khrapak, Physics of Plasmas 17 (10), 104502 (2010).

6 M. Ehbrecht, B. Kohn, F. Huisken, M. A. Laguna, and V. Paillard, Physical Review B 56 (11), 6958 (1997).

7 C. Cong, N. Tingyin, Z. Yueliang, Z. Dongxiang, W. Pei, M. Hai, and Y. Guozhen, Journal of Physics D: Applied Physics 41 (22), 225301 (2008).

8 J. Wang and W. J. Blau, Journal of Optics A: Pure and Applied Optics 11 (2), 024001 (2009).

Appendix A: Introduction to the Anisimov model of plasma plume expansion (Mathematica code)

Solution of the Anisimov model from the papers of Anisimov, Bauerle and Luk'yanchuk, Phys. Rev B 48, 12076 (1993) and Hansen, Schou and Lunney, Appl. Phys. A 69, S604 (1999)

S. Amoruso - May 2009.

Definition of the problem and variables

The model considers the three-dimensional isentropic and adiabatic self-similar solutions of the gas dynamical equations describing the expansion of a plasma plume of energy Ep and mass Mp. As this variables appears as a ratio Ep/Mp they can be also considered (as here) as the energy and mass of a single particle in the plume, a variable which can be determined experimentally. This are related in the value of $\beta=(5\gamma-3)$ Ep/Mp, γ being the adiabatic exponent of the plume. The initial plume has an ellipsoidal shape with dimension 2 X0 and 2 Y0 in the plane of the target and a thickess Z0 along the normal to the target surface. At later time (t), the boundaries of the plume are given by X(t), Y(t) and Z(t) along the respective axes x, y and z. x indicates the axis along the larger dimesion of the initial plume, y indicates the axes along the smaller dimension of the inizial plume and z is the axis of the target normal. For a symmetric plume X0=Y0=R0 and X(t)=Y(t)=R(t). See the schematic drawing and note in the file Anisimov.doc.

Dimensionless variables are introduced to solve the equations, as follows:

$\tau=t/t0=t/(X0/\sqrt{\beta})$;

$\xi=X/X0$; $\eta=Y/X0$; $\zeta==Z/X0$; $\xi^0=X0/X0=1$; $\eta^0=Y0/X0$; $\zeta^0==Z0/X0$.

SI units and dimensionless variables are used in the following.

Clear[X,X0,Y,Y0,Z,Z0,t, τ, ξ, η, ζ, ξ^0, η^0, γ,β,Ep,Mp,g1,g2,g12,sol1,sol2];

X0=1250.0 10^{-6};Y0=750.0 10^{-6};Z0=72.9 10^{-6}; (* initial plume dimensions, in m *)

γ=1.25 ; (* adiabatic coefficient *)

Ep=30 1.602 10^{-19}; (* energy per particle in J = energy per particle in eV × electron charge in C *)

Mp=107.86*1.66*10^{-27};(* mass of the particle in kg = mass of the particle in u × unit atomic mass *)

β:=(5 γ-3) (Ep/Mp) (* τ parameter of the model defining the time-scale parameter - time t=(X0/Sqrt[β])τ *)

ξ [t]:=X[t]/X0; η [t]:=Y[t]/X0; ζ [t]:=Z[t]/X0; (* definition of the dimensionless variables *)

τ[t]:=(t *$\sqrt{\beta}$)/X0; ξ^0=X0/X0; η^0=Y0/X0; ζ^0:=Z0/X0; (* dimensionless time τ, plume initial in-plane, η^0, and normal aspect ratio, ζ^0 *)

t0=X0/$\sqrt{\beta}$; (* time scale parameter in seconds, the time t= τt^0 *)

u0= $\sqrt{\frac{2\,Ep}{Mp}}$;

A sample ion TOF signal using above parameters (probe distance 5.8 cm)

ListPlot[TOF, PlotRange: All, Frame:True, FrameLabel{"time t (s)", "Flux"},PlotLabel "approximate TOF profiles vs time"]

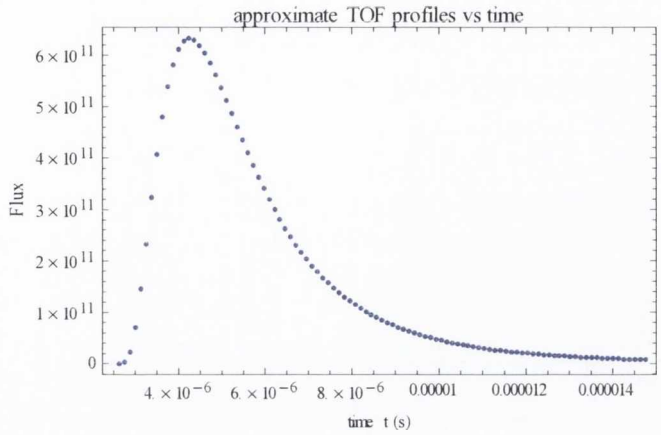

Export["E:\anisimov\TOF.dat",TOF,"Table"]

E:\anisimov\TOF.dat

Generation of the TOF profile in real time coordinates used in the experiment with the same step of the bin used in the acquisition.

Appendix B: Maxwell-Garnett effective medium theory

SetDirectory["E:/college computer/Data/optical properties theoratical/refractive index data Ag"];

Directory[]

FileNames[]

nkin =Import["METALS_Silver_Palik.csv","csv"];

lambda =Take[Flatten[Take[nkin,All,{1}]] ,{2,-1}];

n =Take[Flatten[Take[nkin,All,{2}]] ,{2,-1}];

k =Take[Flatten[Take[nkin,All,{3}]] ,{2,-1}];

$E1=n^2-k^2$;

E2=2n k;

"refractive index of ambient medium"

n1=1+0I

"refractive index for substrate"

n3=1.5+0I;

Enp=E1+I E2 ;

Em=1.625+0I;

f=0.2

d=1;

dfilm=(d/f);

"effective dielectric function"

Eeff= Em(1+(3f((Enp-Em)/(Enp+2Em)))/(1-f((Enp-Em)/(Enp+2Em))));

"refractive index of composite film"

$n2 = \sqrt{\text{Eeff}}$;

neff=Re[n2];

keff=Im[n2];

δ=((2*Pi)/(1000lambda)*n2 *dfilm);

r12=(n1-n2)/(n1+n2);

r23=(n2-n3)/(n2+n3);

t12=2*n1/(n1+n2);

t23=2*n2/(n2+n3);

"Tranmittacne"

T=n3/n1 (Abs[(t12 t23 Exp[I □])/(1+r12 r23 Exp[2I □])])^2;

T1=T*(1/0.96);

"Absorbance"

A=-Log [10,T1];

"Absorption coeffecient"

α=A/(dfilm*10^{-7});

"Plot[neff[lambda],{lambda,0.2,0.8},PlorRange□All]"

"T=Table[{1000 lambda[[i]],neff[[i]]},{i,1,240}];

Clear[T,neff]"

ListLinePlot[Partition[Riffle[1000lambda,neff],2],PlotRange□{{200,800},All},PlotLabel□

"real part of effective dielectric fucntion"]

ListLinePlot[Partition[Riffle[1000lambda,keff],2],PlotRange□{{200,800},All},PlotLabel□"imaginary part of effective dielectric fucntion"]

ListLinePlot[Partition[Riffle[1000lambda,A],2],PlotRange□{{200,800},All},PlotLabel□"absorbance"]

ListLinePlot[Partition[Riffle[1000lambda,T1],2],PlotRange□{{200,800},All},PlotLabel□"tranmittance"]

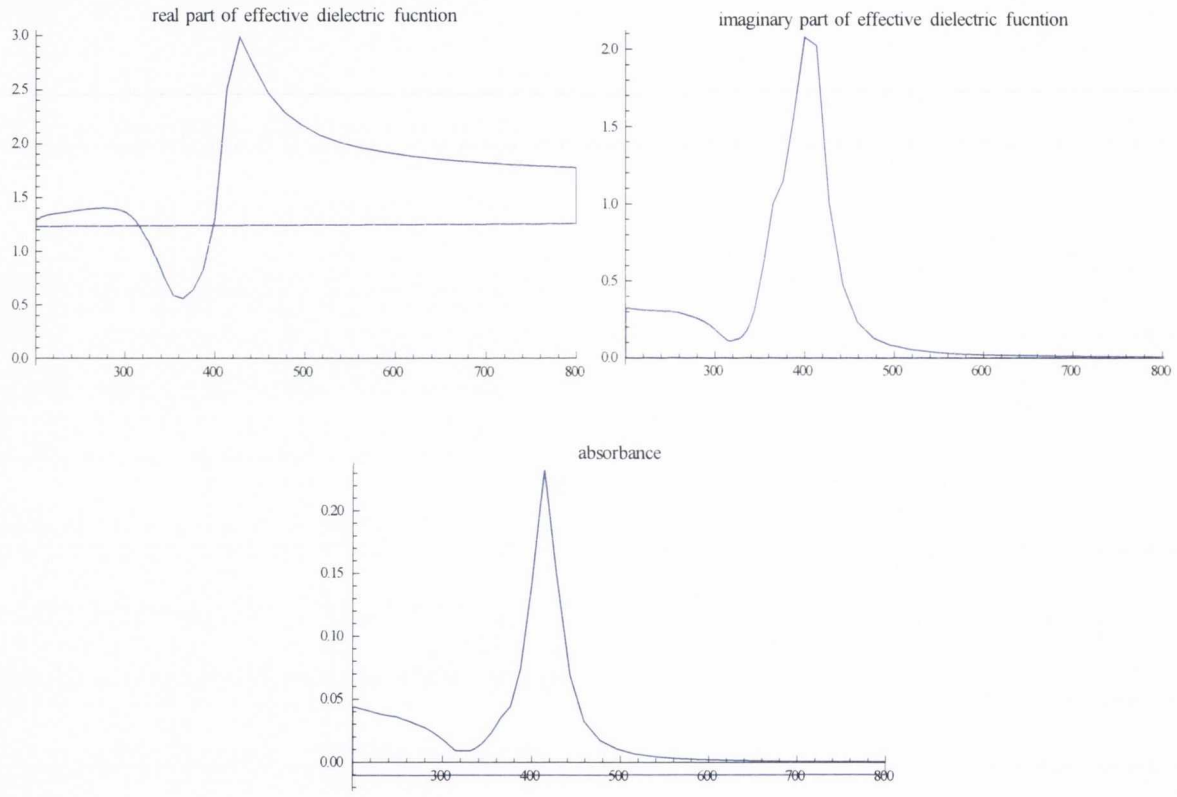

Appendix C: Deflection of a charged particle in the electric field.

Charged particle experiences a force when in the region of an electric field which is given by.

$$\vec{F} = q\vec{E}$$

Where F is the force exerted on particle in electric field q is the charge of particle and E is the electric field strength.

Hence, the magnitude of transverse force on the particle of charge (q= *-e)* due to the electric field is given by

$$eE = ma_x$$

1

using Newtons 2nd law, where a_x is the acceleration for time t given by:

$$t = \frac{L}{v}$$

2

Where L is the length of deflection region and v is the longitudinal velocity of charged particle. The acquired transverse velocity at time t *is* then given by.

$$V_x = a_x t$$

From equation 1 & 2

$$V_x = \frac{eE}{m}\frac{L}{v}$$

3

Deflection of charged particle of mass *m* and charge; *e*

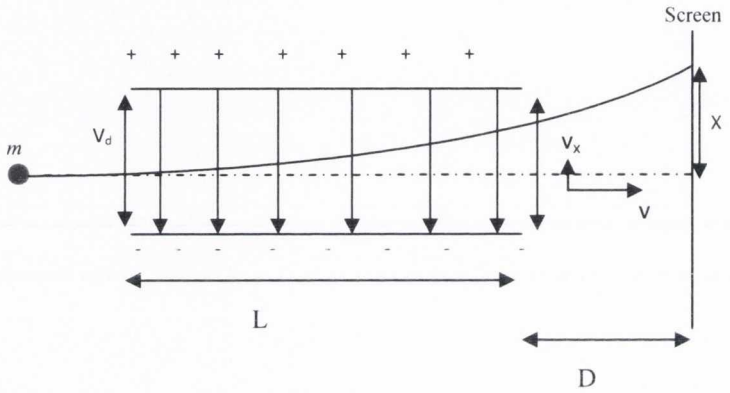

Where *m* is the mass of particle, the particle takes additional time (*D/v*) to reach the screen and travels a longitudinal distance *D* and undergoes here a transverse displacement *x,* which is given by:

$$x = v_x \frac{D}{v}$$

Using equation 3

$$x = \frac{LeED}{mv^2}$$

where *x* is the deflection of the particle on the screen. It can also be shown that the total deflection of charged nanoparticle from the middle of the deflection region is given by

$$x = \frac{eEL}{mv^2}(D + L/2)$$

The corresponding deflection electric field is given by:

$$E_{def} = \frac{xmv^2}{eL(D + L/2)}$$

For a silver nanoparticle of size 10nm and charge q = -e the deflection field we need for a specific L and D can be calculated using above equation.

Suppose

L = 5cm, D=3cm

Mass of Ag nanoparticle of size 10 nm = 5.4×10^{-21} Kg

Using the velocity of charged nanoparticles in a femtosecond plume; v = 0.1 km/sec.

For a 1cm deflection i.e. x = 1 cm

$$E_{def} = 1.2\times10^{3}\ V/m$$

Where the deflection electric field is given by

$$E_{def} = -dV/dx$$

$$= V_{def}/d$$

Where d is the distance between the deflection plates.

Appendix D: Description of lognormal distribution and Feret diameter.

Normal and lognormal distribution:

The Gaussian (normal) distribution is most often assumed to describe the random variation that occurs in the data from many scientific disciplines; the well-known bell-shaped curve can easily be characterized and described by two values: the arithmetic mean $\bar{x}$ and the standard deviation σ, so that data sets are commonly described by the expression $\bar{x} \pm \sigma$.

However many measurements show a more or less skewed distribution. Skewed distributions are particularly common when variance is large, and values cannot be negative[1]. This can be seen in several physical quantities such as distribution of mineral resources in the earth's crust and the distribution of metal nanoparticles, such as silver nanoparticles, fabricated by thermal evaporation. Such skewed distributions often closely fit to the log-normal distribution. By definition if X is a random variable with normal distribution then $Y=exp(X)$ will have lognormal distribution. Likewise, if Y has lognormal distribution if $X=log(Y)$ will have normal distribution.

Now it is important to know about validities of both normal and lognormal distributions. Both forms of variability are based on a variety of forces acting independently of one another. A major difference, however, is that the effects can be additive or multiplicative, thus leading to normal or log-normal distributions, respectively. Galton in 1898 presented a physical model of the distributions generated by additive and multiplicative processes to demonstrate normal and lognormal distributions. Figure 1 shows two panels, panel (a) is made of equally spaced isosceles triangles whereas panel (b) consist of scalene (although they appear to be isosceles in the figure)

triangle with longer side to the right. The metal particles are dropped from the funnel at the top of triangle geometry and allowed to fall into receptacles after many random deviations. The explanation of such processes is given in figure caption.

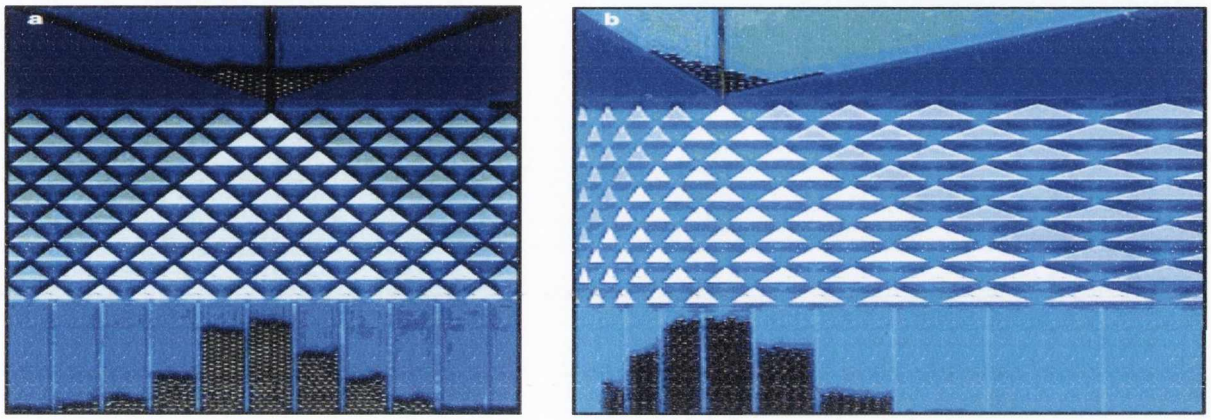

Figure 1 Physical models demonstrating normal and log-normal distributions. Particles fall from a funnel onto tips of triangles, where they are deviated to the left or to the right with equal probability (0.5) and finally fall into receptacles. If the tip of a triangle is at distance x from the left edge of the board, triangle tips to the right and to the left below it are placed at (x + c) and (x – c) for the normal distribution (panel a), and x · c and x / c for the log-normal (panel (b)) and c being a constant. The distributions are generated by many small random effects (according to the central limit theorem) that are additive for the normal distribution and multiplicative for the log-normal.

A model for lognormal distribution of nanoparticles grown by thermal evaporation has been given by J. Soderland et al[2]. In this model the origin of lognormal distribution of nanoparticle size has been associated with the particles growth time i.e. the particle size is assumed to be power function of growth time, which classically was considered as linear, and the distribution of growth time follows a lognormal distribution.

According to this model, during the growth process, the atoms are absorbed by the particle of surface area A at a constant rate γ' i.e. $dV/dt=\gamma'(A)$. Since $V \propto r^3$ and $A \propto r^2$ it follows that $r \propto t$. Since the particle size i.e.r is proportional to time the volume should follow cubic of time i.e. $V \propto t^3$ which shows that the particle volume is a cubic function of growth time.

Feret diameter:

STEM gives us two-dimensional images of randomly shaped nanoparticles distributed on the substrate from which the size distribution analysis can be made. In microscopy, there exist a few useful methods which have mostly been used to determine the particles diameter. These include Martin diameter, Feret diameter, and projected area diameter. The definitions of each one is given in the following section.

Martin diameter is defined as the averaged cord length which equally divides the projected area of the particle. Feret diameter is the distance between pairs of parallel tangents to the two points, such that the points lie at the maximum distance between the boundary of a particle. Some authors also write this as a maximum Feret diameter. The projected area diameter is the diameter of a sphere having the same area as the particle. These diameters are schematically represented in Figure 2. The projected area diameter d_A of a particle can be related to the particle projected A as $dA=(4A/\pi)^{1/2}$.

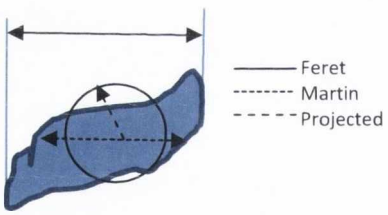

Figure 2 Schematic illustration of different particle diameters based on 2D projected image of a particle.

Martin diameter and Feret diameter are the most commonly measured diameters for particles with random shapes and distribution, since these diameters depend on the particles shape and orientation under which the measurement is made. Thus it gives us a statistically significant measurement. However for these measurements one requires a large number of sampled particles

measured in an arbitrarily orientations. The error associated with such diameter calculation is usually presented as the standard deviation.

In the perspective of this thesis work, Feret diameter was chosen for the size distributions analysis. Since Feret diameter has already been used for the analysis of nanoparticle films prepared by PLD[3]. Also, it gives an insight about the limit of equivalent thickness at which nanoparticles turns into elongated connected structures (the percolated structures), which provide electrical conduction path in thin nanostructured films[3,4].

Referances:

1 E. Limpert., W.A.Stahel., and M.Abbt, Bioscience **51** (5), 341 (2001).

2 J. Söderlund, L. B. Kiss, G. A. Niklasson, and C. G. Granqvist, Physical Review Letters **80** (11), 2386 (1998).

3 J. C. Alonso, R. Diamant, P. Castillo, M. C. Acosta–García, N. Batina, and E. Haro-Poniatowski, Appl Surf Sci **255** (9), 4933 (2009).

4 F. Ruffino and M. G. Grimaldi, Journal of Applied Physics **107** (7), 074301 (2010).